RUHR-UNIVERSITÄT BOCHUM

Cuong Manh Le

Experimental validation of the effective stress concept in unsaturated soils using the suction stress approach across multiple test types and a wide suction range

Bochum 2025

Heft 87

Schriftenreihe des Lehrstuhls für
Bodenmechanik, Grundbau und Umweltgeotechnik

Herausgeber: Torsten Wichtmann

ISSN 2699-1020

Cuong Manh Le Validation of the effective stress concept in unsaturated soils 87

ISSN 2699-1020

Ruhr-Universität Bochum
Schriftenreihe Bodenmechanik, Grundbau und Umweltgeotechnik
Heft 87

Herausgeber:
Prof. Dr.-Ing. habil. Torsten Wichtmann
Ruhr-Universität Bochum
Fakultät für Bau- und Umweltingenieurwissenschaften
Lehrstuhl für Bodenmechanik, Grundbau und Umweltgeotechnik
44801 Bochum
Telefon: 0234/ 3226135
Internet: www.bgu.ruhr-uni-bochum.de

ISSN 2699-1020

Experimental validation of the effective stress concept in unsaturated soils using the suction stress approach across multiple test types and a wide suction range

Dissertation

as a requirement of the degree of
Doktor-Ingenieur (Dr.-Ing.)

at the Faculty of
Civil and Environmental Engineering
Ruhr-Universität Bochum

submitted by
Cuong Manh Le
from Hanoi, Vietnam

Reviewers
Prof. Dr.-Ing. habil. Torsten Wichtmann (Ruhr-Universität Bochum, Germany)
Prof. Dr.-Ing. Gunnar Heibrock (Hochschule Kaiserlautern, Germany)
Prof. Dr. Snehasis Tripathy (Cardiff University, UK)

Bochum, 2025

This work is dedicated to
my beloved parents and sisters (Oanh and Giang),
my lovely supportive wife Ha Ngoc Doan,
and my lovely children Huy Duc Le and Chau Bao Ha Le

Preface of the editor

Many geotechnical structures like backfills, earth dams, dikes or substructures of pavements and railway tracks are composed of compacted unsaturated soils. The moisture content of these soils varies due to drying and precipitation. The presence of both air and water in the pore space leads to additional forces at the particle contacts which increase the effective stress and thus affect important soil properties like stiffness and shear strength. For accurate and reliable analytical or numerical studies of geotechnical structures composed of unsaturated soils under various external and environmental loading conditions, for example dykes under increased impact resulting from climate change, suitable descriptions of the effective stress in unsaturated soils are indispensable.

For that purpose, the suction stress approach has received increasing attention in recent years, where the various interparticle forces resulting from the unsaturated state are captured by the macroscopic variable "suction stress" which represents the gain in effective stress compared to water-saturated soils. The suction stress can be derived from different types of tests, typically by comparing the strength of unsaturated and saturated soil samples. Important influencing parameters on the suction stress are the degree of saturation and suction, the latter being the difference between pore air and pore water pressure. If the effective stress concept is generally valid for unsaturated soils the same suction stress should be obtained from different types of tests. However, most studies in the literature used a certain type of test, mainly shear tests, to derive suction stress. Furthermore, the previous studies were limited to relatively narrow and rather low ranges of suction.

In his doctoral thesis Cuong Manh Le has performed a systematic and detailed experimental investigation on the effective stress concept in unsaturated soils. He has derived the suction stress from different types of tests including biaxial compression, direct shear, unconfined compression and uniaxial tensile tests. These suction-controlled tests on unsaturated soils are technically challenging and time-consuming. The compacted kaolin samples were tested over a wide range of suction and water content, including drying and wetting paths. Suction stress was determined from a comparison of unsaturated and saturated samples. Complementary data was gained on the soil-water characteristic curve, the shrinkage curve and the pore size distribution for different saturation states.

The data set collected by Cuong Manh Le is very comprehensive and unique. In comparison to existing literature, it covers different test types and a wide range of suction for the

first time. Important findings are 1) the significant increase of the friction angle in the high suction range, 2) the hysteresis of suction stress along the drying and wetting path, 3) the considerably lower suction stress values derived from the tensile tests compared to the shear tests performed under compressional loads, and 4) certain discrepancies in the suction stress derived from the biaxial, direct shear, and unconfined compression tests in the high suction range. The differences in suction stress between the various test types demonstrate the challenges of formulating a unique effective stress approach for unsaturated soils. Mr. Le provides plausible micromechanical explanations for his macroscopic observations and sets his results in the context of relevant literature. Furthermore, he demonstrates that some popular equations for the prediction of suction stress lead to significant overestimation, in particular in the high suction range, emphasizing the need for a more appropriate formulation covering a wide range of suction.

Bochum, June 2025 Prof. Dr.-Ing. habil Torsten Wichtmann

Acknowledgements

This research was carried out in the Chair of Soil Mechanics, Foundation Engineering and Environmental Geotechnics, Ruhr-Universität Bochum. First and foremost, I would like to express my deepest gratitude to my supervisor, Prof. Torsten Wichtmann, for kindly accepting me under his supervision at RUB following the untimely passing of Prof. Tom Schanz. His invaluable scientific guidance and continuous support have been instrumental throughout my doctoral journey. I am also grateful to the Vietnamese Government Scholarship Foundation (911 Program) for providing financial support during my research stay in Bochum.

I am sincerely thankful to Prof. Gunnar Heibrock (Hochschule Kaiserslautern, Germany) and Prof. Snehasis Tripathy (Cardiff University, UK) for serving as reviewers of my thesis. Their constructive and insightful comments greatly improved the quality of this work. My heartfelt thanks also go to Dr. Diethard König for his invaluable assistance and numerous constructive suggestions, which guided me through every step of this research.

I would also like to express my gratitude to Dr. Alabdullah for his support at the beginning of my research. Special thanks are extended to the laboratory technicians - Mr. Skubisch, Mr. Müller, Mr. Blazytko, Mr. Schlechter, and Mr. Schudy - for their dedicated help with laboratory equipment during the experimental work.

I am indebted to my wonderful colleagues, including Hanieh, Florian, Debdeep, Peyman, Danial, Frederik, Yukang, Firas, Viktor, Meisam, Timon, Wolfgang, Max, Felipe, and many others with whom I had the pleasure of working and interacting regularly. Their companionship and support enriched both my professional and personal life, making this journey truly memorable.

I am also grateful to my colleagues at Hanoi Architectural University in Vietnam, particularly the university board, the faculty leadership, and the Chair of Geotechnical Engineering and Underground Construction, for their encouragement and support.

Finally, and above all, I would like to express my deepest gratitude to my parents, my family, my brothers and sisters, and the Nhy Star team, whose endless encouragement has carried me through to the completion of this doctorate. To my beloved Ha Ngoc Doan, words cannot fully capture my thanks for your love, patience, understanding, and for always being by my side.

Bochum, 2025 Cuong Manh Le

Abstract

A wide range of earth structures, including backfills, earth dams, embankments, roads, and hydraulic barriers, are built using compacted soils that remain unsaturated both during construction and throughout their service life. The stability of these structures depends on the strength and deformation characteristics of the unsaturated soil when subjected to external loads or environmental influences such as rainfall, transpiration, and evaporation. Traditional soil mechanics considers soils as either fully dry, where the pores are filled with air, or completely saturated, where the pores are entirely filled with water. In unsaturated conditions, soil pores contain both air and water, leading to additional interparticle forces. For instance, the formation of menisci at air-water interfaces generates matric suction, which increases the effective stress and, consequently, influences soil strength and stiffness.

The extension of Terzaghi's (1936) effective stress concept to unsaturated conditions, first proposed by Bishop (1959), remains a widely accepted approach for incorporating the effects of unsaturated soil conditions on strength and deformation. This is achieved by introducing suction and an effective stress parameter χ. Building upon this, Lu and Likos (2006) developed a micromechanical framework to define effective stress in unsaturated soils, introducing the concept of "suction stress" - a macroscopic stress variable that accounts for capillary effects and physicochemical interactions, thereby quantifying the portion of suction that contributes to effective stress. Various approaches exist for determining the effective stress parameter χ or suction stress, depending on factors such as soil conditions (e.g., degree of saturation) and soil characteristics (e.g., soil-water characteristic curve).

Numerous studies have attempted to determine the effective stress parameter or suction stress experimentally, often by comparing the measured strength of soil under unsaturated conditions with that under saturated conditions. If the effective stress concept is universally valid, the suction stress derived from different types of experiments on the same soil under identical initial conditions (i.e., structure, void ratio, degree of saturation, and suction) should be consistent over a wide range of suction. Most previous studies have relied on data from a single type of test and up to relatively low suction levels (below 1500 kPa), limiting the robustness of their conclusions. To date, a comprehensive experimental investigation that integrates multiple testing methods and covers a wide range of suction levels to validate this concept is still lacking.

To address this, a comprehensive dataset was established in this study, incorporating multiple laboratory tests, including biaxial compression tests (BCT), direct shear tests (DST), unconfined compression tests (UCT), and uniaxial tensile tests (UTT). These tests were conducted on a single soil type along both drying and wetting paths over a wide range of suction levels. The suction stress values determined from different test types at the same suction levels were compared. The results indicate that suction stress derived from uniaxial tensile tests (UTT) is significantly lower than that obtained from shear tests conducted in the compression regime (BCT, DST, and UCT), as observed in both the drying and wetting paths. Furthermore, for suction levels above 10 MPa, a considerable discrepancy was observed among the suction stress values obtained from BCT, DST, and UCT.

Additionally, the applicability of the effective stress concept relies on the assumption that the soil's friction angle remains constant with varying suction. However, results from BCT and DST indicate that this assumption holds only up to suction levels of 10 MPa for BCT and 3.7 MPa for DST. Beyond these thresholds, the friction angle exhibits significant variation with suction, challenging the general applicability of the effective stress concept under high-suction conditions.

Moreover, selected equations for predicting suction stress were applied to the dataset. The results showed that while these equations captured the measured suction stress with reasonable accuracy at low suction levels (below 500 kPa along the drying path and below 1000 kPa along the wetting path), they tended to overestimate suction stress beyond these thresholds.

Zusammenfassung

Eine Vielzahl von Erdbauwerken, wie Hinterfüllungen, Deiche, Staudämme, Straßen- und Bahndämme, werden aus verdichtetem Boden errichtet, der sowohl während der Bauphase als auch während der Nutzungsphase weitgehend ungesättigt bleibt. Die Stabilität dieser Bauwerke hängt von der Festigkeit des ungesättigten Bodens ab, wenn er äußeren Belastungen oder Umwelteinflüssen wie Niederschlag und Verdunstung ausgesetzt ist. Die traditionelle Bodenmechanik betrachtet Böden entweder als vollständig trocken, wobei die Poren mit Luft gefüllt sind, oder als vollständig gesättigt, wobei die Poren vollständig mit Wasser gefüllt sind. Unter ungesättigten Bedingungen befinden sich in den Poren des Bodens sowohl Luft als auch Wasser, was zu zusätzlichen Kräften zwischen den Körnern des Bodens führt. So erzeugen Menisken an Luft-Wasser-Grenzflächen Kapillarkräfte, welche die Korn-zu-Korn-Spannungen, also die effektive Spannung, erhöhen und somit die Festigkeit und Steifigkeit des Bodens beeinflussen.

Die Erweiterung des Konzepts der effektiven Spannung von Terzaghi (1936) auf ungesättigte Bedingungen, die erstmals von Bishop (1959) vorgeschlagen wurde, ist ein weithin akzeptierter Ansatz zur Erfassung der Auswirkungen ungesättigter Bodenverhältnisse auf die Festigkeit und die Steifigkeit des Bodens. Dies wird durch die Einführung der Saugspannung und eines effektiven Spannungsparameters χ erreicht. Auf dieser Grundlage entwickelten Lu und Likos (2006) mit dem Konzept des "Suction Stress" einen mikromechanischen Rahmen zur Definition der effektiven Spannung in ungesättigten Böden. Der "Suction Stress" ist eine makroskopische Spannungsvariable, die Kapillareffekte und physikalisch-chemische Wechselwirkungen berücksichtigt und somit den Anteil der Saugspannung quantifiziert, der zur Erhöhung der effektiven Spannung beiträgt. Es existieren verschiedene Ansätze zum Bestimmen des effektiven Spannungsparameters χ oder des "Suction Stress" abhängig von Faktoren wie den Bodeneigenschaften (z. B. Saugspannungs-Sättigungsbeziehung) und dem Zustand des Bodens (z.B. Sättigungsgrad).

In zahlreichen Studien wurde versucht, den effektiven Spannungsparameter oder den "Suction Stress" experimentell zu bestimmen, häufig durch Vergleich der gemessenen Festigkeit des Bodens unter ungesättigten Bedingungen mit der unter gesättigten Bedingungen. Wenn das Konzept der effektiven Spannung universell gültig ist, sollte der "Suction Stress", der aus verschiedenen Arten von Versuchen mit demselben Boden unter identischen Ausgangsbedingungen (d. h. Struktur, Porenanteil, Sättigungsgrad und Saugspannung) abgeleitet wird, über einen weiten Bereich der Saugspannung konsistent sein. Die

meisten bisherigen Studien stützen sich auf Daten aus einer einzigen Versuchsart und bis zu relativ niedrigen Saugspannungswerten (unter 1500 kPa), was die Aussagekraft ihrer Schlussfolgerungen einschränkt. Bis heute fehlt eine umfassende experimentelle Untersuchung, die sich mehrerer Versuchsarten bedient und einen weiten Bereich von Saugspannungen abdeckt, um dieses Konzept zu validieren. In der vorliegenden Studie wird ein umfassender Datensatz erstellt und ausgewertet, der mehrere Versuchsarten umfasst, darunter Biaxialversuche, direkte Scherversuche, einaxiale Druckversuche und einaxiale Zugversuche.

Diese Versuche wurden an einem einzigen Boden sowohl bei Trocknung als auch bei Befeuchtung über einen breiten Bereich von Saugspannungen durchgeführt. Die aus verschiedenen Versuchsarten bei gleichen Saugspannungen ermittelten Werte des "Suction Stress" wurden verglichen. Die Ergebnisse zeigen, dass der aus einaxialen Zugversuchen abgeleitete "Suction Stress" deutlich geringer ist als der aus Scherversuchen im Druckbereich (Biaxialversuche, direkte Scherversuche, einaxiale Druckversuche) erhaltene. Dieses gilt sowohl für den Trocknungspfad als auch den Befeuchtungspfad. Darüber hinaus zeigt sich bei Saugspannungen über 10 MPa eine erhebliche Diskrepanz zwischen den aus Biaxialversuchen, direkten Scherversuchen und einaxialen Druckversuchen erhaltenen Werten des "Suction Stress".

Die Anwendbarkeit des Konzepts der effektiven Spannung basiert auf der Annahme, dass der Reibungswinkel des Bodens bei unterschiedlicher Saugspannung konstant bleibt. Die Ergebnisse der Biaxialversuche und der direkten Scherversuche zeigen jedoch, dass diese Annahme nur bis zu Saugspannungen von 10 MPa für Biaxialversuche und 3,7 MPa für direkte Scherversuche gilt. Oberhalb dieser Schwellenwerte steigt der Reibungswinkel in Abhängigkeit der Saugspannung deutlich an, was die allgemeine Anwendbarkeit des Konzepts der effektiven Spannung bei hohen Saugspannungen in Frage stellt.

Darüber hinaus wurden ausgewählte bekannte Gleichungen zur Berechnung des "Suction Stress" aus der Saugspannungs-Sättigungsbeziehung des Bodens auf den Datensatz angewendet. Die Ergebnisse zeigen, dass diese Gleichungen den gemessenen "Suction Stress" bei niedrigen Saugspannungen (unter 500 kPa entlang des Trocknungspfads und unter 1000 kPa entlang des Befeuchtungspfads) mit angemessener Genauigkeit erfassen, jedoch dazu neigen, den "Suction Stress" oberhalb dieser Schwellenwerte zu überschätzen.

Contents

1. Introduction

1.1. Background and motivation

The traditional soil mechanics framework typically considers geomaterials as either completely dry or fully saturated. However, in practical scenarios, a groundwater table exists within the soil profile, defining the boundary between saturated and unsaturated zones. The unsaturated zone is affected by fluctuations in the water table and meterological influences. Unlike saturated soil, where all pore spaces are filled with water, or completely dry soil, where all pore spaces are filled with air, unsaturated soil contains both air and water within its pore network.

A vast number of earth structures, such as backfills, earth dams, embankments, roads, and hydraulic barriers, are constructed using compacted soils that remain in an unsaturated state both during construction and throughout their service life. The stability of these structures is highly dependent on the strength and deformation characteristics of the soil when subjected to external loads or environmental changes such as rainfall, transpiration, and evaporation.

According to previous studies (Terzaghi 1943; Bishop 1959; Bishop et al. 1960; Lu & Likos 2004; Lu & Likos 2006), effective stress, which is transmitted through the soil skeleton, governs soil strength, deformation, and volume change. It was first introduced by Terzaghi (1936) for soil under saturated conditions and is mathematically expressed as:

$$\sigma' = \sigma - u_w \tag{1.1}$$

Here, σ' is effective stress, σ is the total stress corresponding to the sum of all forces per unit area acting on the soil, including overburden and external loads, and u_w is pore water pressure.

In unsaturated soil conditions, as noted by Fredlund & Morgenstern (1977) and Fredlund & Rahardjo (1993*b*), soil comprises four distinct phases: soil solids, pore water, pore air,

and the air-water interface, commonly referred to as the contractile skin. However, an ongoing debate persists regarding the most effective way to characterize the influence of soil-water interaction on the mechanical behaviour of unsaturated soil. One widely adopted approach is to represent the macroscopic effect of suction through effective stress σ'. Bishop (1959) extended the effective stress concept originally proposed by Terzaghi (1936) for saturated soils to unsaturated conditions:

$$\sigma' = (\sigma - u_a) + \chi(u_a - u_w) \tag{1.2}$$

where σ' represents the effective stress, σ is the total stress, u_a is the pore air pressure, and u_w is the pore water pressure. The term $(\sigma - u_a)$ denotes the net normal stress, while $(u_a - u_w)$ represents the matric suction. The parameter χ is the effective stress parameter.

Originally, Bishop (1959) defined χ as a function of the degree of saturation, ranging from 1 for fully saturated conditions to 0 for completely dry conditions. Under this constraint, Eq. 1.2 seamlessly transitions into Eq. 1.1 at the two extreme states. However, recent experimental studies suggest that the second term on the right-hand side of Eq. 1.2 is zero only for coarse grained soils like sand and gravels without fines but remains nonzero for other soil types, such as silts, sand-clay mixtures, and pure clay (Cui & Delage 1996; Lu & Likos 2004; Pourzargar 2017; Zhang & Lu 2020; Akin & Likos 2020; Salimi et al. 2021). According to Lu & Likos (2006), the magnitude of this term can reach up to 1 MPa in completely dry clayey soils.

Numerous studies have aimed to establish a suitable and unique function for χ (Bishop 1961; Jennings 1961; Khalili & Khabbaz 1998; Zhou, Huang & Sheng 2016; Heibrock et al. 2018; Khalili 2018). However, ongoing debate persists regarding which aspects of soil-water interaction - such as capillary effects and physicochemical forces (e.g., electrostatic or molecular interactions) - should be incorporated into the effective stress framework. While capillary effects are widely accepted as a valid component of effective stress (Lu & Likos 2006; Konrad & Lebeau 2015), there is no consensus on whether physicochemical forces should be included (Khalili et al. 2022).

Lu & Likos (2006) developed a micromechanically based framework to describe effective stress in unsaturated soils, expanding on the approach initially proposed by Bishop (1959). They introduced the concept of "suction stress", a macroscopic stress variable that integrates the influences of capillarity and physicochemical forces, including van der Waals forces, electrical double-layer repulsion, and net attraction forces resulting from chemical cementation at grain contacts.

Various experimental studies were carried out to determine χ or suction stress. However, most of these studies are limited to relatively low suction levels (below 1500 kPa) (Escario & Saez 1986; Cui & Delage 1996; Khalili et al. 2004; Kayadelen et al. 2007; Banerjee 2017; Almahbobi 2018; Chali & Maleki 2021), while fewer studies have explored its validity at higher suction levels (Patil et al. 2020; Akin & Likos 2020; Gao et al. 2020). In saturated soil, the effective stress is considered universal and therefore is applied to describe soil behaviour independent of loading conditions. As expressed in Eq. 1.1, the pore water pressure acts isotropically and does not contribute to the shear strength of the soil, meaning that the effective stress alone governs soil deformation and strength. If the effective stress concept in unsaturated soils is universally valid, the suction stress derived from different types of experiments on the same soil under identical initial conditions (i.e., structure, void ratio, degree of saturation, and suction) should be consistent over a wide range of suction. Most previous studies have relied on data from a single type of test, however, limiting the robustness of their conclusions. To date, a comprehensive experimental investigation that integrates multiple testing methods and covers a wide range of suction levels to validate this concept is still lacking.

To address this, a comprehensive dataset was established in this study, incorporating multiple laboratory tests, including biaxial compression tests (BCT), direct shear tests (DST), unconfined compression tests (UCT), and uniaxial tensile tests (UTT). These tests were performed on a single soil type along both drying and wetting paths over a wide range of suction levels. The primary objective is to validate the effective stress concept in unsaturated soils by analyzing suction stress values derived from different test types. Additionally, selected well-known suction stress models will be applied to the dataset for comparison. This dataset is also valuable for the development and calibration of constitutive models in future research, providing extensive experimental data necessary for accurately predicting the behavior of unsaturated soils under various environmental and loading conditions.

1.2. Study objectives

Considering the limitations of previous studies discussed in the previous section, this research aims to experimentally validate the effective stress concept in unsaturated soil using the suction stress approach. To achieve this, a series of biaxial compression tests (BCT), direct shear tests (DST), unconfined compression tests (UCT), and uniaxial tensile tests (UTT) were conducted on a single soil type. These tests encompass a wide suction

range along both drying and wetting paths, providing a comprehensive assessment of suction stress variations under diverse conditions.

To achieve this objective, the research is structured into the following key tasks:

i. Determining the basic properties of the tested material.

ii. Establishing the soil-water characteristic curve (SWCC) along the drying and wetting paths.

iii. Establishing the soil shrinkage curve (SSC).

iv. Analyzing the evolution of pore size distribution (PSD) along the drying and wetting paths.

v. Conducting different types of tests, including BCT, DST, UCT, and UTT, which form the core of this research.

vi. Determining suction stress from different test types.

vii. Predicting suction stress using well-known equations and comparing the predicted values with the experimentally measured suction stress.

1.3. Contents of the thesis

This thesis is structured into seven chapters, summarized as follows:

- *Chapter 1* introduces the research topic, outlines the motivation and objectives, and provides an overview of the thesis organization.
- *Chapter 2* presents a comprehensive literature review on the fundamentals of unsaturated soil, with a focus on the effective stress concept and its validation using the suction stress approach, which forms the core of this research. Additionally, it reviews methods for determining the SWCC, SSC, and PSD.
- *Chapter 3* details the basic properties of the tested material, sample preparation techniques, experimental procedures, and the overall experimental program.
- *Chapter 4* presents the experimental results, including the SWCC along drying and wetting paths, the SSC, and the PSD evolution. Furthermore, this chapter provides results from various laboratory tests, including BCT, DST, UCT, and UTT.
- *Chapter 5* analyzes and discusses the experimental results presented in Chapter 4 with a focus on determining the suction stress derived from different element tests.

- *Chapter 6* focuses on the prediction of suction stress, comparing measured suction stress from Chapter 5 with predicted values. It also discusses the effectiveness of the applied prediction equations.
- *Chapter 7* summarizes the key findings of the research and offers recommendations for future studies.

2. State-of-the-art review

2.1. Introduction

The current State-of-the-art review considers the relevant and most current research concerning the fundamentals of unsaturated soil, with focus on the effective stress concept, soil-water characteristic curves (SWCC), soil shrinkage curves (SSC), and pore size distribution (PSD). In addition, as the backbone of this study, a comprehensive review on the experimental determination of suction stress characteristic curve (SSCC) and the prediction of the SSCC is presented. Moreover, based on the literature review the need of further research is outlined, which motivated the research presented in subsequent chapters.

2.2. Suction

The concept of suction was introduced by Buckingham (1907), and was later further developed by some authors in the soil physics field (Edlefsen & Anderson 1943; Gardner & Widtsoe 1921; Bolt & Frissel 1960). Suction represents the potential energy required to remove water from soil pores and is divided into two primary components: matric suction and osmotic suction (Aitchison 1965; Fredlund & Rahardjo 1993*b*; Lu & Likos 2004). Matric suction (ψ_m) arises due to capillary and adsorption forces, where water is held in small pores by surface tension and molecular attraction to soil particles. It is defined as the difference between pore air pressure (u_a) and pore water pressure (u_w). Osmotic suction (ψ_π), on the other hand, is caused by the presence of dissolved solutes in the pore water, which lowers the free energy of water and affects its movement through osmosis. The sum of these two components gives the total suction in soil (ψ_t) (Eq. 2.1):

$$\psi_t = \psi_m + \psi_\pi \tag{2.1}$$

Aitchison (1965) defined "Total suction or free energy of the soil water - in suction terms, it is the equivalent suction derived from the measurement of the partial pressure of the

water vapor in equilibrium with a solution identical in composition with the soil water, relative to the partial pressure of water vapor in equilibrium with free pure water." The total suction is related to the relative humidity by Kelvin's law as follows:

$$\psi = -\frac{R \cdot T}{v_{w_0} \cdot \omega_v} ln(RH) \tag{2.2}$$

where, ψ is the total suction (kPa), R is the universal gas constant (8.314 J/mol K), T is the absolute temperature (K), v_{w_0} is the specific volume of water (m^3/kg), ω_v is the molecular mass of water vapor (18.016 kg/kmol), and RH is the relative humidity.

Osmotic suction, as previously discussed, arises from dissolved salts in the pore water. Sreedeep & Singh (2006) determined osmotic suction from the difference of the measured total suction and matric suction using a WP4C hygrometer and a pressure membrane extractor. It can be indirectly determined by measuring the electrical conductivity of the pore water (Fredlund & Rahardjo 1993*b*; ASTM (D4542-95) 2000; Abedi-Koupai & Mehdizadeh 2008). The pore water can be extracted using a pore-fluid squeezer, and its electrical conductivity is then converted to osmotic suction using a calibration curve that relates osmotic suction to electrical conductivity.

A variety of techniques, each corresponding to different suction ranges, have been employed to measure suction in soil. A comprehensive overview of these suction measurement methods is provided in the study conducted by Elgabu (2013).

2.3. Interparticle forces in unsaturated soils

In unsaturated soils, interparticle forces play a crucial role in defining the internal stress state and governing the mechanical behaviour of the soil. These forces arise from the interaction of soil particles through the pore water and air phases, primarily due to capillary forces, van der Waals forces, electrical double-layer forces, and cementation effects (Lu & Likos 2004).

2.3.1. Capillary forces

Capillary forces in unsaturated soils arise from the interaction between pore water and pore air at the air-water interfaces, where surface tension and adhesion generate suction effects. These forces develop because water molecules experience stronger cohesive and

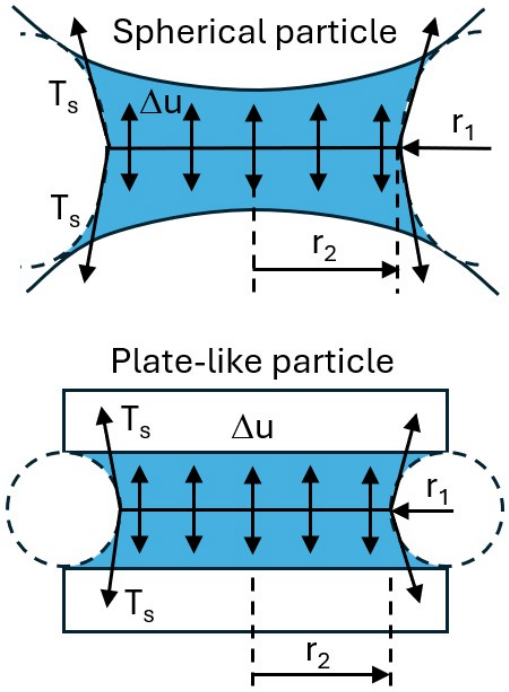

Figure 2.1.: Schematic of capillary forces (modified after Lee et al. 2022)

adhesive forces at the boundary between liquid and gas phases, resulting in the formation of curved menisci between soil particles (Lu & Likos 2004). Figure 2.1 illustrates the components of capillary forces between two spherical particles and two plate-like particles. Capillary forces are influenced by factors such as particle size, particle shape, packing fabric, pore size distribution, degree of saturation, and relative humidity (Cho & Santamarina 2001; Santamarina & Cho 2004; Lu & Likos 2004; Espinoza & Santamarina 2010; Liu et al. 2021). According to Cho & Santamarina (2001), capillary forces originate from two main components: matric suction $(u_a - u_w)$ acting on the cross-sectional area of the meniscus and liquid surface tension (T_s) acting along the perimeter $(2\pi r_2)$ of the capillary neck. The capillary force is thus expressed as follows:

$$F_{cap} = (u_a - u_w)(\pi r_2^2) + T_s(2\pi r_2) \tag{2.3}$$

where r_2 presents the radius of curvature of the water bridge. He et al. (2001) performed a study with measurement of the pull-off force required to separate two nanoparticles using scanning force microscopy with a variation of relative humidity (RH). They used the system consisting of a hydrophilic tip and sample (silicon wafers and epitaxially grown calcium fluoride films). Figure 2.2 shows the test results. In both cases (i.e. between

a hydrophilic tip and a flat silicon sample, and between a hydrophilic tip and a flat ionic calcium fluoride sample), the pull-off force increases to a maximum value and then decreases to a certain value as the RH decreases.

Vesga (2005) inserted a drop of water to a tip of a loading piston and suspended a piece of foam by maintaining the contact of this foam with the water. This configuration created a water bridge between the piston and the foam. The foam was attached to the load piston by the water film. The test was performed in a closed triaxial chamber and under controlled RH. A constant RH was maintained for 48 h, followed by a decrease in RH. As a result, the capillary contact force was reduced and the foam fell. Lu & Likos (2006) introduced a theoretical capillary attraction curve as a function of the degree of saturation. The theoretical capillary stress increases gradually to a maximum value of about 10^6 kPa when the degree of saturation ranges from 80% to about 20%, followed by a significant decline as the degree of saturation drops below 20%.

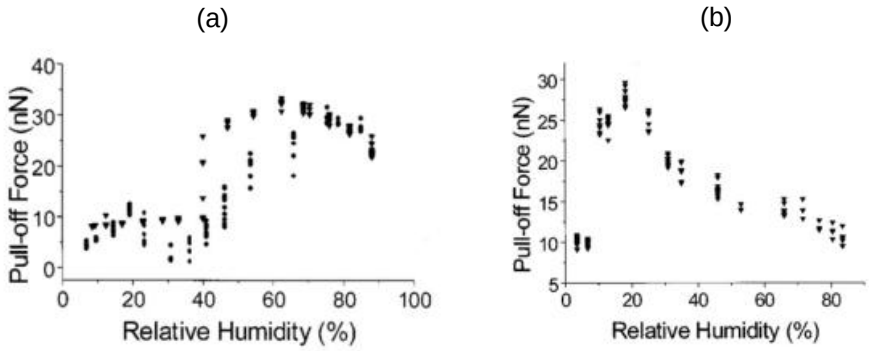

Figure 2.2.: Pull-off force as a function of RH measured between a hydrophilic tip and: (a) a flat silicon sample, and (b) a flat ionic calcium fluoride sample (after He et al. 2001)

2.3.2. van der Waals forces

Van der Waals (vdW) forces are intermolecular attractions that play a critical role in clay particle interactions (Sridharan 2014). These forces operate on nanometer to micrometer scales and significantly influence soil aggregation, swelling, and mechanical behaviour. Israelachvili (2011) provided a comprehensive and unified introduction to intermolecular and surface forces.

In clay systems, van der Waals forces primarily arise from three fundamental types (Giese 2008):

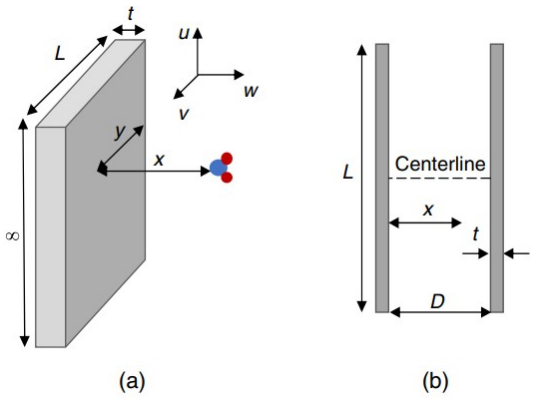

Figure 2.3.: Geometric model: (a) a single plate-like clay particles (gray area), and (b) two parallel plate-like clay particles (gray areas) with seperation distance D (after Lu & Zhang 2019)

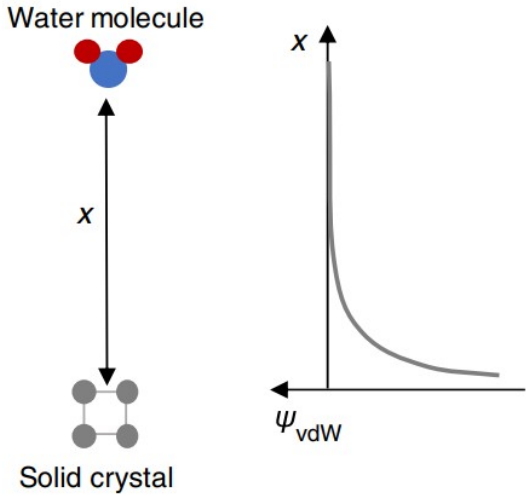

Figure 2.4.: Schematic illustration of van der Waals attraction (after Lu & Zhang 2019)

- (*i*) Keesom forces (permanent dipole-permanent dipole interactions), which occur between permanent dipoles such as water molecules and the surface charges of clay minerals;

- (*ii*) Debye forces (induced dipole-permanent dipole interactions), which occur when a permanent dipole, such as water or clay mineral surfaces, induces a dipole in a neighboring neutral molecule;

- (*iii*) London dispersion forces (instantaneous dipole-induced dipole interactions), which arise from temporary fluctuations in electron clouds, creating momentary dipoles that induce dipoles in adjacent particles.

Figure 2.3a illustrates an idealized geometric model of a semi-infinite, plate-like clay particle, defined by a thickness t and a width L, in interaction with a water molecule. Figure 2.3b depicts two parallel, plate-like clay particles separated by a distance D. Figure 2.4 presents a schematic representation of van der Waals attractions occurring in the presence of water molecules situated between the two parallel clay particles and their associated solid crystal. Van der Waals forces are electromagnetic interactions resulting from fluctuating dipoles within atoms and molecules. When a water layer exists between two clay surfaces (as shown in Fig. 2.3b), the transmission of van der Waals forces is modulated by the dielectric properties and molecular structure of the intervening water medium (Mitchell & Soga, 2005).

Hamaker (1937) formulated the van der Waals forces between two flat surfaces based on the theoretical framework introduced by London (1930). The van der Waals force per unit area is expressed as follows:

$$F_{vdW} = \frac{A}{6\pi D^3} \tag{2.4}$$

where F_{vdW} is the van der Waals forces per unit area (N/m^2), A is the Hamaker constant (J), D is the distance between two surfaces (m). Several studies have been conducted to determine the Hamaker constant (Hamaker 1937; Sridharan 1968; Israelachvili 2011; Spagnoli et al. 2012). Among these, Sridharan (1968) introduced a relationship between the Hamaker constant and the degree of saturation for montmorillonite and kaolinite, as illustrated in Figure 2.5. His findings indicate that as the degree of saturation decreases, the magnitude of the Hamaker constant increases, leading to a stronger van der Waals attraction.

According to Lu & Likos (2006), van der Waals forces can generate a macroscopic attractive interparticle stress with an upper bound of approximately 1 MPa. This suggests that van der Waals interactions may play a non-negligible role in the effective stress state of unsaturated soils, particularly at low degrees of saturation.

Lu & Zhang (2019) introduced a theoretical framework to describe pore-scale water potential in soil, where the sorptive potential is decomposed into matric potential and pressure potential. Their framework provides a more comprehensive understanding of water retention and interaction forces in fine-grained soils.

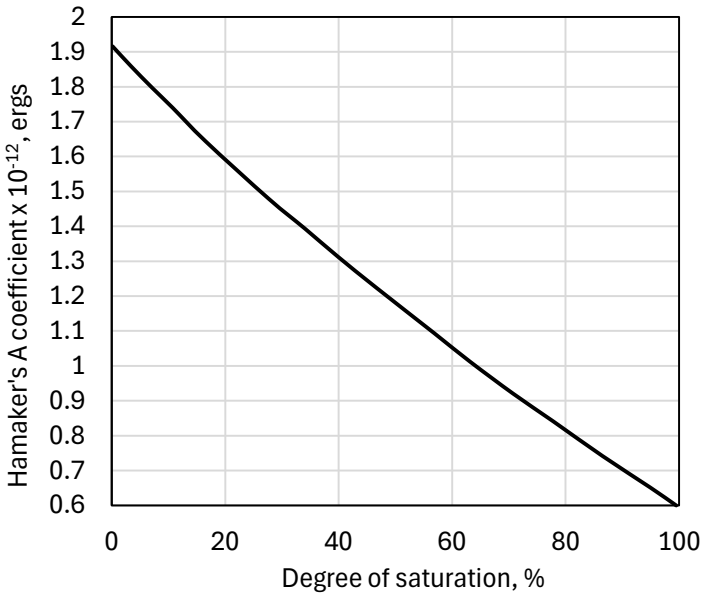

Figure 2.5.: Variation of Hamaker constant (A) with degree of saturation (adopted and redrawn after Sridharan 1968)

According to several studies (Sridharan 2014; Lu & Zhang 2019), the magnitude of attractive van der Waals forces increases as the interparticle distance decreases. This behavior is particularly significant in fine-grained soils, such as clays, where particle spacing is highly dependent on water content, suction, and soil structure. As drying progresses and the distance between clay particles reduces, van der Waals forces contribute more prominently to interparticle attraction, influencing soil aggregation (Lu & Likos 2006; Zhang & Lu 2020), shrinkage (Vesga 2008), and mechanical behaviour (Vesga 2008; Alsherif & McCartney 2014; Akin & Likos 2020).

2.3.3. Electrical double-layer forces

The diffuse double-layer (DDL) in unsaturated soil refers to the region of counterions surrounding charged clay particles in a soil-water system (see Fig. 2.6). Clay minerals, such as montmorillonite, illite, and kaolinite, carry negative surface charges due to isomorphic substitution and broken bonds at their edges (Baille 2014). To maintain electrostatic neutrality, oppositely charged cations (counterions) from the pore water are attracted to these surfaces, forming the electrical double layer. The DDL is located between a Stern layer, where counterions are strongly adsorbed, and the bulk fluid (Mangelsdorf & White

1990), where ions are more loosely distributed due to thermal motion (Mitchell & Soga 2005).

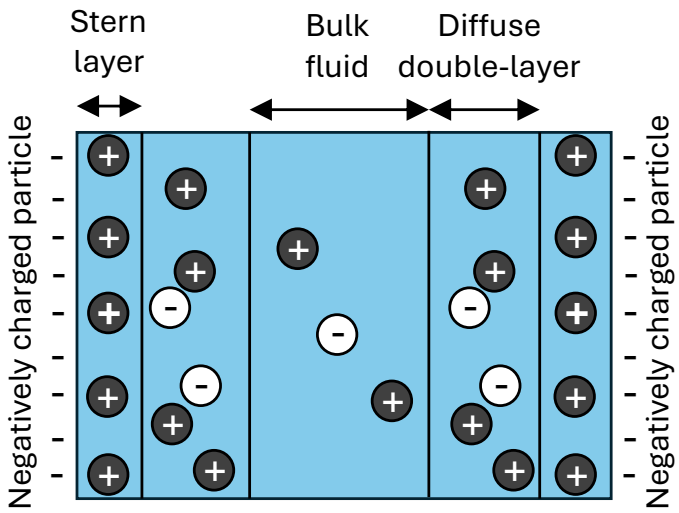

Figure 2.6.: Schematic of formation of diffuse double-layer between two particles (adopted and redrawn after Lee et al. 2022)

In a clay-water electrolyte system, the overlapping of the DDL of adjacent clay particles results in an increase in cation concentration in the central plane between two particles, which creates repulsion between the two particles. Bolt (1956) used the theory introduced by Gouy (1910) and Chapman (1913), referred as the Gouy-Chapman theory, to explain the compressibility of pure clays. Baille (2014) employed the classical Gouy-Chapman DDL theory and the modified DDL theory approach proposed by Tripathy et al. (2004) to calculate the stress-void ratio and dry density-swelling pressure relationship of three pure clays including Calcigel bentonite, NX illite, and Spergau kaolin. The calculation of the repulsive pressure due to overlapping diffuse double-layers may be done based on osmotic pressure approach. The repulsive double-layer pressure is expressed as follows (Bolt 1956; Sridharan & Jayadeva 1982; Baille 2014):

$$R_{DDL} = 2n_0 k_B T(\cosh(u) - 1) \tag{2.5}$$

In Eq. 2.5, R_{DDL} is the repulsive pressure (N/m^2), u is the nondimensional midplane potential, k_B is Boltzmann constant ($= 1.38 \cdot 10^{-23}$ J/K), T is the absolute temperature (K), and n_0 is the ion concentration (m^{-3}).

In unsaturated soils, the thickness of the DDL is influenced by water content, ionic concentration, and cation valency. As water content decreases, the DDL contracts, leading

to stronger interparticle attraction and increased soil cohesion (Olphen 1977). This phenomenon affects soil permeability, shrinkage behaviour, and effective stress in unsaturated conditions. The competition between van der Waals attraction and double-layer repulsion governs clay flocculation or dispersion, significantly impacting soil microstructure (Sridharan 2014).

2.3.4. Cementation effect

Cementation in unsaturated soils refers to the bonding of soil particles through the precipitation of mineral cements, such as calcium carbonate ($CaCO_3$), iron oxides, silica, and gypsum, within the soil matrix. These cementing agents are commonly deposited from pore water during evaporation, drying, or chemical reactions between soil minerals and dissolved ions (Mitchell & Soga 2005). In unsaturated conditions, the presence of water films around particles facilitates solute transport, allowing minerals to precipitate at contact points between grains, strengthening the soil structure. The degree of cementation depends on soil composition, moisture fluctuations, pH, and ion concentration (Fredlund & Rahardjo 1993*b*; Mitchell & Soga 2005). Cemented unsaturated soils exhibit higher shear strength, reduced compressibility, and increased stiffness, making them more resistant to erosion and mechanical loading (Ismail et al. 2002; Kasama et al. 2006; Collins & Sitar 2009; Hossain & Yin 2015; Toll & Ali Rahman 2017; Kardani et al. 2021). However, cementation can degrade over time due to cyclic wetting-drying, dissolution of cementing agents, or mechanical disturbances, leading to a loss of cohesion and potential instability (Coop & Atkinson 1993). Understanding cementation in unsaturated soils is critical in geotechnical engineering for evaluating the long-term stability of natural deposits, road bases, and foundation materials.

The degree of saturation significantly influences the cementation process in unsaturated soils by controlling the dissolution, precipitation, and distribution of cementing agents. At low degrees of saturation, the presence of thin water films around soil particles enhances capillary forces, which promote particle contact and localized cementation. In this state, precipitation of minerals, such as calcium carbonate ($CaCO_3$), silica (SiO_2), or iron oxides, occurs predominantly at interparticle contacts, leading to stronger bonding and higher soil stiffness. As the degree of saturation increases, water becomes more abundant in the pore spaces, facilitating the dissolution and transport of cementing agents, which can either enhance or weaken cementation depending on the mineral solubility and precipitation conditions. When approaching full saturation, cementation is often less effective, as excess

water can dissolve previously formed bonds, reduce suction-induced contact pressure, and lead to a weaker soil structure (Mitchell & Soga 2005).

2.4. Soil-water characteristic curve (SWCC)

Suction is a key stress-state variable in unsaturated soils. It can be expressed as a function of gravimetric water content (w), volumetric water content (θ), or degree of saturation (S_r), forming the soil-water characteristic curve (SWCC). The SWCC is an important input data for understanding the behaviour of unsaturated soil (Fredlund & Rahardjo 1993*b*; Lu & Likos 2004). Many methods have been proposed to predict volume change, shear strength, permeability, shrinkage, thermal conductivity, and a variety of other properties of unsaturated soil based in part on the information derived from the SWCC (Fredlund & Morgenstern 1976; Ho et al. 1992; Fredlund & Rahardjo 1993*a*; Bani Hashem & Houston 2016; Lu & Dong 2017; Heibrock et al. 2018). The SWCC is hysteretic, meaning the wetting and drying curves do not overlap due to differences in pore water displacement mechanisms (Fredlund & Rahardjo 1993*b*; Lu & Likos 2004; Pham et al. 2005; Al-Mahbashi et al. 2018).

2.4.1. Features of SWCC

The SWCC is typically divided into three main regions (see Fig. 2.7): the boundary effect zone, the transition zone, and the residual zone (Yang et al. 2004; Fredlund 2006; Guan 2012). In the boundary effect zone, at high saturation levels, the soil behaves similarly to a saturated material, with a small increase in suction causing only a slight decrease in water content. The transition zone represents the main drying phase, where a gradual reduction in water content occurs as suction increases, influenced by pore size distribution and interparticle forces. Finally, in the residual zone, most of the water is held in very small pores or as adsorbed layers on soil particles, requiring significantly higher suction to remove it (Vanapalli et al. 1998).

Figure 2.7 shows the identifiable stages of typical SWCCs following different hydraulic paths (i.e. drying path and wetting path). The key parameters used to define the drying path of the SWCC include: the saturated volumetric water content (θ_s); the air-entry suction (ψ_{AEV}); the residual volumetric water content (θ_{res}); and the residual suction (ψ_{res}). The air-entry value (AEV) of the soil can be defined as the value of suction at which the air starts entering the largest pores in the soil. The residual water content can be defined

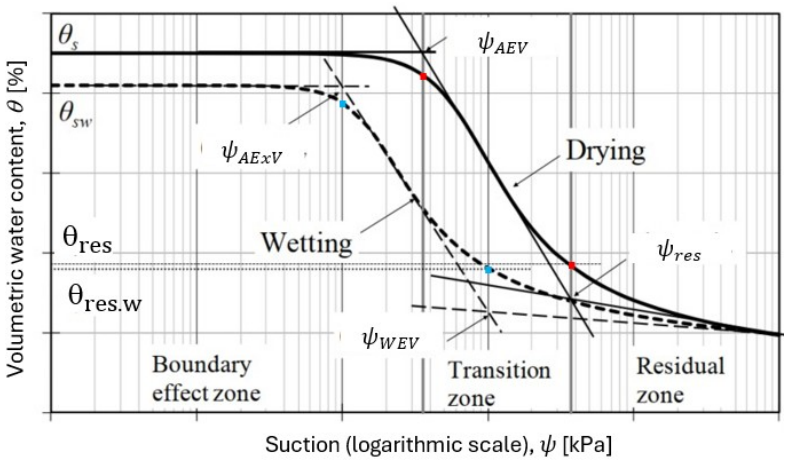

Figure 2.7.: Identifiable stages of typical SWCCs for low-shrinkage soils following different hydraulic paths (modified after Guan 2012)

as the water content at which a further increase in suction does not produce a significant change in water content and the water phase is discontinuous. Meanwhile, the key parameters used to define the wetting path of the SWCC include: the wetting saturated volumetric water content (θ_{sw}); the water-entry value suction (ψ_{WEV}); the water-entry volumetric water content ($\theta_{res.w}$); and the air-expulsion suction (ψ_{AExV}). The water-entry value suction (ψ_{WEV}) can be defined as the value of suction at which the water start entering the pores of the soil (Guan 2012).

Fleureau et al. (1993) determined the soil shrinkage curve (SSC) and considered that the suction corresponding to the shrinkage limit is ψ_{AEV}. Vanapalli et al. (1998) introduced a graphical method to determine ψ_{AEV} and ψ_{res}. For ψ_{AEV}, it can be determined at the intersection point between the horizontal line from the saturated volumetric water content, and the tangent line at the SWCC in the transition zone, which is drawn through the point of maximum slope. Meanwhile, the ψ_{res} can be determined at the intersection point of the tangent line at the SWCC in the transition zone, which is drawn through the point of maximum slope, and the residual line drawn through the suction of 10^6 kPa. Zhai & Rahardjo (2012) proposed an equation to determine ψ_{AEV} from the measured SWCC and the best fit curve from the SWCC model proposed by Fredlund & Xing (1994). Wijaya et al. (2015) used a combination of SWCC and SSC to determine ψ_{AEV}, however this method fixed a fitting parameter of the SSC model proposed by Fredlund & Zhang (2013), which may constrain its application to various kinds of soil.

Pasha et al. (2016) proposed a method for determining ψ_{AEV} when the SWCC data are presented in terms of water content versus suction. In this approach, the water content is

plotted on a logarithmic scale instead of a linear scale. Consequently, the AEV is identified as the intersection point of two distinct slope lines: one representing the data in the saturated state and the other representing the data in the unsaturated state. The primary advantage of this method is the clear identification of the transition point between these two states. Furthermore, this approach eliminates the need for measuring volume changes during SWCC testing, which is often a challenging aspect of SWCC determination.

2.4.2. Hysteresis effect on SWCC

As shown in Figure 2.7, the SWCC exhibits a well-documented hysteresis effect, meaning that the water retention behavior differs between drying (desorption) and wetting (adsorption) paths. This hysteresis arises due to multiple factors, including pore-size distribution, air entrapment, contact angle hysteresis, and swelling-shrinkage effects (Pham et al. 2005; Guan 2012).

Typically, for a given suction level, the water content during the drying path is higher than during the wetting path, leading to two distinct SWCC branches. The primary causes of this hysteresis include ink-bottle effects (Hillel 1981; Klausner 1991), where larger pores drain at lower suction but refill at higher suction due to capillary barriers and contact angle variations, which influence the wetting and drying behavior of pore water. Additionally, in expansive and structured soils, microstructural changes and volume deformation further contribute to the complexity of SWCC hysteresis (Lin & Cerato 2013; Estabragh et al. 2015).

Understanding and modeling SWCC hysteresis is crucial for improving the accuracy of numerical simulations in geotechnical and geo-environmental engineering. Many empirical and theoretical models have been developed to incorporate hysteresis, often using scanning curves between main drying and wetting branches to capture intermediate moisture states (Pham et al. 2005; Lins 2010). However, challenges remain in predicting hysteresis effects across different soil types, stress conditions, and long-term environmental cycles.

2.4.3. Factors influencing the SWCC

The SWCC is influenced by several intrinsic and external factors that affect the soil's ability to retain water at different suction levels. One of the most significant factors is the grain size distribution, where fine-grained soils, such as clays, exhibit a more gradual

desaturation curve due to their small pore sizes and strong adsorption forces, while coarse-grained soils, like sands, drain more quickly at lower suctions (Fredlund & Xing 1994).

Some researchers (Tinjum et al. 1997; Vanapalli et al. 1999; Elgabu 2013) demonstrated that the shape of the SWCC is a function of the initial water content, dry density, and pore size distribution (PSD). Test results presented by these researchers showed that the SWCC (S_r-ψ) for samples compacted dry of optimum plots below those compacted wet of optimum and is relatively steeper. This is because soil compacted dry of optimum retains less water compared to that compacted wet of optimum at a given suction. In other words, samples prepared wet of optimum have lower water content at saturation than that of samples prepared dry of optimum (Elgabu 2013), as the samples compacted dry of optimum absorb more water during saturation due to the presence of larger pores between aggregates (Thom et al. 2007). Samples prepared dry of optimum typically exhibit a bimodal PSD, characterized by larger pores between aggregates (inter-aggregate pores) and smaller pores within aggregates (intra-aggregate pores) (Sivakumar et al. 2006; Thom et al. 2007; Kayser et al. 2023). These characteristic of PSD significantly affects the water retention behaviour and hysteresis of the SWCC.

The effect of initial dry density has been also investigated in some studies (Yang et al. 2004; Birle et al. 2008; Jiang et al. 2017; Gao et al. 2019; Zhang et al. 2020; Raghuram et al. 2024). In general, as the initial dry density increases, the SWCC tends to shift to the right corresponding to an increase in the AEV.

In addition, the shape of the SWCC is influenced by the compaction effort. An increase in compaction effort may result in an increase in dry density and therefore decrease in the void ratio, which affects the soil's ability to retain water at different suction levels. A number of studies have been performed to investigate the impact of compaction effort on the SWCC (Tinjum et al. 1997; Miller et al. 2002; Sun et al. 2006).

Furthermore, there are various factors which also influence the shape of the SWCC including suction measurement methodologies and procedures, sample size, stress history, additives, aging, and mineralogy. A critical review on the influence of these factor on the SWCC can be found in some studies such as Malaya & Sreedeep (2012) and Raghuram et al. (2024).

2.4.4. Methods to establish SWCC

Several experimental methods are available for measuring the SWCC, each tailored to specific suction ranges and soil types. A comprehensive review of SWCC measurement

techniques is provided in previous studies (Elgabu 2013; Rahardjo et al. 2019). These methods can be broadly classified into two main approaches: direct and indirect measurement techniques.

2.4.4.1. Direct measurement techniques

These methods directly regulate or measure matric suction while simultaneously recording the corresponding water content, providing precise experimental data that are widely used in laboratory testing.

The hanging column technique is a direct method for determining the soil-water characteristic curve (SWCC) within low suction ranges, typically between 0 and 10 kPa. This method is particularly suitable for coarse-grained soils, such as sands and silts, where the generation of suction is challenging due to rapid drainage. The test operates based on hydrostatic equilibrium within a water column. A ceramic disk with a high air-entry value is place between sample and the water line connected to the water column. By suspending a soil sample above a water reservoir, a suction gradient develops as water drains from the soil under gravitational forces. The matric suction in the soil corresponds to the negative pressure within the column, which can be varied by changing the height of the column. Several researchers have employed the hanging column method to measure suction in coarse-grained soils (Vanapalli et al. 2009; Likos et al. 2010).

Various devices are commonly used to directly measure matric suction, including tensiometers, high-capacity tensiometers, and null-type axis translation apparatus. These instruments typically rely on the separation of water and air phases, often achieved using a ceramic disk with a high air-entry value, which can be adjusted depending on the required suction range (Elgabu 2013). Conventional tensiometers are limited by cavitation, restricting their measurement capability to approximately 100 kPa (Fredlund & Rahardjo 1993*b*). However, advancements in tensiometer technology have extended this range to 1500 kPa, leading to the development of high-capacity tensiometers (Lourenço et al. 2011; Wijaya & Leong 2016; Li et al. 2019; Mendes et al. 2020; Rahardjo et al. 2021). More recently, Liu et al. (2023) introduced a high-capacity osmotic tensiometer capable of measuring suctions up to 2500 kPa. A comprehensive review of the theoretical and practical aspects of suction measurement using high-capacity tensiometers is provided by Marinho et al. (2008).

2.4.4.2. Indirect measurement techniques

These methods do not directly control suction but instead allow the soil to reach equilibrium with a known external suction source before measuring the corresponding water content. They rely on calibration curves or empirical relationships to estimate suction values (Ridley & Wray 1996; Sreedeep & Singh 2011). The primary methods in this category include psychrometers, chilled-mirror hygrometers, thermal and electrical conductivity sensors, osmotic technique, and the filter paper technique. A comprehensive review of these techniques is available in previous studies (Ridley & Wray 1996; Rahardjo & Leong 2006; Pan et al. 2010; Sreedeep & Singh 2011; Elgabu 2013).

The chilled-mirror dew-point technique is a highly accurate method for measuring total suction in unsaturated soils. It determines suction by measuring the dew-point temperature of air in equilibrium with the soil sample, which is then used to calculate suction based on the Kelvin equation (see Eq. 2.2). This technique is widely implemented in chilled-mirror hygrometers, which provide precise and repeatable suction measurements over a broad suction range. Several studies have employed this method for suction measurement: Agus & Schanz (2005) measured suction values ranging from 150 kPa to approximately 9000 kPa, Rahardjo et al. (2019) reported measurements from 500 kPa to about 5 MPa, and Roy & Rajesh (2018) used a chilled-mirror hygrometer to measure suctions between 1000 kPa and 30 MPa.

2.4.4.3. Suction control techniques

Suction control techniques are fundamental for investigating the behavior of unsaturated soils, as they enable the regulation and maintenance of specific suction values under controlled laboratory conditions.

The axis translation technique (ATT) is a direct method for controlling matric suction by applying an elevated air pressure to a soil sample while maintaining a constant pore water pressure. This approach effectively shifts the reference point for suction measurement, mitigating cavitation issues (Hilf 1956). ATT is widely employed for low to intermediate suction ranges (0-1500 kPa) and is particularly effective when used with saturated porous ceramic plates (see Fig. 3.17 in Section 3.3.1). It has been extensively applied in research to establish the soil-water characteristic curve (SWCC) and regulate suction in laboratory tests (Agus 2005; Ng et al. 2007; Li et al. 2009; Alabdullah 2010; Pourzargar et al. 2014; Ahmadinezhad et al. 2019).

The pressure plate apparatus is a common method for applying matric suction based on the ATT, originally introduced by Hilf (1956) to address cavitation issues at low negative water pressures, which otherwise limit the suction measurement range. The ATT functions by artificially increasing pore air pressure while maintaining pore water pressure at atmospheric or another controlled value. This process effectively "translates" the suction range into measurable values, circumventing the cavitation constraints encountered in traditional tensiometers at low suctions. The technique relies on a saturated high air-entry porous material, typically a ceramic disk, to separate air and water phases. This disk permits the transmission of water while preventing air flow, provided the applied matric suction remains below its air-entry value. Several studies have employed the pressure plate apparatus to determine the soil-water characteristic curve (SWCC) (Fredlund & Rahardjo 1993*b*; Alabdullah 2010). To address air entrapment issues in the outflow tube during pressure plate tests, Leong et al. 2004 introduced a modified pressure plate apparatus. Similarly, Lins et al. (2009) developed a version capable of measuring the SWCC along both drying and wetting paths while also investigating the influence of net stress on SWCC behavior. Additionally, Tripathy et al. (2012) measured the SWCC of compacted soil using a triaxial cell based on the null-type axis-translation technique described by Fredlund & Rahardjo (1993*b*).

The vapor equilibrium technique (VET) is an indirect method that controls total suction by placing soil samples in a sealed chamber containing a salt solution or a controlled humidity environment, allowing moisture exchange until equilibrium is reached (Tessier 1984). VET is particularly suited for high suction levels (several MPa) but requires long equilibration times. This technique has been employed in numerous studies to determine the SWCC and regulate suction in triaxial and biaxial tests (Agus 2005; Alabdullah 2010; Baille 2014).

The osmotic technique (OT) is another indirect method used to impose and control high suctions, typically ranging from 100 kPa to several MPa. This technique operates by generating an osmotic potential difference using a semi-permeable membrane and a concentrated polymer solution, which extracts water from the soil and induces suction. A number of studies in unsaturated soil has been performed using osmotic method (Kassiff & Shalom 1971; Delage 1987; Delage & Suraj de Silva 1992; Fleureau et al. 1993; Cui & Delage 1993; Cui & Delage 1996; Blatz & Graham 2000; Marcial et al. 2002; Delage & Cui 2008; Baille 2014; Tripathy et al. 2014; Lieske et al. 2020). In the osmotic technique, described by Delage & Cui (2008), the sample was brought into contact with a semipermeable membrane that allows the passage of water. An aqueous solution containing large, soluble

polyethylene glycol (PEG) molecules was circulated behind a semi-permeable membrane. Due to the size of the PEG molecules, they were unable to pass through the membrane, thereby generating osmotic suction on the soil sample. As the membrane is permeable to dissolved salts, the chemical equilibrium is maintained, ensuring effective control of suction. The magnitude of the applied suction is governed by the concentration of the PEG solution. It means that higher concentrations correspond to higher levels of osmotic suction.

A comprehensive review of suction control techniques, including the ATT, VET, and OT, is provided by Delage et al. (2008) and Blatz et al. (2008).

2.4.5. Modelling SWCC

Various empirical, analytical, and statistical models have been formulated to characterize the SWCC and fit experimental data. Most of these models are empirical, relying on the observed shape of the SWCC. Comprehensive reviews of existing SWCC models have been conducted by Leong & Rahardjo (1997), Sillers & Fredlund (2001), Pham (2001), and Lins (2010). Among the numerous models proposed, those developed by Van Genuchten (1980), Fredlund & Xing (1994), and Durner (1994) are particularly well recognized and will be presented in the following sections.

2.4.5.1. Van Genuchten (1980)'s SWCC model

Van Genuchten (1980) proposed an equation for the relationship between the effective degree of saturation (S_e) and the suction (ψ) based on the original equation introduced by Mualem (1976). The equation is expressed as follows:

$$S_e = \frac{w_\psi - w_{res}}{w_{sat} - w_{res}} = \left[\frac{1}{1 + (\alpha \cdot \psi)^n}\right]^{1-\frac{1}{n}} \tag{2.6}$$

where w_ψ is the gravimetric water content at a given suction (ψ), w_{sat} is the gravimetric water content at saturation, w_{res} is the residual water content, and α and n are fitting parameters. Equation 2.6 can also be expressed in terms of volumetric water content (θ) or degree of saturation (S_r).

2.4.5.2. Fredlund & Xing (1994)'s SWCC model

Fredlund & Xing (1994) proposed an equation for SWCC based on the assumption that the shape of the SWCC depends on the pore size distribution of the soil. The equation is expressed as follows:

$$S_e = \frac{w_\psi}{w_{sat}} = C(\psi) \cdot \frac{1}{\left\{ \ln \left[e + (\alpha \cdot \psi)^n \right] \right\}^m} \tag{2.7}$$

where w_ψ is the gravimetric water content at a given suction (ψ), w_{sat} is the gravimetric water content at saturationt. e is the Euler number, ln is the natural logarithm, α, and n, m are fitting parameters. Equation 2.7 can also be expressed in terms of volumetric water content (θ) or degree of saturation (S_r). $C(\psi)$ is a correction function enabling the best-fit to reach a suction of 10^6 kPa corresponding to zero water content and is expressed as follows:

$$C(\psi) = 1 - \frac{\ln \left[1 + \frac{\psi}{\psi_{res}} \right]}{\ln \left[1 + \frac{10^6}{\psi_{res}} \right]} \tag{2.8}$$

where ψ_{res} is the residual suction.

2.4.5.3. Durner (1994)'s SWCC model

Durner (1994) proposed a bimodal SWCC model which is a weighted sum of two unimodal Van Genuchten (1980)'s SWCC models. The equation is expressed as follows:

$$S_e = \frac{w_\psi - w_{res}}{w_{sat} - w_{res}} = w_1 \left\{ \left[\frac{1}{1 + (\alpha_1 \cdot \psi)^{n_1}} \right]^{1 - \frac{1}{n_1}} \right\} + (1 - w_1) \left\{ \left[\frac{1}{1 + (\alpha_2 \cdot \psi)^{n_2}} \right]^{1 - \frac{1}{n_2}} \right\} \tag{2.9}$$

where w_ψ is the gravimetric water content at a given suction (ψ), w_{sat} is the gravimetric water content at saturation, w_{res} is the residual water content, and w_1, α_1, n_1, α_2, n_2 are fitting parameters. Equation 2.7 can also be expressed in terms of volumetric water content (θ) or degree of saturation (S_r).

2.5. Soil shrinkage curve (SSC)

2.5.1. Features of SSC

The soil shrinkage curve (SSC) describes the relationship between void ratio or volumetric strain and water content as a soil undergoes drying. It is a crucial tool for understanding the volume change behavior of fine-grained soils, particularly clays, in response to moisture loss. Figure 2.8 shows typical SSC of a non structured soil and a well structured soil.

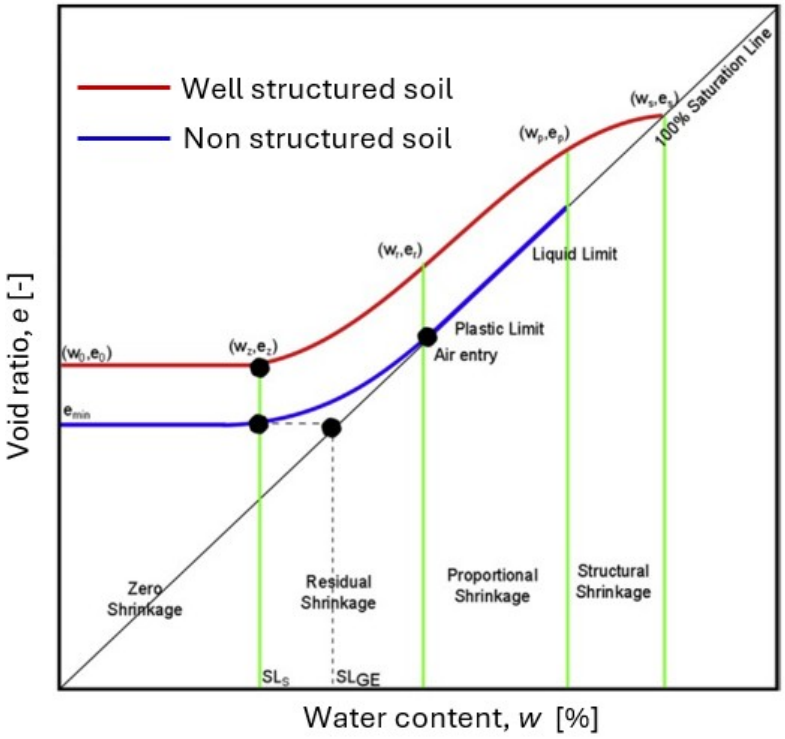

Figure 2.8.: Typical soil shrinkage characteristic curves of a non structured soil and a well structured soil (adapted from Mishra et al. 2019, originally from Cornelis et al. 2006)

The SSC typically exhibits four distinct phases (Haines 1923; Cornelis et al. 2006): structural shrinkage, proportional shrinkage, residual shrinkage, and zero shrinkage, each representing different degrees of volume change as water is removed. In the structural shrinkage phase, minimal volume change occurs due to the expulsion of water from large, interconnected pores. However, the structural shrinkage mostly occurs in case of well structured soil where the water initially drains out from the large inter-aggregate pores and from channels formed by biological activity (Kim et al. 1992; Cornelis et al. 2006; Mishra et al. 2019). The proportional shrinkage phase follows, where the soil volume decreases propor-

tionally with water loss. As drying continues, the soil enters the residual shrinkage phase, where volume change slows despite further water loss. Finally, in the zero shrinkage phase, all volume reduction ceases, and any additional water loss occurs without affecting the soil structure. Wijaya & Leong (2014) indicated that in geotechnical engineering the shrinkage limit is determined as the water content at the intersection point of the saturation line and the extension of the zero shrinkage line (horizontal line with minimum or constant void ratio) (SL_{GE} in Fig. 2.8), while in soil science it corresponds to the water content (SL_S in Fig. 2.8) after which there is no further change in the void ratio of soil sample.

2.5.2. Methods to establish SSC

To establish the SSC, two variables representing the changes in water content and void ratio are required. During the drying process, these variables are measured at regular intervals. During the drying process, while the weight of the sample can be measured by using a precise balance, precise measurement of the sample volume is challenging. Several experimental methods have been developed to measure the volume of the sample during shrinkage. A comprehensive literature review of volume measurement methods has been conducted by Sharanya et al. (2021). The following are some commonly used methods to measure volume of soil samples in the SSC determination.

2.5.2.1. Contact methods

The contact method is widely used due to its convenience; however, it is only suitable for samples with well-defined geometry and relatively high stiffness. Commonly employed instruments include Vernier calipers, flexible tape measures, and electronic contact sensors. To account for potential non-uniformity in the sample, measurements should be taken at a maximum number of fixed positions. Although this method is straightforward and direct, the accuracy of volume measurements depends on careful manual handling of the sample. Several studies have utilized this method (Fredlund & Zhang 2013; Wijaya et al. 2015; Mishra et al. 2019; Mishra et al. 2020).

The liquid displacement method is another widely used technique for determining soil sample volume by measuring the amount of liquid displaced upon submersion. A commonly adopted variation is the wax coating method, which is particularly effective for irregularly shaped or shrinkage-prone samples. In this method, the soil sample is carefully coated with a thin layer of paraffin wax or another waterproof material to prevent water

absorption. Once sealed, the sample is immersed in liquid, and its volume is determined based on the Archimedes principle. This method has been extensively applied in previous research (Lauritzen & Stewart 1942; Pellissier 1991; Cornelis et al. 2006; Soltani et al. 2024).

Additionally, the immersion weighing method, or buoyancy method, is a direct liquid displacement technique that determines the volume of a soil sample by comparing its weight in air to its weight when fully submerged in liquid. This approach relies on the Archimedes principle, which states that the buoyant force on a submerged object is equal to the weight of the displaced liquid. By measuring the weight difference, the volume of the soil sample can be calculated. Low-surface-tension liquids such as kerosene, silicone oil, canola oil, and paraffin oil are commonly used in this technique. Several studies have employed this method (Sibley & Williams 1989; Péron et al. 2007; Christ et al. 2022).

The rubber membrane method is another practical technique for determining the volume of irregularly shaped soil samples (Tariq & Durnford 1993; Gapak et al. 2017; Mishra et al. 2021). In this method, the soil sample is enclosed within a flexible rubber membrane and then submerged in water. The volume of displaced fluid is measured to estimate the sample's volume. A key advantage of this approach is its non-destructive nature. However, the accuracy of the measurement depends on the elasticity of the rubber membrane, which may degrade over time, potentially affecting precision. Additionally, this method is not suitable for undisturbed soft soils due to potential deformation during handling and the small stress exerted by the rubber membrane.

Measurements of soil sample volume using Linear Variable Displacement Transducers (LVDT) have been used in a number of studies (Boivin et al. 2004; Vesga 2008; Liu et al. 2020). The LVDT method is a contact-based technique that measures the volume change of a soil sample by tracking vertical and lateral deformations during shrinkage. It consists of LVDT sensors that detect small displacements at the soil surface, converting them into electrical signals for precise volume measurement. These measurements are performed locally in certain points at the sample.

2.5.2.2. Non-contact methods

Non-contact methods for measuring soil sample volume utilize advanced optical and imaging technologies to capture volume changes without physically disturbing the sample. Laser scanning employs a laser beam to scan the soil surface, measuring distances to create a high-resolution 3D model for precise volume estimation (Rossi et al. 2008; Hirmas

et al. 2016). Digital imaging correlation (DIC) techniques analyze sequential photographs to track soil deformation and volume variations over time (Macari et al. 1997; Puppala et al. 2004; Sutton et al. 2009). Photogrammetry reconstructs a 3D representation of the soil sample by processing multiple images taken from different angles, enabling an accurate volume calculation (Jain et al. 2015; Upreti & Leong 2018; Li & Zhang 2019). These non-contact methods offer high precision, rapid data collection, and real-time monitoring of volume changes, making them particularly useful for studying shrinkage and deformation behaviour of soil. However, they require specialized equipment, controlled imaging conditions, and proper calibration to ensure accuracy.

2.5.3. Modelling SSC

Several approaches have been proposed to model the SSC, including methods that fit piecewise functions to the different shrinkage phases - such as the structural, proportional, residual, and zero shrinkage phases (Braudeau et al. 1999; Groenevelt & Grant 2001; Peng & Horn 2005). Polynomial models (Giráldez & Sposito 1983; Fredlund et al. 2002) and logistic models (McGarry & Malafant 1987) have also been developed. Kim et al. (1992) introduced an SSC model that combines exponential and linear functions to best fit the SSC of unripe marine clay. Similarly, Olsen & Haugen (1998) proposed a second-order hyperbolic function to model SSC in Norwegian soils. A comprehensive review of SSC models was conducted by Cornelis et al. (2006). Among the various models proposed, those developed by Fredlund et al. (2002) and Peng & Horn (2005) are widely used due to their simplicity and practical applicability. These models, which are also employed in the present study, will be described in the following sections.

2.5.3.1. Fredlund et al. (2002)'s SSC model

Fredlund et al. (2002) proposed an equation based on the hyperbolic nature of the shrinkage curve to best-fit experimental data. The equation is expressed as follows:

$$e(w) = a_{sh}\left[\frac{w^{c_{sh}}}{b_{sh}^{c_{sh}}} + 1\right]^{\frac{1}{c_{sh}}} \tag{2.10}$$

where w is water content, $e(w)$ is void ratio as a function of water content, and a_{sh}, b_{sh}, and c_{sh} are fitting parameters. These parameters have distinct physical interpretations: a_{sh} represents the minimum void ratio, b_{sh} characterizes the slope of the SSC in the normal shinkage zone, and c_{sh} defines the curvature of the SSC.

2.5.3.2. Peng & Horn (2005)'s SSC model

Peng & Horn (2005) proposed an equation derived from the inverse of the SWCC model introduced by Van Genuchten (1980). This equation is designed to represent the entire shrinkage range and to mathematically define the different shrinkage zones. It is expressed as follows:

$$e(\vartheta) = \begin{cases} e_r, & \vartheta = 0 \\ e_r + \dfrac{e_s - e_r}{\left[1 + \left(\dfrac{\alpha\vartheta}{e_s - \vartheta}\right)^{-n}\right]^m}, & 0 < \vartheta < \vartheta_s, \quad n > 0 \\ e_s, & \vartheta = \vartheta_s \end{cases} \tag{2.11}$$

here, ϑ is the moisture ratio and is expressed as ratio between the volume of water (V_w) and the volume of solid (V_s) (see Eq. 2.12).

$$\vartheta = \frac{V_w}{V_s} \tag{2.12}$$

In Eq. 2.11, e_r is the residual void ratio, e_s is the saturation void ratio, ϑ_s is the saturation moisture ratio, and α, m, and n are fitting parameters.

2.6. Pore size distribution of unsaturated soils

The microstructural characteristics of unsaturated soils play a crucial role in governing key hydro-mechanical behaviors, including water retention, permeability, and shear strength (Delage et al. 1996; Kodikara et al. 1999; Romero et al. 1999; Sivakumar et al. 2006; Thom et al. 2007; Oualmakran et al. 2016; Cai et al. 2020). Unlike saturated soils, where all pores are completely filled with water, unsaturated soils exhibit a complex interplay between air, water, and solid particles within their pore network. The distribution of pore sizes, in particular, significantly influences water retention and transport mechanisms, impacting various geotechnical applications such as slope stability, foundation performance, and soil-structure interactions (Romero & Simms 2008).

The scanning electron microscope (SEM) and mercury intrusion porosimetry (MIP) are the most widely used techniques for examining soil microstructure. Romero & Simms (2008) provided a comprehensive review of these methods. In the study of unsaturated

soils, microscopic analysis has traditionally concentrated on compacted soils, highlighting the aggregation or matrix arrangement at different stages of the Proctor compaction curve.

Delage et al. (1996) conducted a study on the microstructure of a compacted silt, carried out using SEM and MIP. Their study was conducted on the compacted silt samples at three water content states of a proctor curve including the dry side of the optimum water content, at the optimum water content, and on the wet side of the optimum water content. They indicated that the sample compacted at the dry side of optimum water content shows a bimodal PSD with two distinctly different peaks while the one at the wet side of optimum water content exhibit an unimodal PSD with only one peak occurring. The sample at optimum water content shows a bimodal PSD, however the second peak at the larger pores range is not significant.

Lloret et al. (2003) analyzed the PSD of compacted soil samples at two different dry densities and observed a bimodal distribution. This was attributed to the formation of a flocculated structure, similar to that found in samples compacted on the dry side of the optimum water content (Delage et al. 1996). In a flocculated structure, aggregates form, creating two distinct pore types: inter-aggregate pores (between aggregates) and intra-aggregate pores (within aggregates). The bimodal PSD reflects these two pore systems, with the larger peak corresponding to inter-aggregate pores and the smaller peak to intra-aggregate pores. Figure 2.9 illustrates the incremental pore volume distribution for two compacted bentonite samples with different dry densities, based on MIP tests conducted by Lloret et al. (2003). The figure clearly shows that compaction primarily influences the larger inter-aggregate pores.

Similarly, Sivakumar et al. (2006) examined the impact of compaction pressure on the PSD of compacted kaolin. Their findings confirmed a bimodal PSD, demonstrating that as compaction pressure increases, inter-aggregate pores decrease, while intra-aggregate pores remain relatively unaffected.

Thom et al. (2007) investigated the effect of saturation on the PSD of kaolin samples compacted at 400 kPa and 800 kPa. The samples were saturated under a mean effective pressure of 37.5 kPa using a triaxial apparatus. Figure 2.10 illustrates their findings, comparing the PSD of samples in the as-compacted state and after saturation. The results demonstrate that saturation primarily influences the larger inter-aggregate pores, while the intra-aggregate pores remain largely unaffected. They attributed this to the expansion of aggregates into the inter-aggregate pore spaces during saturation. In contrast, Monroy et al. (2010) studied the change of the PSD of compacted London clay during saturation and found an increase of the inter-aggregate pore spaces accompanied by a decrease of

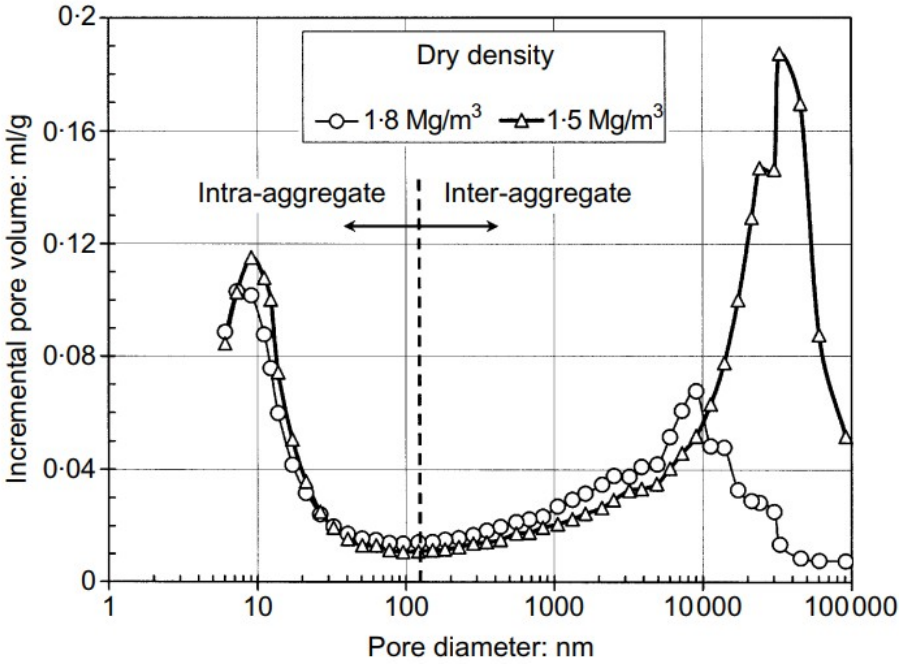

Figure 2.9.: Distribution of incremental pore volume for two compacted bentonite samples at different dry densities from MIP test (after Lloret et al. 2003)

the intra-aggregates pore spaces. They also found a transition from a bimodal PSD to an unimodal PSD during the saturation process.

Cuisinier & Laloui (2004) examined how suction influences fabric modifications in compacted silt. Their findings demonstrated a clear effect of increasing suction on the evolution of the PSD (Fig. 2.11). They observed that the drying process leads to a notable reduction in macropore volume while micropore volume increases. Similarly, Li & Zhang (2009) studied the PSD evolution of lean clay mixed with sand and found that as the degree of saturation decreases from full saturation ($S_r = 1$) to dry conditions ($S_r = 0$), the PSD transitions from a unimodal to a bimodal distribution.

Cui et al. (2002) investigated the effect of the wetting process on the PSD of sand-bentonite mixture samples. Their results showed that, along the wetting path, macro-porosity progressively decreases with decreasing suction. This reduction is attributed to the separation of clay sheets within aggregates and the consequent deformation of the aggregates. In contrast, micro-pores remain relatively stable up to a certain suction threshold, beyond which they increase significantly as suction approaches zero. This increase is likely due to the swelling pressure generated during the wetting process.

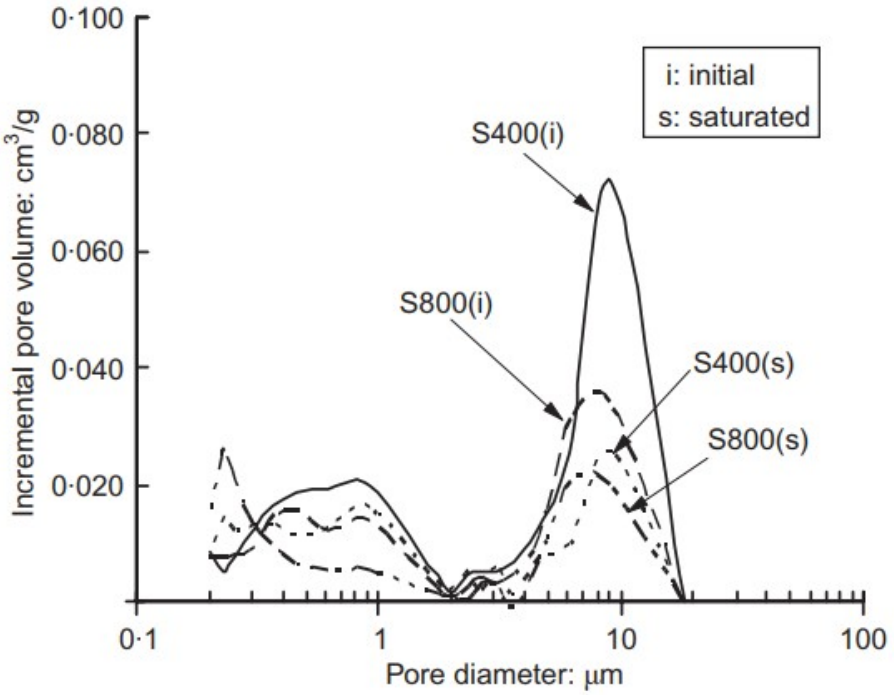

Figure 2.10.: Pore size distribution (PSD) of kaolin samples compacted at 400 kPa (S400) and 800 kPa (S800), in the as-compacted condition and after saturation (after Thom et al. 2007)

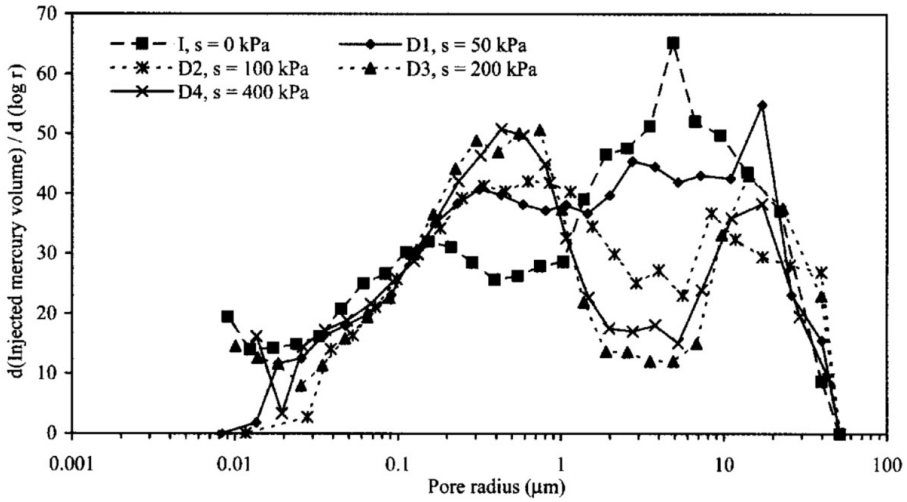

Figure 2.11.: The PSD of compacted silt samples as suction increases from 0 to 400 kPa (after Cuisinier & Laloui 2004)

Despite numerous studies on the microstructure of unsaturated soils, research investigating the evolution of soil microstructure from its initial as-prepared state through successive

drying and wetting processes remains limited. Addressing this gap is one of the primary objectives of this study.

2.7. Effective stress concept in unsaturated soils

The concept of effective stress is fundamental in geotechnical engineering, providing a framework to describe soil behaviour under various loading and environmental conditions. While the effective stress principle, originally proposed by Terzaghi (1936), has been widely accepted for saturated soils, its extension to unsaturated soils remains an ongoing challenge. Unlike saturated soils, where pore water pressure can be uniquely defined and directly subtracted from total stress, unsaturated soils exhibit a more complex stress state due to the presence of both water and air in the pore space (Fredlund & Rahardjo 1993*b*). This dual-phase condition gives rise to additional interparticle forces, such as matric suction and surface tension, which influence soil strength and deformation characteristics.

However, there is an ongoing debate about the most appropriate way to characterize the role of soil-water interactions - particularly suction - in influencing the mechanical behaviour of unsaturated soils. A commonly used approach is to express the macroscopic effect of suction through the effective stress, σ'. Bishop (1959) extended the effective stress principle, originally proposed by Terzaghi (1936) for saturated soils, to unsaturated conditions, defining it as:

$$\sigma' = (\sigma - u_a) + \chi \cdot (u_a - u_w) \tag{2.13}$$

where σ' represents the effective stress, σ is the total stress, u_a is the pore air pressure, and u_w is the pore water pressure. The term $(\sigma - u_a)$ denotes the net normal stress, while $(u_a - u_w)$ represents matric suction. The parameter χ is the effective stress parameter.

Bishop (1959) and Bishop (1961) defined χ as a function of the degree of saturation (S_r), ranging from 1 for fully saturated conditions to 0 for completely dry conditions. However, Coleman (1962) argued that χ depends on soil structure, and therefore making it unsuitable to enforce a direct dependence on S_r. Furthermore, Bishop & Blight (1963) demonstrated that the relationship between S_r and χ is not unique across different soil types. Consequently, the primary criticism of Eq. 2.13 concerns the validity of χ, as its uniqueness and determination remain significant challenges to the broad acceptance of Bishop's effective stress concept.

2.8. Suction stress

Lu & Likos (2006) developed a micromechanical framework for the effective stress concept by introducing the notion of "suction stress." This macroscopic stress variable accounts for the combined effects of capillarity and physicochemical interactions, including van der Waals forces, electrical double-layer repulsion, and net attraction forces arising from chemical cementation at grain contacts. Under the suction stress framework, the effective stress principle can be expressed as follows:

$$\sigma' = (\sigma - u_a) + \sigma^s \tag{2.14}$$

where $\sigma - u_a$ represents the net normal stress, and σ^s denotes the suction stress. According to the definition proposed by Lu & Likos (2006), micromechanical analyses can be applied to a "representative elementary volume" (REV) to describe local interparticle forces in both saturated and unsaturated conditions. Consequently, suction stress is defined as the sum of interparticle forces normalized by the cross-sectional area A of the REV. The expression for σ^s can be formulated as follows:

$$\sigma^s = \sigma_{pc} + \sigma_{cap} + (u_a - u_w) \cdot \left(1 - \frac{A_a}{A}\right) \tag{2.15}$$

Here, σ_{pc} represents the physicochemical stress, while σ_{cap} denotes the capillary stress arising from surface tension. The term $(u_a - u_w) \cdot \left(1 - \frac{A_a}{A}\right)$ accounts for the contribution of suction to the overall suction stress, where A_a is the projected area occupied by the air phase. Lu et al. (2010) suggested that the suction stress concept fundamentally differs from Bishop's effective stress in that it eliminates the need for defining the coefficient χ, as suction stress is considered solely a function of soil suction.

According to Lu et al. (2010), σ^s can be characterized by the suction stress characteristic curve (SSCC), which describes the relationship between suction stress and soil suction. The general functional form of SSCC can be expressed as follows:

$$\sigma^s = f(u_a - u_w) = X \cdot (u_a - u_w) \tag{2.16}$$

Here, X represents a complex function that captures air-water interactions and serves as an upscaling factor, bridging the influence of interparticle forces at the microscopic scale to the macroscopic stress, termed suction stress (σ^s).

In the context of Bishop's effective stress equation, comparing between Eq. 2.13 and Eq. 2.14 indicates that the effective stress parameter χ and the upscaling factor X can be related, but they are not necessarily identical. In other words, the second component on the right-hand side of both equations can be interpreted as suction stress, but their values may differ because the magnitude of χ and X may differ. For instance, Öberg & Sällfors (1997) used the degree of saturation S_r as the parameter χ in determining the shear strength of unsaturated soils, whereas Lu et al. (2010) employed the effective degree of saturation (S_e) as the upscaling factor X. In the following sections, the second component on the right-hand side of both equations (Eq. 2.13 and Eq. 2.14) will be referred to as suction stress.

2.8.1. Prediction of suction stress or effective stress parameter

Experimental measurement of X involves complex and costly unsaturated soil testing procedures, which are particularly time-consuming for fine-grained soils due to the prolonged period required to reach suction equilibrium (Fredlund & Rahardjo 1993*b*; Nuth & Laloui 2008). Consequently, numerous researchers have proposed empirical relationships between X and soil properties (e.g. SWCC, pore-size distribution) to circumvent these challenges. Extensive studies have been conducted to establish an appropriate function for X (Vanapalli et al. 1996; Öberg & Sällfors 1997; Khalili & Khabbaz 1998; Bao et al. 1998; Tekinsoy et al. 2004; Lee et al. 2005; Garven & Vanapalli 2006; Lu & Likos 2006; Alonso et al. 2010; Alonso et al. 2013; Heibrock et al. 2018; Gao et al. 2020; Cavalcante & Mascarenhas 2021).

Vanapalli et al. (1996) proposed a scaling factor X based on the SWCC model introduced by Fredlund & Xing (1994) to predict the shear strength of unsaturated soils. The formulation of the scaling factor can be expressed as follows:

$$X = S_e^{\kappa} \tag{2.17}$$

where S_e represents the normalized water content, obtained by fitting the SWCC model proposed by Fredlund & Xing (1994) (see Eq. 2.7) to measured SWCC data. κ is a fitting parameter. Vanapalli & Fredlund (2000) established a correlation between κ and the plasticity index (I_P), concluding that $\kappa = 1$ provides a good fit between predicted and measured shear strength values for non-plastic soils. However, for plastic soils, due to limited experimental data, a unique relationship was not identified. Subsequently, Garven

& Vanapalli (2006) proposed a mathematical expression relating κ to I_P based on ten sets of shear strength tests on compacted soils, as given in Eq. 2.18.

$$\kappa = -0.0016I_p^2 + 0.0975I_p + 1 \tag{2.18}$$

Khalili & Khabbaz (1998), based on a number of shear strength data set obtained from shear tests on unsaturated soil, established a unique relationship between X and the ratio of matric suction over the air-entry value. The equation of X can be expressed as follows:

$$X = \begin{cases} 1 & \text{if } \psi \leq \psi_{AEV} \\ \left(\frac{\psi}{\psi_{AEV}}\right)^{-0.55} & \text{if } \psi > \psi_{AEV} \end{cases} \tag{2.19}$$

where ψ represents the suction, and ψ_{AEV} denotes the air-entry value. Khalili & Khabbaz (1998) determined ψ_{AEV} by analyzing triaxial test results plotted in a plane of shear strength versus suction. They identified ψ_{AEV} as the suction value at which the shear strength curve transitions from a linear to a nonlinear trend, effectively marking the turning point in the relationship. Therefore, suction stress can be expressed as follows:

$$\sigma^s = \begin{cases} \psi & \text{if } \psi \leq \psi_{AEV} \\ X \cdot \psi & \text{if } \psi > \psi_{AEV} \end{cases} \tag{2.20}$$

Lu et al. (2010) proposed a closed-form equation for determining the suction stress by considering the effective degree of saturation S_e as the upscaling factor X. The equation of suction stress can be expressed as follows:

$$\sigma^s = S_e \cdot \psi \tag{2.21}$$

where ψ is the suction, and S_e is the effective degree of saturation obtained by fitting the SWCC model proposed by Van Genuchten (1980) (see Eq. 2.6) to the measured SWCC data.

Figure 2.12 presents the SSCC for typical soils in terms of the effective degree of saturation and matric suction (Lu et al. 2010). The following key characteristics can be identified from this figure:

- (*i*) Suction stress is zero when matric suction is zero.
- (*ii*) For a given saturation or suction value, clay exhibits the highest suction stress, sand the lowest, and silt falls in between.
- (*iii*) At extremely low degrees of saturation or high suction, the suction stress of sand approaches zero, while that of clay can reach several hundred kilopascals. In the case of silt, suction stress may remain at a certain level even at low degrees of saturation.

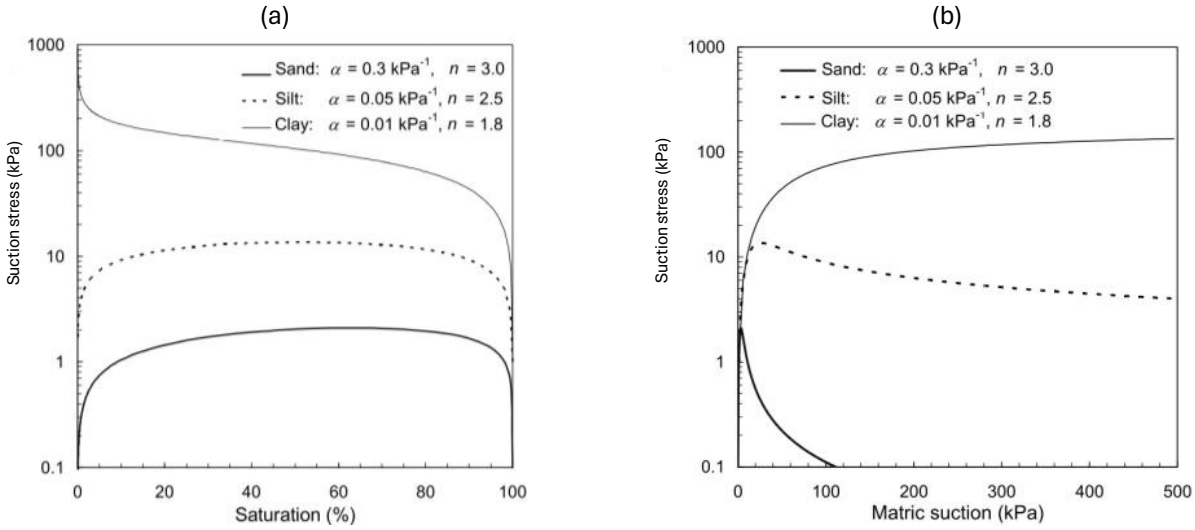

Figure 2.12.: SSCC for typical soils in terms of: (a) effective degree of saturation, and (b) matric suction (after Lu et al. 2010)

Recently, Zhang & Lu (2020) proposed a suction stress equation that integrates both capillary and adsorption effects. Figure 2.13 provides a conceptual illustration of the suction stress characteristic curve. A key advantage of this equation, compared to the suction stress equation introduced by Lu et al. (2010), is its ability to quantitatively separate the contributions of capillary and adsorption effects within the overall suction stress formulation. The equation is expressed as follows:

$$\sigma^s(w) = \sigma^s_{ads}(w) + \sigma^s_{cap}(w) \tag{2.22}$$

$$\sigma^s_{cap}(w) = -\frac{f_{cap}(w)}{\alpha^{ss}} \frac{w}{w_s} \left[\left(\frac{w}{w_s} \right)^{n^{ss}/(1-n^{ss})} - 1 \right]^{1/n^{ss}} \tag{2.23}$$

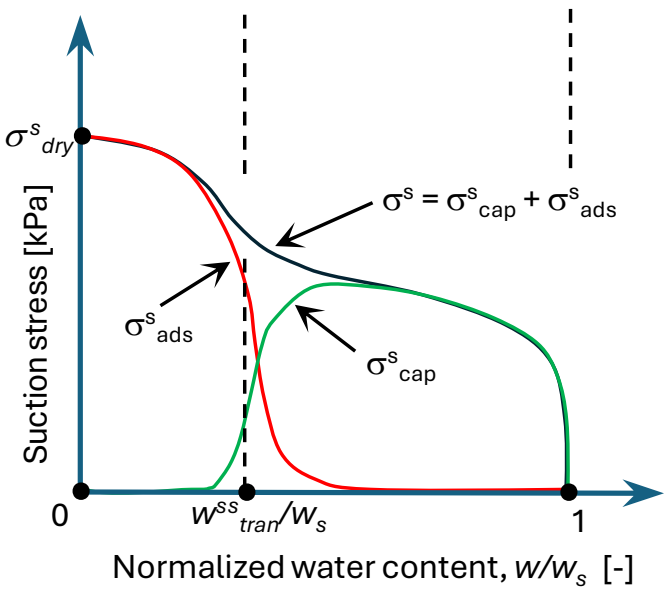

Figure 2.13.: Conceptual illustration for the SSCC (modified and redrawn from Zhang & Lu 2020 for clarity and readability)

$$f_{cap}(w) = \frac{1}{2}\left[1 + erf\left(4\frac{w - w^{ss}_{tran}}{w^{ss}_{tran}}\right)\right] \tag{2.24}$$

$$\sigma^s_{ads}(w) = f_{ads}(w)\sigma^s_{dry} \tag{2.25}$$

$$f_{ads}(w) = \frac{1}{2}\left[1 - erf\left(\beta\frac{w - w^{ss}_{tran}}{w^{ss}_{tran}}\right)\right] \tag{2.26}$$

where $\sigma^s(w)$ represents the total suction stress; $\sigma^s_{cap}(w)$ denotes the capillary suction stress; $\sigma^s_{ads}(w)$ corresponds to the adsorptive suction stress; $f_{cap}(w)$ is a dimensionless scaling function for capillary water; $f_{ads}(w)$ is a dimensionless scaling function that accounts for the competition among physicochemical forces in terms of probability; w_s is the gravimetric water content at saturation; σ^s_{dry} represents the suction stress at the oven-dry state, which macroscopically manifests the van der Waals attraction between particles; w^{ss}_{tran} is the water content marking the upper bound of the adsorptive suction stress range and the cavitation water content for capillary suction stress (see Fig. 2.13); α^{ss} is a fitting parameter related to the inverse of the average capillary suction stress; n^{ss} is a fitting parameter associated with the pore-size distribution for capillary suction stress; and β is a fitting parameter that reflects the strength of adsorptive suction stress, governing the

transition from the adsorption regime to the capillary regime, and is dependent on soil type and fabric.

2.8.2. Experimental determination of suction stress

Experimental investigations in unsaturated soil mechanics are inherently complex and costly. However, numerous studies have been conducted to experimentally validate the effective stress concept, with a particular focus on suction stress. The primary objective of these experiments is to indirectly quantify suction stress through element testing methods, including triaxial tests, direct shear tests, biaxial tests, unconfined compression tests, and uniaxial tensile tests. The validity of the effective stress concept implies that variations in soil strength due to changes in water content or suction can be fully attributed to corresponding changes in effective stress. Consequently, shear and tensile tests serve as viable approaches for determining suction stress (Lu & Likos 2006; Lu et al. 2009; Lu et al. 2010; Akin & Likos 2020).

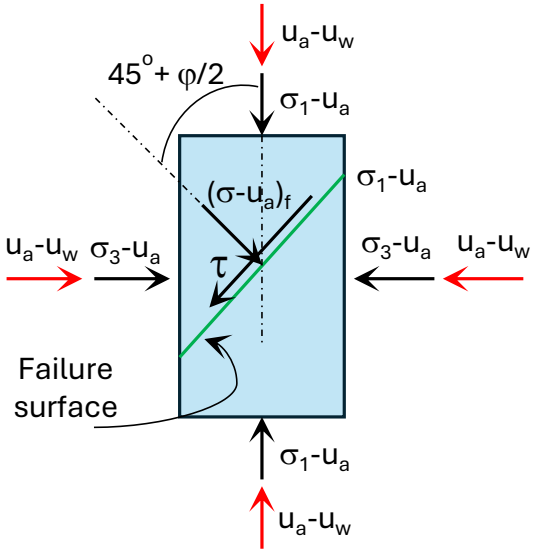

Figure 2.14.: State of stress at failure in a triaxial test on unsaturated soil (adapted from Niu et al. 2024)

Figure 2.14 illustrates the state of stress at failure for a triaxial test on unsaturated soil. The stress state at failure, as determined through shear or tensile tests, is often represented using an extended Mohr-Coulomb diagram (Fredlund & Rahardjo 1993*b*; Lu & Likos 2004). This diagram incorporates three axes: shear stress, net normal stress, and suction. Notably, most experimental validation studies assume that the internal friction

angle remains constant across varying suction levels when plotting results in this extended framework. Figure 2.15 illustrates the failure surface projection onto the shear stress versus net normal stress plane. In this figure, the solid line represents the failure envelope derived from saturated soil tests, while the dashed line corresponds to unsaturated soil tests. Using the effective stress equation (Eq. 2.14), the equation for the shear strength of unsaturated soil can be expressed as:

$$\tau = \left[(\sigma - u_a)_f + \sigma^s\right] \tan \varphi_0' + c_0' \tag{2.27}$$

Suction stress, σ^s, is then determined as:

$$\sigma^s = \frac{c_i' - c_0'}{\tan \varphi_0'} \tag{2.28}$$

where $(\sigma - u_a)_f$ is the net normal stress on the failure plane at failure, c_i' denotes the cohesion obtained from tests on unsaturated soil samples (with results expressed in terms of total stress), meanwhile c_0' and φ_0' are the shear strength parameters determined from tests on saturated soil samples (with results expressed in terms of effective stress).

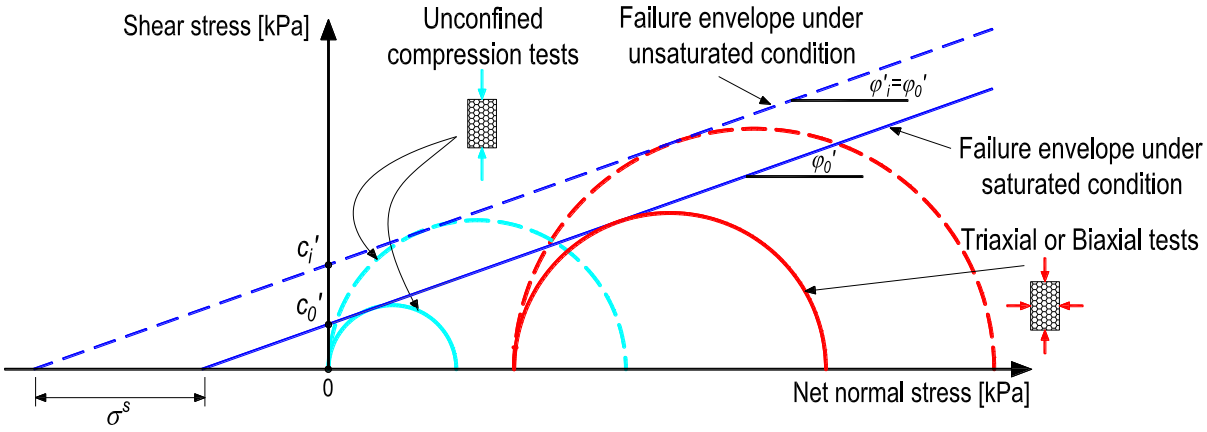

Figure 2.15.: Conceptual illustration for the determination of suction stress from shear test results, where dashed lines and circles represent the test results in total stress, and solid lines and circles represent the test results in effective stress (adapted from the concept of Lu & Likos 2004)

A number of experimental studies on the shear strength of unsaturated soil samples have been conducted using triaxial tests (Lu et al. 2010; Khalili & Khabbaz 1998; Khalili et al. 2004; Guan 2012; Banerjee 2017; Almahbobi 2018; Patil et al. 2020), direct shear tests

(Vanapalli et al. 1996; Lu et al. 2010; Hamid & Miller 2009; Zhou, Xu & Garg 2016), biaxial tests (Alabdullah 2010; Soleimani Fard 2015; Pourzargar 2017; Patil et al. 2020), or unconfined compression tests (Vanapalli & Fredlund 2000; Chae et al. 2010; Zhou, Xu & Garg 2016; Oh & Vanapalli 2018).

Futai & Almeida (2005) and Alsherif & McCartney (2014) reported a significant increase in the friction angle derived from the tests at very high suction levels (several hundred megapascals). This finding raises questions about the validity of assuming a constant friction angle with varying suction when calculating shear strength based on the effective stress concept.

On the other hand, to determine the suction stress using uniaxial tensile tests, a number of studies have been performed (Vesga 2008; Lu et al. 2010; Akin & Likos 2020; Bulolo et al. 2021; Salimi et al. 2021). In general, similar to shear tests, the stress state at failure of the sample in tensile tests is often represented using an extended Mohr-Coulomb diagram. Figure 2.16 illustrates the failure surface projection onto the shear stress versus net normal stress plane. In this figure, the solid line represents the failure envelope derived from saturated soil tests, while the dashed line corresponds to unsaturated soil tests. Suction stress, σ^s, is then determined as:

$$\sigma_{its-i} = \frac{\sigma_{uts-i}}{2 \cdot \tan \varphi'_0 \cdot \tan(\frac{\pi}{4} - \frac{\varphi'_0}{2})} \tag{2.29}$$

$$\sigma_{its-0} = \frac{c'_0}{\tan \varphi'_0} \tag{2.30}$$

$$\sigma^s = \sigma_{its-i} - \sigma_{its-0} \tag{2.31}$$

In Eq. 2.29 and Eq. 2.30, c'_0 and φ'_0 represent the shear strength parameters at saturated conditions. σ_{uts-i} is the uniaxial tensile strength derived from the tests on unsaturated samples, while σ_{its-0} and σ_{its-i} are the isotropic tensile strength at saturated and unsaturated condition, respectively.

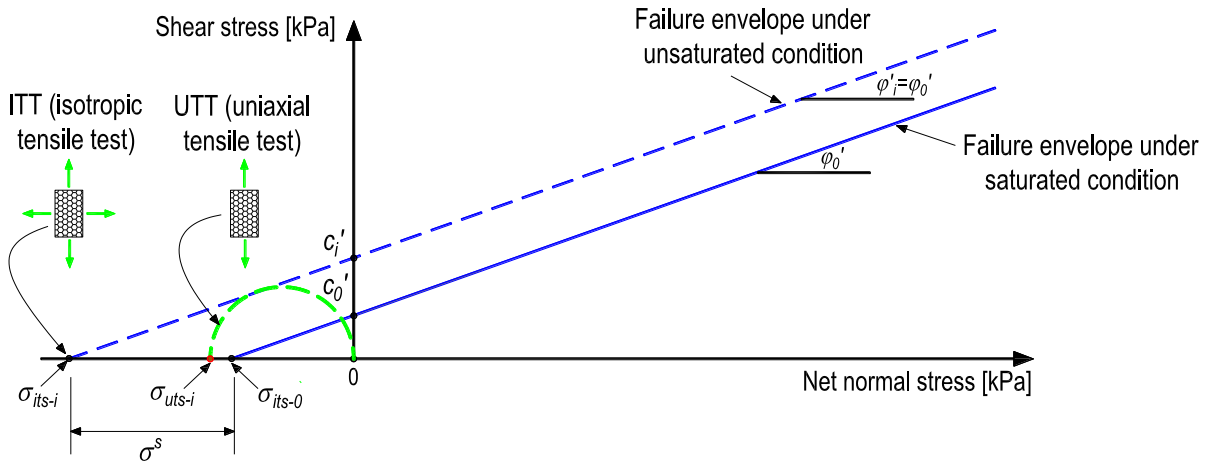

Figure 2.16.: Conceptual illustration for the determination of suction stress from tensile test results, where dashed lines and circles represent the test results in total stress, and solid lines represent the test results in effective stress (adapted from the concept of Lu et al. 2009)

2.9. Summary of existing research gaps and outline of the research program

In general, as previously discussed, numerous studies have been conducted to determine the effective stress parameter or suction stress, aiming to validate the effective stress concept in unsaturated soils. Figure 2.17 provides an overview of experimental studies that have attempted to validate this concept.

For coarse-grained soils, due to their narrow suction range characterized by the soil-water characteristic curve (SWCC), investigations have typically been conducted at low suction levels (below 200 kPa), as demonstrated in studies on Ottawa sand and Macau silty sand. In the case of silts, silty sands, or sand-clay mixtures with a high sand content, the studied suction range extends up to approximately 1000 kPa. For these soil types, the contribution of suction to effective stress is primarily attributed to capillary effects arising from negative pore water pressure and surface tension at the air-water interface menisci (Lu & Likos 2004; Mitchell & Soga 2005).

However, for clay, as shown in Figure 2.17, most investigations have been limited to suction levels below 1500 kPa, with only a few studies exploring the validation of effective stress at higher suction levels. This upper limit remains relatively low compared to the full suction range typically characterized by the SWCC of clay, highlighting a gap in experimental validation at higher suctions.

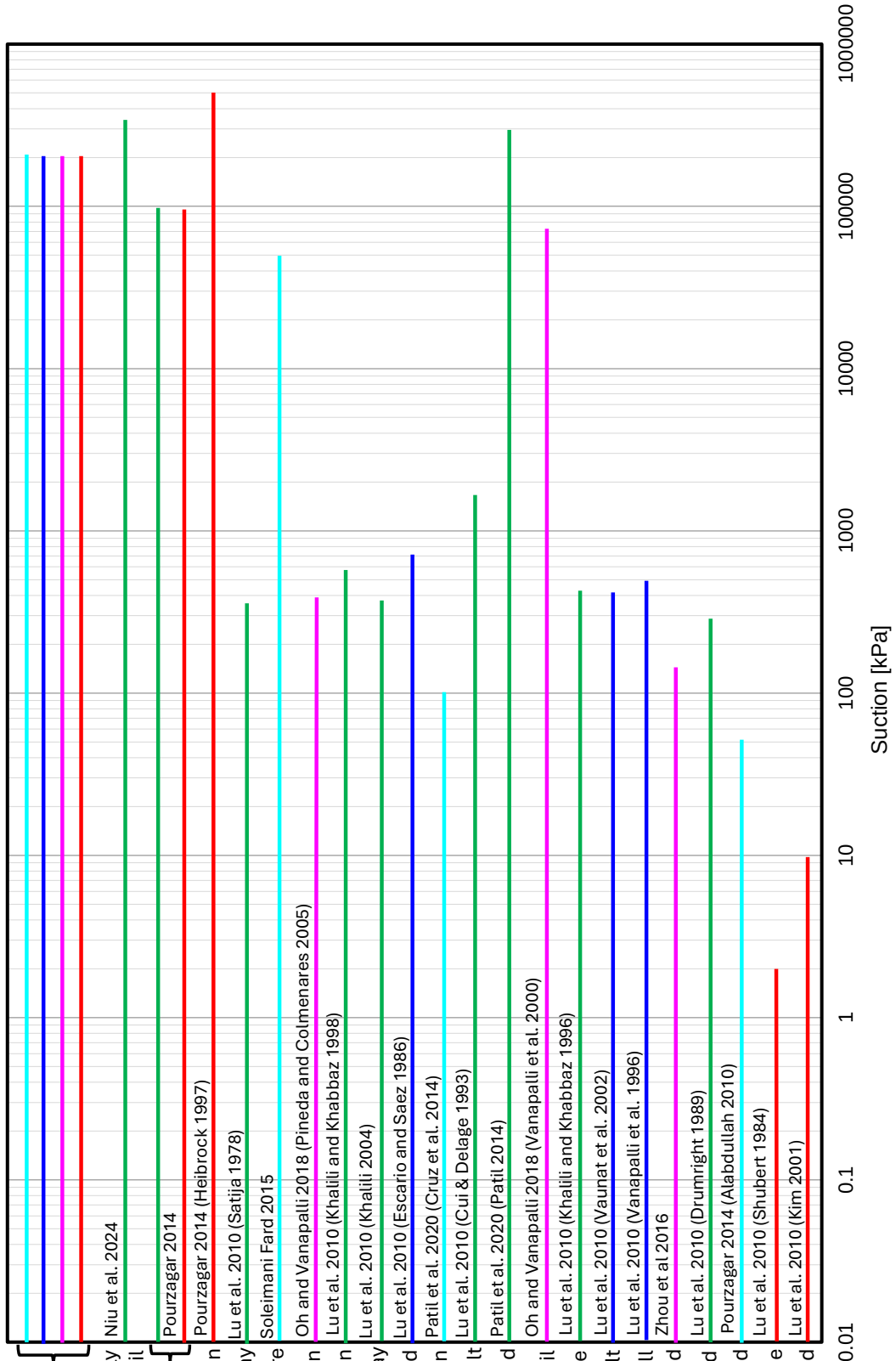

Figure 2.17.: Some experimental studies on validation of the effective stress concept: vertical axis = soil type, red line = uniaxial tensile tests, purple line = unconfined compression tests, blue line = direct shear tests, cyan line = biaxial compression tests, name in parentheses = data source

If the effective stress concept is universally valid, the suction stress derived from different experimental methods on the same soil under identical initial conditions (i.e., structure, void ratio, degree of saturation, and suction) should be consistent across a wide range of suction levels. However, most previous studies have relied on data from a single type of test, limiting the robustness of their conclusions. As illustrated in Fig. 2.17, apart from Pourzargar (2017) where suction stress was determined from a series of triaxial and uniaxial tensile tests on sand-kaolin mixtures, no study has systematically determined suction stress from multiple test types on a single soil type with identical initial conditions. Consequently, a comprehensive experimental investigation that integrates various testing methods and spans a broad range of suction levels to rigorously validate the effective stress concept in unsaturated soils is still lacking.

To address this, a comprehensive dataset will be established in this study, incorporating multiple laboratory tests, including biaxial compression tests (BCT), direct shear tests (DST), unconfined compression tests (UCT), and uniaxial tensile tests (UTT). These tests were performed on kaolin along both drying and wetting paths over a wide range of suction levels. The primary objective is to validate the effective stress concept in unsaturated soils by determining and analyzing suction stress values derived from different test types. Suction stress were determined from a comparison of unsaturated and saturated samples. Additionally, selected well-known suction stress models will be applied to the dataset for comparison. This dataset is also valuable for the development and calibration of constitutive models in future research, providing extensive experimental data necessary for accurately predicting the behavior of unsaturated soils under various environmental and loading conditions.

Figure 2.18 outlines the research program conducted in this study. In addition to the main group of tests (BCT, DST, UCT, and UTT), which form the backbone of this research, a series of triaxial compression tests (consolidated-drained conditions) under saturated conditions will also be performed. These triaxial tests are essential, as their shear strength parameters will be used to back-calculate the suction stress for the UCT and UTT, where conducting tests under fully saturated conditions is challenging.

Moreover, since suction is neither measured nor controlled during UCT and UTT, the soil-water characteristic curve (SWCC) is required to determine the suction corresponding to the water content measured after testing. The best-fit SWCC parameters will also be utilized to predict suction stress. Additionally, a soil shrinkage curve (SSC) is established to describe the volume change of the soil (i.e., void ratio) during the drying process.

Linking the SWCC with the SSC allows for a more accurate assessment of key SWCC features, such as the air-entry value, which is relevant for suction stress prediction.

Furthermore, to enhance the understanding of the relationship between soil microstructure and its macroscopic behaviour under varying suction conditions, pore-size distribution (PSD) analysis is also performed. This provides insight into how changes in suction influence soil fabric and mechanical response.

It is important to note that the UCT along the drying path and the UTT were carried out at Hochschule Kaiserslautern (HSKL) by Yukang Wang. Additionally, the determination of the SWCC (drying path) and SSC was also performed at HSKL. The remaining tests were conducted in the laboratory of the Chair of Soil Mechanics, Foundation Engineering, and Environmental Geotechnics at Ruhr University Bochum (RUB).

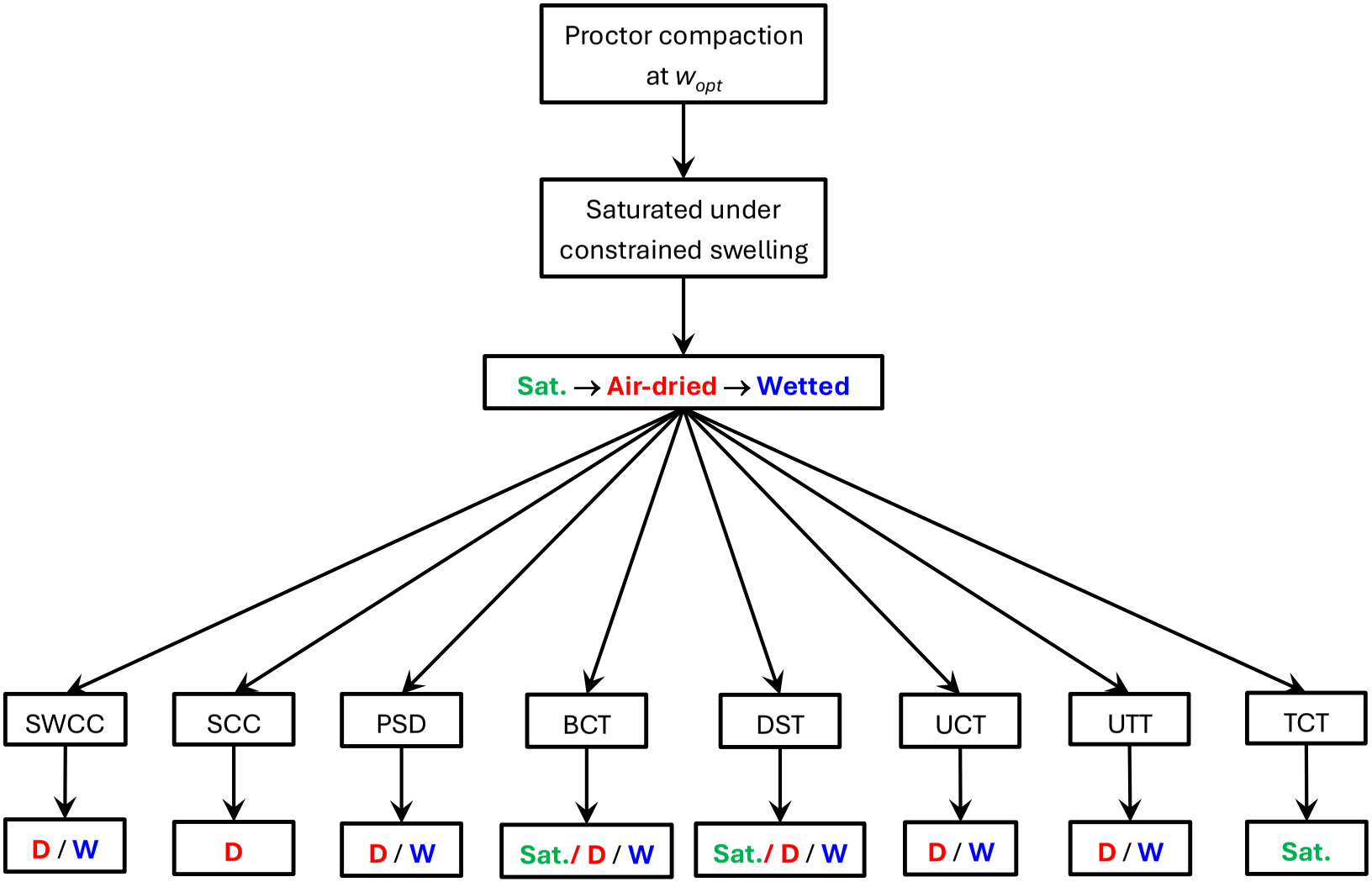

Figure 2.18.: Outline of the experimental program (SWCC = Soil-water characteristic curve, SSC = Soil shrinkage curve, PSD = Pore-size distribution, BCT = Biaxial compression test, DST = Direct shear test, UCT = Unconfined compression test, UTT = Uniaxial tensile test, TCT = Triaxial compression test, Sat. = Saturation, D = Drying path, W = Wetting path)

3. Material and methods

3.1. Material

In this study, Amberger Kaolin (AK) was used for the experiments. It was sourced from Quarzwerke GmbH, Frechen, Germany, sold under the name CHINA FILL BSK-H. The kaolin is supplied as a powder in 25 kg bags. Amberger kaolin, which primarily consists of the mineral kaolinite, is a cohesive material with low-swelling potential.

The physical properties of AK are detailed in Table 3.1, while the grain size distribution (GSD) is illustrated in Figure 3.1. The grain density of the soil was determined in accordance with the DIN 18124 standard method. The liquid limit and plastic limit were ascertained using the procedure outlined in the DIN 18122 standard. The GSD curve was obtained from a hygrometer analysis following the DIN 18123 standard.

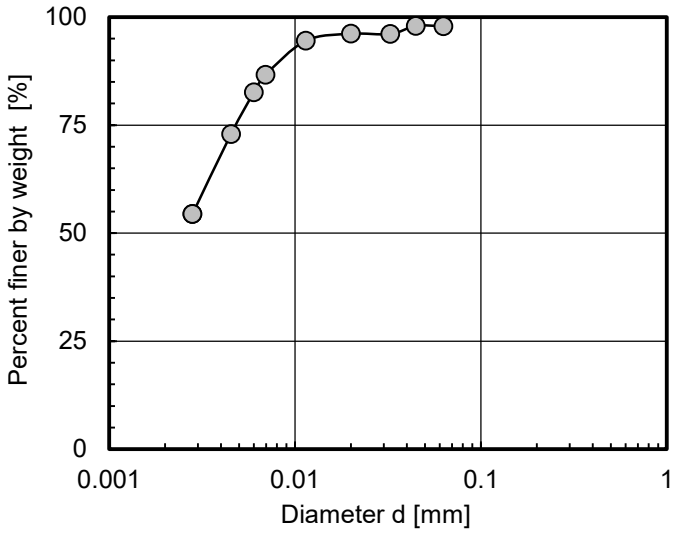

Figure 3.1.: Grain size distribution of Amberger kaolin

Table 3.1.: Physical properties of Amberger kaolin

Soil properties	Value
Grain density, ρ_s	2.64 g/cm^3
Liquid limit, w_L	56.60%
1.1·Liquid limit, 1.1·w_L	62.26%
Plastic limit, w_P	40.10%
Plasticity index, I_P	16.50%
Optimum water content, w_{otp}	30.2%
Proctor density, $\rho_{d,max}$	1.38 g/cm^3

To determine the relationship between the molding water content and dry density of the soil, the Proctor curve was determined in accordance with the DIN 18127 standard. A mixture of the dry AK and de-aired, distilled water was carefully prepared and dynamically compacted in a standard mold. To establish the Proctor curve, the proportion of the mixture (i.e. the amount of water and the mass of the dry kaolin) was varied. The resulting Proctor curve for AK is presented in Figure 3.2.

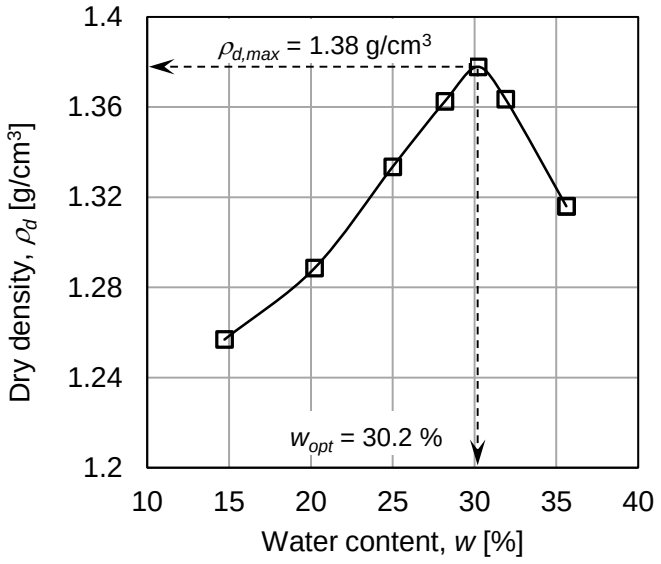

Figure 3.2.: Proctor compaction curve of Amberger kaolin

3.2. Sample preparation

3.2.1. Concept

All samples were prepared using AK, compacted at the optimum water content using Proctor energy. The compacted material was then saturated under confined conditions to prevent swelling. After saturation, the samples were trimmed and subsequently brought to the target water content or suction - either by air drying or, for the wetting path, by controlled humidification.

Due to differences in sample sizes and equipment at the partner laboratory (HSKL), slight variations in the sample preparation procedures were applied. The general procedure is described in detail in Section 3.2.3, while specific modifications for individual test types are descibed in the following sections.

3.2.2. Sample preparation for SWCC, SSC, and PSD

3.2.2.1. Sample preparation for SWCC

a) Drying path (SWCC-D)

The soil-water characteristic curve (SWCC) along the drying path (SWCC-D) was conducted at HSKL using the simplified evaporation method (Wind 1966; Schindler 1980; Schindler et al. 2010). This method was implemented using a specialized drying apparatus, commercially known as HYPROP (Peters & Durner 2008*a*; Peters & Durner 2008*b*) (Fig. 3.3a), in combination with a WP4C chilled-mirror hygrometer (Fig. 3.3b). Both devices were manufactured by METER Group, Inc., Pullman, WA, USA.

At HSKL, a procedure similar to that employed at RUB (see Section 3.2.3) was used to prepare samples under constrained swelling conditions during the saturation process, which will be presented in the next section. However, there were slight differences in the methodology, as outlined below:

- The Proctor mold used at HSKL had a diameter of 10 cm and a height of 12 cm.
- To constrain swelling during saturation, an oedometer cell with an applied load was used. In contrast, at RUB, a mini saturation cell was employed to prepare samples for the SWCC along the wetting path. The detailed operation of the mini saturation cell is described in the following section.

For the low suction range, following compaction, a HYPROP sampling ring (diameter = 8 cm, height = 5 cm) was used to extract a soil specimen from the compacted soil block. This was done using a specialized extraction toolkit designed specifically for the HYPROP device, both provided by METER Group. After extraction, the soil sample was placed in an oedometer setup for the saturation process, during which constrained swelling conditions were maintained by applying a load of 160 kPa on top of the specimen. Once saturated, two tensiometers were inserted into the sample to measure suction at two different depths: approximately 13 mm and 38 mm from the top of the sample. Simultaneously, a balance was used to monitor the weight loss of the sample throughout the air-drying process. The HYPROP apparatus was employed to measure suction values up to 160 kPa, with an additional measurement recorded at approximately 700 kPa, corresponding to the air-entry value of the ceramic tip used in the tensiometers.

Figure 3.3.: Devices used to determine the SWCC: (a) HYPROP device (accessed from: metergroup.com), and (b) WP4C (accessed from: edaphic.com.au)

For the higher suction range, the sample was carefully extruded from the HYPROP sampling ring and divided into smaller portions, which were then placed into specialized sample cups designed for use with the WP4C hygrometer. This approach enhances the precision of relative humidity (RH) and temperature measurements. During the air-drying process, which corresponds to the higher suction measurement range, the cups containing the soil samples were periodically placed in the WP4C hygrometer to measure RH and temperature. These measurements were subsequently used to calculate the sample's suction using Kelvin's equation (see Eq. 2.2).

b) Wetting path (SWCC-W)

The SWCC along the wetting path (SWCC-W) was measured at RUB. After the compaction process described in step 2 of Section 3.2.3, the compacted soil at optimum water content was extruded from the mold using a hydraulic jack. Several samples were carefully extracted from the middle layer (thickness of 6.7 cm) of the compacted soil block (d = 25 cm, h = 20 cm) using stainless steel rings measuring 3.6 cm in diameter and 1.5 cm in height. These special rings were designed with one sharpened edge to facilitate sample extraction. Prior to sample extraction, the rings were lubricated with a very thin layer of silicone grease. The samples were constrained against swelling during saturation. For that purpose, after extracting from the compacted soil block, the sample was placed on a bottom platen (Fig. 3.4a) of a mini saturation cell, which comprises two porous stones, two filter papers, a top cap, a bottom platen, three threaded rods, and six screws (Fig. 3.4b). The rods and screws were used to securely fix the components together, ensuring that the samples remained constrained during the saturation process (Fig. 3.4c). The assembled saturation cells were then submerged in de-aired and distilled water for several days (normally 5 days) to achieve full saturation (Fig. 3.4d). To verify the degree of saturation, selected samples were removed from the cell and weighed. The degree of saturation was then calculated from the measured weight and the known sample volume. Upon completion of the saturation process, the mini saturation cells were disassembled, and the samples were carefully removed. The saturated samples were then air-dried to an extremely low water content (w = 0.6%). Subsequently, the wetting process was conducted. Details of the wetting process and suction measurement techniques will be presented in subsequent sections.

3.2.2.2. Sample preparation for SSC

The soil shrinkage curve (SSC) of compacted samples saturated under constrained swelling conditions was measured at HSKL. A procedure similar to that used for the SWCC-D sample preparation was followed. Detailed information on the sample preparation and testing process can also be found in Heibrock et al. (2023). A cylindrical sample with dimensions of 2.4 cm in diameter and 8 cm in height was extracted from a saturated soil block. To monitor deformation during testing, the digital image correlation (DIC) method (Sutton et al. 2009) was employed. Additionally, a drying cell (HSKL-drying cell) was specifically designed to control the drying environment and to measure the change

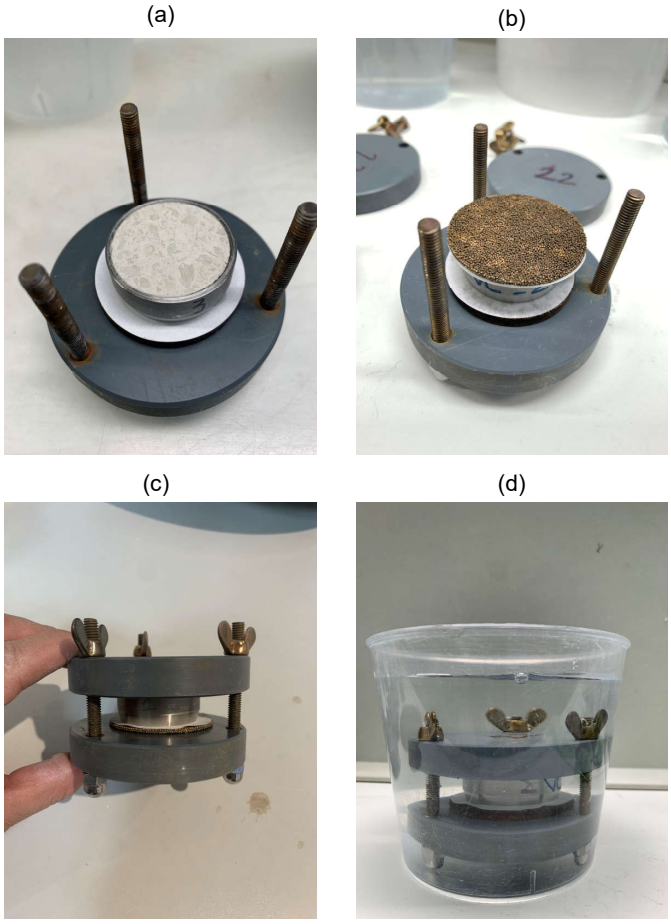

Figure 3.4.: Sample preparation for SWCC (constrained swelling condition during saturation) following the wetting path: (a) sample after extraction from the compacted soil block, (b) sample placed between two porous stones and filter papers, (c) full setup of the mini saturation cell, and (d) sample saturation by submerging of the cell in water

in the sample's weight simultaneously. Figure 3.5 illustrates the sample placed in the HSKL-drying cell.

3.2.2.3. Sample preparation for determining pore size distribution of the soil

The pore size distribution (PSD) determination was conducted on compacted samples, which were initially saturated under constrained conditions. The test was performed along both the drying path and wetting paths of the SWCC.

A procedure similar to that used for the SWCC-W sample preparation was followed. For the drying path, the saturated samples were gradually air-dried to predetermined water

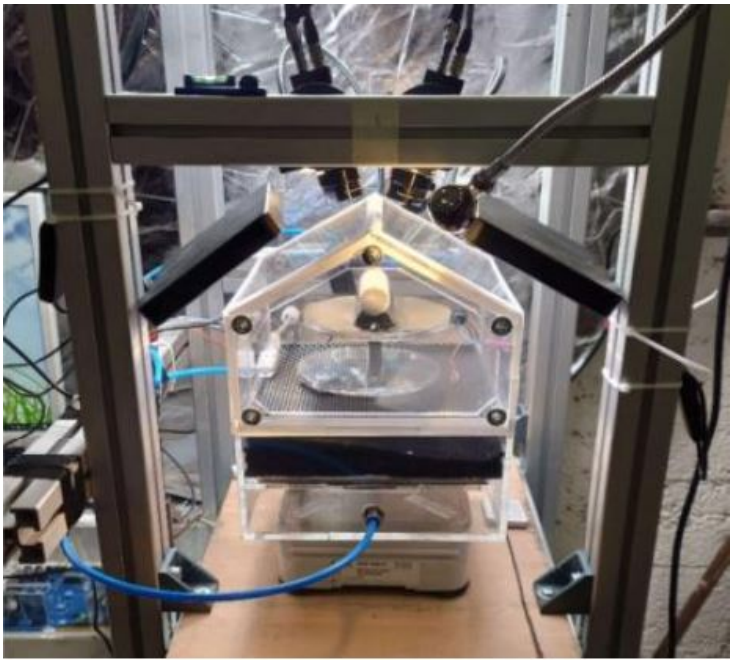

Figure 3.5.: Sample during testing using the HSKL drying cell integrated with DIC measurement (after Heibrock et al. 2023)

content levels. Once the target water content was achieved, the samples were sealed and stored in a closed container. For the wetting path, the samples were first air-dried to a low water content (approximately 1.4%) and subsequently re-saturated using water vapor supplied from a humidifier (RUB-humidifier). After reaching the desired water content, the samples were carefully sealed and stored for further analysis.

3.2.3. Sample preparation for biaxial compression tests and direct shear tests

The sample preparation process for the biaxial compression tests (BCT) and the direct shear tests (DST) utilized in this study follows the methodology previously established by Le et al. (2023). A flowchart of the sample preparation for BCT and DST is shown in Figure 3.6. The specific steps for sample preparation are detailed as follows:

- Step 1: The dry AK was thoroughly mixed with de-aired, distilled water at optimum water content. To ensure a uniform distribution of moisture, the mixture was stored in sealed bags (Fig. 3.7a) and closed buckets for 2 days.

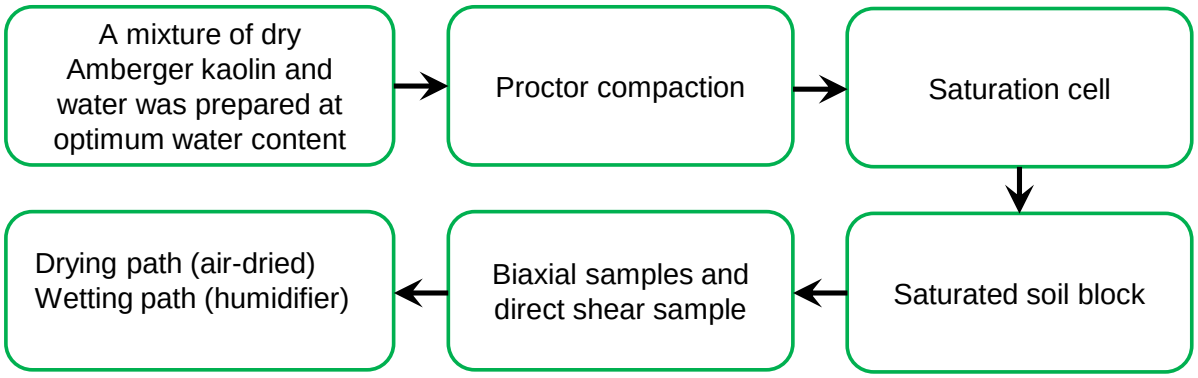

Figure 3.6.: Flowchart of sample preparation procedure for biaxial and direct shear samples

- Step 2: The mixture was subjected to dynamic Proctor compaction in three layers, each approximately 6.7 cm thick. A Proctor mold with a diameter of 25 cm and a height of 20 cm was used for this purpose (Fig. 3.7b). Each layer received 22 blows, with particular care taken to scarify the interface between successive layers to ensure proper bonding.

- Step 3: A large saturation cell, designed to facilitate the saturation of the compacted soil block under constrained swelling conditions, was utilized. Following the compaction step, the mold containing the compacted soil was placed on the bottom platen of the saturation cell (Fig. 3.7c), and a top cap was secured tightly using rods and screws (Fig. 3.7d). Both the bottom and the top cap were equipped with porous plates and a drainage system, which was connected with a water tank via tubes. Before placing the sample in the saturation cell the porous plates and the drainage lines were saturated with water. The saturation cells were subjected to a stepwise increase in back pressure values (70, 150, and 280 kPa) over a period of 9 days. During the saturation process, a venting valve situated on the top of the saturation cell was intermittently opened for a period of 5 hours per day to release trapped water and air. Based on several trial tests, a duration of 9 days was determined to be optimal for the saturation process.

- Step 4: Upon completion of the saturation process, the back pressure was removed, the saturation cell was disassembled, and a hydraulic jack was used to extrude the saturated soil block (Fig. 3.7e) from the mold. The water content of the saturated soil block was approximately 35%.

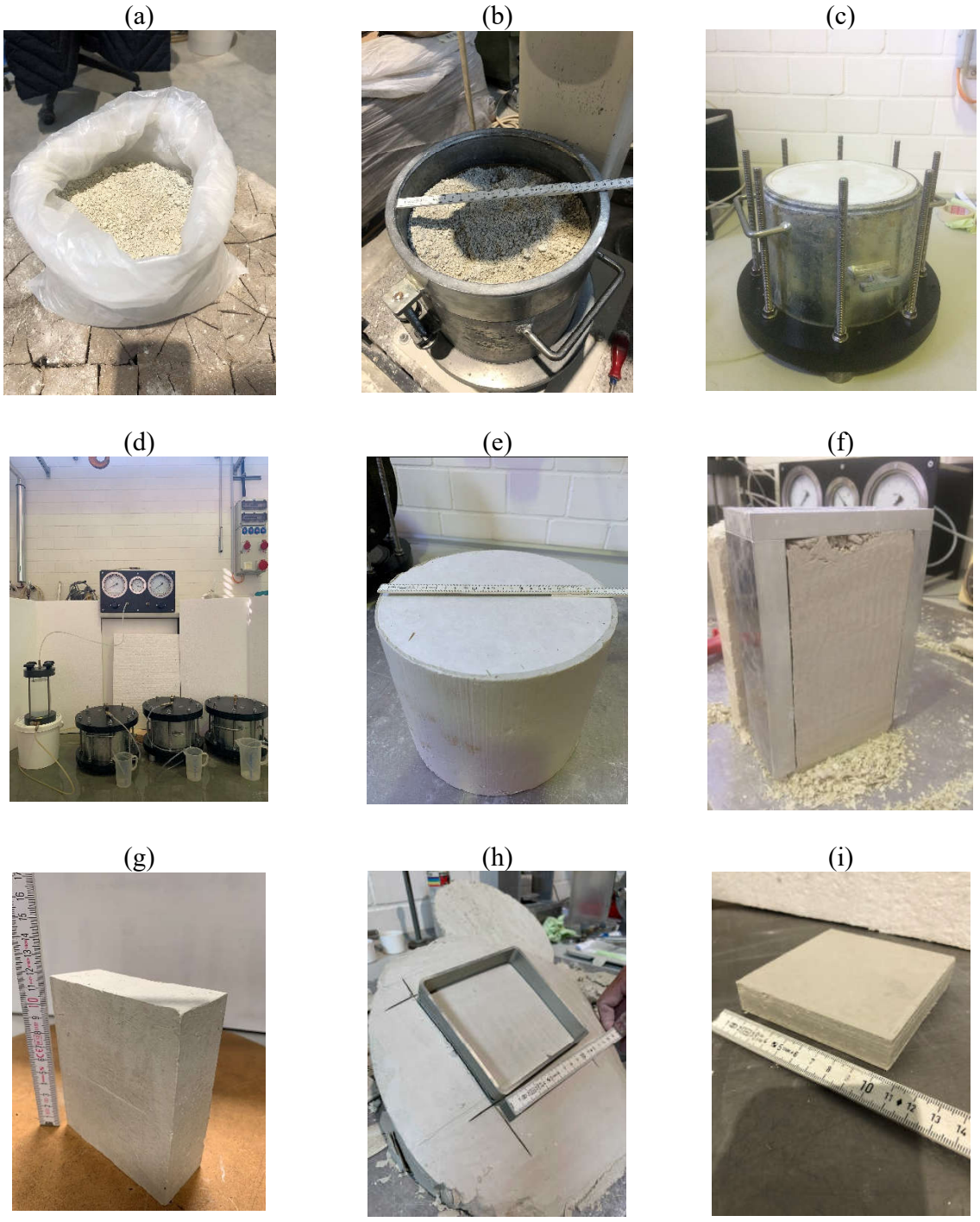

Figure 3.7.: Sample preparation for BCT and DST: (a) kaolin mixture, (b) Proctor compaction, (c) compacted soil inside the mold, (d) saturation of compacted block, (e) saturated compacted block, (f) biaxial sample during cutting process, (g) biaxial sample after cutting process, (h) direct shear sample during cutting process, and (i) direct shear sample after cutting process

- Step 5: Using the saturated soil block and a specially designed cutting frame (Fig. 3.7f, h), a series of test samples were prepared. These included biaxial test samples (cuboid shape: a = 10 cm, b = 4 cm, h = 12 cm) (Fig. 3.7g) and direct shear test samples (cuboid shape: a = 10 cm, b = 10 cm, h = 2 cm) (Fig. 3.7i). It is important to note that the direct shear samples were extracted in such a way that the horizontal plane of the sample was inclined at 45° to the horizontal plane of the compacted blocks. This 45° inclination was intentionally adopted to predefine a failure plane, aligning with the typical orientation of failure planes observed in biaxial and triaxial tests. To account for shrinkage during the air-drying process (refer to Step 6), the cutting dimensions of the samples were 5 mm larger than the actual dimensions. This was applied for both biaxial and direct shear tests.

- Step 6: In this study, the air-drying method was used to adjust the water content of the initially saturated samples to specific predetermined levels. To ensure uniformity and prevent crack formation, the sample underwent a controlled, stepwise air-drying process (Fig. 3.8a). Samples were placed in a plastic bucket with perforations in the lid, facilitating a drying period of 5 hours per day (Fig. 3.8b). Throughout this process, the weight of the samples was meticulously monitored using a precision balance, and their dimensions were measured with a caliper. Following each drying session, the samples were hermetically sealed in plastic bags and stored in enclosed containers for 3 days. This procedure was repeated in an environment with controlled humidity and temperature until the target water content was achieved. Upon reaching the desired water content, which corresponded to the specified suction value, the samples were stored in sealed bags for an additional period of 4 days prior to testing. To validate the uniform distribution of water content post-drying, several identical samples were prepared and sectioned to assess the internal water content distribution. The observed variation in water content among these sections was only approximately 0.3%.

- Step 7: To prepare the samples according to the wetting path, a number of samples were initially air-dried to a dry state (w = 0.6%). Subsequently, a stepwise wetting process was applied to ensure homogeneity and to minimize the risk of crack initiation and sudden swelling caused by excessive water absorption (Fig. 3.8c). The samples were placed in a plastic bucket connected to a humidifier (RUB-humidifier), which controlled the intensity of water vapor (Fig. 3.8d). The wetting process consisted of two phases: the wetting phase (4 hours per day, with regular weight checks every 2 hours) and the storing phase (following the wetting phase, the samples were

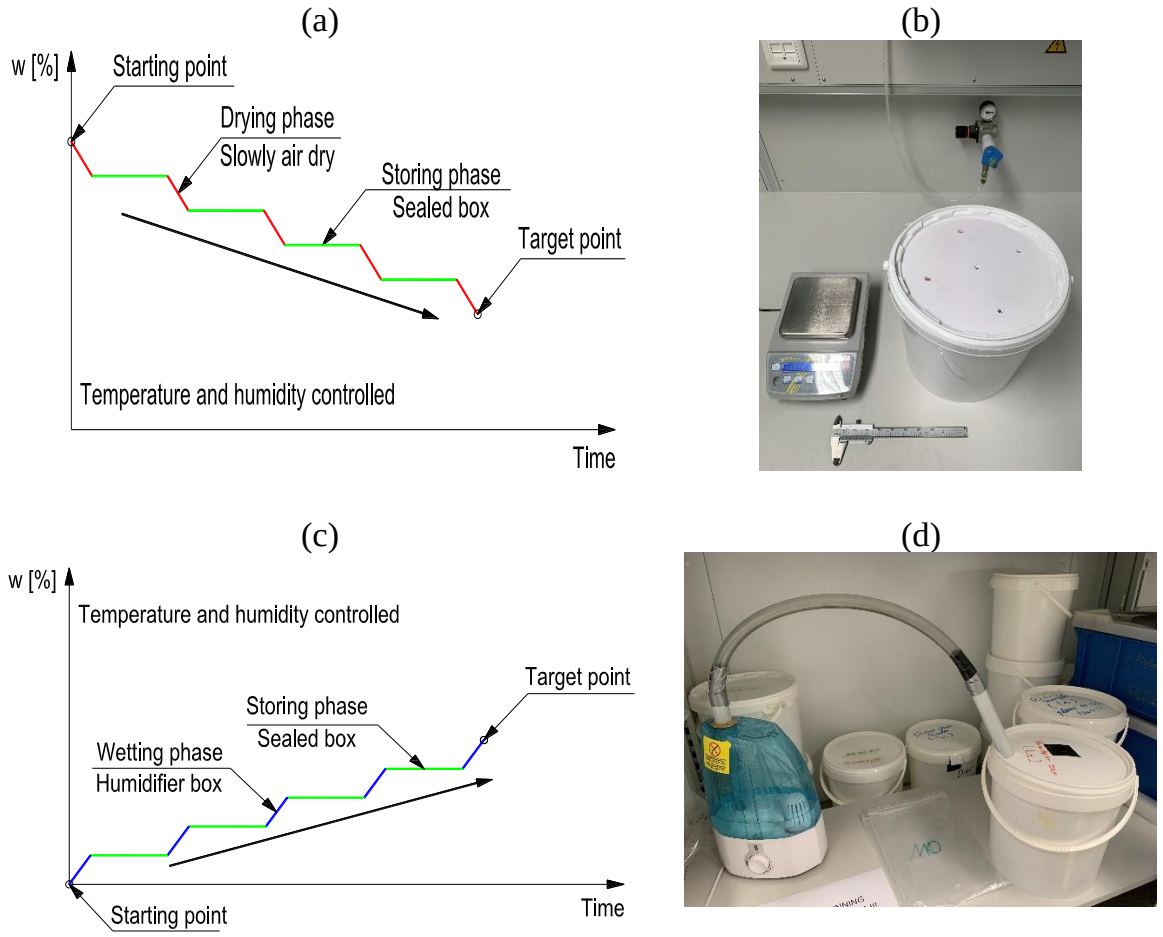

Figure 3.8.: Drying and wetting methods used for sample preparation for biaxial and direct shear tests: (a) illustration of the drying process, (b) tools used for the drying process, (c) illustration of the wetting process, and (d) RUB humidifier used for the wetting process

sealed in plastic bags and stored in enclosed containers for 3 days). This procedure was repeated in a controlled humidity and temperature room until the target water content was achieved. Once the target water content, corresponding to the desired suction value, was attained, the samples were stored in sealed bags for 4 days before being positioned within the test devices.

On the other hand, an investigation of the effects of anisotropy on the shear strength of the compacted soil was conducted using the BCT. Therefore, two primary groups of BCT samples were prepared:

- Vertically cut samples (B-VC): These samples were extracted from the compacted blocks along the vertical direction, meaning the sample height (h = 12 cm) was

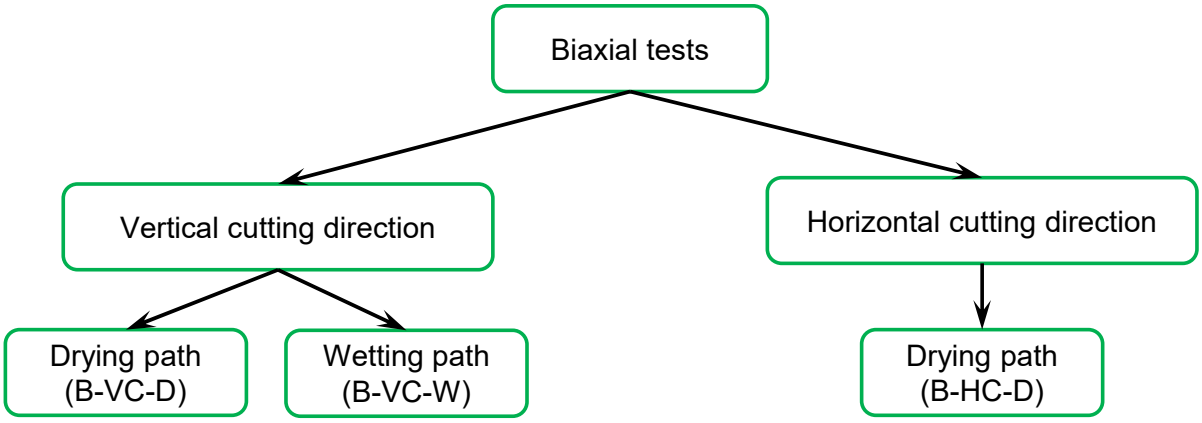

Figure 3.9.: Groups of biaxial testing series

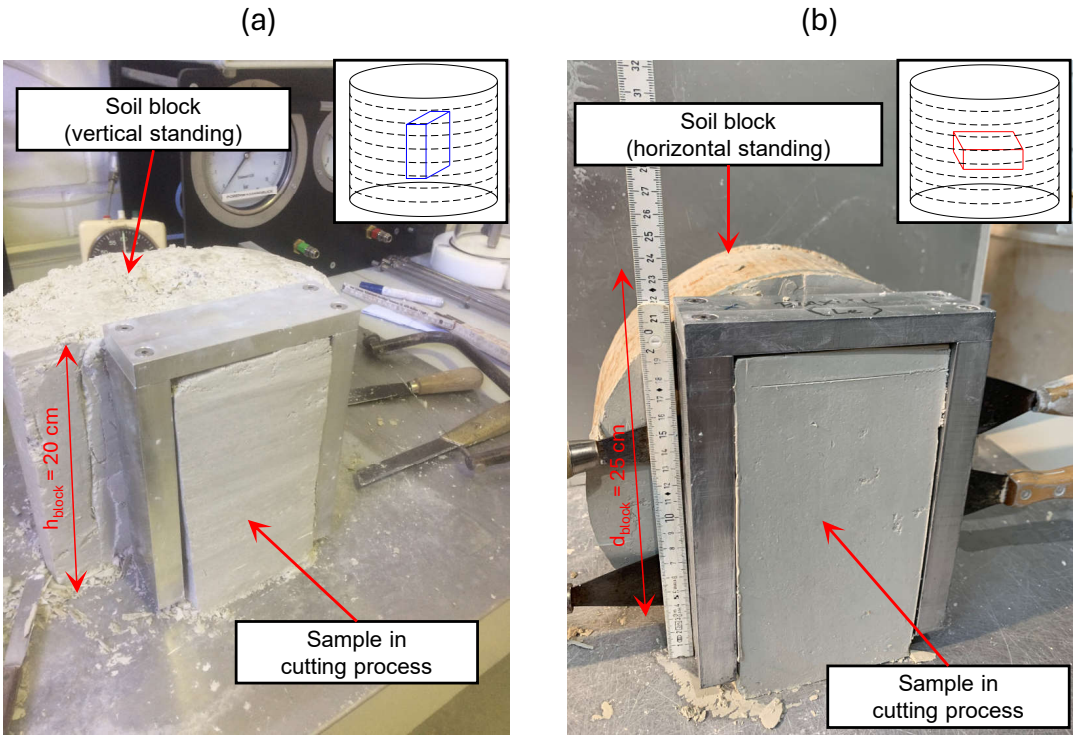

Figure 3.10.: Sample in cutting process: (a) vertical cutting direction (B-VC), and (b) horizontal cutting direction (B-HC)

aligned with the height of the compacted block ($h = 20$ cm). Samples were prepared for both the drying (B-VC-D) and wetting paths (B-VC-W).

- Horizontally cut samples (B-HC): These samples were extracted along the horizontal direction, where the sample height ($h = 12$ cm) was aligned with the radius of the

compacted block (d = 25 cm). These samples were prepared only for the drying path (B-HC-D).

Figure 3.9 presents the categorization of the biaxial sample groups, while Figure 3.10 depicts the cutting directions for vertical (Fig. 3.10a) and horizontal (Fig. 3.10b) samples.

3.2.4. Sample preparation for unconfined compression tests and uniaxial tensile tests

Uniaxial tensile tests (UTT) following both the drying path (UT-D) and the wetting path (UT-W), as well as the unconfined compression tests (UCT) following the drying path (UC-D), were conducted by Yukang Wang at HSKL. At HSKL, a procedure similar to that employed at RUB was used to prepare BCT and DST samples under constrained swelling conditions during the saturation process. However, there were slight differences in the methodology, as outlined below:

- The Proctor mold used at HSKL had a diameter of 10 cm and a height of 12 cm.
- To constrain swelling during saturation, an oedometer cell was utilized with a vertical load of 160 kPa applied to the samples. In contrast, at RUB, the large saturation cell was used for this purpose.

Therefore, the sample preparation for the UCT and UTT at HSKL can be described as follows:

- Step 1: Following compaction, the top and bottom layers were trimmed, utilizing only the middle layer, approximately 4 cm thick, for sample preparation. An oedometer ring, measuring 10 cm in diameter and 3 cm in height, was carefully inserted into the middle soil layer. Excess soil was meticulously removed from both sides of the ring. The oedometer ring containing the soil was then precisely placed into the base of an oedometer device (Fig. 3.11a). The top cap and loading frame were subsequently positioned on the sample, and a vertical stress of 160 kPa was applied by placing weights on a loading beam (Fig. 3.11b), ensuring that the stress was transmitted to the soil through the top cap. This procedure ensured uniform stress distribution and constrained swelling during the saturation process. For saturation the sample was submerged in water by filling the Plexiglas cylinder surrounding the sample with water. Based on several trial tests, a duration of 2 days was deemed optimal for saturation. Observations of vertical displacement confirmed that no consolidation or swelling of the soil occurred during the saturation process.

- Step 2: Following the saturation process, the saturated soil was carefully extruded from the oedometer ring. Utilizing the saturated soil block and a cutting frame (Fig. 3.11c, d), a series of test samples were prepared. These included UCT samples (cylindrical shape: $d = 2.4$ cm, $h = 5$ cm) (Fig. 3.11e) and UTT samples (cylindrical shape: $d = 2.4$ cm, $h = 7.8$ cm) (Fig. 3.11f - the borehole was made just before testing).

- Step 3: The UCT and UTT samples underwent a three-step drying procedure in a plastic chamber connected to a humidifier (HSKL-humidifier) (Fig. 3.12) with regulated air circulation. Initially, the samples were dried at a relative humidity (RH) of 80%. In the second step, the RH was reduced to 60%, and in the final step, it was further decreased to 10%, corresponding to a suction of approximately 300 MPa at 20°C. The weight of the samples was determined from time to time to control the achieved water content. Upon reaching the predefined water content, the samples were removed from the chamber, sealed, and stored for a minimum of 3 days to ensure a homogeneous distribution of water content.

- Step 4: To prepare the samples for UTT following the wetting path, a spray bottle was used to add the water to the sample in a stepwise manner. Between each time of spraying, the sample underwent a storing phase in sealed bags and closed buckets for 3 days.

At RUB, unconfined compression tests (UCT) following the wetting path (UC-W) were conducted. A series of saturated samples, each measuring 5 cm in diameter and 10 cm in height, were prepared using a procedure similar to that employed for the preparation of BCT and DST samples along the wetting path (see Step 7).

To ensure a perfectly horizontal plane on both the top and bottom surfaces of the samples, a specialized cutting tool was designed. Figure 3.13a and 3.13b illustrate the procedure for leveling the sample surfaces, while Figure 3.13c and 3.13d depict the verification of the sample's level.

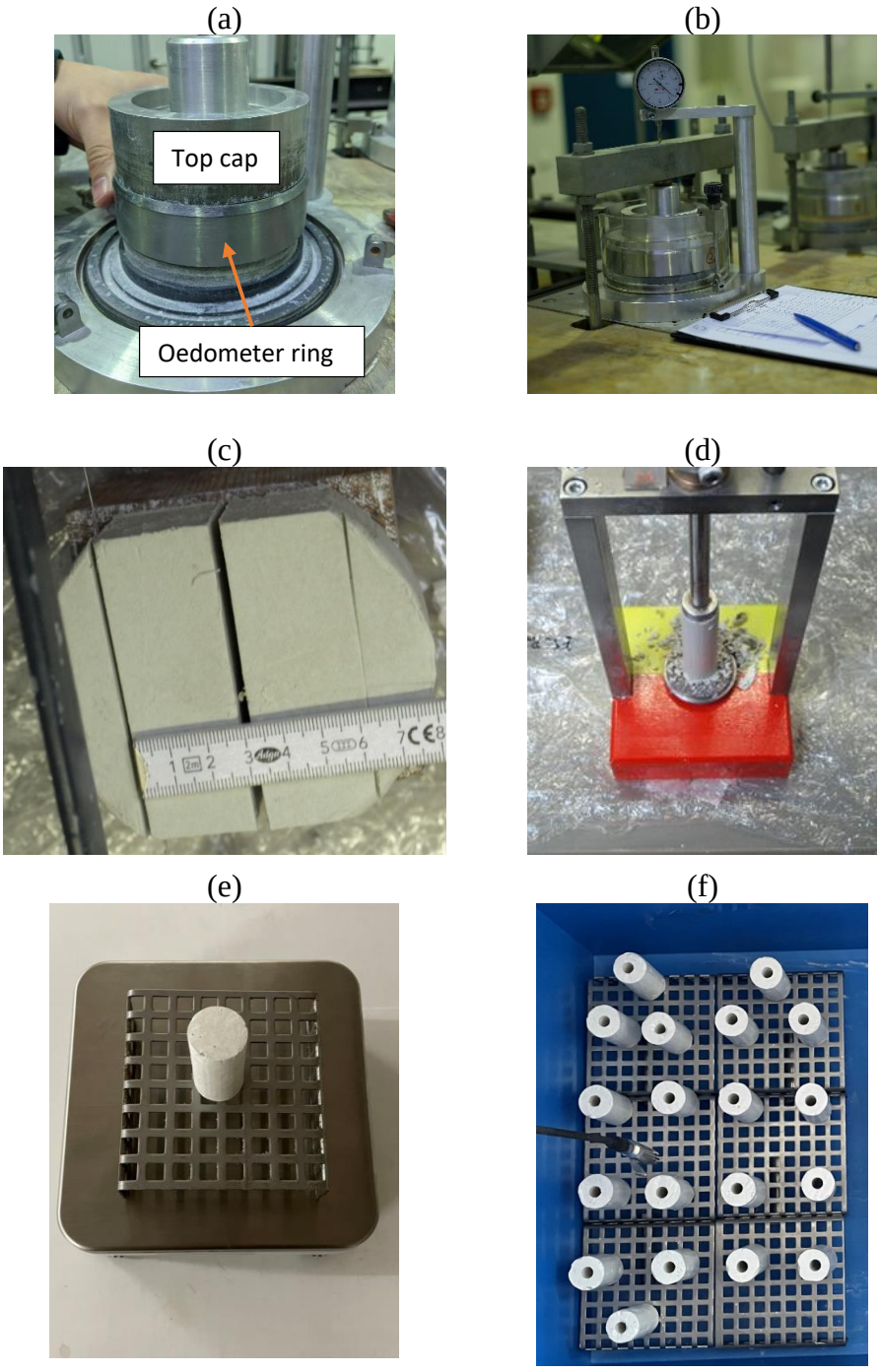

Figure 3.11.: Sample preparation for UCT and UTT at HSKL: (a) assembling the oedometer system to saturate the compacted soil block, (b) the soil block during the saturation process, (c) and (d) cutting the samples, (e) a UCT sample after cutting, (f) the UTT samplea ready for testing (the borehole was made before testing)

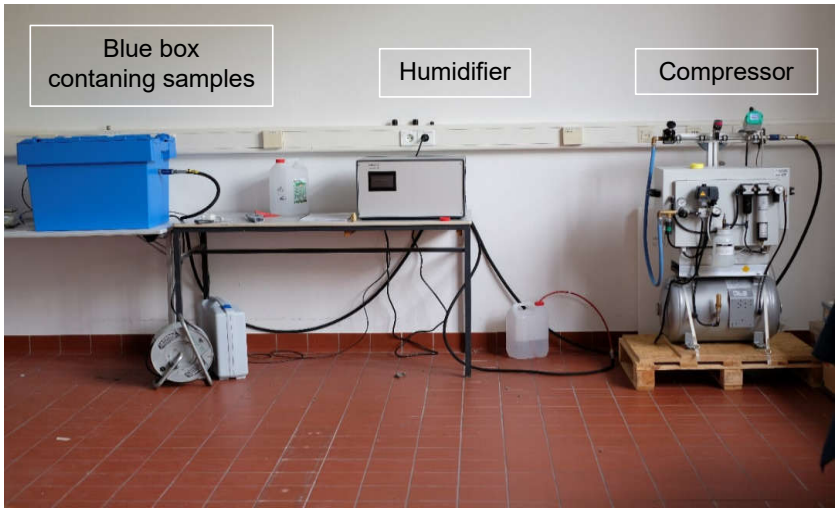

Figure 3.12.: Drying device setup used for sample preparation for unconfined compression tests and uniaxial tensile tests at HSKL

3.3. Techniques, experimental procedure, and experimental program

3.3.1. Techniques, procedures, and experimental program for SWCC tests

The laboratory program includes the determination of both the drying and wetting paths of the SWCC. An overview illustrating the techniques used to establish the SWCC is presented in Figure 3.14. It is important to note that volume changes of the SWCC samples were not measured during testing. As a result, the outcome of these tests is the relationship between gravimetric water content (w) and suction (ψ).

3.3.1.1. Techniques

Chilled-mirror dew-point technique

The chilled-mirror dew-point technique is an indirect method for measuring soil suction, commonly used for determining total suction in unsaturated soils. This technique operates by cooling a mirror until condensation occurs, at which point the dew-point temperature is recorded. The relative humidity of the air in equilibrium with the soil sample is then used to determine the corresponding suction value based on the psychrometric relationship.

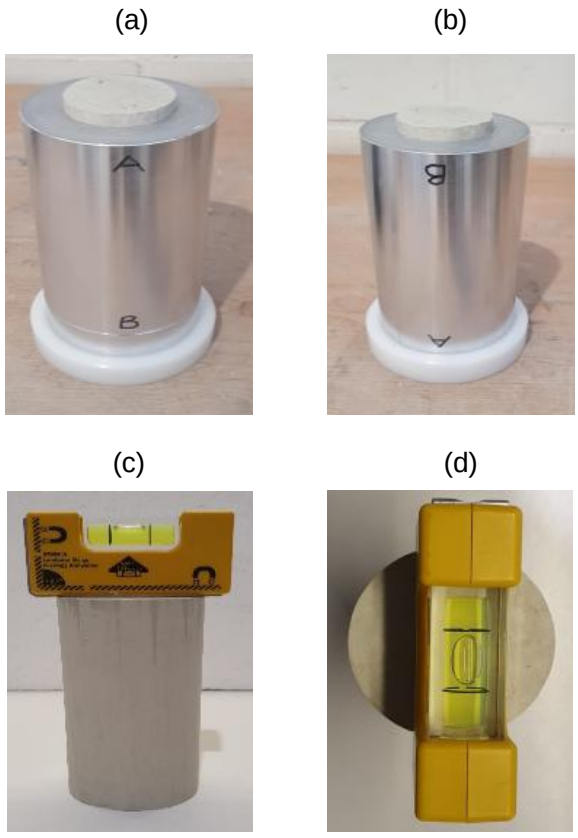

Figure 3.13.: Preparation of UCT-W samples following the wetting path: (a) levelling the top surface of sample, (b) levelling the bottom surface of sample, (c) check the level of sample, a front view, and (d) check the level of sample, a top view

In this study, different models of chilled-mirror hygrometers were employed at RUB and HSKL:

- At RUB, an AquaLab chilled-mirror hygrometer (model series 3TE from Decagon Devices, Inc.) was used to measure total suction. A photograph of the device is shown in Figure 3.15.
- At HSKL, the WP4C chilled-mirror hygrometer was used for the same purpose. A photograph of the device is shown in Figure 3.3b.

The chilled-mirror hygrometer operates based on the thermodynamic relationship between relative humidity, temperature, and total suction, as governed by Kelvin's equation. The test procedures for measuring suction using the AquaLab device began with checking the linear offset of the instrument. The components used by the device to measure relative humidity are prone to changes that can impact its performance, often due to contami-

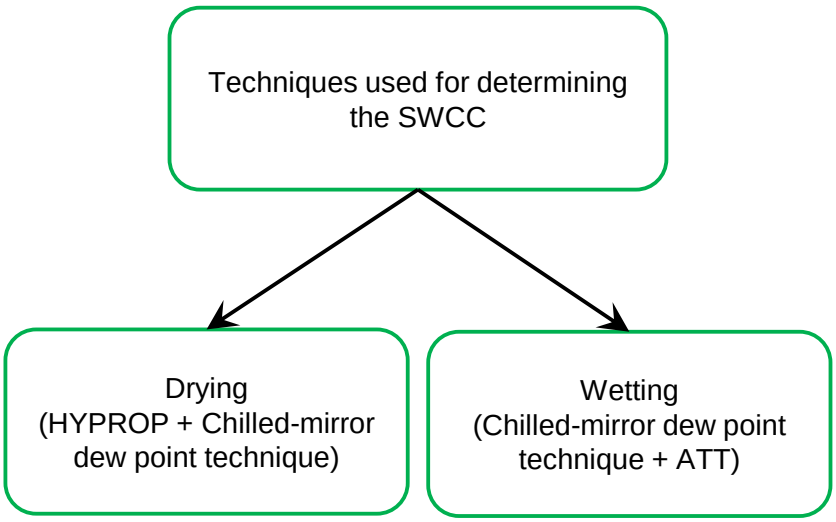

Figure 3.14.: An overview of techniques used to establish the SWCC

nation. Such changes can affect the accuracy of the measurements. To verify the linear offset, a standard solution provided by the manufacturer is used. Detailed procedures for verifying and adjusting the linear offset are available in the AquaLab Operator Manual, published by Decagon Devices, Inc., Pullman, WA. Leong et al. (2003) and Baille (2014) provided comprehensive descriptions of the device operation.

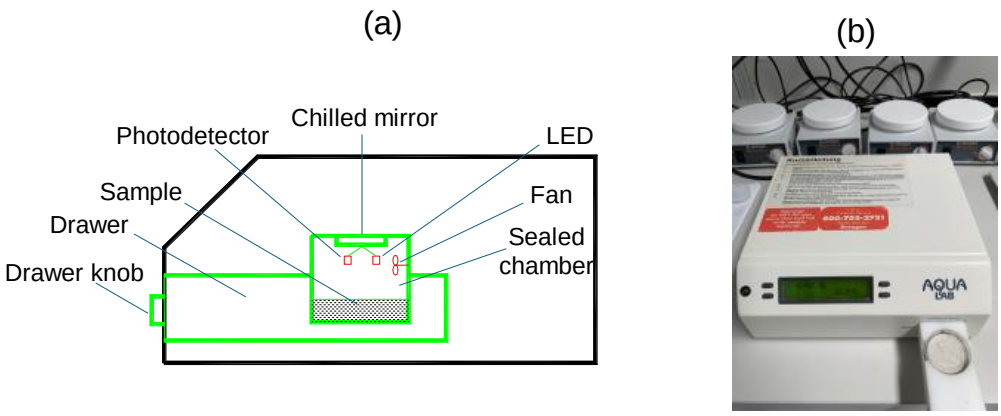

Figure 3.15.: The chilled-mirror hygrometer AquaLab used in this study: (a) the schematic of the device, and (b) the device with the sample

3.3.1.2. Axis-translation technique

The axis-translation technique (ATT), developed by Hilf (1956), was primarily to address the issue of cavitation that occurs at sufficiently low negative water pressures. This technique shifts the reference point for pore water pressure (u_w) from its current value to a higher value that is equivalent to the air pressure applied to the soil sample (u_a). By doing so, the matric suction ($u_a - u_w$) of the soil sample remains constant, irrespective of the translation of pore air and pore water pressures.

In this study, a pressure plate extractor based on the ATT was utilized. A pressure plate extractor consists of a pressure chamber, an air supply system, a water supply system, and a ceramic disk with specific air-entry value serving as a separator for the air and water pressures. The ceramic disk is covered on one side by a rubber membrane which is sealed to the edges of the ceramic disk. The space between the rubber membrane and the ceramic disc creates a compartment which is filled completely with water before doing the test. In this study, the pressure plate extractor was used to apply suction values between 10 and 1000 kPa using four ceramic discs with different air-entry values (1 bar, 3 bar, 5 bar, and 15 bar) depending on the applied suction. Figure 3.16 shows the pressure plate extractor used in this study.

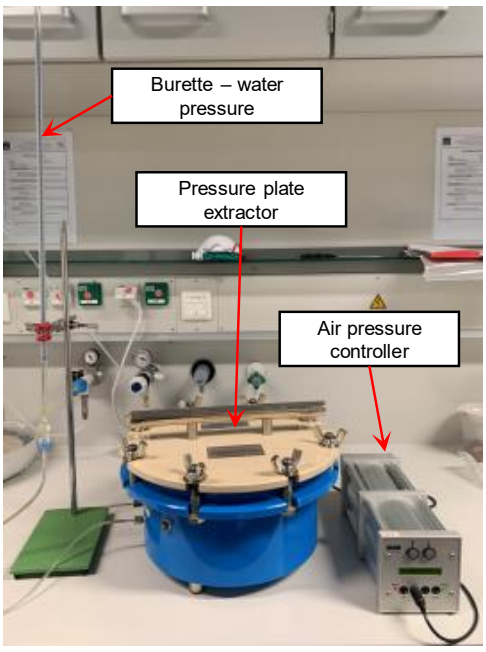

Figure 3.16.: Pressure plate extractor

One of the most crucial points is to maintain continuity of the water phase between the water in the ceramic disc and the water in the compartment beneath it. The tests began by saturating the ceramic disc, which involved placing it under deaired water for 3 days initially and for 1 hour each time the sample was checked during the test.

To remove all air bubbles from the ceramic disc, the following two steps were implemented:

- Step 1: Filling the water compartment by adding water from a burette connected to it. This step was repeated several times until there was no movement in the water level of the burette.

- Step 2: Pouring water over the ceramic disc (Fig. 3.17a), then sealing the pressure chamber. The air pressure was gradually increased up to 100 kPa for several hours while water remained on the disc. The saturation process was considered complete when no more air bubbles appeared in the burette. This process allowed water to pass through the ceramic disc, effectively expelling any air bubbles.

Diffused air bubbles in the water can lead to a discontinuity between the sample's pore water and the water in the ceramic disc. To ensure that the ceramic disc remained fully saturated and to remove any diffused air bubbles that accumulated beneath it, periodic flushing of the water compartment was performed during the testing procedure. During the flushing process, the samples were stored in a small, closed chamber to prevent water loss due to evaporation.

After completing the saturation of the ceramic disc and flushing the water in the compartment, the samples were carefully placed on the saturated ceramic disc (Fig. 3.17b). To ensure good contact between the samples and the ceramic disc, a thin water layer approximately 1 mm in depth was maintained on the ceramic disc (Cresswell et al. 2008, Elgabu 2013) and a Whatman filter paper was positioned between the sample and the ceramic disc (Klute 1986) (Fig. 3.17b). The lid was then closed, and the air pressure was increased to the desired level, while the water pressure was held constant at 10 kPa by maintaining the water level of the burette at 1 m.

The samples were weighed periodically until equilibrium was achieved. Equilibrium was defined as the point at which no significant change in the sample weight was observed. A precision balance with an accuracy of 0.0001 g was used for weighing the samples. The volume change of the samples was not measured during this test. Once all samples in the apparatus reached equilibrium, the next level of suction could be applied.

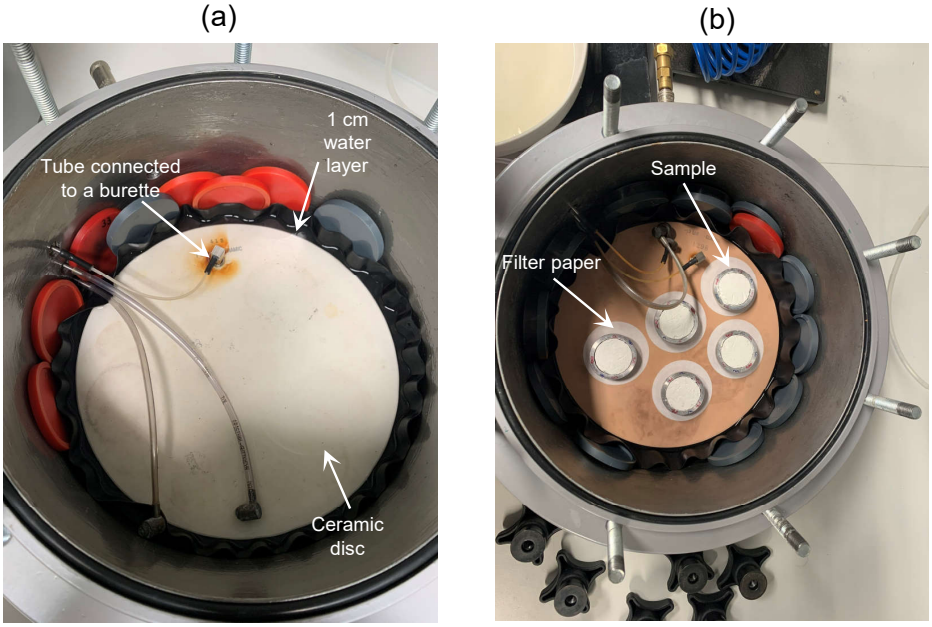

Figure 3.17.: Pressure plate extractor: (a) saturation of the ceramic disc, and (b) sample placed on the ceramic disc

3.3.1.3. Procedures and program

Drying path

Suction measurement following the drying path was carried out using two different methods to cover the wide range of suction. For the measurement of low suction values ($\leq$ 700 kPa), a HYPROP device, which is designed based on the principle of the simplified evaporation method (Wendroth et al. 1993, Schindler 1980, Peters & Durner 2008*a*, Peters & Durner 2008*b*) was utilized. The device consists of two mimi-tensiometers and a precision balance.

To measure higher suction values ($>$ 700 kPa), the chilled-mirror hygrometer (WP4C) was used (Agus & Schanz 2003, Leong et al. 2003). Both devices are manufactured by METER Group, Inc., Pullman, WA, USA.

The HYPROP device includes both a sensor unit and a sampling unit, both of which must undergo thorough degassing before any measurements can be taken. It is essential to fully saturate the mini-tensiometers and the sensor head, which are components of the sensor unit, because even a small amount of air can cause substantial inaccuracies in suction readings. To achieve proper degassing, the procedure outlined in the HYPROP manual

by METER Group was followed, utilizing vacuum syringes. The system was degassed over a period of two days before the mini-tensiometers were connected to the sensor head of the HYPROP setup. During assembly, special attention was given to prevent excessive pressure buildup, which could damage the pressure transducer. The pressure inside the sensor unit was closely monitored throughout the process using TENSIOVIEW software (developed by UMS GmbH, Germany), as recommended by the HYPROP manual.

As outlined in the sample preparation section, samples were extracted from the saturated compacted block using HYPROP sampler rings. After extraction, two boreholes were drilled into the sample using the provided auger, and the tensiometers were placed into these holes. The entire setup was then placed on a precision laboratory scale to monitor changes in weight. The tensiometers recorded suction at two distinct heights within the sample at 10-minute intervals, while the balance tracked the weight loss of the sample. Data on both suction and weight were recorded simultaneously using the TENSIOVIEW software.

For measurements at higher suction values, the sample was carefully removed from the HYPROP sampler ring and divided into smaller portions, which were then placed in specialized sample cups. These samples were air-dried in a room with controlled relative humidity and temperature. Throughout the drying process, the sample cups were periodically placed on the WP4C dew point device to measure the relative humidity (RH) and temperature, and on a precision scale to measure changes in weight. The recorded RH and temperature data were subsequently used to calculate the suction of the sample using the Kelvin equation (Eq. 2.2). Meanwhile, the changes in the weight of the sample were used to determined the changes in water content. At the end of the test, the samples were placed in an oven for 24 hours at 110 $\pm$ 5°C to determine their dry weight used to calculate the water content.

Wetting path

For the wetting path of the SWCC, suction measurements employed two different methods to cover a wide range of suction values. For low suction values (less than 1500 kPa), the ATT (Hilf 1956) was used. For higher suction values (greater than 1500 kPa), measurements were taken using the chilled-mirror hygrometer AquaLab. As described in the section about sample preparation, the saturated samples were air-dried to a very low water content ($w = 0.6\%$). These dried samples were then gradually re-wetted in two stages, as follows:

- State 1 ($w \leq 10\%$): The dried samples were placed in a plastic bucket connected to a humidifier (RUB-humidifier) to reintroduce water vapor. Once a specific water content was reached, an individual sample was taken out of the bucket and stored in sealed bags within a closed container for one day to ensure uniform moisture distribution. Subsequently, the samples were divided into three portions: two were used to measure relative humidity (RH) and temperature using the AquaLab device. For determining the suction using the AquaLab, these portions were cut into smaller pieces to fit into the cages of the instrument. The third portion was oven-dried to determine the corresponding water content. The remaining samples continued the wetting process until reaching the target water content of 10%. A total of five samples, each corresponding to a specific water content value, were tested.

- Stage 2 ($w > 10\%$): Upon completion of the wetting process using the humidifier, several soil samples were transferred to the pressure plate apparatus, where lower suction levels were applied using the ATT to achieve higher water content. Suction values of 10, 200, 400, 600, and 1000 kPa were applied. At suctions of 10 and 200 kPa, to prevent sample swelling during suction application, a heavy load of 5 kg was placed on top of the sample, with a porous plate positioned in between.

3.3.2. Techniques, procedures, and experimental program for SSC tests

As introduced in the sample preparation section, the SSC test was conducted at HSKL. To establish the SSC for compacted samples that were saturated under constrained swelling, a custom drying cell was designed. This drying cell offers several key advantages:

- Dual drying modes: the drying cell allows for two modes of drying - continuous and stepwise - which provides flexibility in controlling the drying process.

- Controlled environmental conditions: the device is capable of supplying air with a known relative humidity (RH) and temperature, which is critical for managing the drying process. RH and temperature within the drying cell are continuously monitored using RH sensors and temperature sensors.

- Precision measurements: the sample's weight is measured with an electronic scale, while deformation is recorded using two cameras. These measurements are crucial for calculating changes in water content and void ratio during the drying process.

The drying cell operates in two modes: (1) Continuous mode, in which air flows continuously in and out of the cell; and (2) Stepwise mode, which alternates between drying phases (with air flow) and storage phases (without air flow). An electrical board was designed to control the drying modes and the operational timing of the electrovalves and ventilators. Additionally, all sensor and scale output data are automatically recorded on an SD card integrated into the board. The stepwise drying mode was employed in this test series, with the following input parameters:

- Relative humidity (RH) of drying air RH = 14%; temperature T = 20–21°C
- Drying time t_{drying} = 1 hour; storing time $t_{storing}$ = 1 hour
- Electrovalve activation: on time $t_{valve-on} = 3$ seconds; off time $t_{valve-off} = 60$ seconds
- Fan activation: on time t_{fan-on} = 60 seconds; off time $t_{fan-off}$ = 60 seconds
- Data logging interval $t_{data-save}$ = 1 minute

A transparent chamber constructed from acrylic panels was specifically designed to maintain stable humidity and temperature conditions during testing (Figure 3.5). The digital image correlation (DIC) method was employed to capture and analyze the displacement field across the surface of a soil sample during the drying process. A random speckle pattern was applied to the surface of the soil, serving as reference points for tracking deformation.

Two high-resolution cameras, manufactured by NIKON, captured a series of images of the speckle pattern as the soil deformed during drying. The DIC software compared the initial reference image (undeformed state) with subsequent images (deformed states), tracking the displacement of the speckle pattern by dividing the images into small subsets and calculating the movement of these subsets relative to the reference image. From the displacement fields, the software calculated the strain distribution across the sample's surface.

To minimize light refraction, the angle between the two acrylic panels facing the DIC cameras was set at 150 degrees. Additionally, a digital precision balance was employed to monitor the sample's weight changes throughout the drying process. The saturated sample, measuring 2.4 cm in diameter and 8 cm in height, was placed on a base atop the balance, with both the balance and the cameras connected to a PC for continuous data acquisition and recording.

3.3.3. Techniques, procedures, and experimental program for pore size distribution determination

In this study, mercury intrusion porosimetry (MIP) was used to determine the pore size distribution (PSD) of the samples. Upon completion of the sample preparation, some cuboid-shaped specimens, measuring 5 mm on each side, were cut from the prepared samples at specific water content values. A prerequisite for MIP analysis is that the samples must be thoroughly dried without disturbing the pore structure. To achieve this, freeze-drying method was employed. Details of the freeze-drying method are provided in the Appendix A.

The PSD determination was performed in the chemical laboratory at RUB. The laboratory housed two pressure porosimeters: the Pascal series 140, a low-pressure porosimeter capable of measuring pores in the size range of 135 μm to 4.5 μm, and the Pascal series 240, a high-pressure porosimeter designed to measure pores ranging from 7.7 μm to 0.0012 μm. Table 3.2 shows the experimental program for the PSD determination on samples along the drying path and the wetting path. Figure 3.18 depicts the Pascal pressure porosimeters utilized in this study.

Table 3.2.: Experimental program for pore size distribution determination

Drying path, w (%)	Wetting path, w (%)
30.2 (w_{opt})	11.3
32.4	16.4
28.9	28.4
20.4	32.3
13.2	
1.4	

3.3.4. Techniques, procedures, and experimental program for biaxial compression tests

3.3.4.1. Introduction of double-wall biaxial device

The biaxial apparatus offers a precise and dependable approach for testing soil materials under true plane strain conditions, enabling the assessment of shear banding and stress-strain behavior. In this research, the RUB double-wall biaxial device, developed

(a) (b)

Figure 3.18.: Pressure porosimeters (Chemical laboratory of RUB): (a) low pressure porosimeter Pascal 140 series, and (b) high pressure porosimeter Pascal 240 series (after Pourzargar 2017)

by Alabdullah (2010) in collaboration with Wille Geotechnik GmbH, was employed. The experiments were conducted under plane strain conditions, with suction applied using two experimental techniques: the axis translation technique (ATT) (Hilf 1956) and the salt vapor flow technique (SVFT) (Blatz & Graham 2000; Oldecop & Alonso 2004; Hoffmann et al. 2005), based on the vapor equilibrium method (Tessier 1984).

As outlined in the sample preparation section 3.2.3, the test sample had a cuboid shape, measuring 12 cm in height, 10 cm in width, and 4 cm in thickness. Deformation was restricted in one direction ($\epsilon_2 = 0$) along the long dimension of the cross-section by two fixed steel platens, maintaining a constant width of 10 cm. Figure 3.19 illustrates the sample geometry and the applied stress and strain conditions during testing.

The main advantages of the biaxial device are as follows: (1) it allows testing under plane strain conditions, (2) it enables the control of a wide range of suction using various techniques, and (3) it facilitates the measurement of sample volume change during testing based on the principle of double cells (i.e., using a combination of inner and outer cells).

Figure 3.20 presents a schematic diagram of the biaxial device, while a photograph of the device is shown in Figure 3.21.

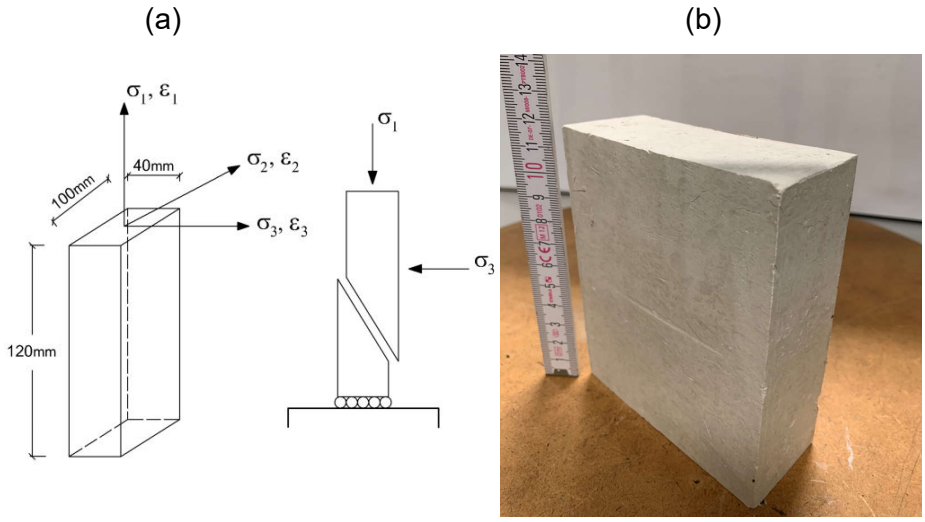

Figure 3.19.: Biaxial sample: (a) geometry of the sample, stress and strain condition (Alabdullah 2010), and (b) biaxial sample before testing

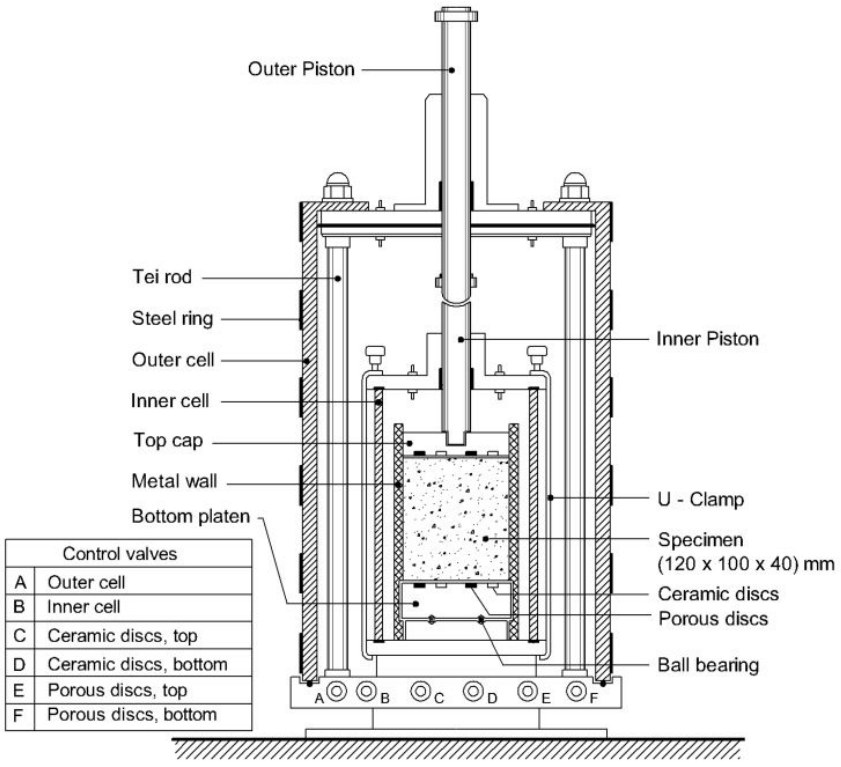

Figure 3.20.: Schematic diagram of double-wall biaxial device (Alabdullah 2010)

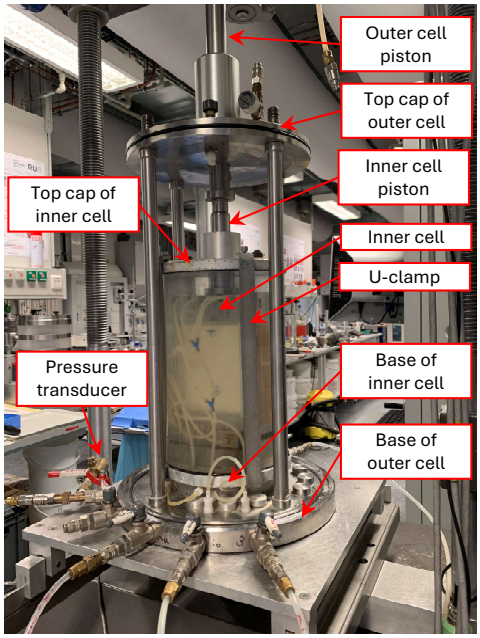

Figure 3.21.: Photograph of double-wall biaxial device without outer cell

a) Loading system

The loading system comprises a loading frame, outer and inner pistons, and a load cell. The loading frame, as depicted in Figure 3.22, consists of a horizontal beam supported by two vertical steel rods. A load cell, with a maximum capacity of 20 kN, was mounted beneath the horizontal beam to measure the applied load. The outer and inner pistons, both with diameters of 3 cm (Figure 3.23), transmitted the axial load from the frame to the sample. The outer piston penetrated the top cap of the outer cell, while the inner piston passed through the top cap of the inner cell.

b) Double wall cell

The double-wall cell technique has been employed in several previous studies (Bishop 1961; Cui & Delage 1996; Ng et al. 2002; Mendes et al. 2012; Alabdullah 2010) to measure the volume changes in unsaturated soil samples during shear tests by monitoring the water flow to or from the inner cell. In this study, the double-wall cell consisted of an inner and outer cell, both subjected to equal pressure. A schematic diagram of the double-wall cell concept is presented in Figure 3.24. The inner cell was fully filled with deaired, distilled water. For the outer cell, there were two possible configurations: (1) the outer cell was completely filled with water and connected to a cell pressure water tank linked

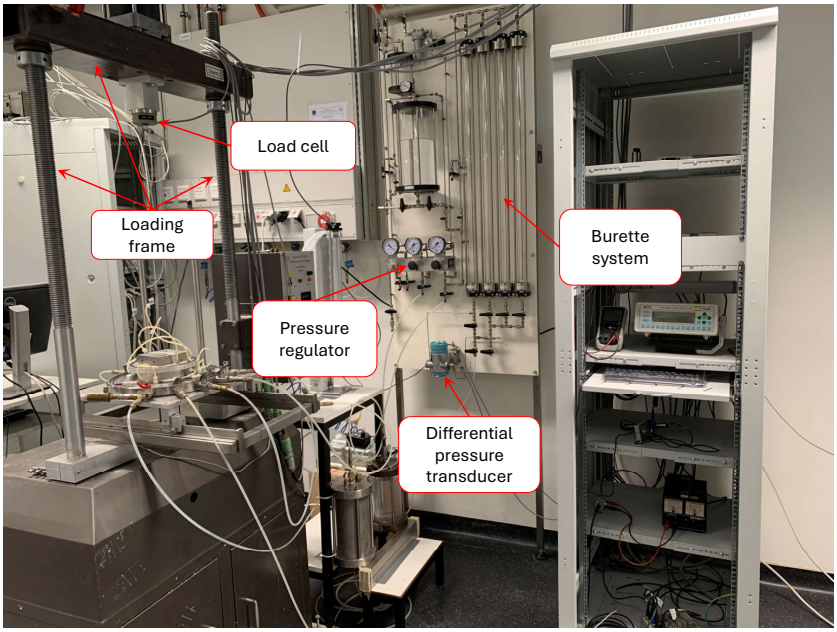

Figure 3.22.: Loading frame and burette system used for volume change measurement

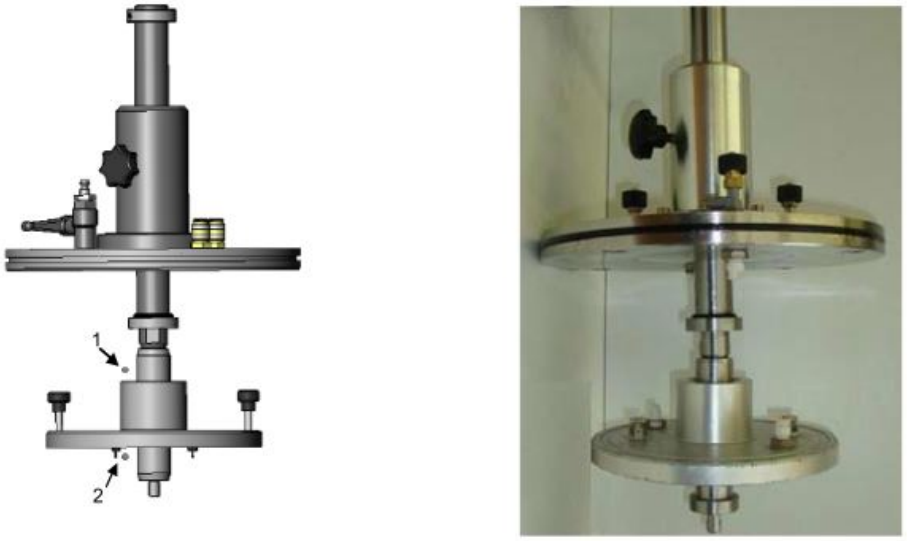

Figure 3.23.: Outer and inner pistons (Alabdullah 2010)

to an air pressure regulator, or (2) the outer cell was partially filled with deaired, distilled water, leaving a gap of approximately 2 cm below the top cap. In this second option, pressure was applied to the outer cell via the air-water interface through a valve located on the top cap. Figure 3.24 illustrates the second configuration for applying outer cell

pressure. Any pressure applied to the outer cell was automatically transferred to the inner cell, ensuring that the inner cell experienced equal external and internal pressures. This arrangement prevented differential pressures, cell expansion, water leakage, and minimized system compliance errors.

To withstand confining pressures of up to 10 bar, the outer cell was reinforced with steel bands (rings), whereas the inner cell required no metal or fiberglass reinforcement. A differential pressure transducer mounted on the burette system board was used to precisely measure the volume of water entering or exiting the inner cell. This configuration ensured precise measurement of volume changes in the sample throughout the testing process.

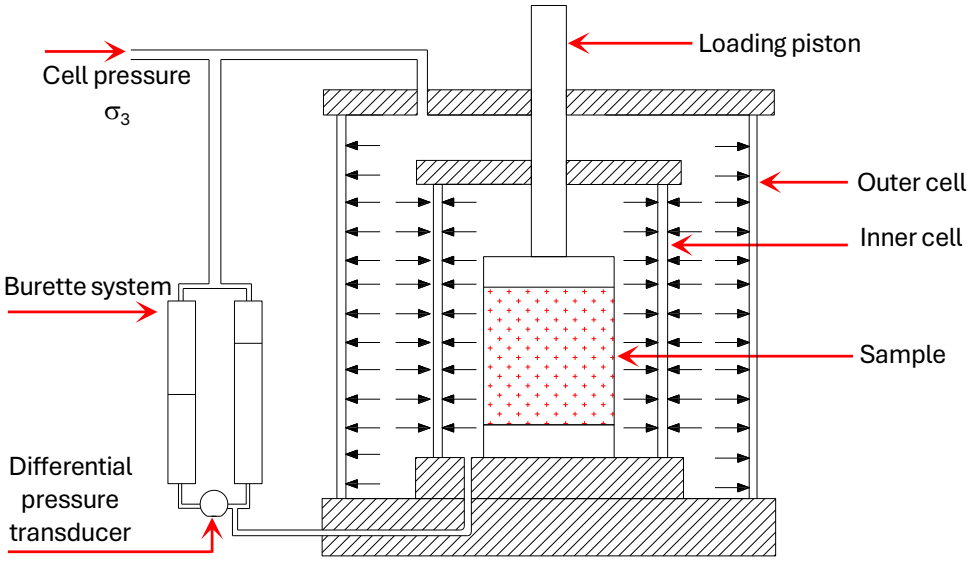

Figure 3.24.: Schematic diagram of the double wall cell

c) Side platens and membrane

The plane-strain condition was maintained using two fixed stainless steel walls, each with a thickness of 15 mm and a width of 101 mm. To reduce friction between the membrane and the metal side walls, two 0.25 mm Teflon sheets coated with silicone grease were employed, a method previously applied in studies by Wanatowski (2005) and Tatsuoka et al. (1986). Additionally, to minimize friction between the base block and the bottom platen, a ball bearing system with a sliding mechanism was installed at the base of the specimen. This anti-friction system facilitated the movement of the lower part of the sample relative to

the upper part after the initiation of the shear band. Figure 3.25a shows the metal side platens with two teflon sheets. Meanwhile, the ball bearings are visible in Figure 3.25b.

In this study, a rectangular latex membrane with a thickness of 0.4 mm and a height of 200 mm was employed. Figure 3.26a illustrates the specimen enclosed by the prismatic-shaped membrane, which was trimmed to match the height of the sample. Due to the unique geometry of both the specimen and membrane, traditional circular O-rings could not effectively secure and seal the membrane at the top cap and bottom platen. As a solution, four metal plates were used to firmly fasten the O-rings and the membrane around the periphery of both the top cap and bottom platen. The tightening metal plates are visible in Figure 3.26b.

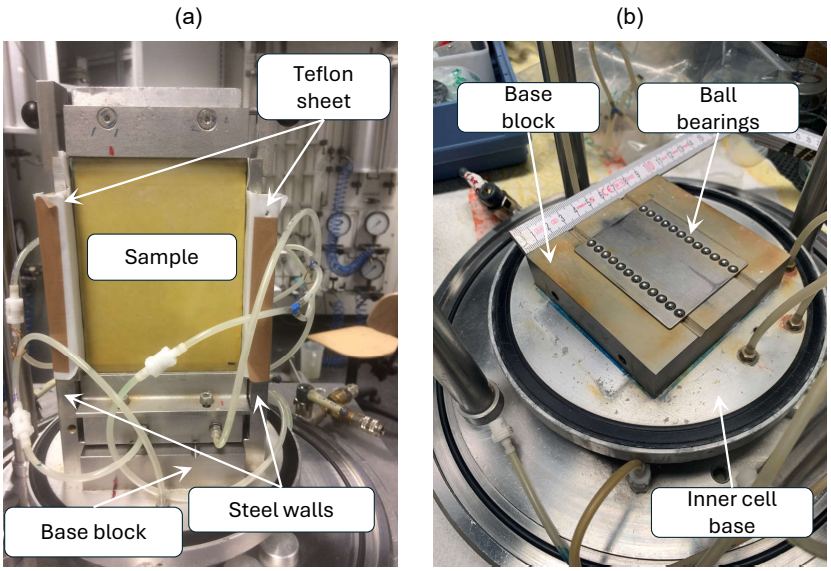

Figure 3.25.: (a) Side platens and teflon sheets, and (b) ball bearings

d) Top cap, bottom platen, and systems to apply suction

Two main types of tests were conducted in this study using the biaxial device: (1) saturated soil biaxial testing and (2) unsaturated soil biaxial testing. To accommodate both test types, the top cap and bottom platen were designed for easy switching between the two setups.

For biaxial compression tests (BCT) on saturated soil samples, the top cap and bottom platen were fitted with four porous stones, allowing for the application of back pressure to the sample throughout the testing process.

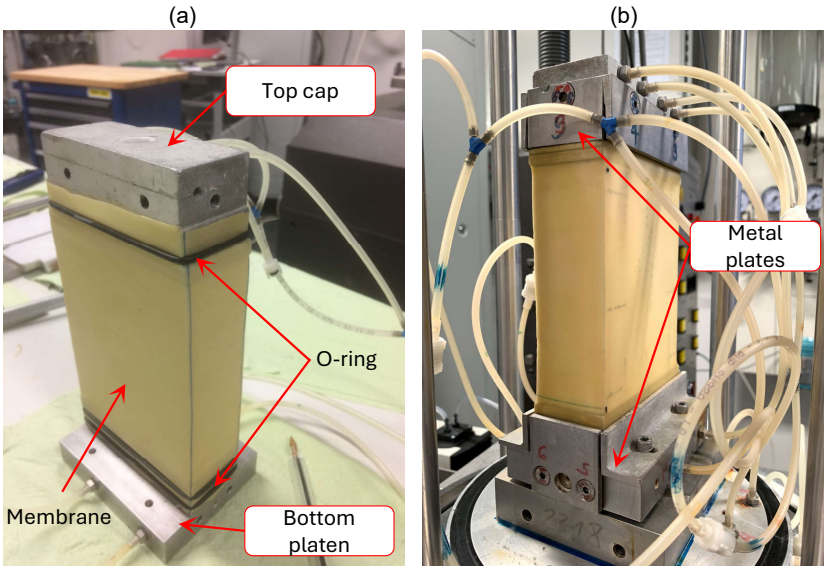

Figure 3.26.: (a) Sample covered by a membrane with O-rings, and (b) membrane fixed by O-rings and metal plates

For the BCT on unsaturated soil samples, the axis translation technique (ATT) (Hilf 1956) and the salt vapor flow technique (SVFT) (Blatz & Graham 2000) based on the vapor equilibrium technique (VET) (Tessier 1984) were utilized. The details of the ATT were already discussed in the section on techniques used for SWCC determination. To apply suction using the ATT (for suction values smaller than 500 kPa) in the biaxial device, porous and ceramic discs were employed to regulate pore-air and pore-water pressures (u_a and u_w) within the soil sample. These discs were mounted onto metal plates, which were affixed to both the top cap and bottom platen, as depicted in Figure 3.27a, b. The metal plates could be easily replaced with alternatives equipped with ceramic discs of higher air-entry values, allowing for the application of higher matric suctions, thus enabling the testing of unsaturated soils across a broad range of matric suction values. In this study, ceramic discs with 3-bar and 5-bar air-entry values were used. Figure 3.28 illustrates the schematic setup for applying suction via the ATT in this research.

To apply the SVFT for suction values exceeding 1500 kPa, vapor generated from salt solutions with specified molarities was circulated over the sample using a pump. The vapor was directed through both the top cap and bottom platen, which were equipped with two metal plates containing four porous stones each (see Fig. 3.27c, d), similar to those used in the saturated soil biaxial tests. Figure 3.29 illustrates the schematic setup for applying suction via the SVFT in this study.

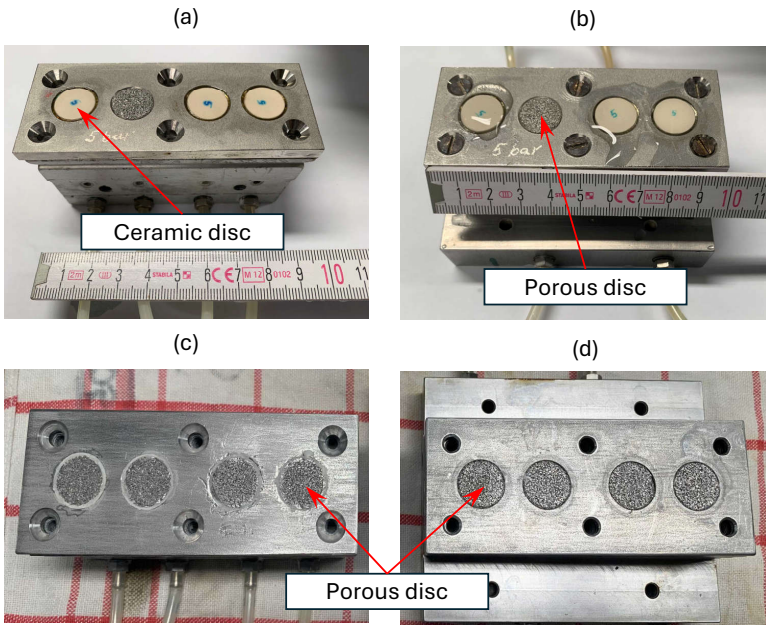

Figure 3.27.: Top cap and bottom platen: (a) Top cap with three ceramic discs and one porous disc, (b) bottom platen with three ceramic discs and one porous disc, (c) top cap with four porous discs, and (d) bottom platen with four porous discs

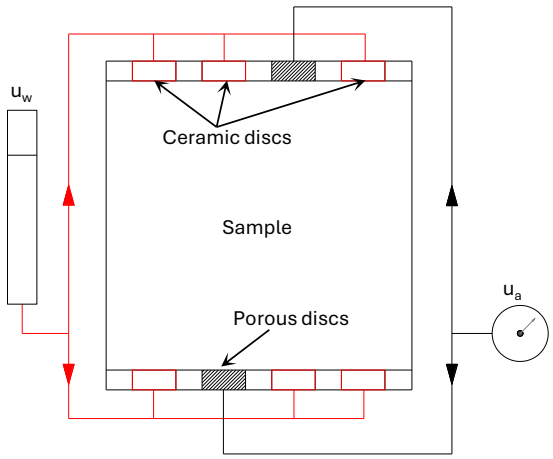

Figure 3.28.: Schematic setup of applying suction via ATT (this figure is not scaled)

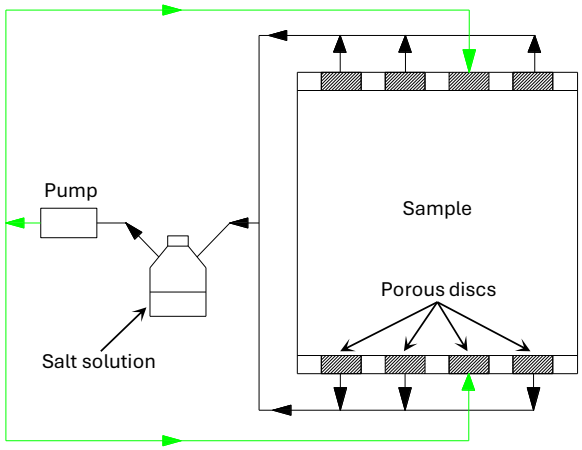

Figure 3.29.: Schematic setup of applying suction via SVFT (this figure is not scaled)

3.3.4.2. Testing procedure

a) Saturated soil testing

i) Sample preparation and setup

The biaxial samples used in the saturated tests were extracted from a saturated compacted soil block (h = 20 cm, d = 25 cm) as detailed in Section 3.2.3. For these tests, the top cap and bottom platen were equipped with metal plates containing four porous stones. To prevent air entrapment during assembly, the metal plates were integrated into the bottom platen while submerged in water. A deaired water tank, filled to approximately 2 cm below its top cap, was used. A valve located at the bottom of the tank was connected to the water pressure line, while another valve mounted on top of the tank was linked to an air pressure regulator, facilitating the application of back pressure to the sample.

Prior to installation, the dimensions and weight of the sample were carefully measured. The sample was then encased in a latex membrane and placed on the bottom platen, followed by the positioning of the top cap on the sample. Moist filter paper was placed between the sample and both the bottom platen and top cap to enhance contact and to prevent the clogging of the porous discs. The O-rings were secured to the top cap and bottom platen using four metal plates. Subsequently, the inner cell, along with its top cap and piston, was installed. The inner cell was sealed using two flat rubber rings at the top and bottom, fastened tightly with four clamps, and completely filled with deaired distilled water. A pipeline was used to connect the inner cell to the volume change burette system,

and a pressure of 20 kPa was applied to the inner cell for 30 minutes to check for any leakage.

After verifying the integrity of the inner cell, the outer cell, along with its top cap and piston, was installed. The outer cell was securely fastened to the base using four stainless steel rods and screws. Following this, the outer cell was completely filled with water and connected to a cell pressure water tank, which was regulated by an air pressure system (configuration 1 mentioned above). To check for leakage, a pressure of 20 kPa was applied to the outer cell for 30 minutes. Subsequently, a back pressure of 10 kPa was introduced, maintaining an effective confining pressure of 10 kPa. Additionally, a seating vertical stress of 5 kPa was applied to the sample via the axial actuator to ensure proper contact with the top surface of the sample.

ii) Saturation of the sample

The degree of saturation of the sample, upon extraction from the saturated compacted block, was approximately 96%, calculated based on the water content and void ratio of the sample. To ensure full saturation, the back pressure method was employed to saturate the sample within the biaxial device. The saturation process was conducted in two stages: the initial stage involved saturating the sample using deaired and distilled water, typically lasting 4 days, followed by the second stage of back pressure saturation, which usually lasted for 3 days.

Initially, the back pressure and cell pressure were gradually increased to 70 kPa and 80 kPa, respectively. Water was allowed to flow from the water tank into the bottom of the sample. Under this back pressure, the water flowed from the bottom through the sample to the top cap and exited into a collection container. Once water began to flow out through the top cap, the water line of the top cap was connected to the back pressure line. At this point, the back pressure method was fully implemented. According to ASTM D7181-11, the specimen is considered fully saturated when Skempton's pore-water parameter (B) exceeds 0.96. The B-value represents the ratio of the increase in pore water pressure (Δu) due to an increase in cell pressure ($\Delta\sigma_3$) applied under closed drainage conditions, and is defined as follows:

$$B = \frac{\Delta u}{\Delta \sigma_3} \tag{3.1}$$

The back pressure of 70 kPa and cell pressure of 80 kPa were maintained for 3 days. After this period, the saturation level of the sample was assessed using Skempton's B-value test. For that purpose, the water inflow and outflow lines were closed, and the cell

pressure was incrementally increased by 50 kPa. The resulting excess pore water pressure (Δu) generated by the increase in cell pressure ($\Delta\sigma_3$) was recorded once the pore water pressure stabilized via a pore water pressure transducer. The B-value was then calculated using Equation 3.1.

In this research, in accordance with ASTM D7181-11, the criterion for complete saturation was set at a B-value of 0.96. The B-value was evaluated after both the cell and pore pressure had stabilized. If the criterion for full saturation was not met, the back pressure was set to a value 10 kPa smaller than the current cell pressure and the back pressure valve was opened (i.e. the net confining pressure of 10 kPa was maintained). A waiting period of 20 minutes was followed after each back pressure increment before conducting the subsequent B-check. It was observed that the back pressure required to achieve full saturation ranged from a minimum of 290 kPa to a maximum of 480 kPa.

iii) Isotropic consolidation of the sample

After the saturation process, the sample underwent isotropic consolidation to reach a target mean effective stress. This consolidation phase allowed the dissipation of excess pore water pressure generated by the application of the target effective stress, which would be used during the subsequent shearing phase. To achieve the target consolidation stress, the cell pressure was gradually increased to the desired value, while the back pressure was held constant. Both ends of the sample were kept open for drainage, allowing pore water to flow into the connected water tank.

The sample's volume change was monitored through the burette system linked to the inner cell, and consolidation was considered complete once the volume of the sample remained relatively constant over an extended period. Typically, the consolidation process took approximately 24 hours. In this study, saturated tests were performed under net confining pressures of 50, 100, and 200 kPa.

iv) Shearing under drained conditions

After the consolidation process, the sample was subjected to monotonic shearing under drained conditions. During this phase, both the cell pressure and back pressure were kept constant, while axial loading was applied at a constant displacement rate. In this study, an axial displacement rate of 0.0019 mm/min was selected, in accordance with the recommendations of Fredlund & Rahardjo (1993*b*), to ensure adequate dissipation of excess pore water pressure throughout the sample.

Axial deformation was monitored using an external Linear Variable Differential Transducer (LVDT) with a 50 mm range, mounted on the outer piston. The applied load was measured with a load cell (20 kN capacity) positioned beneath the horizontal beam. Changes in the sample's volume were recorded by measuring the water exchange from the inner cell, which was connected to a differential pressure transducer integrated into the burette system. All data generated during the tests, including measurements from the load cell, pressure transducers including cell pressure transducer and pore water pressure transducer, LVDT, and volume change system, were automatically recorded onto a computer using the HP-Vee software developed by Hewlett-Packard.

The shearing continued until a visible shear band and post-peak behavior were observed. Upon completion of the test, the pressure was gradually released, the cells were emptied and dismantled, and the sample was removed. Portions of the sample were then collected for water content analysis. A schematic setup of the biaxial tests on saturated samples is illustrated in Figure 3.30.

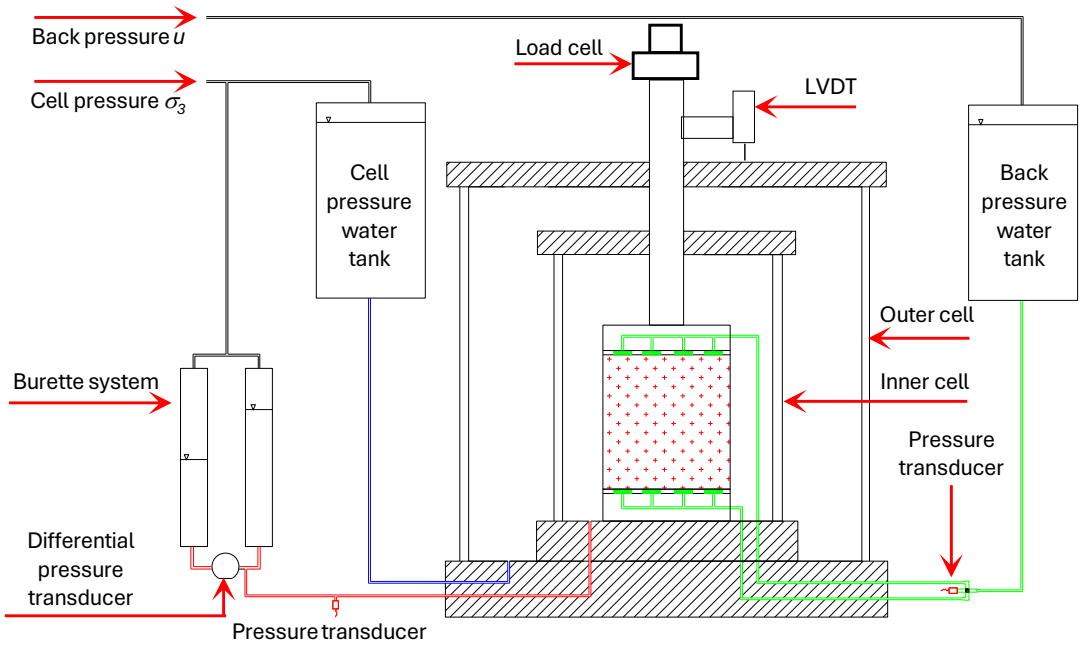

Figure 3.30.: Schematic setup of biaxial saturation tests

b) Unsaturated soil testing

i) Sample preparation and setup

If directly built into the biaxial device, the compacted sample could take several weeks or even months to achieve the required suction, i.e. the equilibrium time was very large. This would lead to an enormous delay in completion of a test. Therefore, before mounting the sample in the biaxial device, the sample was pre-equilibrated to the desired suction (or desired water content) outside the test chamber. This method has been also used in some studies (Patil 2014; Banerjee 2017; Gao et al. 2019). Details of the sample preparation for the unsaturated tests were described in the sample preparation section 3.2.3.

As mentioned in Section 3.3.4.1, the ATT and SVFT were employed to apply suction to the unsaturated samples to cover a wide range of suction. The following is the experimental setup for suction application in the biaxial device:

Setup for ATT

To control suction using the ATT, metal plates equipped with three ceramic discs and one porous disc were mounted on both the top cap and bottom platen. In this study, a ceramic disc with an air-entry value of 3 bar was employed to apply a suction value of 100 kPa. For a higher suction value of 400 kPa, ceramic discs with an air-entry value of 5 bar were used. The system for applying suction via the ATT method was previously detailed in section 3.3.4.1. To prevent drying of the ceramic discs, they were stored in a plastic container filled with water, even when the tests were not active. The procedure for saturating the ceramic discs is presented in the Appendix A.

Cell pressure (σ_3) and pore water pressure (u_w) were monitored using two pressure transducers, while pore air pressure (u_a) was regulated by an air pressure controller manufactured by Wille Geotechnik GmbH. The setup for measuring axial deformation, applied axial load, and volume change of the sample was identical to the system used in the saturated tests. Figure 3.31 provides a schematic of the biaxial device setup for controlling suction using the ATT method during the series of the unsaturated soil samples.

Setup for SVFT

To control suction using the SVFT, metal plates containing four porous discs, identical to those used in the saturated tests, were installed on the top cap and bottom platen.

A bottle of salt solution with a known suction value and a pump were employed. The salt vapor from the bottle was circulated to both the top cap and bottom platen, and consequently to the sample, using the pump. The system for applying suction via the SVFT method was previously detailed in Section 3.3.4.1.

Cell pressure (σ_3) was monitored using a pressure transducer. The systems for measuring axial deformation, applied axial load, and volume change of the sample were the same as those utilized in the saturated tests. The specific salt solutions used will be described later in the section outlining the experimental program. Figure 3.32 provides a schematic of the biaxial device setup for controlling suction using the SVFT method during the series of tests on unsaturated soil samples.

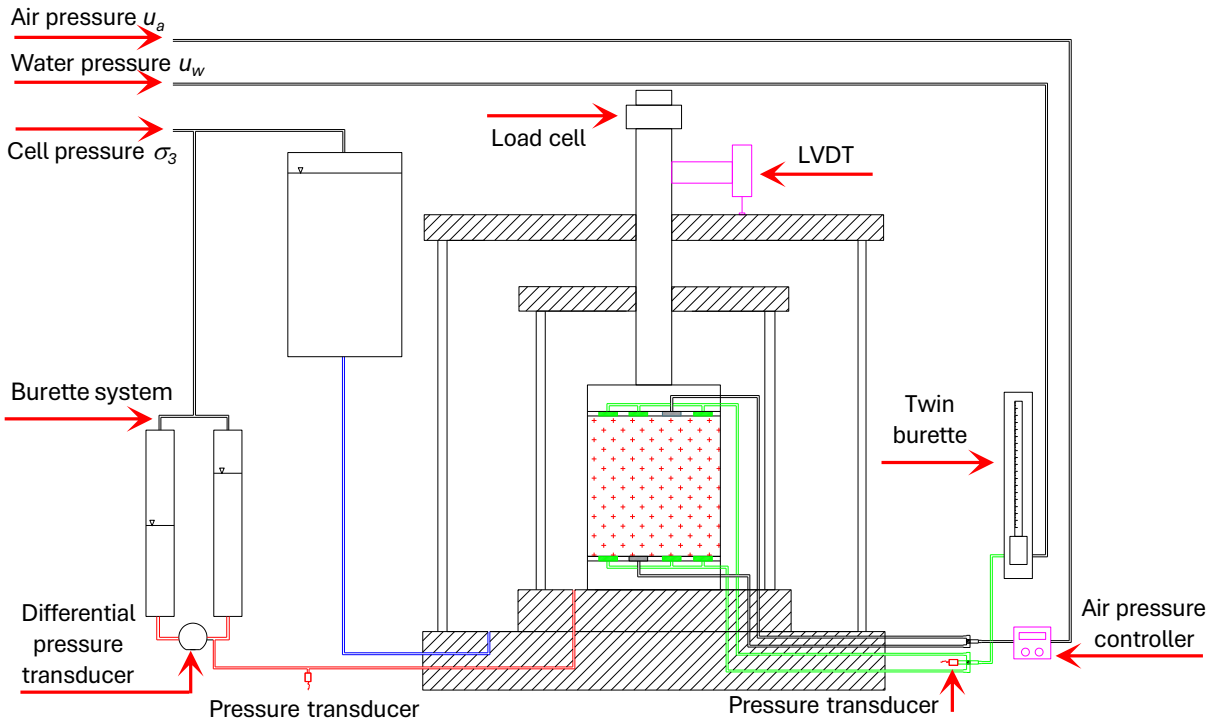

Figure 3.31.: Schematic of the biaxial device setup for controlling suction using the ATT method

ii) Suction equalization

After achieving the desired water content, which corresponds to the target suction (determined based on the soil-water characteristic curve), the samples were sealed and stored in a closed container for four days, as previously detailed in Section 3.2.3. Prior to mounting the sample on the bottom platen of the biaxial device, both the mass and dimensions of the sample were carefully measured.

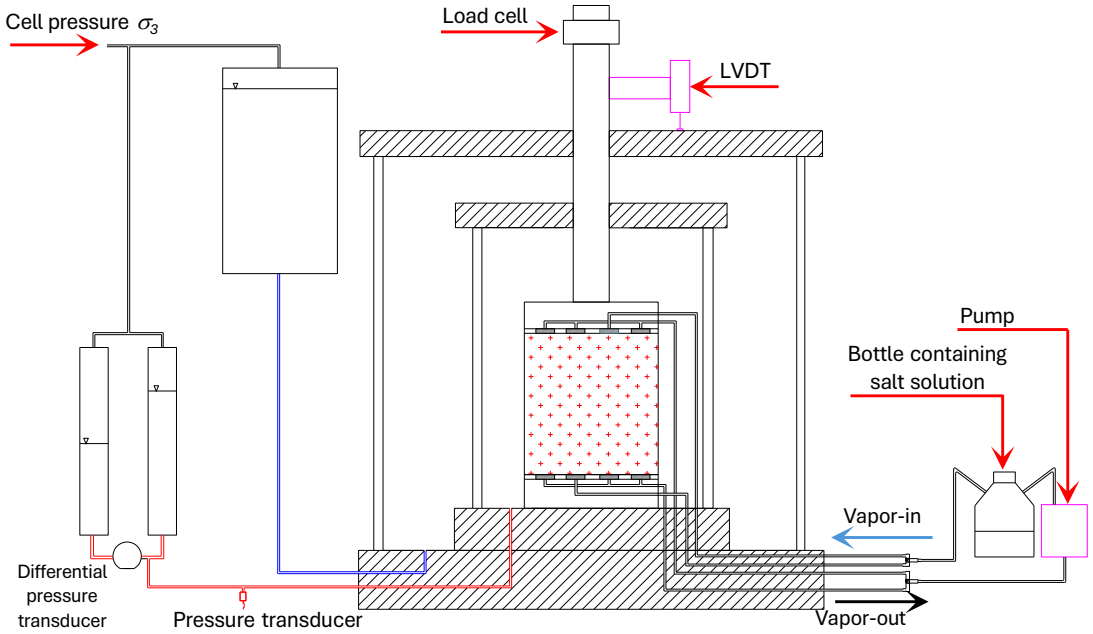

Figure 3.32.: Schematic of the biaxial device setup for controlling suction using the SVFT method

Suction equalization when applying ATT

The procedure for installing the sample into the biaxial device followed the steps outlined previously in Section 3.3.4.1. After positioning the double-wall cell and sealing the chamber, initial pressures were applied: a cell pressure (σ_3) of 90 kPa, an air pressure (u_a) of 60 kPa, and a water pressure (u_w) of 20 kPa. Consequently, the initial net confining pressure (σ_3 - u_a) was set at 30 kPa, while the initial matric suction (u_a - u_w) was 40 kPa.

The cell pressure, pore air pressure, and pore water pressure were gradually increased at a constant rate of 10 kPa per hour. When the pore water pressure reached 50 kPa, it was maintained at this level, while the cell pressure and pore air pressure continued to rise at the specified rate to achieve the target suction value. The desired matric suction was then maintained until suction equilibrium was reached. This technique has been also applied in some studies (Patil 2014; Banerjee 2017). Following the criteria established by Sivakumar (1993), Ng & Zhou (2014), and Banerjee (2017), suction equilibration was considered complete when the water content change of the sample was less than 0.04% per day or 0.5 cm^3 per day. In this study, suction equilibration was confirmed when the water flow from the soil sample was less than 0.5 cm^3 per day, as monitored via the twin burette, as illustrated in Figure 3.31. It generally required 5 days to achieve equilibrium

for the suction value of 100 kPa and 8 days for the suction value of 400 kPa, since the samples were pre-equilibrated at a nearby suction level outside of the device, and suction was applied on both sides of the sample.

Suction equalization when applying SVFT

For suction equalization using the SVFT method, after placing the double-wall cell and sealing the chamber, a cell pressure of 30 kPa was applied. The desired suction was applied by circulating salt vapor with a known suction value, which was determined based on the relative humidity and temperature obtained from the AquaLab chilled mirror hygrometer and the employment of Kelvin's equation (see Eq. 2.2). A pump facilitated the vapor circulation, as shown in Figure 3.32.

To prevent any pressure buildup from the pump, grooves measuring 8 cm in length, 3 mm in width, and 3 mm in depth were made on the top and bottom surfaces of the sample, forming a channel between the porous discs. These grooves ensured that the pump operation did not interfere with cell pressure or volume change measurements.

Using a similar suction control method, Alsherif & McCartney (2014) conducted triaxial tests on unsaturated silt samples with low degrees of saturation using the vapor flow technique and found that 14 days were required to achieve suction equilibrium throughout the sample. In this study, suction measurements within the sample were not taken during the tests. Therefore, trial tests were conducted to verify the suction of the sample after 6 and 10 days of suction application. These trial samples were divided into sections, and the suction was measured using the AquaLab chilled mirror hygrometer. Typically, it took 10 days to reach the desired suction value, as the samples had been pre-equilibrated at a nearby suction level before installation, and vapor circulation was applied on both sides of the sample.

iii) Isotropic consolidation

Once the target suction was achieved, the isotropic consolidation stage began. For biaxial tests with suction controlled by the axis translation technique (ATT), matric suction was maintained by keeping both pore air pressure and pore water pressure constant, while the cell pressure was gradually increased at a rate of 10 kPa per hour until the desired net confining pressure was reached. For tests with suction controlled by the salt vapor flow technique (SVFT), the cell pressure was increased at a rate of 20 kPa per hour. Gao et al.

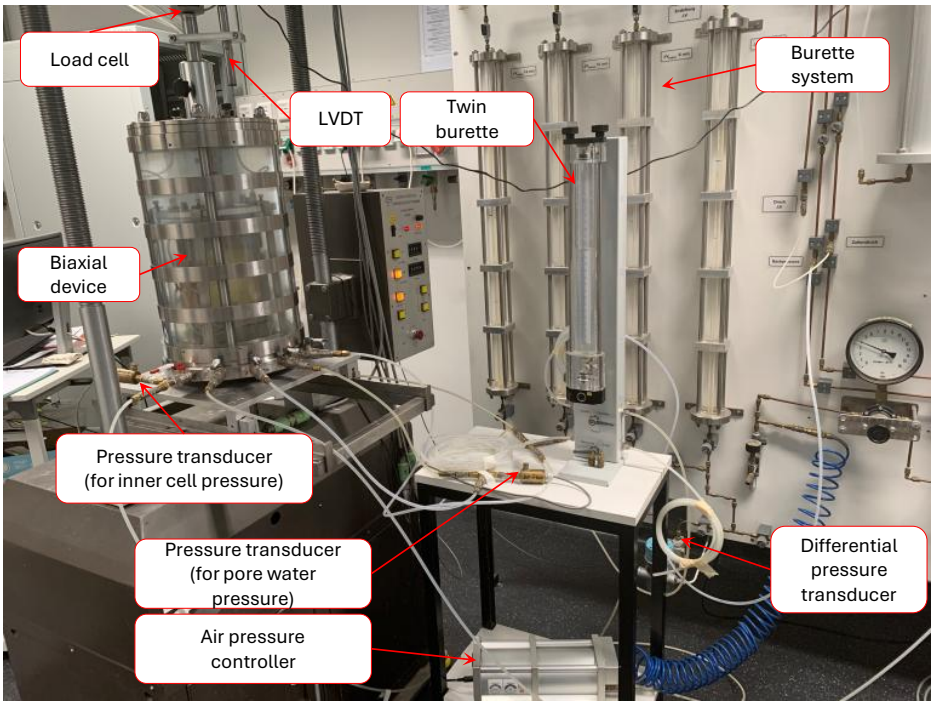

Figure 3.33.: Biaxial test with suction controlled by ATT

(2019) indicated that, at higher suction levels, the suction and void ratio of the sample exhibit minimal change under mechanical loading. Each specimen was consolidated for over 24 hours, with the volume change recorded throughout this stage.

iv) Shearing

Following isotropic consolidation, the specimens were subjected to monotonic shearing through axial loading at a constant axial displacement rate of 0.0019 mm/min, in a displacement-controlled test. Throughout the test, the net confining pressure and matric suction were kept constant to ensure controlled testing conditions. Figure 3.33 shows a photo of a biaxial test on an unsaturated sample with suction controlled by ATT, while Figure 3.34 presents a photo of a biaxial test on an unsaturated sample with suction controlled by SVFT. After testing, the sample was sectioned into multiple parts to measure water content and suction using the Aqualab device.

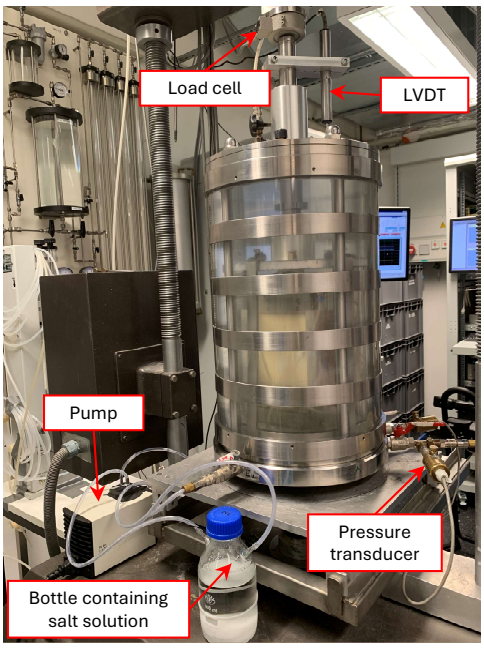

Figure 3.34.: Biaxial test with suction controlled by SVFT

3.3.4.3. Experimental program

As previously discussed, the series of BCT were conducted under both saturated and unsaturated conditions. Additionally, to investigate the influence of anisotropy, samples were prepared with two cutting orientations (i.e., vertical and horizontal), as explained in section 3.7. For the BCT under saturated conditions, experiments were carried out

Table 3.3.: Experimental program of biaxial tests on unsaturated samples following the drying path (vertical cutting direction) (B-VC-D)

Suction control technique	Suction (MPa)	AEV of ceramic disc (bar)	Salt solution
ATT	0.1	3 bar	-
ATT	0.4	5 bar	-
SVFT	3.7	-	(Sat.) K_2SO_4
SVFT	10	-	2.2M NaCl
SVFT	22	-	(Sat.) KCl
SVFT	98	-	(Sat.) K_2CO_3
SVFT	200	-	(Sat.) LiCl

under three different net confining pressures: 50, 100, and 200 kPa. In the BCT under

Table 3.4.: Experimental program of biaxial tests on unsaturated samples following the wetting path (vertical cutting direction) (B-VC-W)

Suction control technique	Suction (MPa)	AEV of ceramic disc (bar)	Salt solution
ATT	0.4	5 bar	-
SVFT	2.4	-	0.5M NaCl
SVFT	7.0	-	1.5M NaCl

Table 3.5.: Experimental program of biaxial tests on unsaturated samples following the drying path (horizontal cutting direction) (B-HC-D)

Suction control technique	Suction (MPa)	AEV of ceramic disc (bar)	Salt solution
ATT	0.4	5 bar	-
SVFT	3.7	-	(Sat.) K_2SO_4
SVFT	10	-	2.2M NaCl

unsaturated conditions, experiments were performed on samples subjected to both drying and wetting paths over a wide range of suctions for the samples with vertical cutting direction. For horizontally cut samples, tests were conducted only along the drying path. Similar to the saturated tests, net confining pressures of 50, 100, and 200 kPa were applied in the unsaturated tests. Tables 3.3 and 3.4 present the experimental program for vertically cut samples on the drying path (B-VC-D) and wetting path (B-VC-W), respectively. The experimental program for horizontally cut samples (B-HC-D) is shown in Table 3.5. As shown in these tables, both saturated salt solutions (Sat.) and unsaturated salt solutions (with specified molarity) were used for the SVFT.

3.3.5. Techniques, procedures, and experimental program for direct shear tests

3.3.5.1. Introduction of direct shear device

A direct shear apparatus manufactured by Wille Geotechnik GmbH was used to perform a series of direct shear tests (DST) under both saturated and unsaturated conditions. The sample size was 10 cm by 10 cm in horizontal dimensions and 2 cm in vertical height. The sample was placed within a shear box, which was divided into two halves: an upper

half and a lower half, designed to create a shear plane at the contact interface between the two sections.

The lower half of the shear box was positioned on a base mounted on a slide rail, allowing horizontal movement driven by a motor and gear system integrated into the device. The upper half was secured by three vertical rods and screws, preventing any movement. A loading plate transferred the vertical load to the sample. The design of the apparatus prevents free rotation of both the upper half of the shear box and the loading plate. Vertical stress was applied through a loading frame controlled by a motor and gear system. The loading plate was permanently fitted with a porous plate. However, in the lower half of the shear box, either a porous plate or a plate containing a ceramic disc could be used, depending on the test condition or applied technique. For DST on saturated samples, a porous plate was placed in the lower half of the shear box. For DST on unsaturated samples, the ATT (Hilf 1956) and the SVFT (Blatz & Graham 2000) were employed, similar to the methods used for suction control in the BCT on unsaturated samples. To apply suction using ATT (where $\psi = 200$ kPa), a metal plate containing a ceramic disc with an air-entry value (AEV) of 3 bar was used. For the SVFT (in this study, $\psi \geq 3.7$ MPa), a porous plate was used to allow circulation of salt vapor, generated from a salt solution, over the sample via a pump. Further details of the suction control techniques will be discussed later.

In this study, both vertical and horizontal displacements were recorded using two displacement sensors. Vertical and horizontal loads were measured by two load cells with capacities of 10 kN and 5 kN, respectively. The sample and shear box were placed inside a two-part cell: the lower part, made of stainless steel, was fixed to the device base, while the upper part, made of plexiglass, was detachable to facilitate sample installation. The upper cell was securely fastened to a top cap with three screws. The apparatus, along with its measurement and control system, was connected to a computer equipped with GEOsys 8.7.8.2 software for data logging. Figure 3.35 shows a view of the direct shear apparatus used in this study.

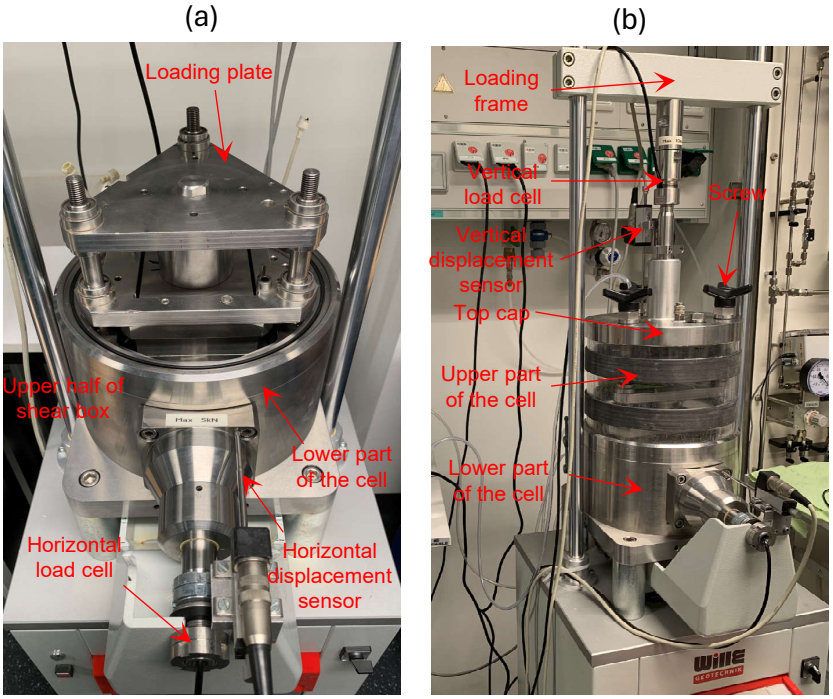

Figure 3.35.: The Wille direct shear apparatus used in this study: (a) view of shear box, and (b) device after assembly of components

3.3.5.2. Testing procedure

a) Saturated soil testing

i) Sample preparation and setup

The direct shear samples, measuring 10 cm in horizontal dimensions and 2 cm in height, were extracted from a saturated compacted soil block as described in Section 3.2.3. As previously explained, in the series of tests on saturated samples, the porous disc was employed in the lower half of the shear box.

ii) Installation, saturation, consolidation, and shearing

First, the dimensions and weight of the sample were carefully measured before placing it into the shear box. To prevent any potential damage to the sample during installation, the upper and lower halves of the shear box were temporarily fixed together using two screws. To ensure uniform transmission of the shearing forces along the length of the sample, grid plates were positioned between the porous plate and the sample at both the bottom and

top. Once the sample was securely installed, the loading plate was placed on the sample, and the screws were detached.

To ensure that the sample was fully saturated, deaired and distilled water was poured into the lower part of the cell until the sample was completely submerged. The upper part of the cell was then positioned, and the loading frame was gently lowered onto the loading plate. The top cap was securely fixed to the cell using three screws. Subsequently, the desired normal load was applied, with vertical displacement and load data recorded via the software throughout the consolidation process. The vertical displacement stabilized after approximately 24 hours.

Following consolidation, the sample was sheared at a constant deformation rate of 0.0019 mm/min, consistent with the strain rate used in the biaxial tests. The maximum horizontal displacement was set at 9 mm, although the shearing process could be terminated once the peak shear stress was reached. Figure 3.36 shows a view of the saturated sample before and after the test.

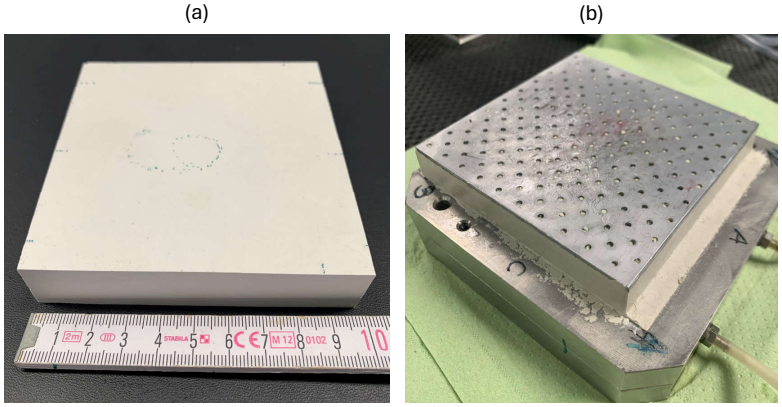

Figure 3.36.: A direct shear sample in the saturated testing condition: (a) before the test, and (b) after the test

b) Unsaturated soil testing

i) Sample preparation and setup

The compacted sample could take several weeks to achieve the required suction (i.e. the equilibrium time). This would lead to an enormous delay in completion of a test. Therefore, before mounting the sample in the direct shear device, the sample was pre-equilibrated

to the desired suction (or desired water content) outside the test chamber. To prepare the samples following the drying path, the air drying method was used, while to prepare the samples following the wetting path, the RUB-humidifier was utilized. Details of the sample preparation for the unsaturated tests were outlined in Section 3.2.3.

As mentioned previously, the ATT and SVFT were employed to apply suction to the unsaturated samples to cover a wide range of suction. The following is the experimental setup for suction application in the direct shear device:

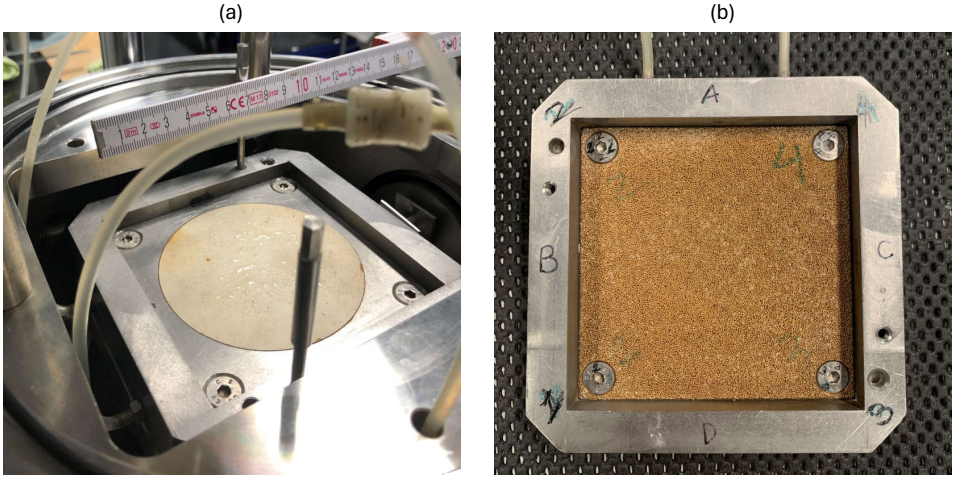

Figure 3.37.: Plates mounted on the lower half of the shear box to control suction: (a) metal plate fitted with a ceramic disc used for ATT, and (b) porous plate used for SVFT

Setup for ATT

To control suction using the ATT method, a metal plate fitted with a ceramic disc with an AEV of 3 bar was mounted on the lower half of the shear box (Fig. 3.37a). Water pressure was applied to the sample through the ceramic disc using an open burette, while air pressure was applied to the cell housing the shear box, regulated via an air pressure controller. During the test, water pressure was maintained at 10 kPa by keeping the water level in the burette at 1 meter, while air pressure was increased to the desired value by adjusting the air pressure controller. The difference between pore air pressure (u_a) and pore water pressure (u_w) represented the desired suction value.

The measurement system was the same as that utilized in the saturated tests. The vertical load and horizontal load were measured by two load cells. The vertical and horizontal displacement were monitored using two sensors. Figure 3.38 provides a schematic of the

direct shear device setup for controlling suction using the ATT method during the series of tests on unsaturated soil samples.

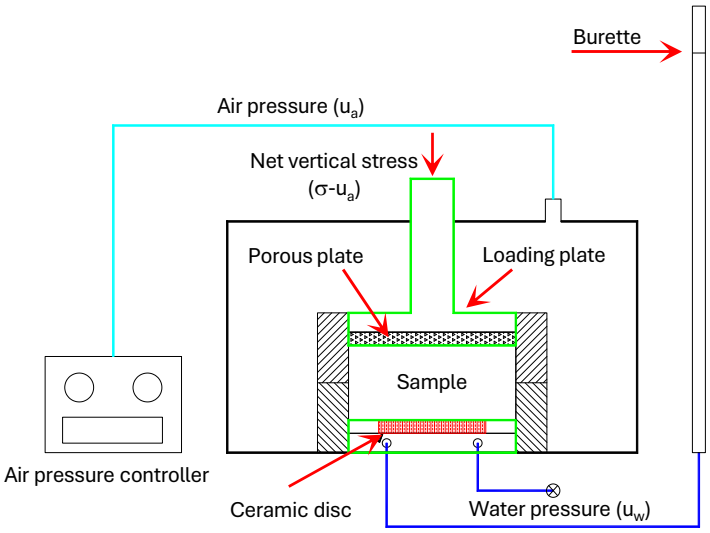

Figure 3.38.: Schematic of direct shear device setup for controlling suction using the ATT method

Setup for SVFT

To control suction using the SVFT method, a porous plate, similar to the one employed during the saturated tests, was installed on the lower half of the shear box (Fig. 3.37b). Two bottles of salt solutions, each with a known suction value, along with two pumps, were used. Salt vapor from the bottles was circulated to both the cell and the lower portion of the shear box, and subsequently to the sample, via the pumps. The measurement systems for vertical load, horizontal load, vertical displacement, and horizontal displacement were identical to those utilized in the saturated tests. Details of the specific salt solutions used will be provided in the section discussing the experimental program. Figure 3.39 illustrates the direct shear device setup for suction control using the SVFT method in the tests on unsaturated soil samples.

ii) Suction equalization, consolidation and shearing process

As described in the sample preparation section 3.2.3, following the attainment of the desired water content, the direct shear samples were sealed and stored in a closed container for a period of four days. To accommodate any shrinkage during the drying process, the

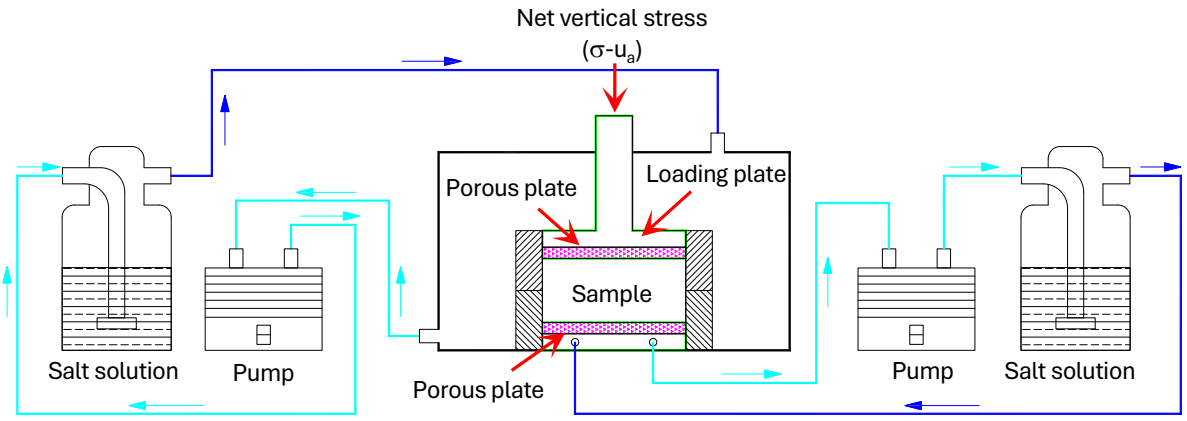

Figure 3.39.: Schematic of direct shear device setup for controlling suction using the SVFT method

samples were initially prepared with dimensions larger than the standard size (10 x 10 x 2 cm). Before installation in the testing device, the samples were trimmed to the standard dimensions, and the trimmed material was used to reassess both the water content and suction levels. The mass and dimensions of the sample were then carefully measured.

Tests with suction controlled by ATT

To control suction in the direct shear tests using the ATT method, similar to the biaxial tests, the ceramic disc must be fully saturated before use to ensure continuity of the water phase between the sample, the ceramic disc, and the compartment beneath the disc. The procedure for saturating the ceramic disc is detailed in the Appendix A.

The specimen was carefully positioned in the shear box to prevent any potential damage. Two long screws were used to temporarily secure the upper and lower halves of the shear box. After proper installation, the loading plate was placed on top of the sample, and the screws were then removed. The upper section of the cell was installed, and the loading frame was gently lowered onto the loading plate. The top cap of the cell was firmly secured with three screws. An initial vertical stress (σ) of 5 kPa was applied to the specimen. The air pressure (u_a), controlled by the air pressure regulator, was incrementally increased at a rate of 10 kPa per hour until reaching the target pressure.

In this experiment, a matric suction ($\psi = u_a$ - u_w) of 200 kPa was applied using the ATT. Accordingly, the air pressure (u_a) was set to 210 kPa, while the water pressure (u_w) was held constant at 10 kPa. This suction value was maintained until equilibrium

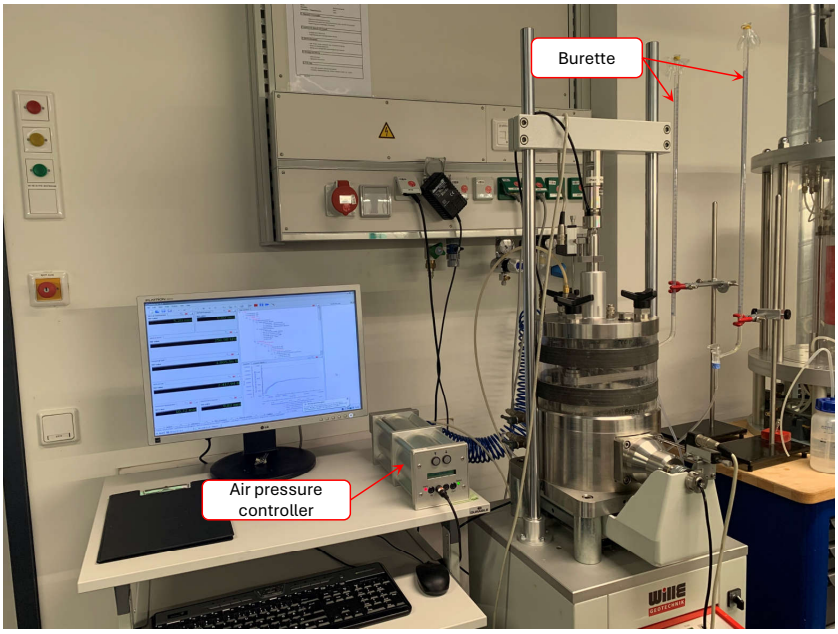

Figure 3.40.: Direct shear device setup for controlling suction using the ATT method

was achieved. Consistent with the approach used in the biaxial tests with ATT, suction equilibrium was considered to be attained when the change in water content fell below 0.04% per day or the water volume change was less than 0.5 cm^3 per day (Sivakumar 1993). During the test, the water level in the burette was regularly monitored, and when the water flow rate from the sample was less than 0.5 cm^3 per day, it was concluded that suction equilibration had been reached. Given the relatively small thickness of the sample ($h = 2$ cm) and its pre-equilibration at a near-suction level outside the apparatus, it typically took 5 to 6 days to reach the target suction of 200 kPa.

Once the target suction was achieved, the required net vertical stress (σ-u_a) was applied under controlled suction conditions. The sample was then consolidated for a duration of 24 hours, during which the vertical displacement stabilized, indicating the completion of the consolidation process.

Following consolidation, the specimen was subjected to shear at a constant shearing rate of 0.0019 mm/min. The maximum allowable horizontal displacement was set at 9 mm, although the shearing process could be terminated earlier if the peak shear stress was reached. Figure 3.40 provides a photo with an overview of the complete setup of the direct shear device for controlling suction using the ATT method.

Tests with suction controlled by SVFT

For suction equalization using the SVFT method, after positioning the sample in the shear box, the loading plate was placed on top of the sample, and the cell was carefully installed and sealed. Two pumps were then utilized to circulate salt vapor from a salt solution reservoir to the cell and sample. The sample remained in this suction-controlled environment for 7 days. Preliminary trial tests, conducted to verify the suction using the AquaLab chilled mirror hygrometer, confirmed that 7 days was sufficient for achieving suction equilibrium.

Following the suction equalization process, the sample was consolidated for 24 hours under the desired net vertical stress before being sheared at a constant shearing rate of 0.0019 mm/min. Figure 3.41 provides a photo with an overview of the complete setup of the direct shear device for controlling suction using the SVFT method.

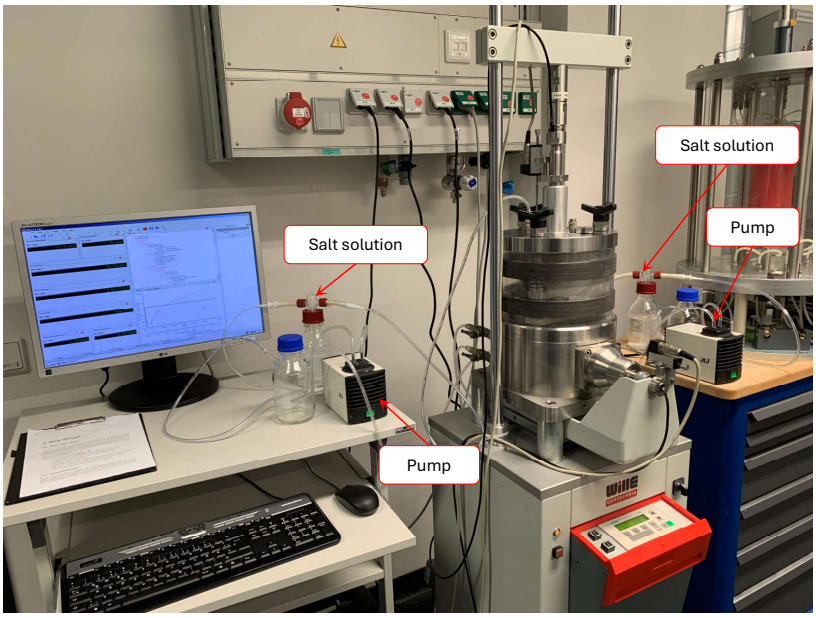

Figure 3.41.: Direct shear device setup for controlling suction using the SVFT method

3.3.5.3. Experimental program

As previously discussed, the series of DST were conducted under both saturated and unsaturated conditions. For the saturated tests, experiments were performed under three net normal stresses: 50, 100, and 200 kPa. In the unsaturated tests, samples were subjected to both drying and wetting paths across a broad range of suctions. Consistent with the

saturated tests, net normal stresses of 50, 100, and 200 kPa were applied in the unsaturated tests. Tables 3.6 and 3.7 outline the experimental program of the direct shear tests on unsaturated samples following the drying (DS-D) and wetting (DS-W) paths, respectively. As shown in these tables, both saturated salt solutions (Sat.) and unsaturated salt solutions (with specified molarity) were used for the SVFT.

Table 3.6.: Experimental program of direct shear tests on unsaturated samples following the drying path (DS-D)

Suction control technique	Suction (MPa)	Net normal stress (kPa)	AEV of ceramic disc (bar)	Salt solution
ATT	0.2	50; 100; 200	3 bar	-
SVFT	3.7	50; 100; 200	-	(Sat.) K_2SO_4
SVFT	10	50; 100; 200	-	2.2M NaCl
SVFT	22	50; 100; 200	-	(Sat.) KCl
SVFT	98	50; 100; 200	-	(Sat.) K_2CO_3
SVFT	200	50; 100; 200	-	(Sat.) LiCl

Table 3.7.: Experimental program of direct shear tests on unsaturated samples following the wetting path (DS-W)

Suction control technique	Suction (MPa)	Net normal stress (kPa)	AEV of ceramic disc (bar)	Salt solution
ATT	0.2	50; 200	3 bar	-
SVFT	2.4	50; 100; 200	-	0.5M NaCl
SVFT	7.0	50; 200	-	1.5M NaCl

3.3.6. Techniques, procedures, and experimental program for unconfined compression tests

3.3.6.1. Tests on samples along the drying path (UC-D)

As detailed in the sample preparation section 3.2.4, the series of unconfined compression tests (UCT) were conducted on specimens following both the drying and wetting paths. The UCT along the drying path (UC-D) were carried out by Yukang Wang at HSKL.

Comprehensive information regarding the testing equipment and procedure can be found in Yukang Wang's PhD thesis.

The UC-D in this study closely aligned with the principles of conventional unconfined compression testing, while incorporating specific modifications to suit the study's objectives. The test specimens, which had dimensions of 2.4 cm in diameter and 5 cm in height, were carefully positioned between a top cap and a bottom pedestal within the loading apparatus. This apparatus was equipped with a load cell capable of measuring forces up to 10 kN, ensuring precise measurement of the applied loads throughout the testing process.

In order to accurately capture the deformation and strain distribution of the samples during loading, the digital image correlation (DIC) technique was utilized. This method allowed for a non-contact, high-resolution analysis of the deformation patterns on the surface of the sample, thereby providing detailed insights into the mechanical behavior under compression. The testing setup was housed within a transparent chamber constructed from acrylic glass, which was specifically designed to maintain a stable and controlled environment throughout the duration of each test.

To regulate the environmental conditions, a humidifier was connected to the upper part of the acrylic enclosure. This system allowed for the precise control of relative humidity (RH), which was varied between 2% and 97%, depending on the test requirements. The temperature within the chamber was maintained at a constant 22°C to eliminate any potential temperature-related variations in the material behavior. This controlled environment was essential for replicating conditions that would affect the sample's water content and, consequently, its mechanical response.

The axial compression was applied at a constant loading rate of 0.06 mm/min, ensuring uniform deformation and preventing sudden failures due to rapid loading. This strain rate was chosen to allow for the observation of gradual deformation processes and to provide sufficient time for the sample to respond to the applied load. Over the course of the study, a total of 26 unconfined compression tests were performed on samples along the drying path (UC-D) with varying initial water contents, allowing for a comprehensive investigation into the influence of water content on the mechanical behavior of the material.

3.3.6.2. Tests on samples along the wetting path (UC-W)

The UCT following the wetting path (UC-W) were conducted at RUB. The UC-W were performed using a uniaxial compression apparatus manufactured by Wykeham Farrance Eng. Ltd., England. Figure 3.42a provides an illustration of the device used for these tests,

which were performed on cylindrical soil samples measuring 5 cm in diameter and 10 cm in height. The vertical load applied to the samples was measured via a load cell attached to the horizontal beam of the loading frame, while the vertical displacement was monitored using an external LVDT. The sample was placed on the device's bottom platen, which moved vertically to apply compressive force to the specimen. The displacement velocity of the bottom platen was controlled by selecting the appropriate gear position, following the manufacturer's guidelines.

The procedure for preparing samples along the wetting path was described in Section 3.2.4. After being wetted to the target water content, corresponding to the desired suction level, the samples were sealed in plastic bags and stored in enclosed containers for 4 days prior to testing.

Before placing the sample on the lower platen, its weight and dimensions were carefully measured. Once positioned on the platen, a leveling tool was used to ensure the sample was vertically aligned. Following this, the top cap was placed on the sample, and the bottom platen was slowly raised until the top cap made contact with the load cell, as indicated by a positive reading of vertical load from the load cell. To minimize moisture loss during the test, the sample was covered with a plastic foil, as shown in Figure 3.42b. The sample was then subjected to axial compression at a rate of 0.06 mm/min. During testing, the vertical load and displacement were continuously recorded. The compression process continued until the sample reached failure. After the test, the sample was immediately removed from the device and sectioned to measure its water content and suction, using an AquaLab chilled mirror hygrometer.

A total of 8 groups of samples were prepared, each with varying water contents of 0.6%, 6%, 10%, 12%, 18%, 24%, 30%, and 33%. For each group, a minimum of three identical samples were tested to ensure repeatability and accuracy of the results.

3.3.7. Techniques, procedures, and experimental program for uniaxial tensile tests

As outlined in Section 3.2.4, a series of uniaxial tensile tests (UTT) was conducted on samples subjected to both the drying path (UT-D) and the wetting path (UT-W). These tests were performed by Yukang Wang at HSKL. Detailed information regarding the testing apparatus and procedures can be found in Yukang Wang's PhD thesis.

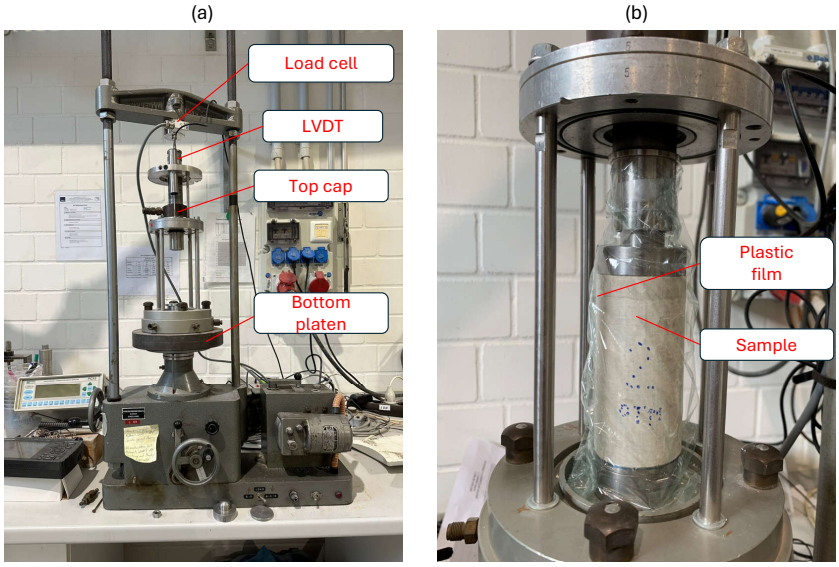

Figure 3.42.: Unconfined compression tests on samples along the wetting path: (a) used device, and (b) sample during the test covered by a plastic foil to prevent drying

In this study, the experimental setup developed by Heibrock (1996) and Heibrock et al. (2005) was adapted to investigate the variation in tensile strength of unsaturated soil samples under different water contents. Figure 3.11f illustrates the direct tensile samples, which measured 24 mm in diameter and 78 mm in height. The samples were suspended in a universal testing machine manufactured by Zwick Roell Group. This testing machine consists of two components: the upper part remains stationary, while the lower part moves vertically. The Digital Image Correlation (DIC) technology was employed to record both vertical and horizontal displacements, enabling precise strain calculations. A load cell with a 2 kN capacity was used to measure the vertical load. The entire system, including the testing apparatus and the control units, was connected to a computer running VIC-3D software for data acquisition and analysis. Figure 3.43 shows a scheme of the UTT sample. To ensure that the maximum tensile stress was concentrated in the middle of the sample, a borehole, measuring 8 mm in diameter and 24 mm in height, was drilled along the sample's longitudinal axis. A filter textile was placed at the center of the sample, and the remaining portion of the boreholes was filled with epoxy resin. Two threaded rods were inserted into the borehole. The alignment of the borehole, rods, and the central axis of the cylindrical sample was carefully ensured using a boring slide and mounting frame for drilling and placement, while a line laser was employed to visually verify axial alignment. This hollow-cylinder configuration was chosen to maximize the likelihood of achieving uniaxial stress conditions.

The samples were subjected to tensile forces applied at a constant extension rate of 0.06 mm/min until failure occurred. Similar to the UCT along the drying path, the testing environment was controlled using an acrylic enclosure equipped with a humidifier to regulate relative humidity (RH) and temperature. In total, 24 tests were conducted on unsaturated samples along the drying path (DT-D) with varying water content, while 17 tests were performed on unsaturated samples along the wetting path (DT-W) under different water content conditions.

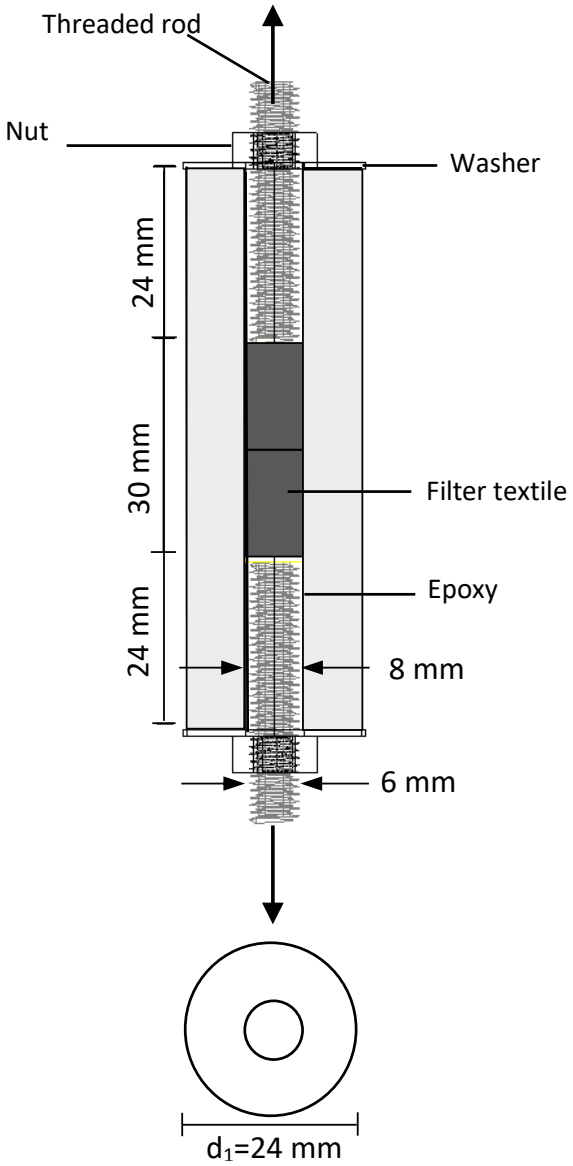

Figure 3.43.: Uniaxial tensile sample

3.3.8. Techniques, procedures, and experimental program for triaxial compression tests

A series of triaxial compression tests (consolidated-drained condition) on saturated samples under net confining pressure of 50, 100, and 200 kPa was performed in this study to determine the shear strength parameters which will be used to derive the suction stress from unconfined compression tests and uniaxial tensile tests. Figure 3.44 shows the triaxial device used in this study. The sample size is 5 cm in diameter and 10 cm in height. With a back pressure of 300 kPa, a B-value of 0.98 was reached. The strain rate is 0.025 mm/min.

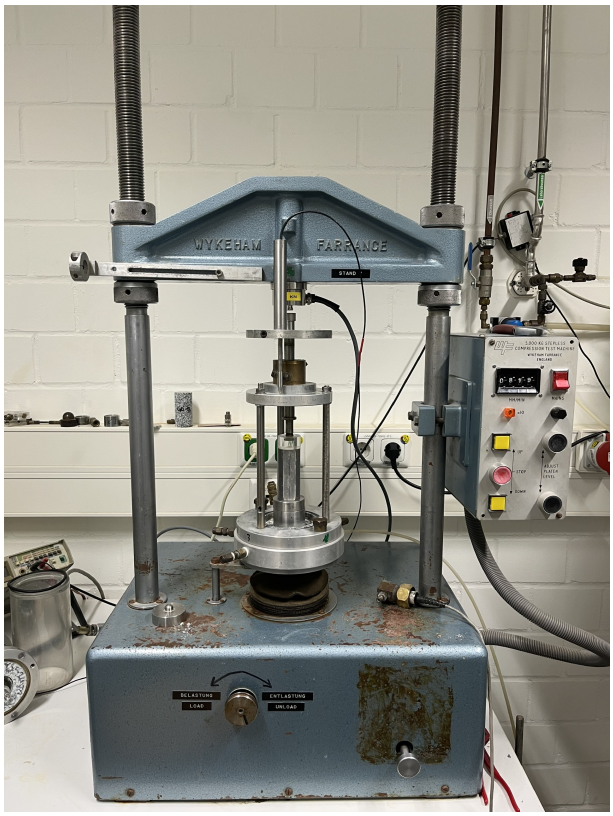

Figure 3.44.: Triaxial device used in this study

4. Experimental results

4.1. Introduction

The following chapter provides the experimental results derived from the laboratory program described in Chapter 3. First, the measured soil-water characteristic curves (SWCC) are presented (Section 4.2), which show the relationship between water content and suction along the drying and wetting path. From the results of shrinkage tests the soil shrinkage curve (SSC) is derived (Section 4.3). The SSC is used to express the SWCC as a relationship between the degree of saturation and suction (see Chapter 5). In addition, the results of the PSD determination are given in Section 4.4.

On the other hand, the experimental results obtained from the systematic experimental program including different element tests, i.e. biaxial compression tests, direct shear tests, unconfined compression tests, and uniaxial tensile tests, which was outlined in Chapter 3, are presented in this chapter (from Section 4.5 to Section 4.8). The experimental results will be further discussed and analysed in Chapter 5.

4.2. Soil-water characteristic curves

4.2.1. Experimental results

The SWCC was determined along both drying and wetting paths. Figure 4.1 presents the SWCC, with gravimetric water content plotted against suction. The SWCC generally reveals three distinct zones:

- Zone I: This zone indicated by AB in the drying path corresponds to suction values between 0 and approximately 150 kPa, with a slight decrease in water content from 35% to about 32%. In the wetting path, marked by A'B', this zone spans suction values from 200 kPa to about 0 kPa, with the corresponding water content increasing from 28% to 34%.

- Zone II: This transitional zone, indicated by BC in the drying path, spans a suction range from 150 kPa to 15 MPa. Here, the water content significantly reduces from approximately 32% to 3.2%. In the wetting path, marked by B'C', this zone spans suction values from 10 MPa to approximately 200 kPa, with water content increasing from 4% to around 28%.
- Zone III: This final zone, indicated by CD in the drying path, corresponds to suction values between 15 MPa and 300 MPa, with a gradual reduction in water content from around 3.2% to 0.1%. In the wetting path, indicated by C'D', suction values range from 173.4 MPa to approximately 10 MPa, with water content rising from 0.6% to around 4%.

Furthermore, the results indicate slight hysteresis between the drying and wetting paths.

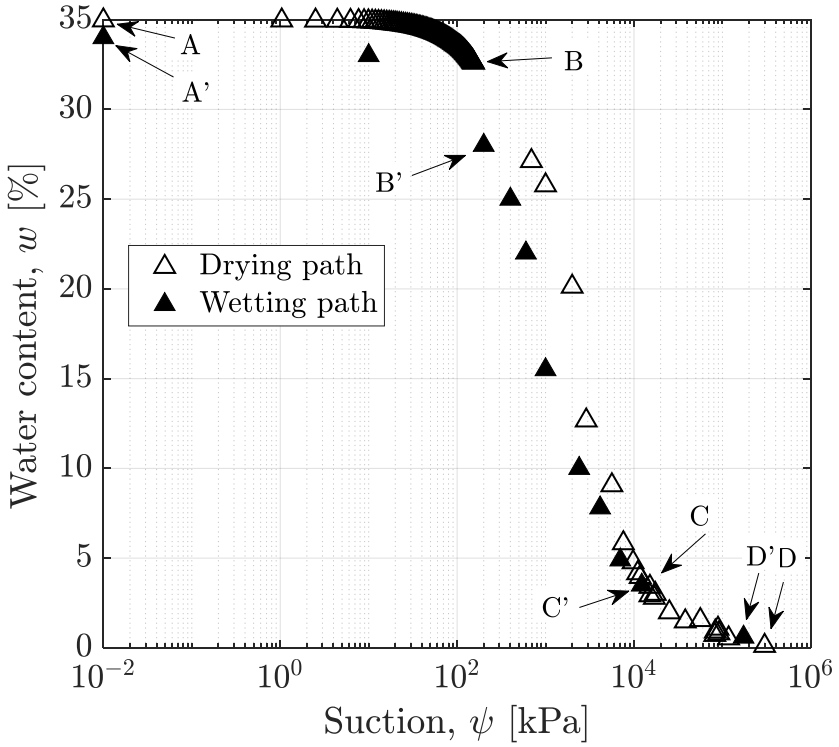

Figure 4.1.: Soil-water characteristic curves along the drying path (provided by the partner laboratory at HSKL) and the wetting path

4.2.2. Modelling the SWCC

In this section, the measured SWCC data were analyzed using several well-established models. A comprehensive description of these SWCC models can be found in the State-

of-the-art chapter. This analysis is presented here because in subsequent unconfined compression tests and uniaxial tensile tests, where suction was not directly controlled, the fitted SWCC will be used to estimate the corresponding suction values based on the measured water content. Curve fitting was performed using the Solver add-on in Microsoft Excel and re-checked by using the HYPROP-FIT software (Version 4.2.2.0), developed by METER Group in collaboration with Prof. Uwe Schindler, Prof. Wolfgang Durner, and Dr. Andre Peters.

The models of Van Genuchten (1980), Fredlund & Xing (1994) and Durner (1994) were fitted to the measured data to identify the best-fit curve, which minimizes the sum of squared deviations between the observed water content values and those predicted by the regression equation. This optimization process, commonly referred to as the least squares method, ensures an accurate representation of the observed data. To assess the quality of the fit, the coefficient of determination (R^2) was calculated. An R^2 value of 1 indicates perfect agreement between observed and predicted values, with no error. Thus, R^2 values approaching 1 signify a high-quality fit. The fitting was done separately for the drying and the wetting path. The fitting parameters obtained for the SWCC description by the three employed models are summarized in Table 4.1, along with the corresponding R^2 values.

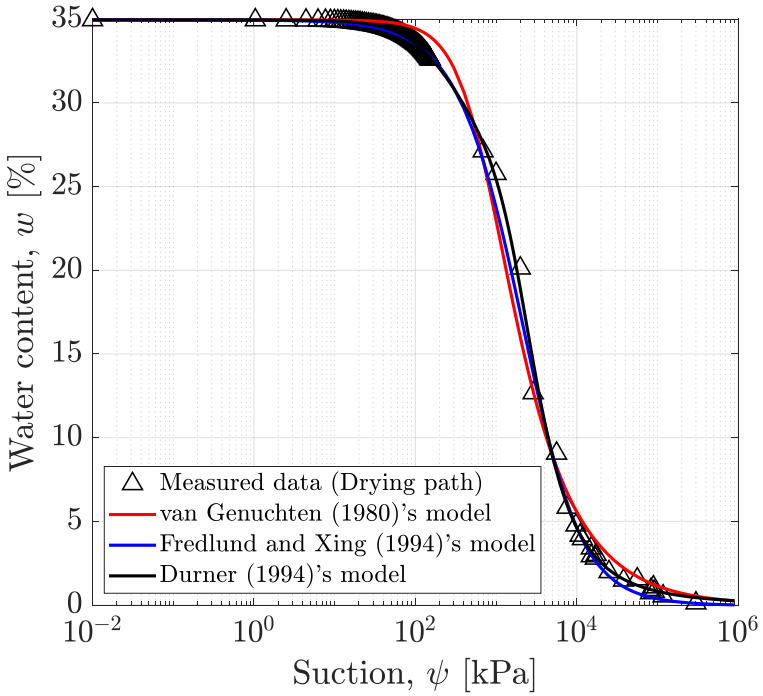

Figure 4.2.: Measured SWCC data along the drying path and best fit models

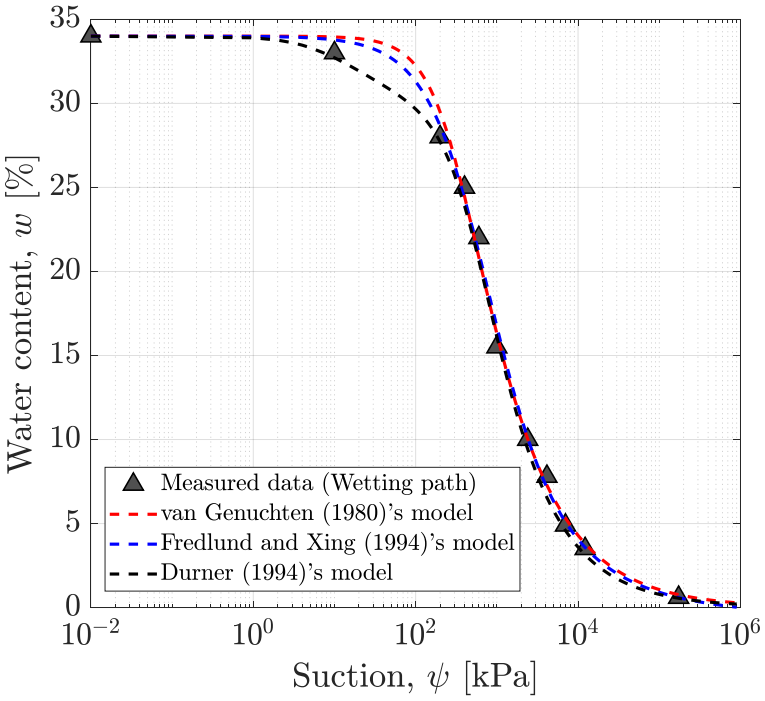

Figure 4.3.: Measured SWCC data along the wetting path and best fit models

Figure 4.2 displays the measured SWCC data along the drying path, along with the respective best-fit curves. Similarly, Figure 4.3 presents the measured SWCC data along the wetting path, along with the corresponding best-fit curves.

In general, the selected SWCC models show an excellent fit to the measured SWCC data, demonstrating the models' effectiveness in capturing the soil's water retention behaviour during both drying and wetting processes. The best fit of the measured SWCC with Durner (1994)'s model will be used for estimating the corresponding suction values based on the measured water content from the unconfined compression tests and uniaxial tensile tests.

4.3. Soil shrinkage curve

The measured data from the shrinkage test conducted at HSKL on a sample with a diameter of 2.4 cm and a height of 8 cm are presented in terms of the relationship between water content and time (Figure 4.4a) and between void ratio and time (Figure 4.4b).

Overall, the water content of the sample decreases significantly from the start of the test until approximately 75 hours, after which it stabilizes at around 2% for the remaining time

Table 4.1.: Fitting parameters derived from the application of SWCC models including van Genuchten (vG) (1980), Fredlund and Xing (FX) (1994), and Durner (1994) to the measured SWCC data

Model	Parameter	SWCC		R^2	
		Drying path	Wetting path	Drying path	Wetting path
vG (1980)	α (1/kPa)	0.0014	0.0031	0.9947	0.9951
	n (-)	1.692	1.631		
	w_{sat} (%)	35	34		
	w_{res} (%)	0	0		
FX (1994)	α (1/kPa)	0.0004	0.0018	0.9989	0.9971
	n (-)	1.014	1.126		
	ψ_{res} (kPa)	15000	6000		
	w_{sat} (%)	35	34		
	m (-)	2.908	1.582		
Durner (1994)	α_1 (1/kPa)	0.00051	0.0020	0.9995	0.9980
	n_1 (-)	2.2988	1.7264		
	w_{res} (%)	0	0		
	w_{sat} (%)	35	34		
	α_2 (1/kPa)	0.0057	0.1334		
	n_2 (-)	1.4618	1.3600		
	w_1 (-)	0.6329	0.8250		

of the experiment. In contrast, the void ratio exhibits a sharp initial decrease, reaching a minimum at around 25 hours, followed by a slight increase between 25 and 60 hours. After 60 hours, the void ratio remains nearly constant until the end of the test.

Figure 4.5 shows the SSC in terms of void ratio versus water content. The void ratio decreases linearly as water content declines from 33% to 27%, followed by a more gradual decrease as the water content further drops from 27% to about 19%. As the water content decrease from 19% to about 10%, the void ratio relatively stablizes at 0.76. When the water content reduces from 10% to around 2.5%, the void ratio slightly increases again, reaching 0.773. Interestingly, as the water content decreases further to 1.79%, the void ratio shows a slight reduction to 0.770.

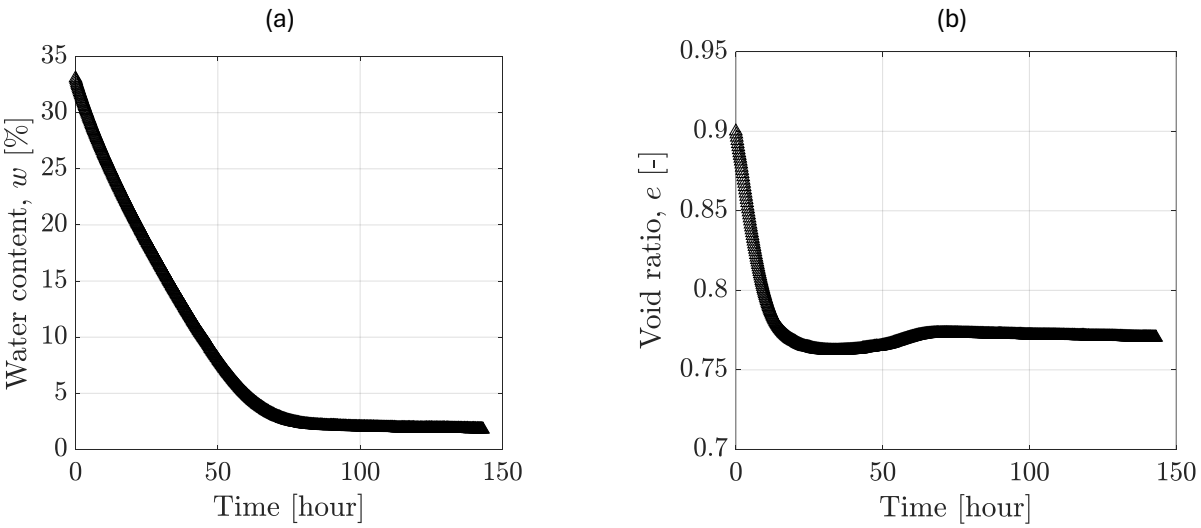

Figure 4.4.: Measured data from the test: (a) water content versus time, and (b) void ratio versus time

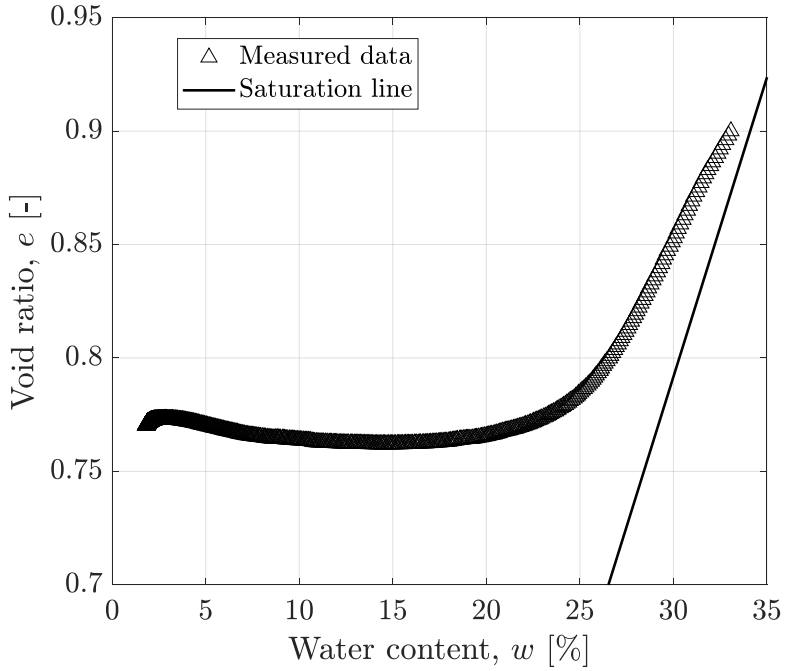

Figure 4.5.: Soil shrinkage curve (data provided by the partner laboratory at HSKL)

4.4. Pore size distribution along drying and wetting path

Figure 4.6 presents the PSD of samples along the drying path in terms of cumulative pore volume (CPV). Samples 1 through 5 were air-dried from a fully saturated state (initial water content $w = 35\%$), while the sample at optimum water content was obtained directly after compaction. Generally, the sample at optimum water content exhibits the highest CPV. As dewatering progresses along the drying path, the maximum CPV decreases (from approximately 350 mm^3/g for sample 1 to around 320 mm^3/g for Sample 4) before stabilizing, as observed in Samples 4 and 5.

The PSD for samples along the wetting path is presented in Figure 4.7. As the sample is wetted from $w = 1.4\%$ (Sample 5) to $w = 32.3\%$ (Sample 9), the maximum CPV increases (from around 320 mm^3/g for Sample 5 to approximately 350 mm^3/g for Sample 9).

Figures 4.8 to 4.12 illustrate the density functions of the PSD in terms of differential pore volume for samples at optimum water content and those following the drying path (Sample 1 to Sample 5). Figure 4.8 shows that the Sample at optimum water content and Sample 1 exhibit a nearly unimodal PSD, with peak pore sizes of about 300 nm. Similarly, Sample 2 ($w = 28.9\%$) shows an unimodal PSD (Fig. 4.9). With further dewatering (Figs. 4.10, 4.11, and 4.12), the PSD changes from unimodal (Sample 2) to distinctively bimodal in samples 3, 4, and 5, with two prominent peak pore sizes.

Figures 4.13 to 4.16 present the PSD density functions for samples along the wetting path (Sample 5 to Sample 9). In Fig. 4.13, with an increase in water content from 1.4% (Sample 5) to 11.3% (Sample 6), both samples show a bimodal PSD. The first peak remains relatively stable around a pore diameter of 300 nm on both samples, while the second peak shifts from 650 nm in sample 5 to 550 nm in Sample 6. Sample 7 exhibits a similar PSD to Sample 6 (Fig. 4.14). As water content continues to increase, the PSD gradually transitions from bimodal to unimodal, as shown in Figs. 4.15 and 4.16.

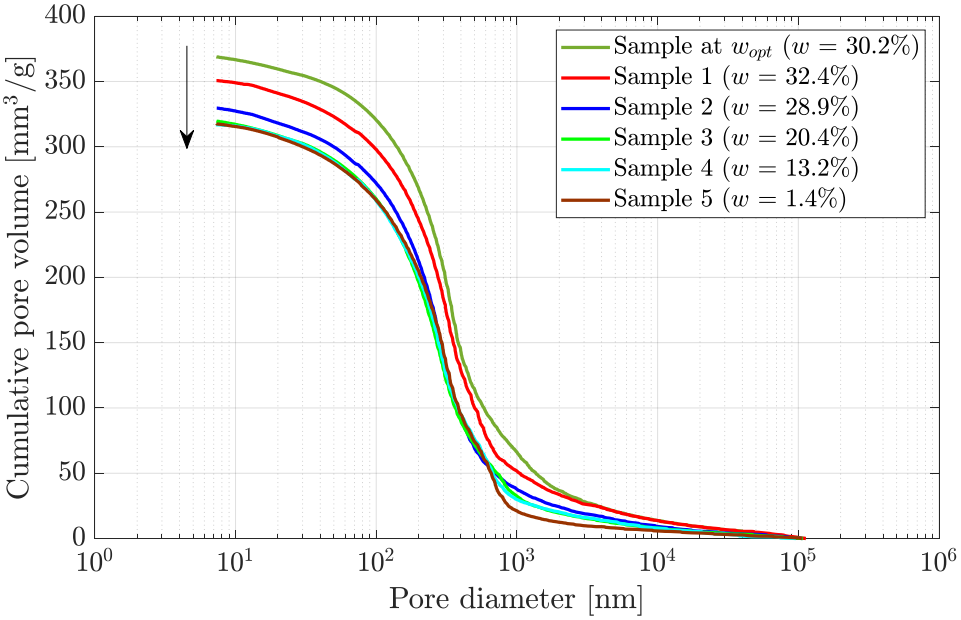

Figure 4.6.: Cumulative pore volume versus pore diameter of the compacted samples along the drying path

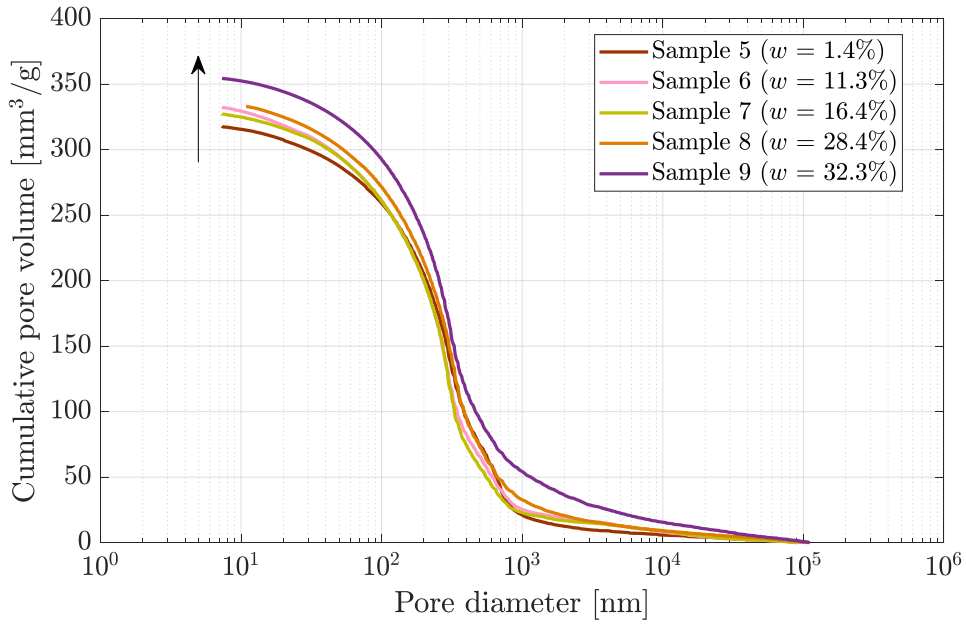

Figure 4.7.: Cumulative pore volume versus pore diameter of the compacted samples along the wetting path

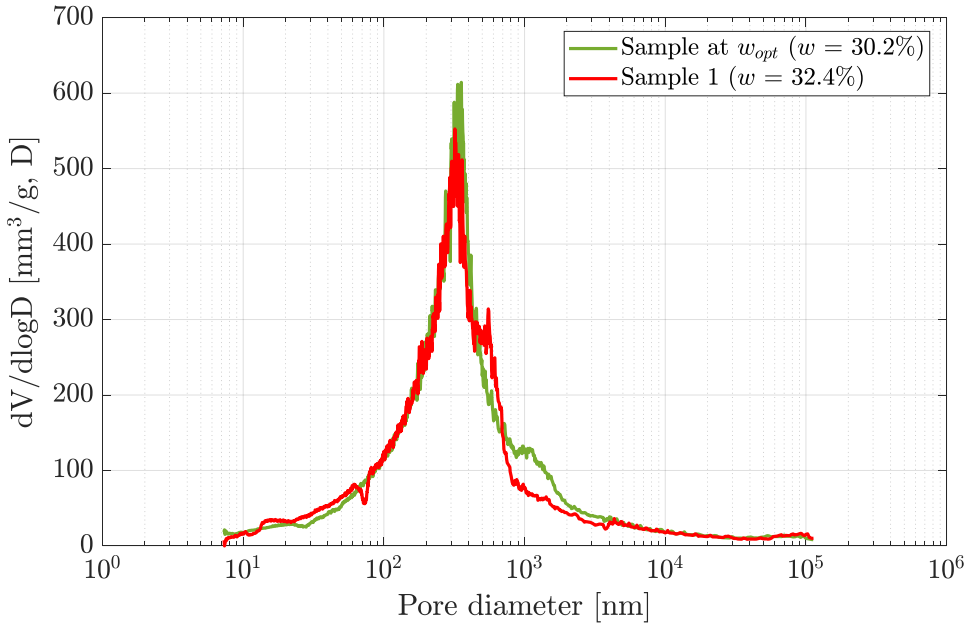

Figure 4.8.: Differential pore volume versus pore diameter of the compacted samples at w_{opt} = 30.2% and w = 32.4%

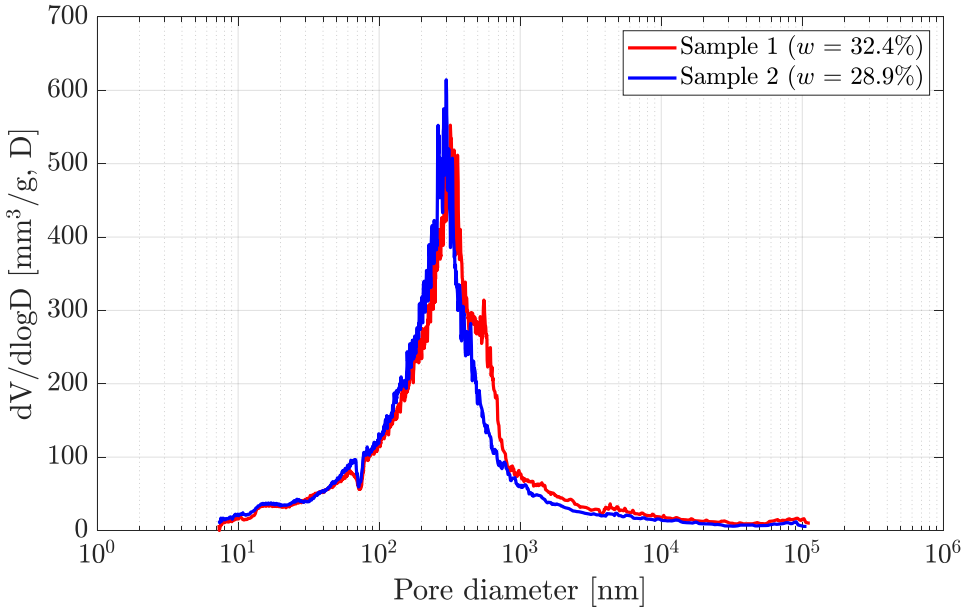

Figure 4.9.: Differential pore volume versus pore diameter of the compacted samples along the drying path at w = 32.4% and w = 28.9%

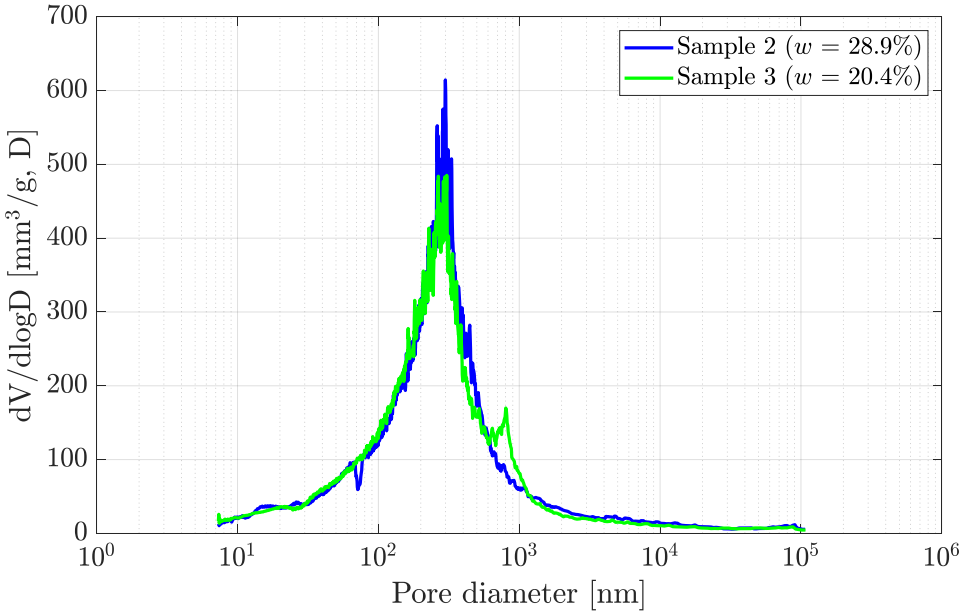

Figure 4.10.: Differential pore volume versus pore diameter of the compacted samples along the drying path at $w = 28.9\%$ and $w = 20.4\%$

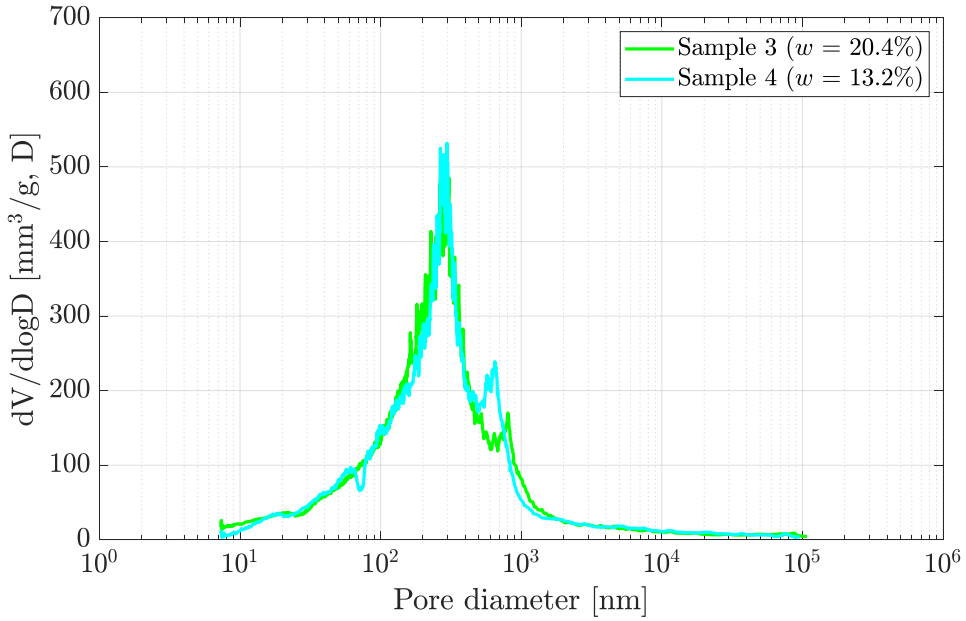

Figure 4.11.: Differential pore volume versus pore diameter of the compacted samples along the drying path at $w = 20.4\%$ and $w = 13.2\%$

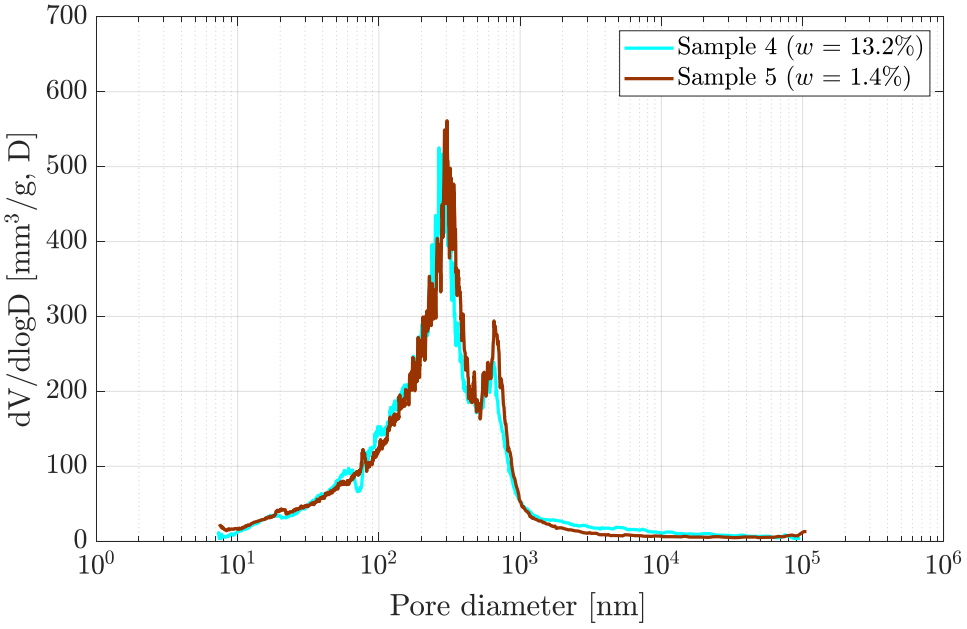

Figure 4.12.: Differential pore volume versus pore diameter of the compacted samples along the drying path at $w = 13.2\%$ and $w = 1.4\%$

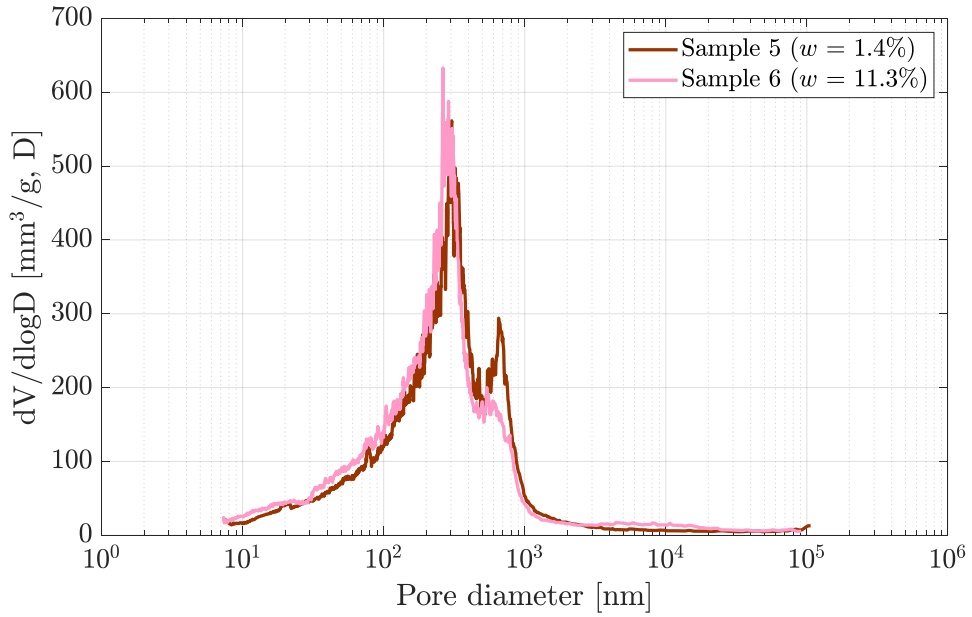

Figure 4.13.: Differential pore volume versus pore diameter of the compacted samples along the wetting path at $w = 1.4\%$ and $w = 11.3\%$

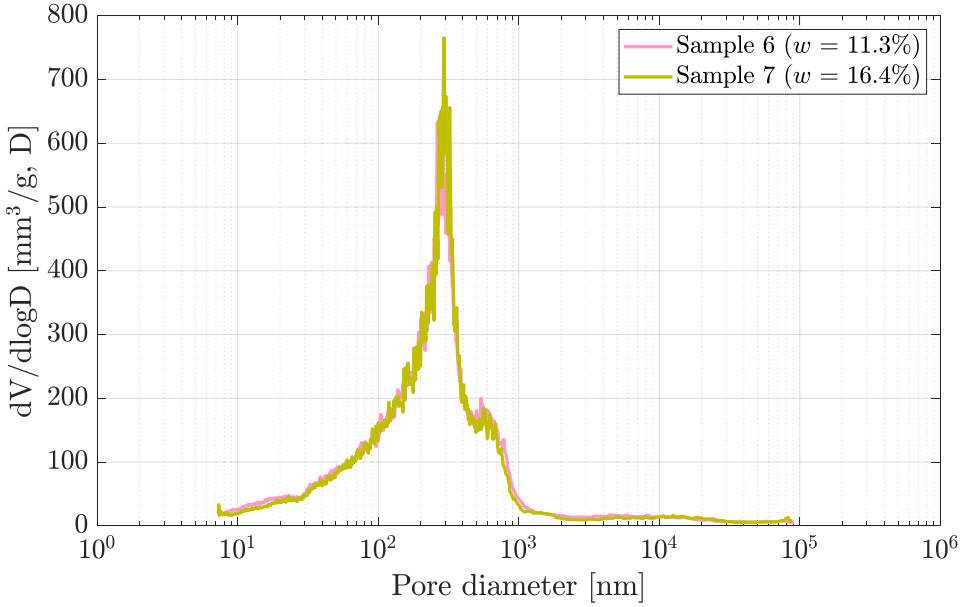

Figure 4.14.: Differential pore volume versus pore diameter of the compacted samples along the wetting path at $w = 11.3\%$ and $w = 16.4\%$

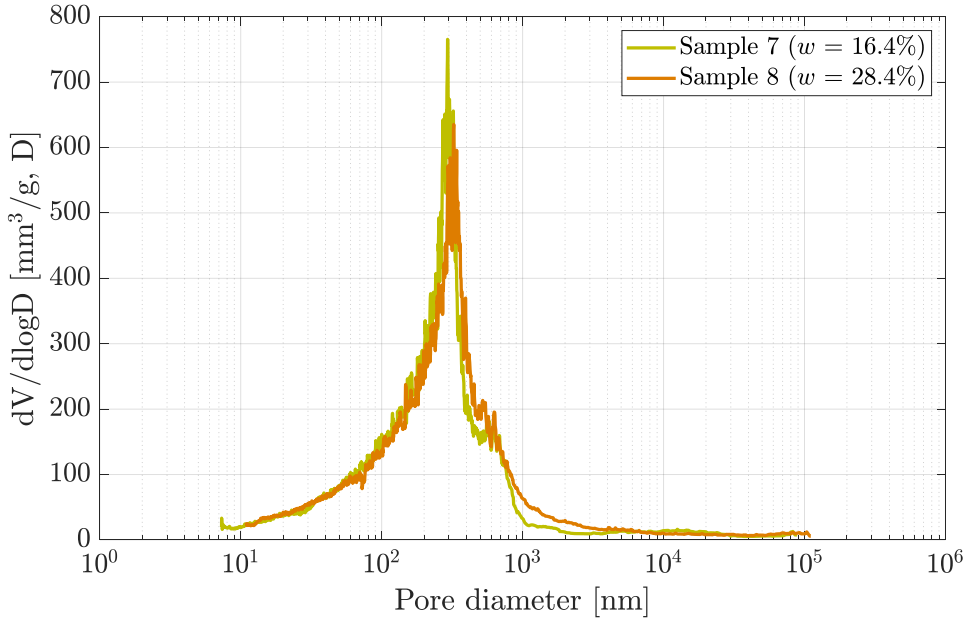

Figure 4.15.: Differential pore volume versus pore diameter of the compacted samples along the wetting path at $w = 16.4\%$ and $w = 28.4\%$

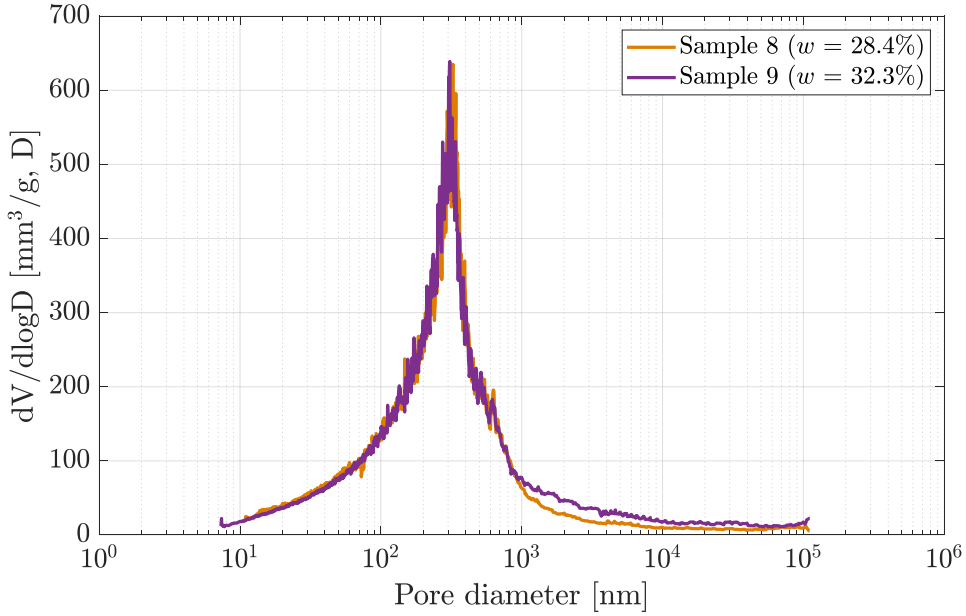

Figure 4.16.: Differential pore volume versus pore diameter of the compacted samples along the wetting path at $w = 28.4\%$ and $w = 32.3\%$

4.5. Biaxial tests

4.5.1. Definitions

For the biaxial compression tests (BCT) conducted on compacted samples under both saturated and unsaturated conditions, axial strain (ϵ_h) and volumetric strain (ϵ_v) are calculated using the following equations:

$$\epsilon_1 = \frac{\Delta h}{h_0} \tag{4.1}$$

$$\epsilon_v = \frac{\Delta V}{V_0} \tag{4.2}$$

Here, h_0 denotes the initial height of the sample, and Δh represents the change in height, as measured by the LVDT. The initial volume of the sample is represented by V_0, while ΔV indicates the change in volume. The deviator stress ($\Delta\sigma$) is calculated as the difference between the major and minor principal stresses.

For saturated condition:

$$\Delta\sigma = (\sigma_1 - u_w) - (\sigma_3 - u_w) \tag{4.3}$$

For unsaturated condition:

$$\Delta\sigma = (\sigma_1 - u_a) - (\sigma_3 - u_a) \tag{4.4}$$

At the failure state, the major principal stress attains its maximum value. Using a plotting technique derived from Mohr circles (Lambe 1964), the biaxial test results can be effectively represented in a $t - s$ diagram, with t and s defined as follows:

$$s = \frac{(\sigma_1 - u_a) + (\sigma_3 - u_a)}{2} \tag{4.5}$$

$$t = \frac{(\sigma_1 - u_a) - (\sigma_3 - u_a)}{2} \tag{4.6}$$

As outlined in Section 3.2.3, the biaxial test series was divided into two main groups: (*i*) vertically cut samples (B-VC), which were tested along both the drying path (B-VC-D) and the wetting path (B-VC-W), and (*ii*) horizontally cut samples, for which tests were conducted only along the drying path (B-HC-D). The experimental program for the biaxial test series was detailed in Section 3.3.4.3.

4.5.2. Vertically cut sample (B-VC)

4.5.2.1. Samples tested along the drying path (B-VC-D)

Figure 4.17 illustrates the relationship between deviator stress ($\Delta\sigma$) and axial strain (ϵ_1) (Fig. 4.17a) and between volumetric strain (ϵ_v) and axial strain (Fig. 4.17b) for tests conducted under a net confining pressure of σ_{net} = 50 kPa. Overall, the maximum deviator stress increases as suction rises, with failure occurring at progressively lower axial strains - decreasing from approximately 5% in saturated conditions to around 2.5% at ψ = 200 MPa. The increase in suction leads to a more pronounced brittle response in the stress-strain behaviour. As shown in Figure 4.17b, all samples exhibit initial contraction followed by dilation. With higher suction levels, the initial contraction phase becomes less pronounced, while dilation in the subsequent phase becomes more marked.

At higher net confining pressures, there is also a clear increase in maximum deviator stress and a notable transformation in the stress-strain curve profiles towards a more brittle behaviour with rising suction, as depicted in Figure 4.18a for σ_{net} = 100 kPa and Figure 4.19a for σ_{net} = 200 kPa. In the volumetric strain versus axial strain relationship, similar

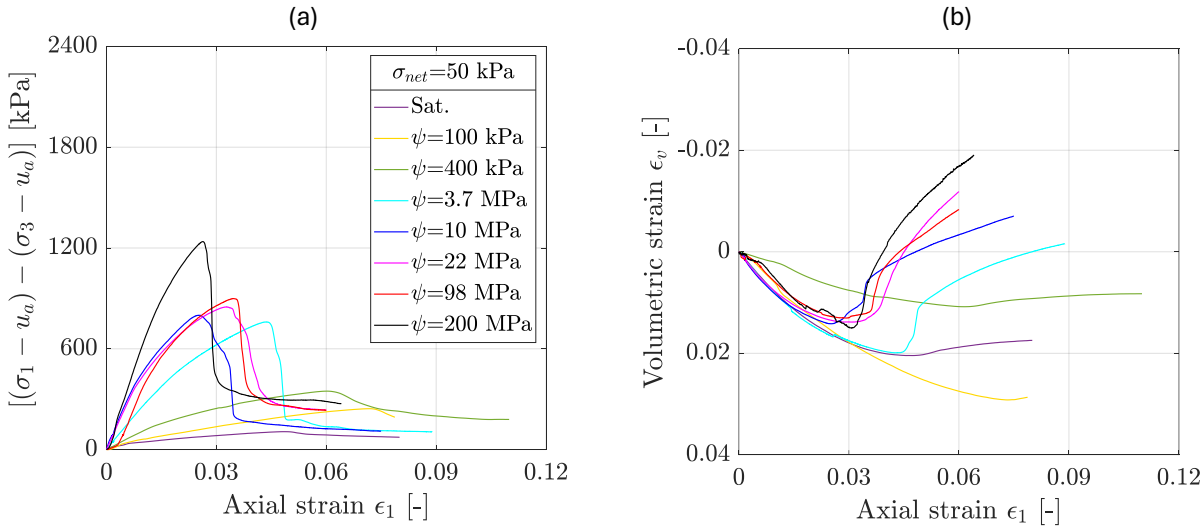

Figure 4.17.: Biaxial test results from series B-VC-D under σ_{net} = 50 kPa: (a) deviator stress versus axial strain, and (b) volumetric strain versus axial strain

to the case of σ_{net} = 50 kPa, all samples generally display initial contraction followed by dilation, as shown in Figure 4.18b for σ_{net} = 100 kPa and Figure 4.19b for σ_{net} = 200 kPa. Increased suction levels again result in a less pronounced initial contraction phase and an enhanced dilation phase.

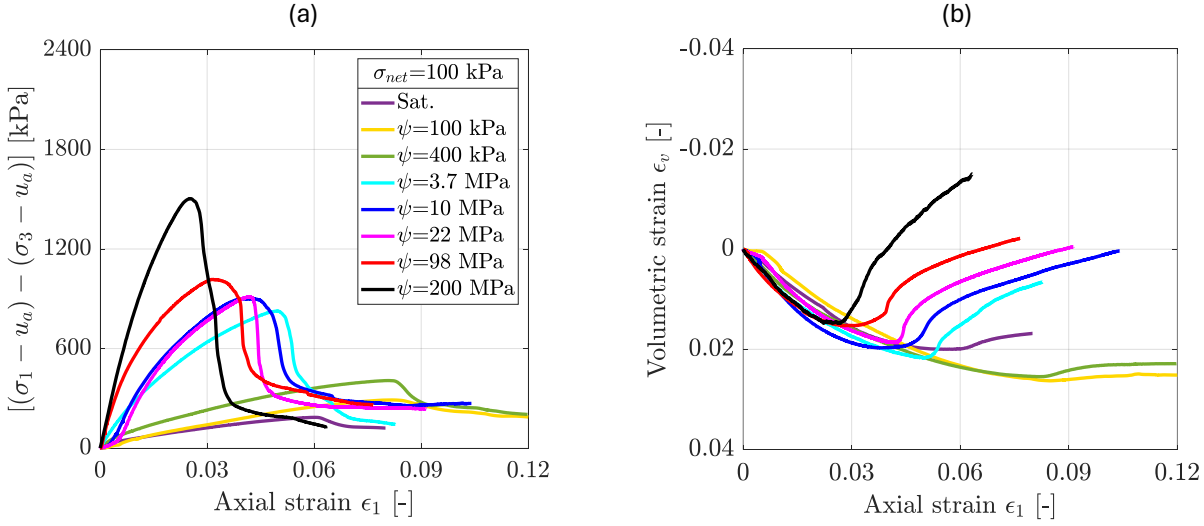

Figure 4.18.: Biaxial test results from series B-VC-D under σ_{net} = 100 kPa: (a) deviator stress versus axial strain, and (b) volumetric strain versus axial strain

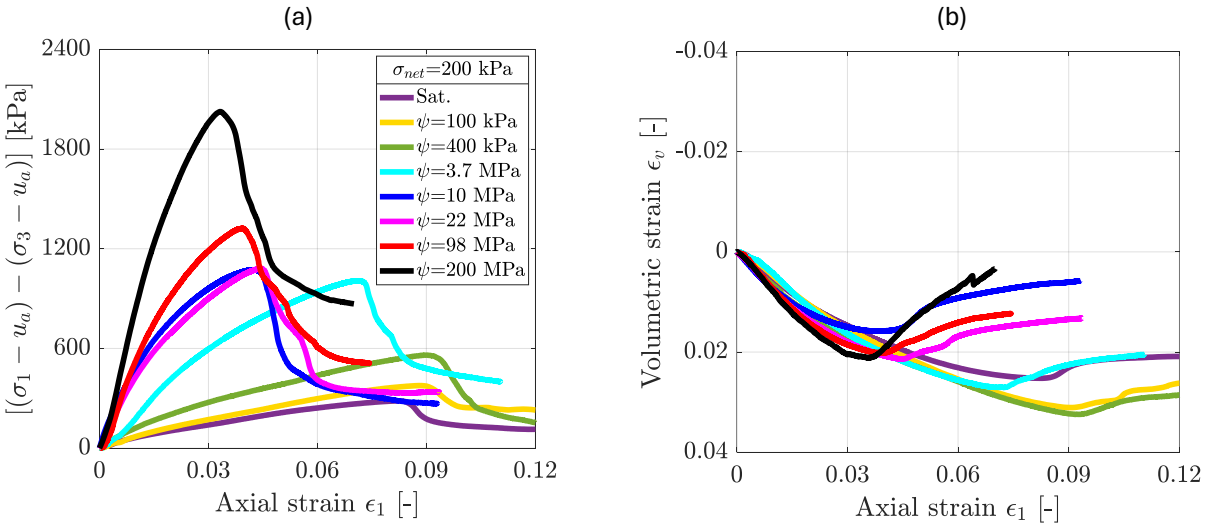

Figure 4.19.: Biaxial test results from series B-VC-D under σ_{net} = 200 kPa: (a) deviator stress versus axial strain, and (b) volumetric strain versus axial strain

Figure 4.20a presents a comparison of stress-strain curves across three representative suction levels under three distinct net confining pressures, highlighting the influence of confining pressure at each suction level. As shown, the maximum deviator stress increases with higher net confining pressures. Moreover, at a given suction level, an increase in net confining pressure corresponds to a stress-strain response that shows reduced brittleness. Figure 4.20b compares the volumetric strain-axial strain relationships at three representative suction levels under different net confining pressures. Overall, the results indicate that dilation becomes less pronounced with increasing net confining pressure.

The biaxial test results are presented in the *t-s* space in Figure 4.21a. For each series of tests performed at a specific suction but under varying confining pressures, the evaluated failure condition produces a set of three stress points. Shear strength parameters - cohesion (c') and friction angle (φ') - were derived by fitting a straight line (the K_f line) through each set, relating it to the failure tangent line in the Mohr circle analysis, following methods outlined by Lambe (1964), Head (2006), and Lade (2016). The relationship between the shear strength parameters and water content (corresponding to suction values) is shown in Figure 4.21b. Overall, the friction angle (indicated by square symbol) increase slightly from 21.5° to 28.5° as the water content decreases from approximately 35% to 5%, followed by a decrease to 26° as water content drops to 2.5%. However, when water content falls below 2.5%, the friction angle rises sharply, reaching a maximum value of 46°. Cohesion (indicated by triangle symbol) gradually increases from about 20 kPa to

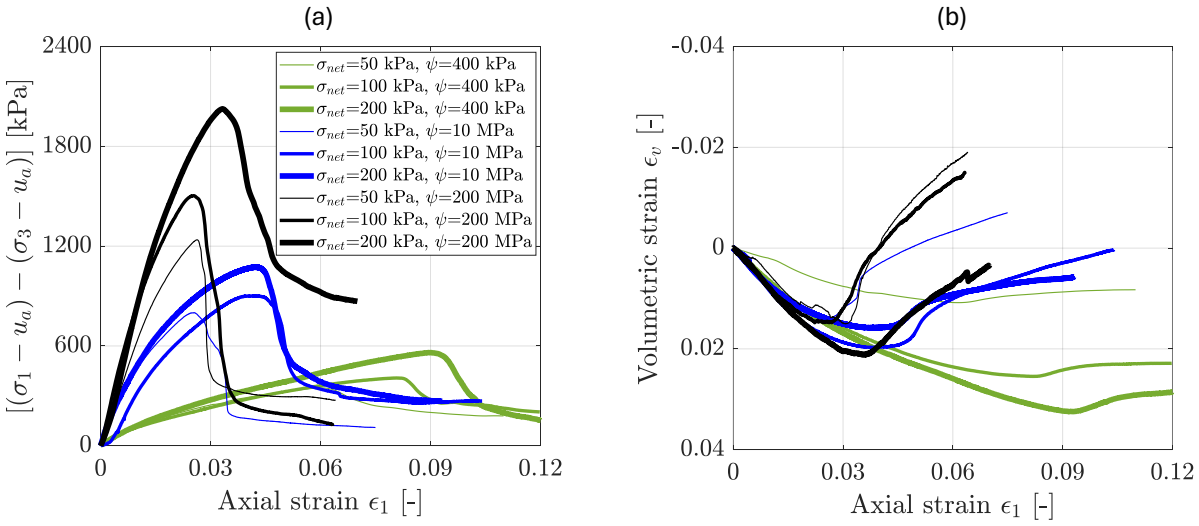

Figure 4.20.: Biaxial test results from series B-VC-D under σ_{net} = 50; 100; 200 kPa at typical suction values: (a) deviator stress versus axial strain, and (b) volumetric strain versus axial strain

about 250 kPa as water content decreases from around 35% to 2.5%, after which it declines to about 200 kPa as water content continues to drop. Notably, friction angle shows a significant change with suction, particularly at high suction values of 98 MPa and 200 MPa. This trend is consistent with findings by Futai & Almeida (2005) in natural soil and Alsherif & McCartney (2014) in compacted silt.

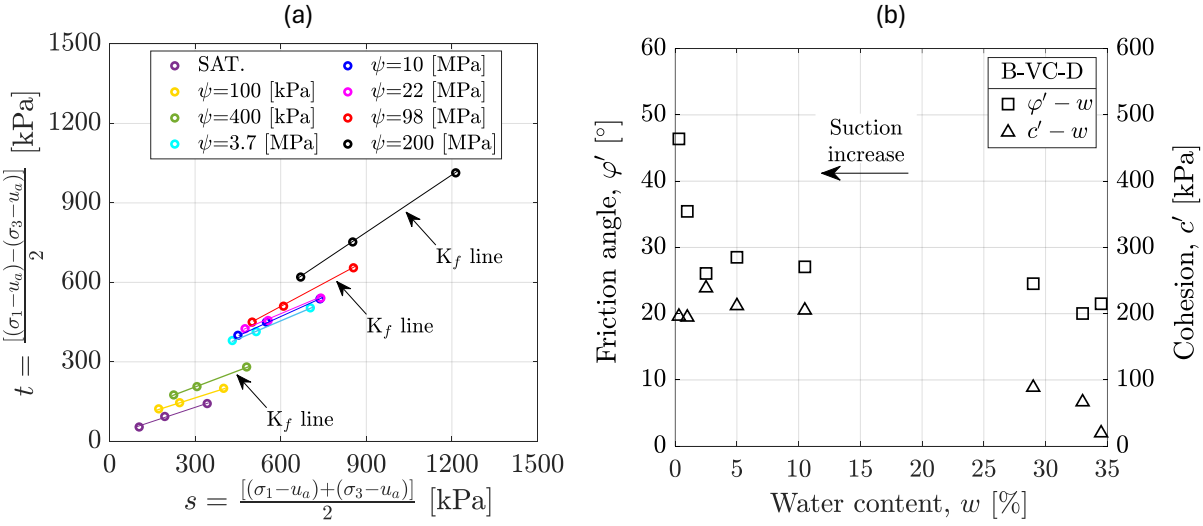

Figure 4.21.: Biaxial test results from series B-VC-D: (a) $t - s$ diagram, and (b) friction angle vs. water content and cohesion vs. water content

Figure 4.22 illustrates the relationship between the maximum value of t reached in the individual tests and water content (Fig. 4.22a) and between the maximum value of t and suction (Fig. 4.22b) under the three tested net confining pressures. As water content decreases from approximately 35% to around 10% (corresponding to a suction increase from $\psi = 0$ kPa to $\psi = 3.7$ MPa), t increases gradually. In the subsequent range, as water content reduces from about 10% to 2.5% (or suction rises from $\psi = 3.7$ MPa to $\psi = 98$ MPa), the increase in t is minimal. However, when water content drops below 2.5% (with suction further increasing from $\psi = 98$ MPa to $\psi = 200$ MPa), there is a pronounced increase in t.

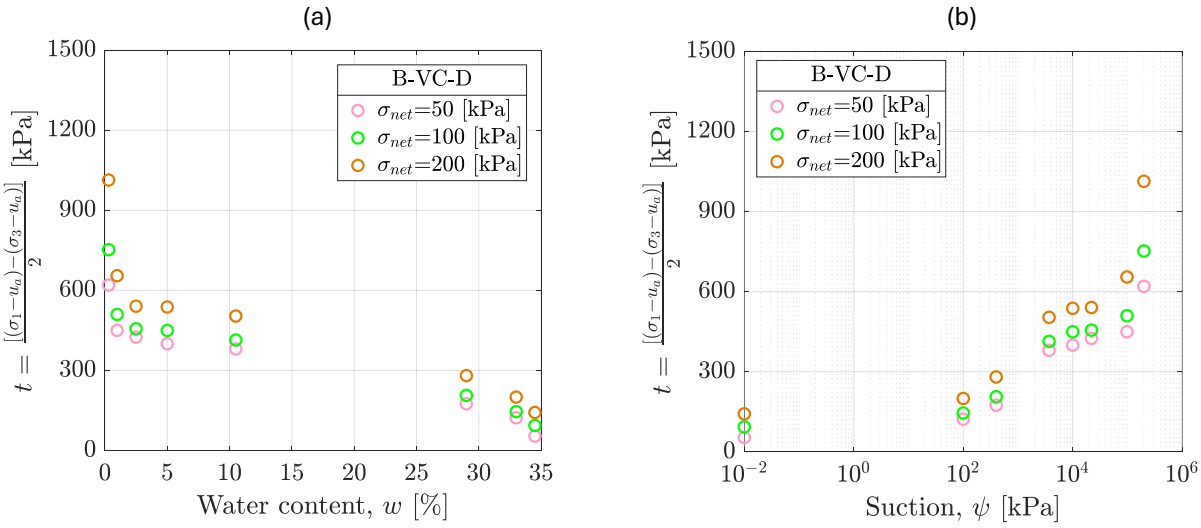

Figure 4.22.: Biaxial test results from series B-VC-D: (a) maximum t vs. water content, and (b) maximum t vs. suction

4.5.2.2. Samples tested along the wetting path (B-VC-W)

Figure 4.23 presents the relationship between deviator stress ($\Delta\sigma$) and axial strain (ϵ_1) (Fig. 4.23a), and between volumetric strain (ϵ_v) and axial strain (Fig. 4.23b) for tests conducted at net confining pressures of $\sigma_{net} = 50$ kPa, 100 kPa, and 200 kPa. In general, maximum deviator stress decreases both with lower suction and lower net confining pressure. Decreased suction leads to a more ductile response in the stress-strain behaviour. As observed in Fig. 4.23b, samples initially show contraction followed by dilation, with lower suction levels resulting in a more pronounced contraction phase and a less marked dilation phase.

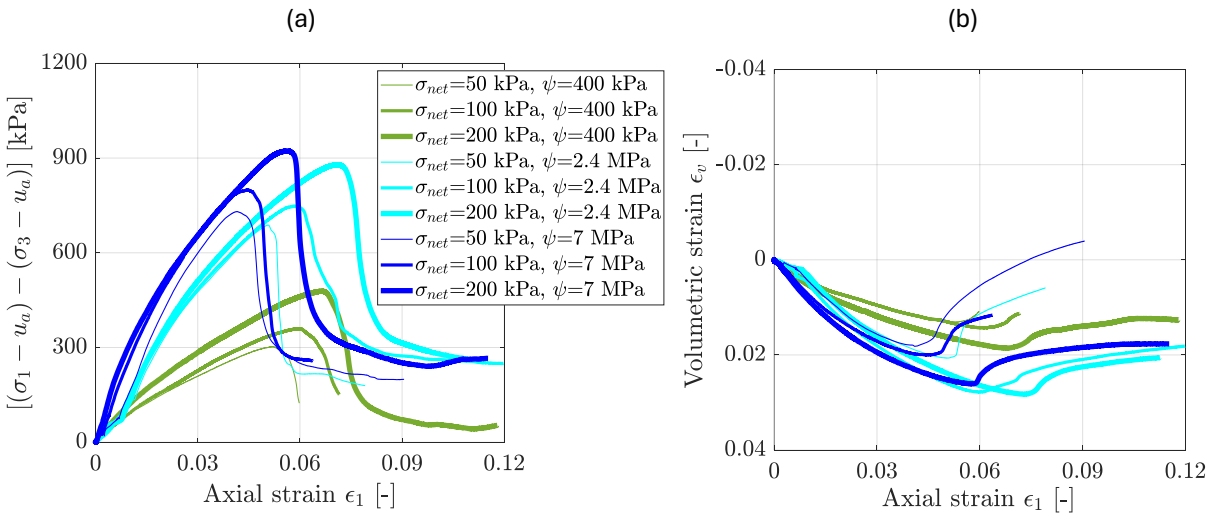

Figure 4.23.: Biaxial test results from series B-VC-W under σ_{net} = 50; 100; 200 kPa at three suction values: (a) deviator stress versus axial strain, and (b) volumetric strain versus axial strain

Figure 4.24a shows the biaxial test results plotted in the t-s space. For each series of tests conducted at a specific suction but different confining pressures, the evaluated failure conditions yield three stress points. Shear strength parameters - cohesion (c') and friction angle (φ') - were determined by fitting a straight line (K_f line) through each set, in relation to the failure tangent line from the Mohr circle analysis. The variation of these parameters with water content, corresponding to different suction levels, is depicted in Figure 4.24b. Generally, the friction angle (indicated by black solid square symbol) remains steady at approximately 22°, while cohesion (indicated by black solid triangle symbol) decreases gradually from about 210 kPa to about 90 kPa as water content rises from around 5% to 25%.

Figure 4.25 illustrates the relationships between maximum t and water content (Fig. 4.25a) and maximum t and suction (Fig. 4.25b) under the three net confining pressures. As water content increases from approximately 5% to 10% (corresponding to a reduction in suction from ψ = 7.0 MPa to ψ = 2.4 MPa), t decreases slightly. In the subsequent range, with water content rising from 10% to 25% (or suction decreasing from ψ = 2.4 MPa to ψ = 400 kPa), the reduction in t becomes more pronounced.

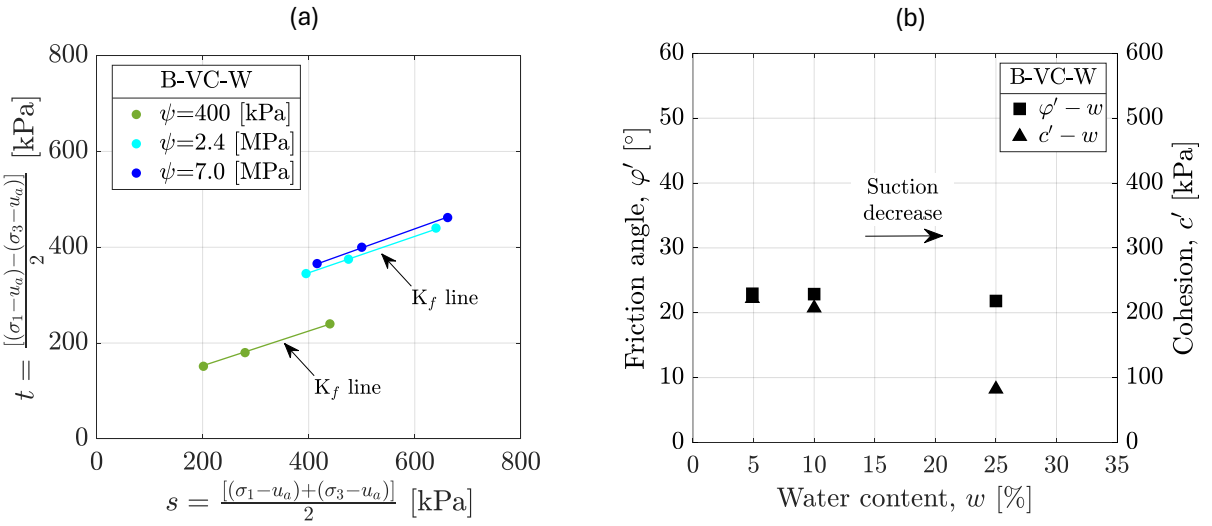

Figure 4.24.: Biaxial test results from series B-VC-W: (a) $t - s$ diagram, and (b) friction angle vs. water content and cohesion vs. water content

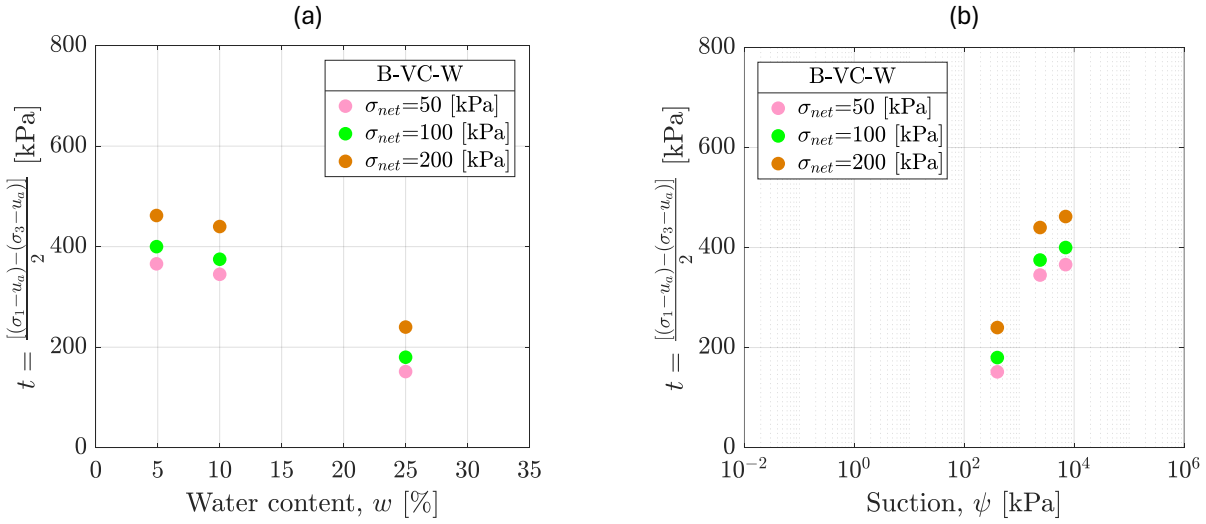

Figure 4.25.: Biaxial test results from series B-VC-W: (a) maximum t vs. water content, and (b) maximum t vs. suction

4.5.3. Horizontally cut sample (B-HC)

Figure 4.26 presents the relationships between deviator stress ($\Delta\sigma$) and axial strain (ϵ_1) (Fig. 4.26a), and between volumetric strain (ϵ_v) and axial strain (Fig. 4.26b) for the tests on horizontally cut samples conducted under net confining pressures of σ_{net} = 50 kPa, 100 kPa, and 200 kPa. Generally, maximum deviator stress increases with both

higher suction and greater net confining pressure. For a given suction level, higher net confining pressure is associated with a less brittle behaviour and an increase in axial strain at failure. As shown in Figure 4.26b, samples initially exhibit contraction followed by dilation. Notably, greater net confining pressure intensifies the contraction phase while diminishing the extent of dilation. In addition, the results indicate that dilation becomes more pronounced with increasing suction.

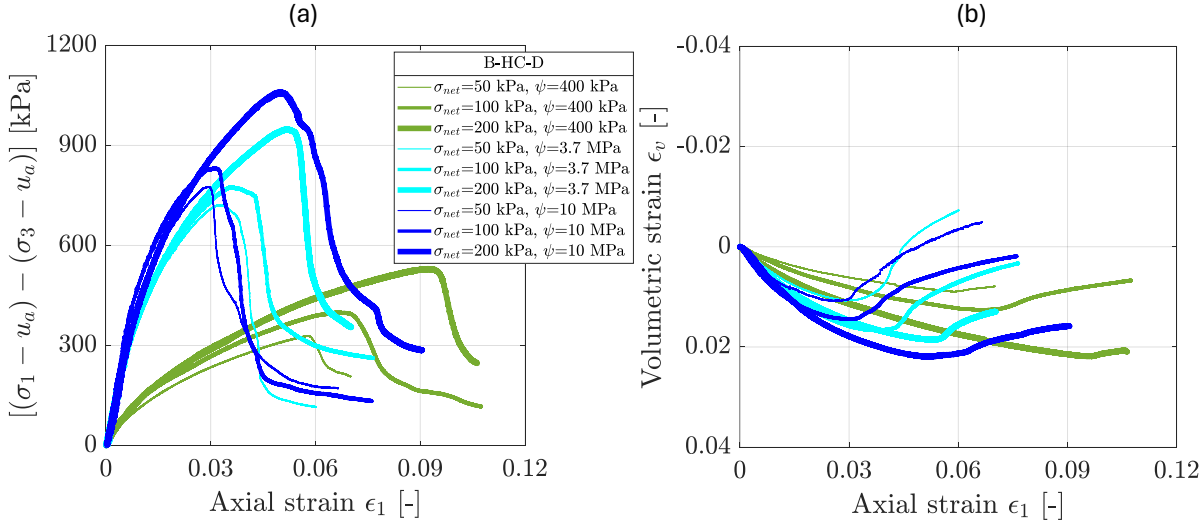

Figure 4.26.: Biaxial test results from series B-HC-D under σ_{net} = 50; 100; 200 kPa at three suction values: (a) deviator stress versus axial strain, and (b) volumetric strain versus axial strain

Figure 4.27a presents the biaxial test results in the *t*-*s* space. For each series of tests at a constant suction but varying confining pressures, the failure conditions yield three stress points. Shear strength parameters - cohesion (c') and friction angle (φ') - were obtained by fitting a straight line (K_f line) through each set, aligning with the failure tangent line in the Mohr circle analysis. The variation of these parameters with water content, reflecting different suction levels, is shown in Fig. 4.27b. The friction angle (denoted by red squares) generally rises from approximately 23° to 26° as water content decreases from 29% to 10%, followed by a further increase to 30° as water content drops to around 5%. Cohesion (represented by red triangles) gradually increases from about 90 kPa to 200 kPa as water content reduces from 29% to 10%, then shows a slight decrease to about 195 kPa as water content falls below 10%.

Figure 4.28 shows the relationships between t and water content (Fig. 4.28a) as well as t and suction (Fig. 4.28b) across the three net confining pressures. As the water content

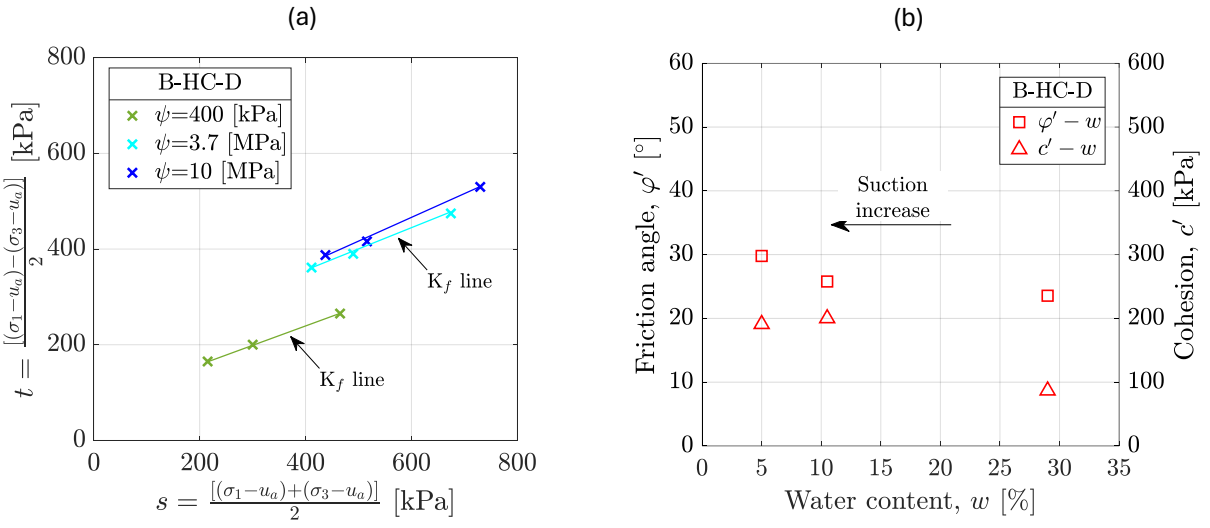

Figure 4.27.: Biaxial test results from series B-HC-D: (a) $t - s$ diagram, and (b) friction angle vs. water content and cohesion vs. water content

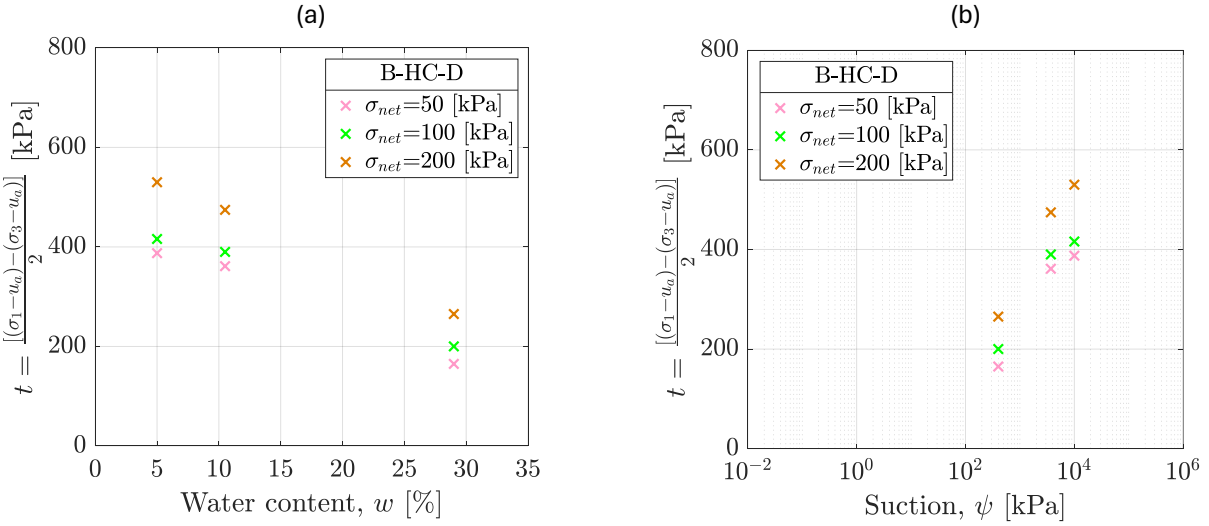

Figure 4.28.: Biaxial test results from series B-HC-D: (a) maximum t vs. water content, and (b) maximum t vs. suction

decreases from approximately 29% to 10% - corresponding to an increase in suction from $\psi = 400$ kPa to $\psi = 3.7$ MPa - t rises gradually. In the subsequent range, as water content further declines from 10% to 5% (or suction increases from $\psi = 3.7$ MPa to $\psi = 10$ MPa), t shows a slight further increase.

4.6. Direct shear tests

4.6.1. Definitions

This section presents the results of the series of direct shear tests (DST) on saturated samples and unsaturated samples under three net normal stresses of 50 kPa, 100 kPa and 200 kPa. The normal stress is determined using the following equation (Eq. 4.7):

$$\sigma_n = \frac{F_n}{A_0} \tag{4.7}$$

where σ_n is the normal stress, F_n is the applied normal force, and A_0 is the initial area of the square sample, which has a side length L. The shear stress is calculated as (Eq. 4.8):

$$\tau = \frac{F_s}{A} \tag{4.8}$$

where F_s is the applied shear force, and A is the corrected shear area of the sample calculated as:

$$A = L(L - \Delta L) \tag{4.9}$$

Here, ΔL represents the horizontal displacement of the sample. Bulolo & Leong (2023) analyzed results from a series of direct shear tests using both the area-correction and no-area-correction approaches. They reported that the influence of area correction is almost negligible for small horizontal displacements (less than 2 mm) in both square and circular shear boxes. In the present study, the no-area-correction approach was also examined. Overall, the shear strength values obtained without area correction were several kilopascals lower than those derived using the area-correction method. Unless otherwise stated, the results presented herein correspond to the area-correction approach.

4.6.2. Samples tested along the drying path (DS-D)

The results of the tests along the drying path conducted under a net normal stress of 50 kPa are presented in Figure 4.29a, showing the relationship between shear stress and horizontal displacement. As suction increases, the maximum shear stress increases and the relationship between shear stress and horizontal displacement transitions from ductile to

brittle. Additionally, the horizontal displacement at peak shear stress (i.e., shear strength) decreases with increasing suction.

Figure 4.29b illustrates the relationship between vertical and horizontal displacement. Overall, all samples exhibit dilation during testing, with the rate of dilation increasing as suction rises.

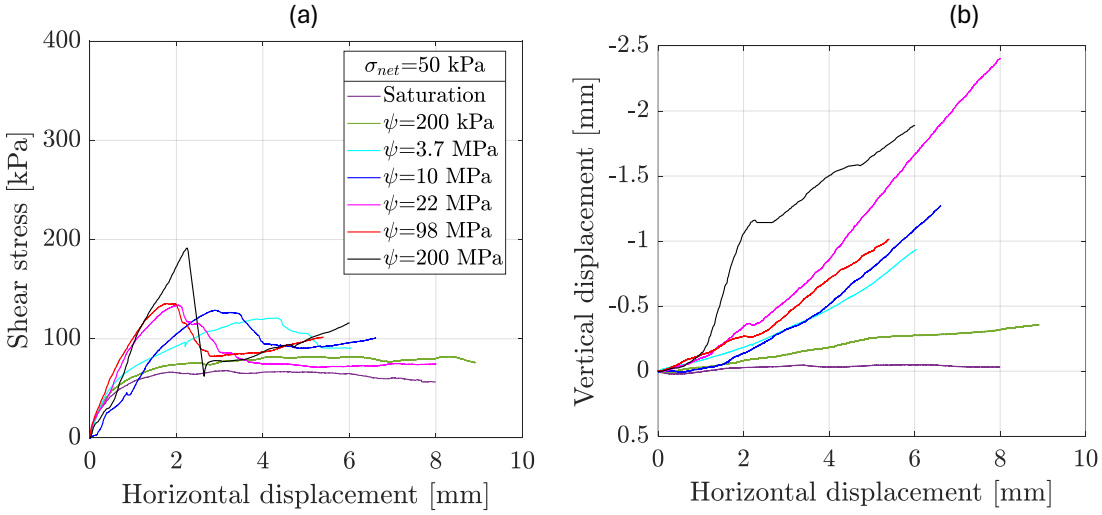

Figure 4.29.: Direct shear test results from series DS-D under σ_{net} = 50 kPa: (a) shear stress versus horizontal displacement, and (b) vertical displacement versus horizontal displacement

At higher net normal stresses, there is also a noticeable increase in the maximum shear stress, accompanied by a pronounced shift from ductile to brittle behaviour in the stress-displacement curve profiles, as suction increases. This trend is shown in Fig. 4.30a for σ_{net} = 100 kPa and Fig. 4.31a for σ_{net} = 200 kPa.

The vertical displacement versus horizontal displacement relationship, similar to the behaviour observed at σ_{net} = 50 kPa, consistently indicates dilation in all samples, as illustrated in Fig. 4.30b for σ_{net} = 100 kPa and Fig. 4.31b for σ_{net} = 200 kPa. Furthermore, higher suction levels lead to increasingly pronounced dilation.

Figure 4.32 compares the shear stress-horizontal displacement curves for three representative suction levels under varying net normal stresses, demonstrating the influence of net normal stress at each suction level. As depicted in Figure 4.32a, the maximum shear stress increases with higher net normal stress. Additionally, at a given suction level, an increase in net normal stress leads to a reduction in the rate of dilation, as shown in Figure 4.32b.

Figure 4.33a illustrates the direct shear test results plotted in the shear strength-net normal stress (τ-σ_{net}) space. For each test series conducted at a specific suction under

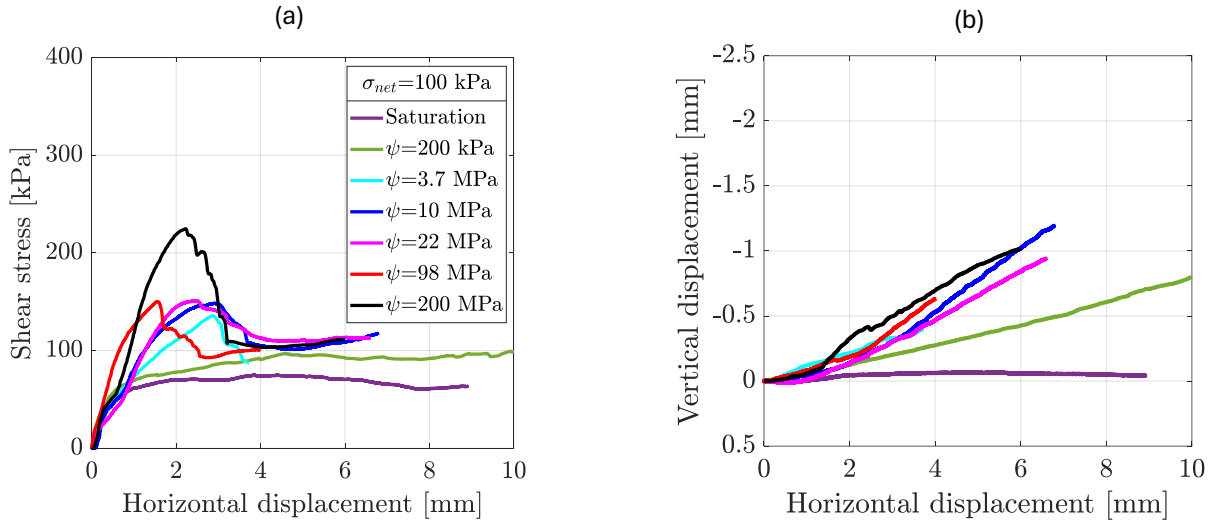

Figure 4.30.: Direct shear test results from series DS-D under σ_{net} = 100 kPa: (a) shear stress versus horizontal displacement, and (b) vertical displacement versus horizontal displacement

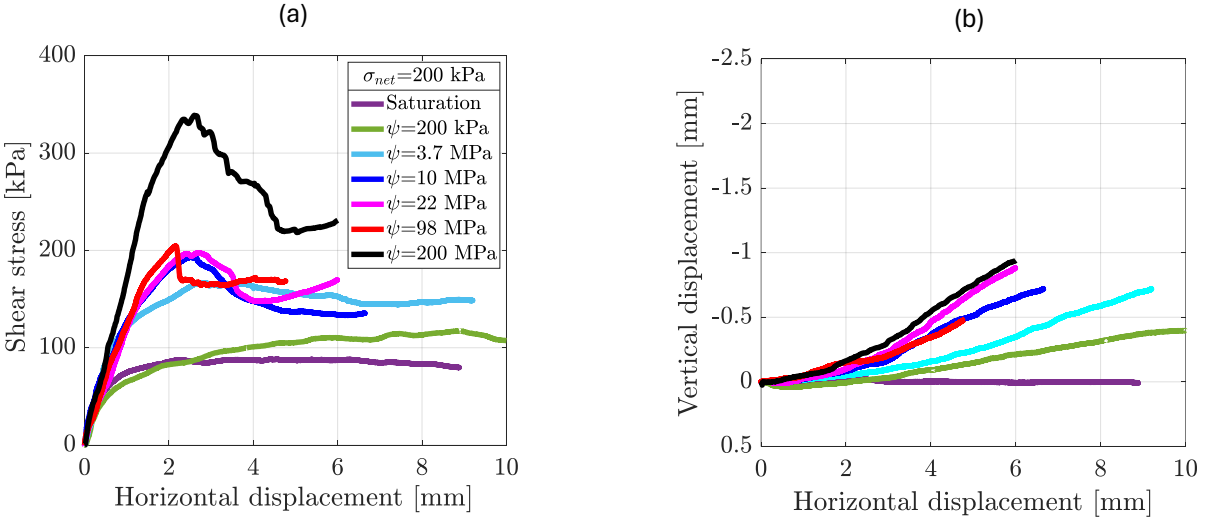

Figure 4.31.: Direct shear tests results from series DS-D under σ_{net} = 200 kPa: (a) shear stress versus horizontal displacement, and (b) vertical displacement versus horizontal displacement

varying net normal stresses, the evaluated failure conditions produce three stress points. The shear strength parameters - cohesion (c') and friction angle (φ') - were determined by fitting a straight line through these points. The variation of these parameters with water content, corresponding to different suction levels, is presented in Figure 4.33b.

The friction angle obtained from the tests under saturated conditions is 8.7°, which is significantly lower than the value of 21.5° derived from the biaxial compression tests

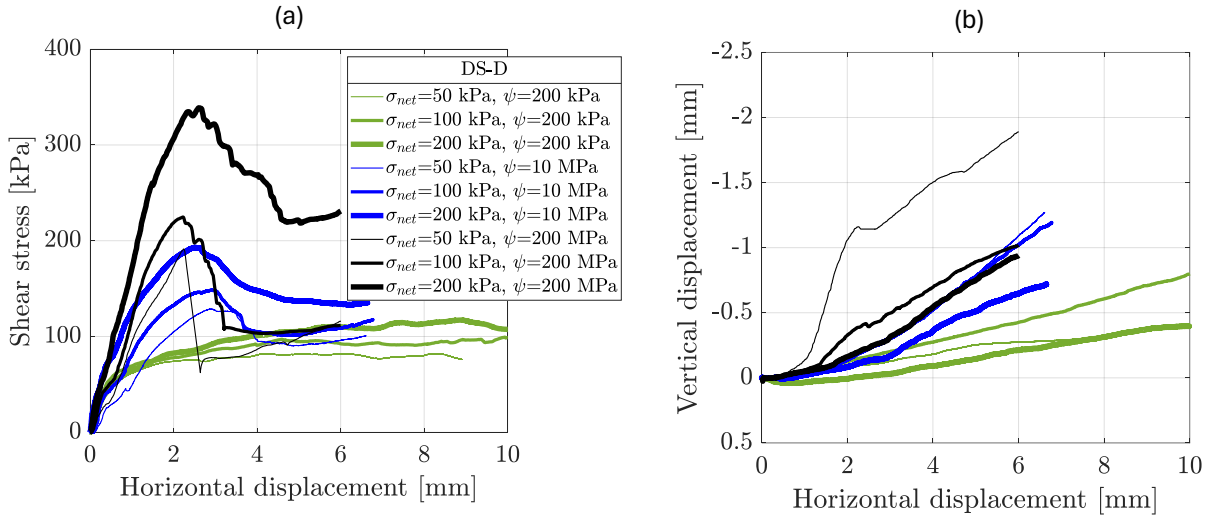

Figure 4.32.: Direct shear test results from series DS-D under σ_{net} = 50; 100; 200 kPa at three suction values: (a) shear stress versus horizontal displacement, and (b) vertical displacement versus horizontal displacement

under the same conditions. Conversely, the cohesion obtained from the direct shear tests under saturated conditions is about 60 kPa, being significantly higher than the value of about 19.8 kPa derived from the saturated biaxial compression tests. This discrepancy will be further discussed in Chapter 5. The friction angle (indicated by black squares in Fig. 4.33b) generally increases from approximately 8.7° to 23° as the water content decreases from 35% to 5%, stabilizing within the range of 5% to 1%. Beyond this point, as the water content drops below 1%, the friction angle rises sharply to about 45°. This observation qualitatively aligns with the findings of Bai & Liu (2012), who conducted a series of direct shear tests on unsaturated Nanyang expansive soil over a wide range of water content. Similarly, cohesion (represented by black triangles in Fig. 4.33b) increases progressively as the water content reduces from 35% to 5%. Within the range of 5% to 1%, cohesion shows a slight increase, followed by a substantial rise when the water content decreases further below 1%.

Figure 4.34 presents the relationships between shear strength and water content (Fig. 4.34a) as well as shear strength and suction (Fig. 4.34b) for the three net vertical stresses. As the water content decreases from approximately 35% to 1% - corresponding to a suction increase from ψ = 0 kPa (saturated condition) to ψ = 98 MPa - shear strength increases gradually. Beyond this range, as the water content declines further from 1% to 0.3% (or

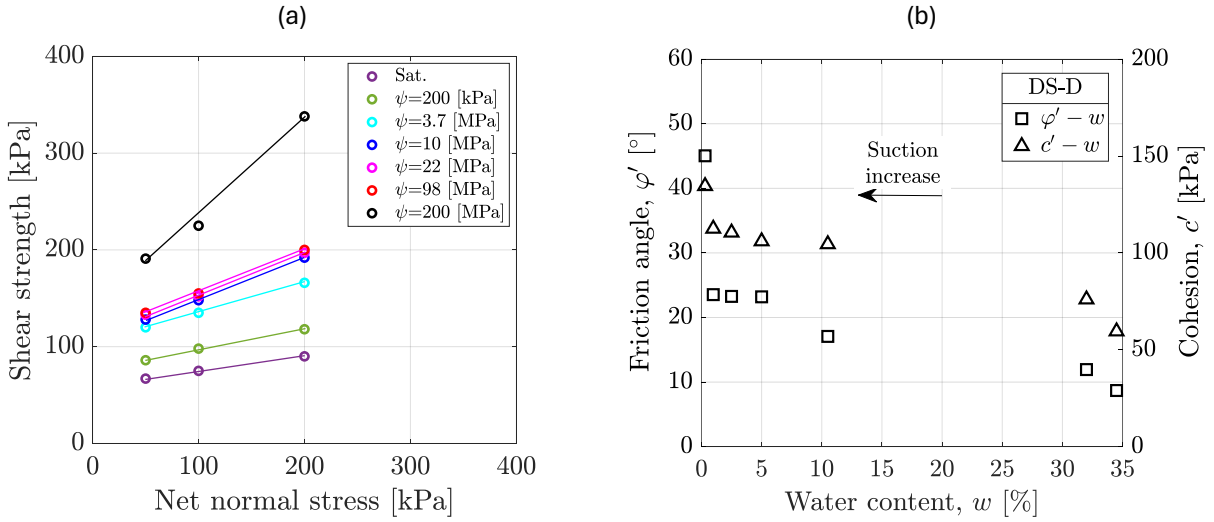

Figure 4.33.: Direct shear test results from series DS-D: (a) shear strength vs. net normal stress, and (b) friction angle vs. water content and cohesion vs. water content

suction rises from $\psi = 98$ MPa to $\psi = 200$ MPa), shear strength experiences a significant increase.

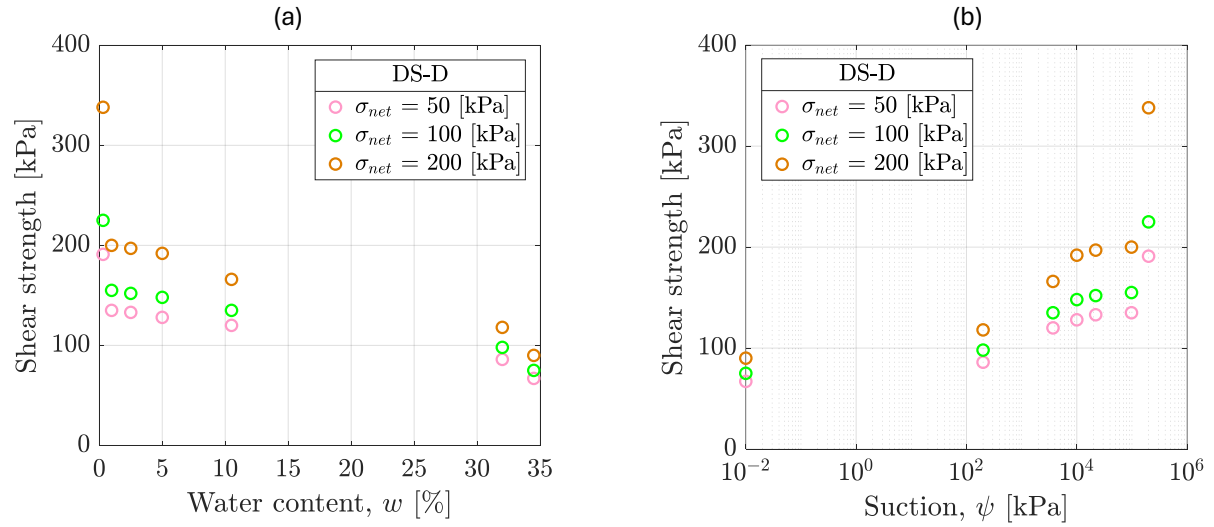

Figure 4.34.: Direct shear test result from series DS-D: (a) shear strength vs. water content, and (b) shear strength vs. suction

4.6.3. Samples tested along the wetting path (DS-W)

Figure 4.35 illustrates the relationships between shear stress and horizontal displacement (Fig. 4.35a) and between vertical displacement and horizontal displacement (Fig. 4.35b) for tests conducted along the wetting path under net normal stresses of σ_{net} = 50 kPa, 100 kPa, and 200 kPa. As suction decreases along the wetting path, the maximum shear stress decreases and the shear stress-horizontal displacement relationship transitions from brittle to ductile behaviour. At a constant suction value, an increase in net normal stress results in a higher peak shear stress. As depicted in Figure 4.35b, all samples demonstrate dilation throughout the testing process. The rate of dilation decreases as suction decreases. In addition, for a given suction level, increasing the net vertical stress results in less pronounced dilation.

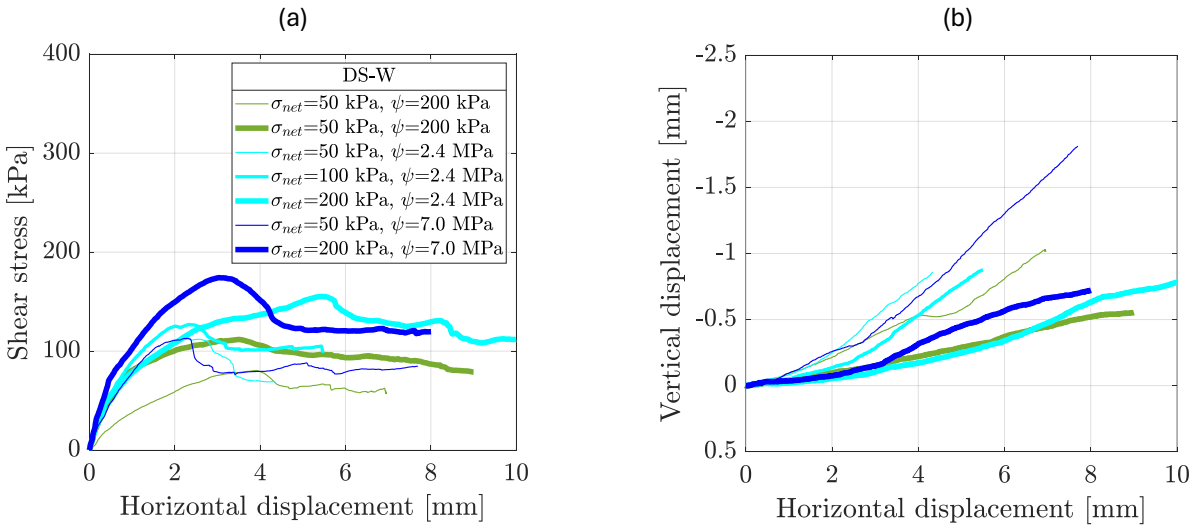

Figure 4.35.: Direct shear test results from series DS-W under σ_{net} = 50; 100; 200 kPa at three distinct suction values: (a) shear stress versus horizontal displacement, and (b) vertical displacement versus horizontal displacement

Figure 4.36a presents the test results plotted in the shear strength-net normal stress space. For each series of tests performed at a constant suction under varying net normal stresses, the failure conditions produce three stress points. It is evident that shear strength increases with increasing net normal stress. The shear strength parameters - cohesion (c') and friction angle (φ') - were determined by fitting a straight line through these points.

The variation of these parameters with water content, reflecting different suction levels, is shown in Figure 4.36b. The friction angle (denoted by black squares) decreases progressively from approximately 22.5° to 12° as the water content increases along the wetting

path from 5% to 28%. Cohesion (represented by black triangles) shows a slight increase from about 91 kPa to 98 kPa as the water content rises from 5% to 10%. However, with further increases in water content, cohesion decreases from approximately 98 kPa to 69 kPa.

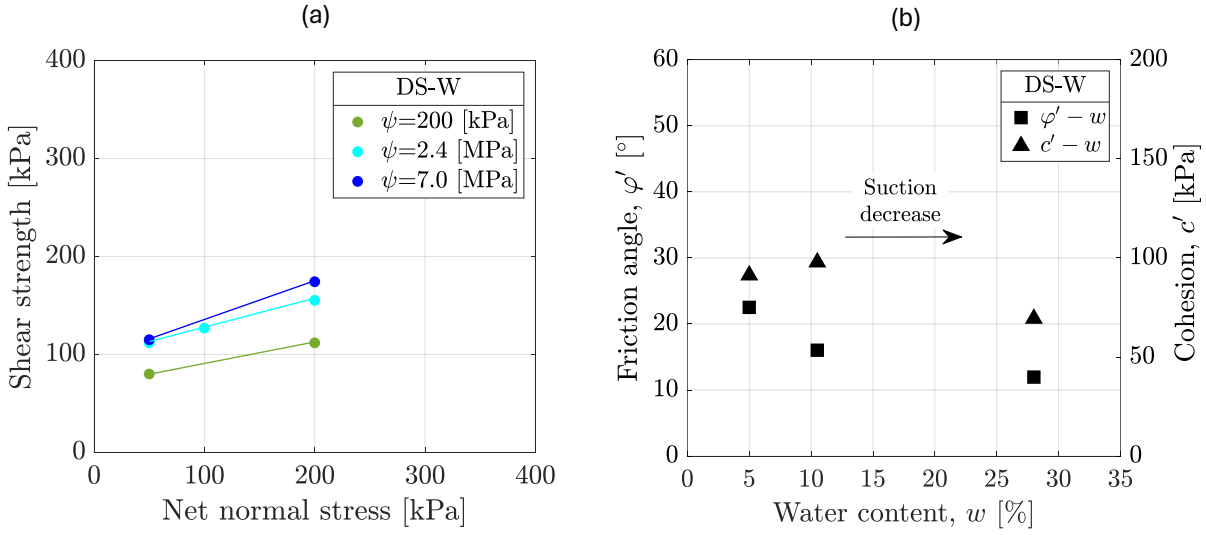

Figure 4.36.: Direct shear test result from series DS-W: (a) shear strength vs. net normal stress, and (b) friction angle vs. water content and cohesion vs. water content

Figure 4.37 illustrates the relationships between shear strength and water content (Fig. 4.37a) as well as shear strength and suction (Fig. 4.37b) under the three net vertical stresses. For $\sigma_{net} = 200$ kPa, shear strength decreases gradually as water content increases along the wetting path from approximately 5% to 28%, corresponding to a suction reduction from $\psi = 7.0$ MPa to $\psi = 200$ kPa. In contrast, for $\sigma_{net} = 50$ kPa, shear strength remains relatively unchanged as water content increases from 5% to 10.5% (or suction decreases from $\psi = 7.0$ MPa to $\psi = 2.4$ MPa), followed by a notable decrease as water content increases further (or suction decreases further). For $\sigma_{net} = 100$ kPa, only one test at $\psi = 2.4$ MPa was conducted, with the resulting shear strength falling between those observed for $\sigma_{net} = 50$ kPa and $\sigma_{net} = 200$ kPa.

4.7. Unconfined compression tests

For samples tested along the drying path (UC-D), which were conducted by Yukang Wang at HSKL, the vertical stress was computed based on the axial load and the initial cross-sectional area of the sample. Axial strain was determined using the DIC method. The

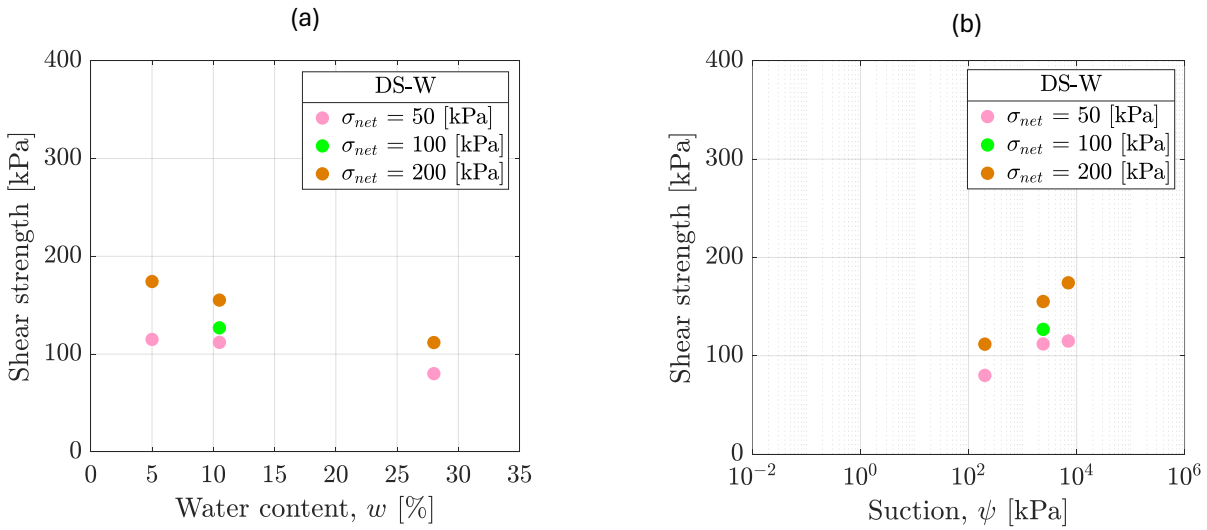

Figure 4.37.: Direct shear test results from series DS-W: (a) shear strength vs. water content, and (b) shear strength vs. suction

water content of each sample was measured both before and after testing. In general, due to the regulation of relative humidity (RH) and temperature by the humidifier, the difference in water content before and after the test was negligible. The corresponding suction values were then calculated using the measured post-test water content and the best-fit parameters from the SWCC model proposed by Durner (1994) for the drying path.

Figure 4.38 illustrates typical stress-strain curves obtained from the UC-D at different water contents (or corresponding suction levels). The results show that as the water content decreases (or suction increases), the peak unconfined compressive stress and initial modulus both increase. Furthermore, the axial strain at peak stress decreases with increasing suction or decreasing water content.

For samples tested along the wetting path (UC-W), the vertical stress was computed using the axial load and the cross-sectional area of the sample, which was determined under the assumption of constant sample volume during the testing process (i.e., corrected area) (Head 2006). In the present study, the no-area-correction (i.e., initial cross-sectional area) approach was also examined. Overall, the shear strength values obtained without area correction were several kilopascals higher than those derived using the area-correction method. Axial strain was calculated based on the measured change in sample height, recorded using the LVDT. The water content of each sample was measured both before and after testing. In general, despite the use of a plastic foil to minimize evaporation, a water content difference of approximately 1% to 2% was observed between pre- and

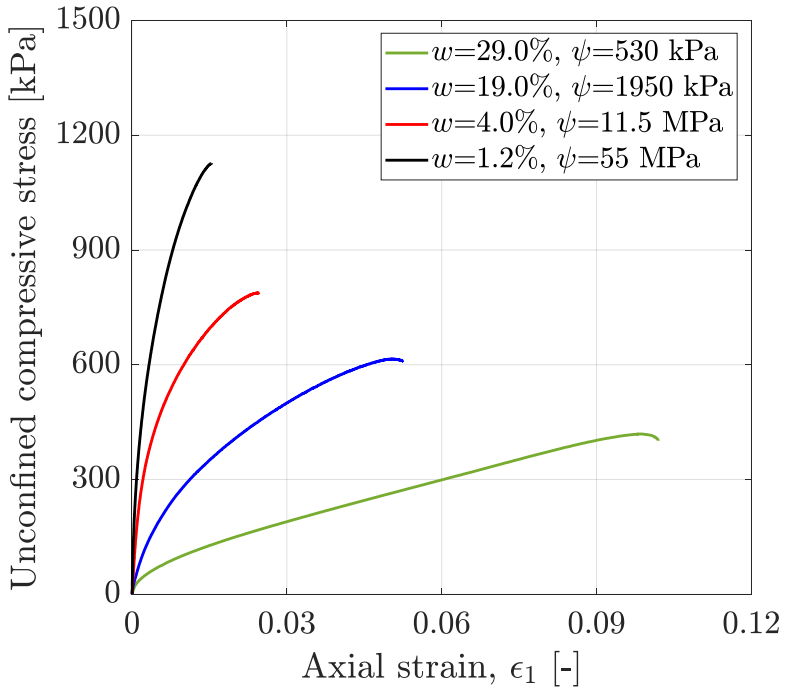

Figure 4.38.: Typical unconfined compressive stress-strain curves from the tests following the drying path (UC-D) (data provided Yukang Wang from the partner laboratory at HSKL)

post-test measurements. The corresponding suction values were then calculated using the measured post-test water content and the best-fit parameters from the SWCC model proposed by Durner (1994) for the wetting path.

Figure 4.39 presents representative stress-strain curves obtained from the UC-W conducted at various water contents (or corresponding suction levels). The results demonstrate that with increasing water content (or decreasing suction), both the unconfined compressive strength and the inclination of the stress-strain curve exhibit a noticeable reduction. Additionally, the axial strain at the peak stress increases progressively as suction decreases or water content rises along the wetting path.

Figure 4.40 compares the relationship between unconfined compressive strength (q_u) and water content (w) in the UC-W and UC-D series. Overall, the results highlight a clear hysteresis effect on q_u between the drying and wetting paths.

For the drying path, q_u increases as water content decreases. Specifically, within the water content range of 35% to approximately 26%, q_u exhibits a gradual increase. This is followed by a relatively modest rise as water content decreases further from 26% to around 4%. Finally, a significant increase in q_u is observed as water content drops below 4%.

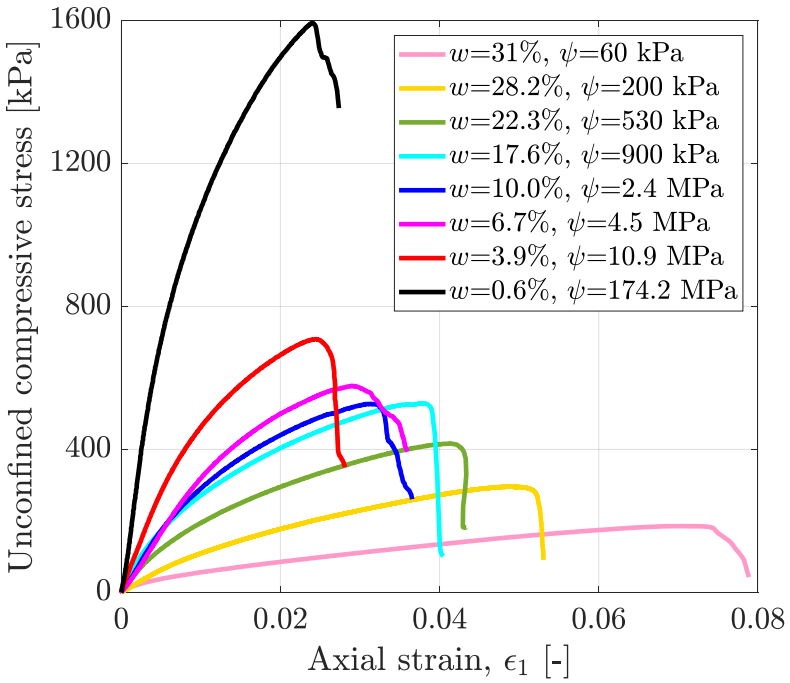

Figure 4.39.: Typical stress-strain curves from the unconfined compression tests following the wetting path (UC-W)

For the wetting path, q_u decreases as water content increases. In particular, a sharp decline in q_u is observed within the water content range of 0.6% to approximately 4%, followed by a more moderate decrease as water content increases from 4% to around 23%. At higher water contents, the reduction in q_u becomes more gradual. It is important to note that additional tests at $w = 26\%$ are needed to establish a clearer trend of q_u within the water content range of 23% to 28%.

Figure 4.41 presents a comparison of the relationship between q_u and suction (ψ) in the UC-D and UC-W series. Overall, q_u increases with increasing suction along the drying path, whereas it decreases with decreasing suction along the wetting path. Notably, the q_u values obtained from the drying path (UC-D) are generally higher than those from the wetting path (UC-W), further highlighting the hysteresis effect.

4.8. Uniaxial tensile tests

This section presents the results obtained from the uniaxial tensile test series, which were conducted by Yukang Wang at HSKL. The uniaxial tensile stress was determined based on

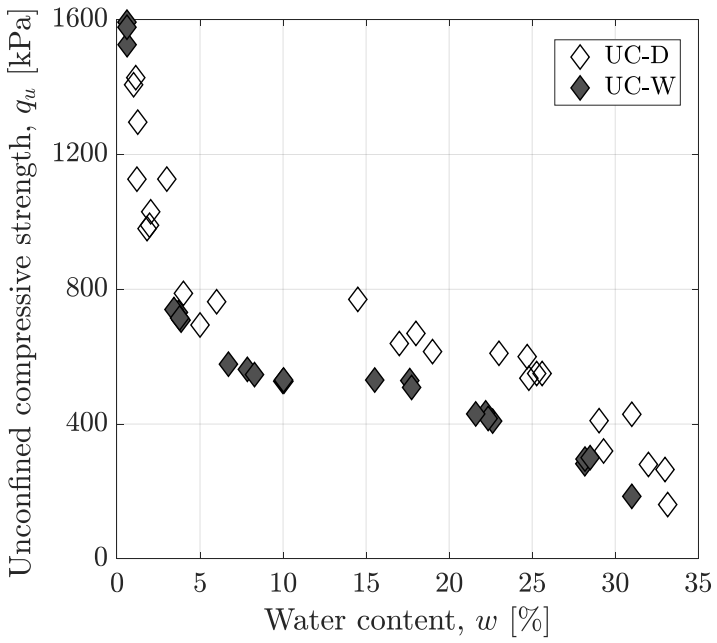

Figure 4.40.: Comparison of the relationship between water content and unconfined compressive strength in series UC-D (data provided Yukang Wang from the partner laboratory at HSKL) and UC-W

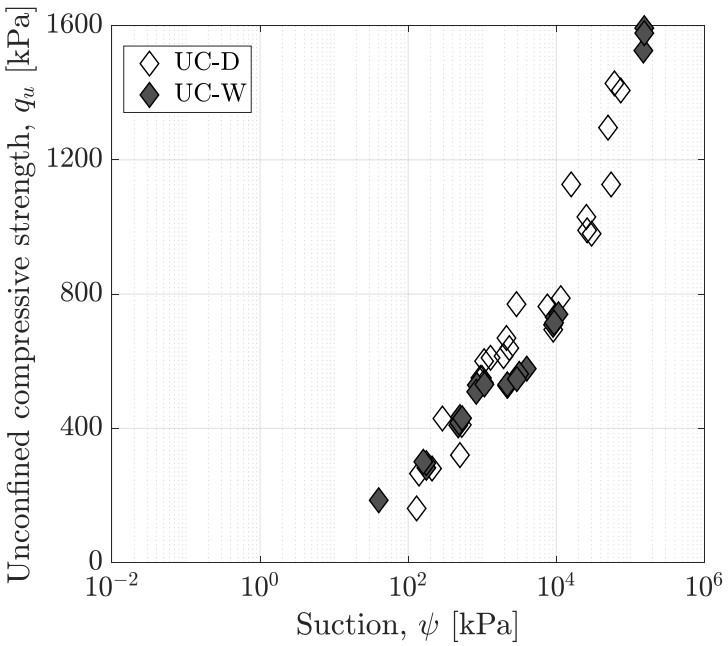

Figure 4.41.: Comparison of the relationship between suction and unconfined compressive strength in series UC-D and UC-W

the applied tensile load and the initial cross-sectional area of the sample, while axial strain was measured using the Digital Image Correlation (DIC) method to ensure precise strain assessment throughout the testing process. The tensile strength is the maximum tensile stress. The water content of each sample was recorded both before and after testing. Due to the regulation of relative humidity (RH) and temperature by the humidifier, the variation in water content before and after testing was negligible. The corresponding suction values were calculated using the measured water content and the best-fit parameters from the SWCC models proposed by Durner (1994) for the drying and wetting path.

Figure 4.42 presents the stress-strain responses obtained from representative tests along the drying path (UT-D), illustrating the relationship between tensile stress and axial strain. The results demonstrate that an increase in suction (associated with a reduction in water content) results in a higher maximum tensile stress (tensile strength) and a decrease in axial strain at failure.

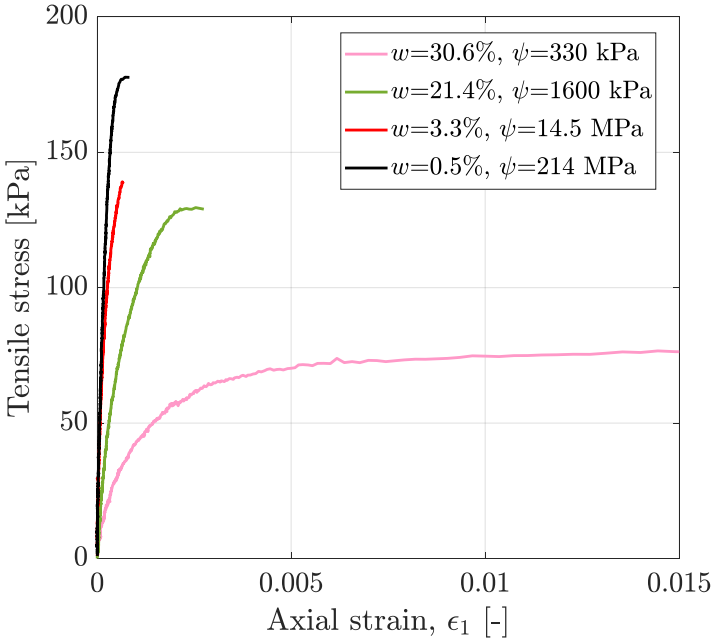

Figure 4.42.: Typical uniaxial tensile stress-strain curves from series of uniaxial tensile tests following the drying path (UT-D) (data provided by Yukang Wang from the partner laboratory at HSKL)

Figure 4.43 compares the relationship between tensile strength and water content (w) in the tests along the drying (UT-D) and wetting path (UT-W) series. The tensile strength obtained from tests along the UT-D is generally higher than that obtained from tests along the UT-W within the water content range between 25% and 10%. Meanwhile, Figure 4.44

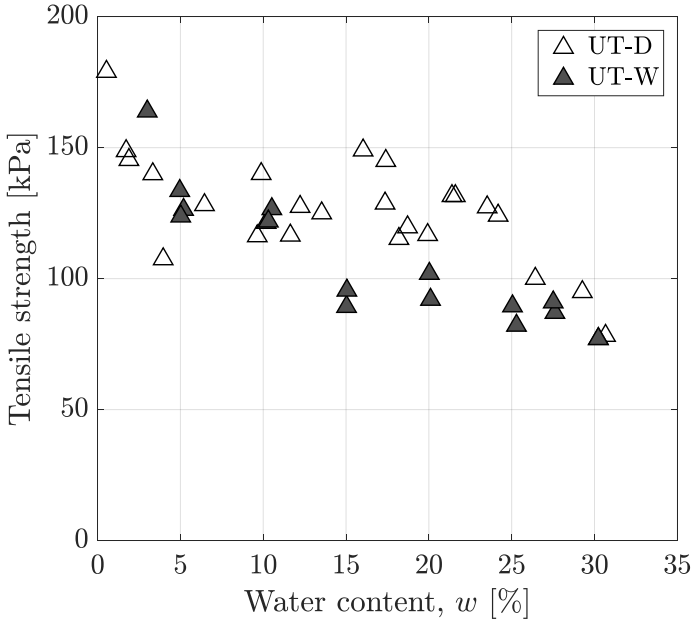

Figure 4.43.: Comparison of the relationship between water content and uniaxial tensile strength in series UT-D (data provided by Yukang Wang from the partner laboratory at HSKL) and UT-W

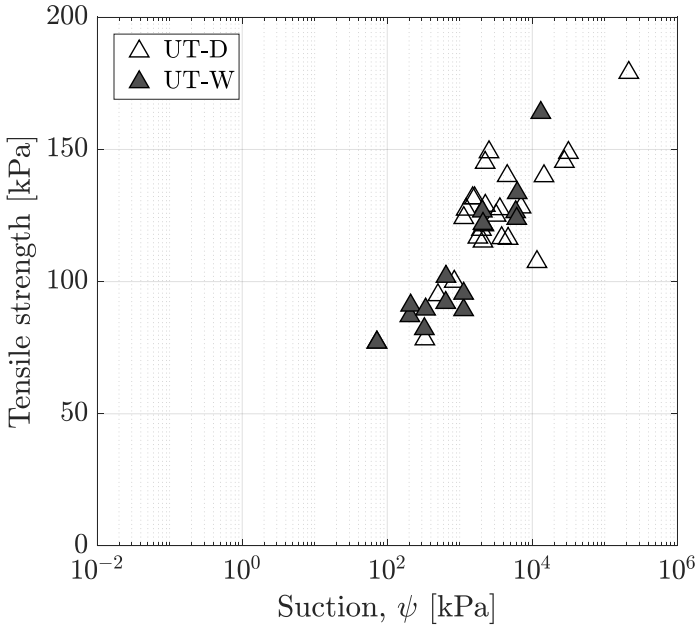

Figure 4.44.: Comparison of the relationship between suction and uniaxial tensile strength in series UT-D and UT-W

compares the relationship between tensile strength and suction in the tests along the drying (UT-D) and wetting path (UT-W) series.

For the drying path, tensile strength shows an initial increase from 76 kPa to 100 kPa as water content decreases from $w = 30.6\%$ to $w = 24\%$ (or suction increase from $\psi = 330$ kPa to $\psi = 1600$ kPa). This is followed by slight fluctuations in tensile strength as the water content further decreases within the range of $w = 24\%$ to about $w = 3.3\%$ (or the suction ranging from $\psi = 1600$ kPa to $\psi = 14.5$ MPa). Finally, as the water content drops below $w = 3.3\%$ (corresponding to $\psi = 14.5$ MPa), a marked increase in tensile strength is observed.

For the wetting path, the results indicate a general decrease in tensile strength as water content increases or suction decreases. A pronounced reduction in tensile strength is observed as the water content rises from approximately 3% to 5% (or as suction decreases from 13 MPa to approximately 7 MPa). Between 5% and 10% water content (corresponding to suction decreasing from approximately 7 MPa to 2.4 MPa), the tensile strength remains nearly constant. Beyond this point, a more gradual decline in tensile strength occurs as the water content increases to around 15% (or suction approximately 1.2 MPa). Further increases in water content (or decreases in suction) result in minimal changes in tensile strength.

4.9. Triaxial compression tests

Figure 4.45a shows the stress-strain curves from the triaxial test series on samples at saturated conditions, while Figure 4.45b shows the representation of the failure states in these tests in terms of t and s. From a fitting of the K_f line to the three failure stress states, the shear strength parameters c'_0 and φ'_0 are 7.36 kPa and 21.55°, respectively. It is important to note that the friction angle derived from the triaxial tests at saturated conditions is virtually similar to that derived from the biaxial tests at saturated conditions ($\varphi'_{0,BCT} = 21.5°$). However, the cohesion derived from the triaxial tests at saturated conditions is lower than that determined from the biaxial tests at saturated conditions ($c'_{0,BCT} = 19.9$ kPa).

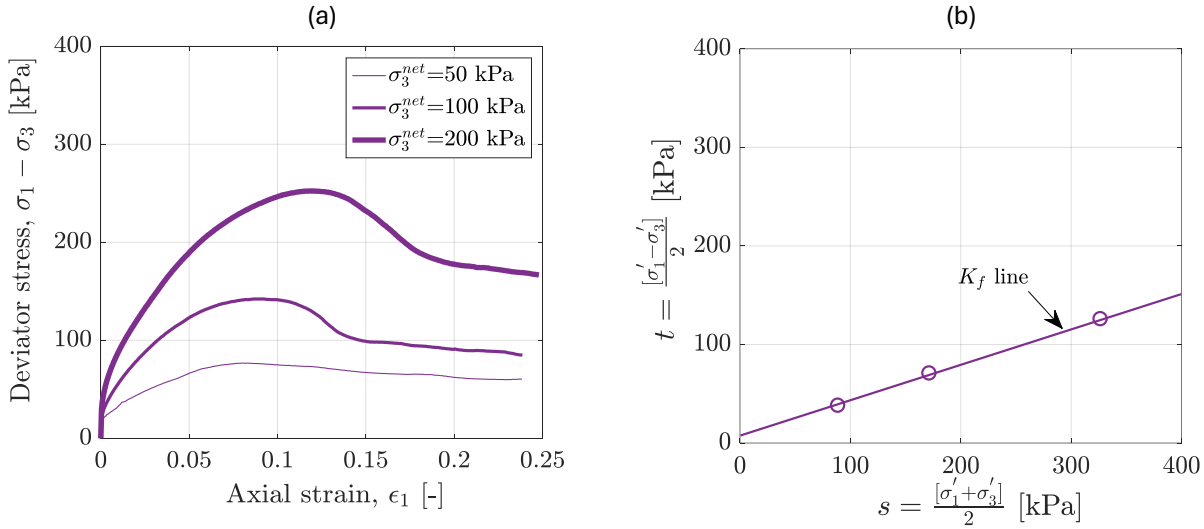

Figure 4.45.: Triaxial test results: (a) deviator stress vs. axial strain, and (b) representation of the test failure stress states in terms of t and s

5. Analysis and discussion of the experimental results

5.1. Soil-water characteristic curves

5.1.1. SWCC parameters

During the drying process, the transition from the saturated to the unsaturated state of soils is marked by the air-entry value (AEV), as described by Fredlund & Rahardjo (1993*b*). The air-entry value represents the suction (ψ_{AEV}) at which air begins to enter the largest soil pores during drainage. Conversely, along the wetting path, the soil rehydrates from a dry state. The suction at which the soil transitions from an unsaturated to a saturated state is referred to as the air-expulsion value (AExV) (ψ_{AExV}) (Khalili et al. 2008; Pasha et al. 2016). These parameters are crucial as they will be used to predict suction stress based on the equation proposed by Khalili & Khabbaz (1998). The corresponding predictions will be presented in Chapter 6.

As discussed in the literature review, several well-known methods exist for determining the AEV, including the graphical method (Vanapalli et al. 1998) and the log-log scale method (Pasha et al. 2016). Pasha et al. (2016) pointed out that the graphical method is suitable when the SWCC is presented in terms of S_r - ψ. However, when the SWCC is expressed as w - ψ, they proposed an alternative approach using a log-log scale representation of both w and ψ. In this method, the AEV is determined at the intersection of two distinct straight-line segments: one corresponding to the saturated state and the other to the unsaturated state.

In the following, the log-log scale method is employed to determine the AEV when the measured SWCC is presented in terms of gravimetric water content (w) versus matric suction (ψ). For the wetting path, a similar application was followed to determine the AExV.

Figure 5.1 depicts the SWCC along with its SWCC parameters in a diagram with log-log scale. The air-entry value, ψ_{AEV}, is identified as 680 kPa, corresponding to the intersection of two distinct constant-slope lines (red solid lines in Fig. 5.1). The water content at ψ_{AEV} is approximately 27.7%, as determined by the best-fit curve of the measured data using Durner (1994)'s SWCC model (discussed in the following section). Similarly, for the wetting path, the air-expulsion value, ψ_{AExV}, is determined to be 400 kPa, corresponding to a water content of 24.5% (see red dashed lines in Fig. 5.1).

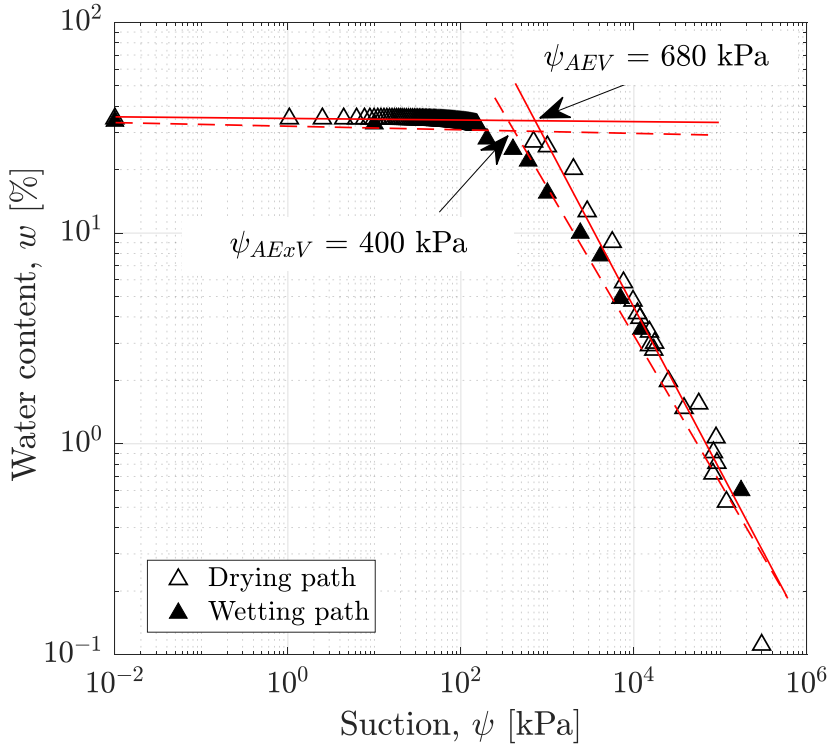

Figure 5.1.: Determination of the SWCC parameters using the log-log method

5.1.2. Hysteresis of drying and wetting SWCC

A pronounced hysteresis effect is evident in the SWCC along the drying path and the wetting path (Figures 4.1 and 5.1). For a given matric suction, the water content in the soil during the drying path is higher than that during the wetting path. This phenomenon can be attributed to several factors, including the ink-bottle effect (Haines 1923; Miller & Miller 1956), the raindrop effect (Bear 1972; Lu & Likos 2004), and the presence of entrapped air within the soil matrix (Richards 1931; Philip 1957; Mualem 1974).

The pore structure of the soil, comprising both small and large pores (Sivakumar et al. 2006; Thom et al. 2007; Romero & Simms 2008), plays a critical role in this behavior. During the drying path, water strongly adheres to soil particles and forms menisci at the pore throats, resulting in higher water content at a given suction. Conversely, during the wetting path, refilling these pores requires overcoming the energy barrier imposed by the menisci, leading to lower water content at the same suction level. This hysteresis can also be explained by the mechanisms of swelling and shrinkage that occur during the wetting and drying processes, respectively. Guan (2012) suggested that the hysteresis arises from irreversible soil volume changes during the drying-wetting cycle, as some portions of the soil's volume may not recover completely. Consequently, the reduced pore volume during the wetting path results in a lower water content compared to the drying path.

5.2. Soil shrinkage curve

The results of the soil shrinkage curve (SSC), as shown in Figure 4.5 in Section 4.3 of Chapter 4, are further analysed in this section. When compared with the typical SSC introduced by Cornelis et al. (2006) (see Fig. 2.8 in State-of-the-art chapter), the measured SSC generally follows the characteristics of a well-structured soil. According to Cornelis et al. (2006), the SSC of a well-structured soil can be divided into four distinct phases: structural shrinkage, normal shrinkage, residual shrinkage, and zero shrinkage.

In this study, the structural shrinkage phase appears to be absent from the measured SSC. Due to the lack of measurements between a water content of 35% (saturated condition) and 33%, it is difficult to draw a definitive conclusion regarding SSC behaviour within this range. However, if a line is drawn from the void ratio corresponding to $w = 35\%$ to that at $w = 33\%$, the slope of this line is slightly different from the linear trend observed within the water content range of 33% to 27%. This suggests that if the test had started at $w = 35\%$, the structural shrinkage phase might have been captured. The missing measurements between $w = 35\%$ and $w = 33\%$ are likely due to water loss during sample installation and device assembly.

The measured SSC exhibits a clear proportional shrinkage phase within the water content range of 33% to 27%. Cornelis et al. (2006) and Encalada López et al. (2023) suggested that the water content at the end of the proportional shrinkage phase corresponds to the air-entry value. Based on the measured SSC, this water content is approximately 27%, which aligns well with the water content corresponding to the air-entry value presented in Section 5.1.1 ($w = 27.7\%$ corresponding to $\psi_{AEV} = 680$ kPa).

Following the proportional shrinkage phase, the residual shrinkage phase occurs between water contents of 27% and 19%. As the water content decreases from 19% to 10%, the void ratio generally remains constant, marking the zero shrinkage phase. Interestingly, as the water content drops below 10%, the void ratio increases again. This phenomenon is not described in the typical SSC introduced by Cornelis et al. (2006). However, similar behaviour has been reported by Vesga (2008) for commercial kaolin, Lu & Dong (2017) for Georgia kaolinite, and Dong & Wang (2021) for clayey soils. Vesga (2008) hypothesized that this behaviour might be due to the breakdown of pre-existing capillary contacts between particles, leading to an expansion of the soil.

5.2.1. Modelling the SSC

In this section, the measured soil shrinkage curve (SSC) data were analyzed using established SSC models to evaluate their ability to represent the observed behavior. Curve fitting was performed using the Solver add-on in Microsoft Excel. The applied models include those proposed by Fredlund et al. (2002) and Peng & Horn (2005), which have been widely used to analyze SSC behavior. A detailed description of these models is provided in Section 2.5.3 of the State-of-the-art chapter.

The fitting process involved minimizing the sum of squared deviations between the observed void ratio values and those predicted by the models. This optimization approach, commonly known as the least squares method, ensures an accurate representation of the measured data. The quality of the curve fits was assessed using the coefficient of determination (R^2).

Figures 5.2 illustrates the measured SSC data, along with their corresponding best-fit curves obtained from the applied models. The fitting parameters derived for the drying path are summarized in Table 5.1. Obviously, the model proposed by Peng & Horn (2005) consistently exhibited higher R^2 values compared to the model by Fredlund et al. (2002), demonstrating its superior performance in capturing the shrinkage behaviour. However, neither model accurately captured the course of the SSC when the water content dropped below 20%. This discrepancy arises because most SSC models in the literature have been developed under the assumption of zero shrinkage beyond the residual shrinkage phase. However, as analysed in the previous section, the findings of this study contradict this assumption, revealing an increase in void ratio at relatively low water contents.

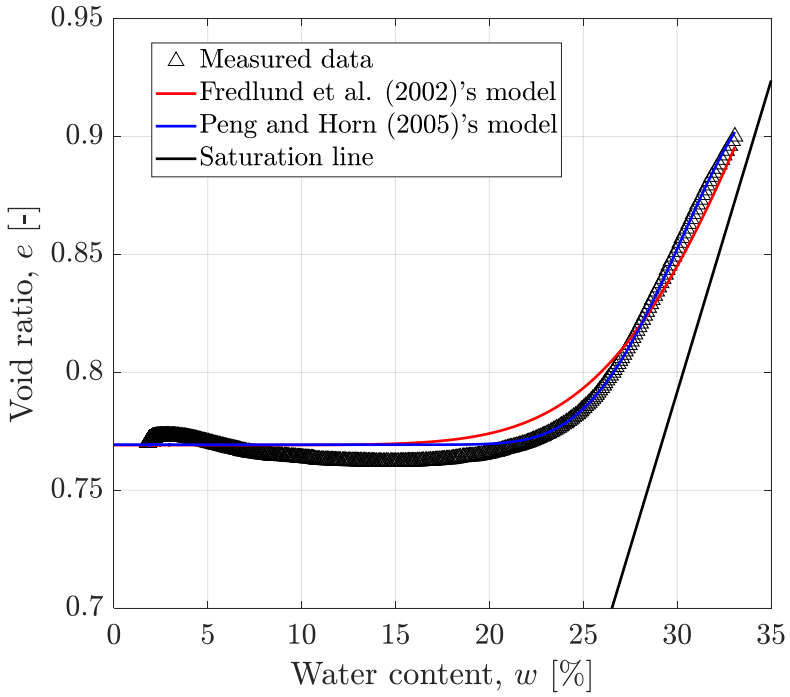

Figure 5.2.: Measured SSC data and best fit models

Table 5.1.: Fitting parameters derived from the application of SSC models (Fredlund et al. 2002 and Peng & Horn 2005) to measured SSC data

Model	Parameter		R^2
Fredlund et al. (2002)	a_{sh} (-)	0.769	0.949
	b_{sh} (-)	0.2990	
	c_{sh} (-)	7.500	
Peng and Horn (2005)	α (-)	7.679	0.973
	n (-)	1.530	
	m (-)	219.394	
	e_s (-)	0.915	
	e_r (-)	0.769	
	v_s (-)	0.915	

5.2.2. Combination of SSC and water content-suction SWCC

The measured SWCC (w-ψ), presented in Chapter 4, and the SSC (w-e) were combined to establish the relationship between the degree of saturation and suction (S_r-ψ).

Based on the measured SSC data, the relationship between water content and degree of saturation (w-S_r) was analysed. From the SSC shown in Fig. 4.5, the degree of saturation was calculated from the measured values of void ratio, water content, and grain density (see Table 3.1). The calculated degree of saturation versus measured water content is shown in Figure. 5.3. The best-fit curve to these data was obtained using a polynomial function, performed through the *Curve Fitting* application in MATLAB software (version 2024a). This function enabled a best fit of the measured data ($R^2 = 0.9998$) over a wide range of water content. The polynomial function is expressed as follows:

$$S_r = a_1 w^6 + a_2 w^5 + a_3 w^4 + a_4 w^3 + a_5 w^2 + a_6 w + a_7 \tag{5.1}$$

In Eq. 5.1, w is water content (%), S_r is degree of saturation (-), and a_1 to a_7 are fitting parameters which are shown in Table 5.2. Figure 5.3 shows the measured water content and calculated degree of saturation (w-S_r) along with the best fitting curve.

Table 5.2.: Fitting parameters of the polynomial function 5.1 to fit the measured w-S_r

Parameter	Value [-]
a_1	$3.389 \cdot 10^{-9}$
a_2	$-3.035 \cdot 10^{-7}$
a_3	$9.38 \cdot 10^{-6}$
a_4	-0.0001271
a_5	0.0007563
a_6	0.03295
a_7	0

Based on Eq. 5.1 and the measured water content in the SWCC test, the corresponding degree of saturation was calculated. Therefore, the relationship between the degree of saturation and suction was established. The SWCC in terms of degree of saturation versus suction (S_r-ψ) is presented in Figure 5.4. Initially, within the suction range of 0 to approximately 100 kPa, S_r exhibits a slight decrease from 100% to around 97%. As suction increases from 100 kPa to approximately 1000 kPa, S_r gradually declines to about 85%. Beyond this range, a more pronounced reduction in S_r is observed, dropping sharply to approximately 15% as suction rises to 10 MPa. For suctions exceeding 10 MPa, S_r continues to decrease gradually with further increase in suction.

The measured SWCC data in terms of S_r versus ψ were fitted using several well-known SWCC models, including those proposed by Van Genuchten (1980), Fredlund & Xing (1994), and Durner (1994). The fitted curves are presented in Figure 5.4. Overall, the

selected models exhibit an excellent agreement with the SWCC data, demonstrating their suitability for characterizing the soil's water retention behaviour. The corresponding fitting parameters obtained for each model are summarized in Table 5.3.

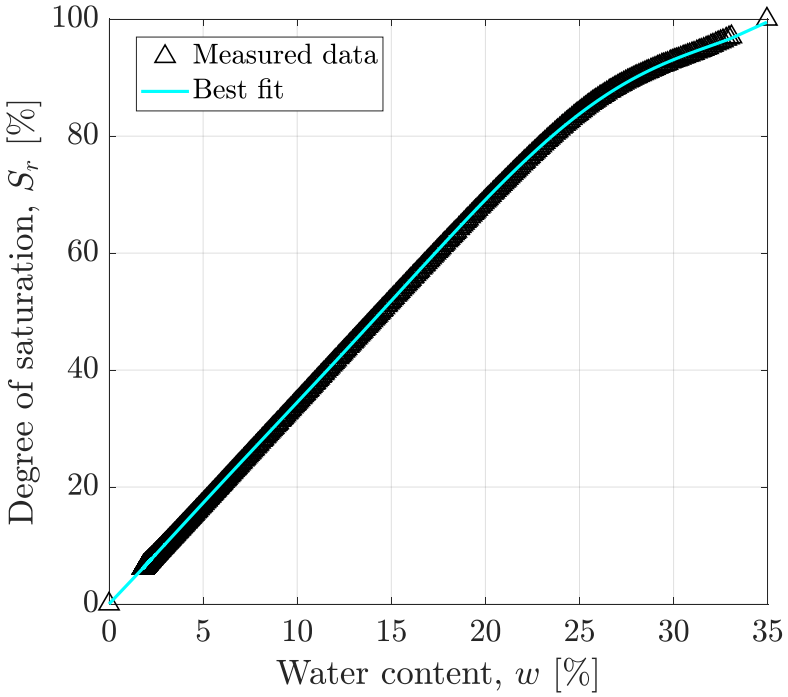

Figure 5.3.: Relationship between water content and degree of saturation (w-S_r) derived from the SSC test

To determine the SWCC (S_r-ψ) parameters, the graphical method proposed by Vanapalli et al. (1998) (see Section 2.4.1 in State-of-the-art chapter) was used. The AEV was established at the intersection of the horizontal line representing the saturated state and the tangent line fitted to the best-fit curve of Fredlund & Xing (1994)'s SWCC model through its inflection point. Similarly, ψ_{res} was obtained at the intersection of the tangent line at the inflection point and a line extending from a suction value of 10^6 kPa, which is also tangent to the best-fit curve. The inflection point corresponds to the location of maximum slope on the best-fit SWCC curve. The variation in slope along the SWCC was quantified using an equation proposed by Wijaya et al. (2015), expressed as follows:

$$m_s = \frac{S_r(\psi) - S_r(\psi - \Delta\psi)}{\log(\psi/(\psi - \Delta\psi))} \tag{5.2}$$

where m_s represents the slope of the best-fit SWCC obtained using the model proposed by Fredlund & Xing (1994), $S_r(\psi)$ denotes the degree of saturation derived from the best fit curve, and $\Delta\psi$ is the incremental change in suction. The calculated values of m_s using Eq.

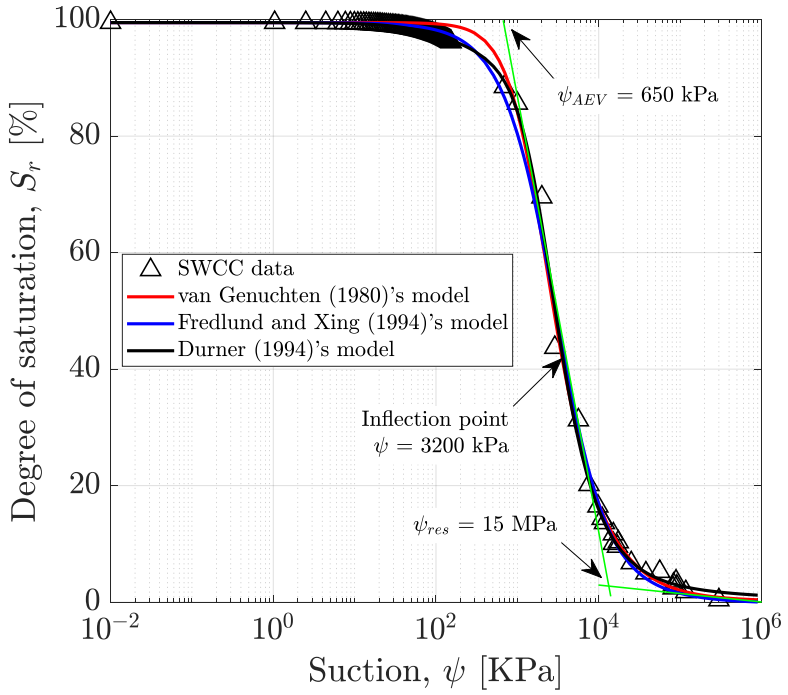

Figure 5.4.: SWCC in terms of S_r-ψ derived from a combination of SWCC in terms of w-ψ and SSC (w-e)

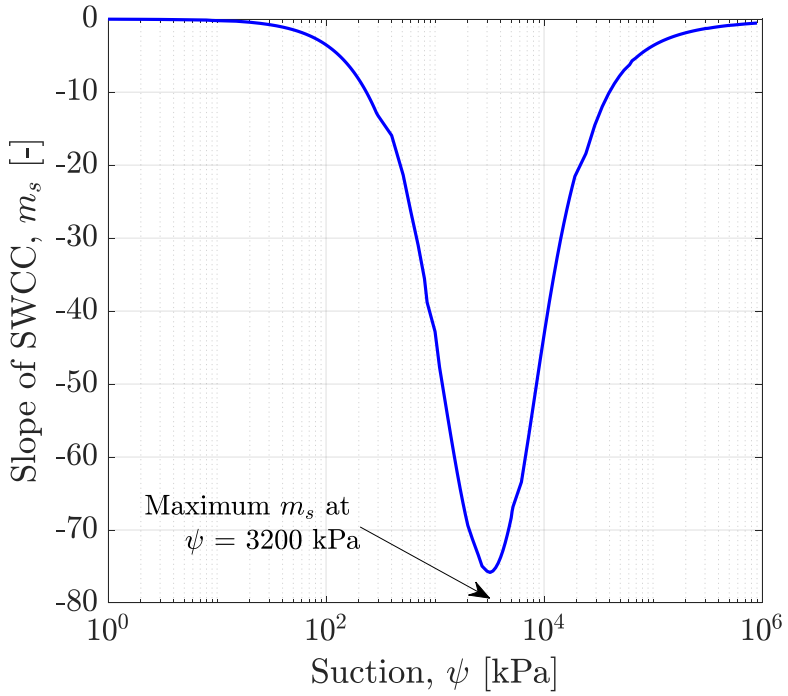

Figure 5.5.: Variation of the slope of the best-fit SWCC using Fredlund & Xing (1994)'s model as a function of suction

Table 5.3.: Fitting parameters derived from the application of SWCC models including van Genuchten (vG) (1980), Fredlund and Xing (FX) (1994), and Durner (1994) to the SWCC data

Model	Parameter		R^2
vG (1980)	α (1/kPa)	0.00063	0.9974
	n (-)	1.959	
	S_{sat} (%)	99.5	
	S_{res} (%)	0.18	
FX (1994)	α (1/kPa)	0.00034	0.9984
	n (-)	1.278	
	ψ_{res} (kPa)	15000	
	S_{sat} (%)	99.5	
	m (-)	2.35	
Durner (1994)	α_1 (1/kPa)	0.0005	0.9992
	n_1 (-)	2.222	
	S_{res} (%)	0	
	S_{sat} (%)	99.5	
	α_2 (1/kPa)	0.0107	
	n_2 (-)	1.273	
	w_1 (-)	0.8587	

5.2 for the entire SWCC are presented in Figure 5.5. The inflection point, used to draw the tangent line, is located at $\psi = 3200$ kPa. Figure 5.4 shows the air-entry value (AEV) and the residual suction (ψ_{res}) determined based on the graphical method. The air-entry value (AEV) was determined to be 650 kPa, while the residual suction (ψ_{res}) was identified as 15 MPa. When comparing the AEV obtained from the SWCC representation in terms of w-ψ (see Figure 5.1), it is observed that the AEV derived from the w-ψ relationship (ψ_{AEV} = 680 kPa) closely matches the AEV determined from the S_r-ψ relationship ($\psi_{AEV} = 650$ kPa. This consistency confirms the reliability of the AEV estimation across different forms of SWCC representation. Moreover, it aligns with the conclusion of Pasha et al. (2016), which demonstrates that the AEV derived from S_r-ψ and the AEV from w-ψ (with w presented on a logarithmic scale) are comparable.

5.3. Pore size distribution along drying and wetting path

The results of the pore size distribution (PSD) analysis along the drying and wetting paths are presented in Section 4.4. Figure 5.6 illustrates the experimental program for the PSD determination, alongside the best-fit curves obtained from the measured SWCC data (Fig. 5.6a) and the measured SSC data (Fig. 5.6b). Using the maximum cumulative pore volume (max. CPV) extracted from Figures 4.6 and 4.7, the variation of max. CPV with water content along the drying and wetting paths is shown in Fig. 5.7. In addition, a zoomed-in view of the differential pore volume within the pore diameter range of 400 nm to 1600 nm is provided in Fig. 5.8 (for the drying path) and Fig. 5.9 (for the wetting path).

Following the drying path, as shown in Figure 5.7, the max. CPV decreases as the water content decreases. Subsequently, along the wetting path, the max. CPV increases with increasing water content.

In this study, as shown in Figure 5.8 (the light green line), the sample at the optimum water content generally exhibits a nearly unimodal PSD, which aligns with the findings of previous studies (Delage et al. 1996; Kayser et al. 2023). As the sample transitions from the optimum water content to a saturated state under constrained swelling conditions, the aggregates are expected to expand and occupy the inter-aggregate voids, which may be less pronounced in the sample at optimum water content. According to Sivakumar et al. (2006), the size of the aggregates is influenced by sample preparation, where the mixture of dry kaolin and water forms aggregates, and their size governs the resulting pore size distribution.

For the drying path, as shown in Figure 4.8 to Figure 4.12, and Figure 5.8, a transition from an unimodal to a bimodal PSD is observed. This transition indicates that, during the drying of compacted kaolin, the PSD evolves due to microstructural changes and the interplay of interparticle forces, particularly van der Waals attraction and capillary forces. At high water content, the diffuse double layers are thick (Baille 2014), keeping particles apart and resulting in a dispersed structure with relatively uniform pores - hence, an unimodal PSD (Kodikara et al. 1999). As the water content decreases, van der Waals attraction becomes more dominant due to reduced interparticle distances, promoting the aggregation of clay particles. Simultaneously, increasing suction induces strong capillary forces that pull particles together, enhancing aggregation and leading to the formation of intra-aggregate micropores (Kodikara et al. 1999). In the present study, the micropores (approximately 300 to 400 nm) are slightly changed by the variation in water content or

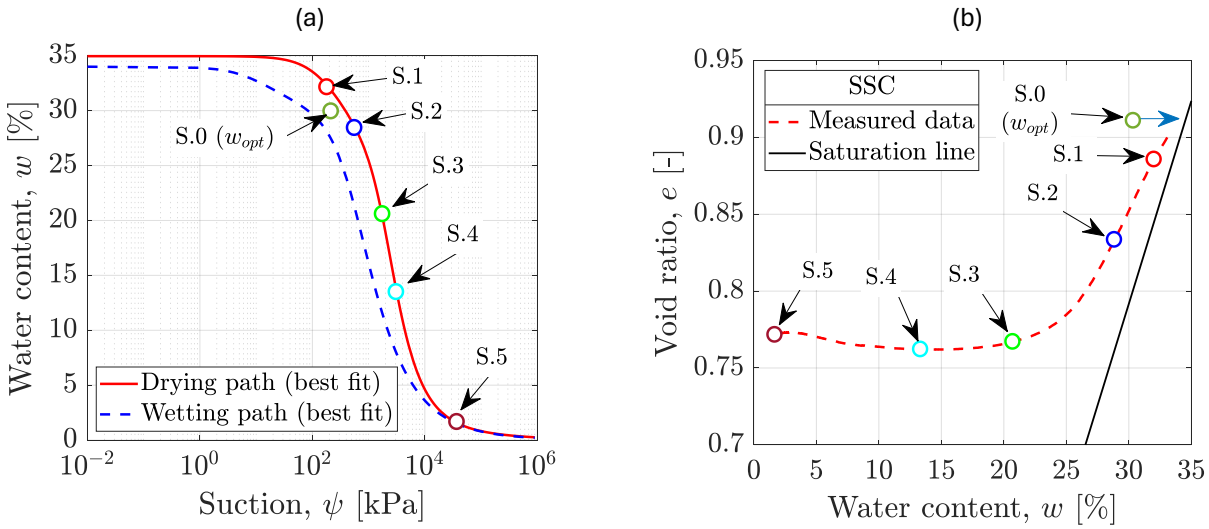

Figure 5.6.: The experimental program of PSD determination accompanied by: (a) SWCC, and (b) SSC

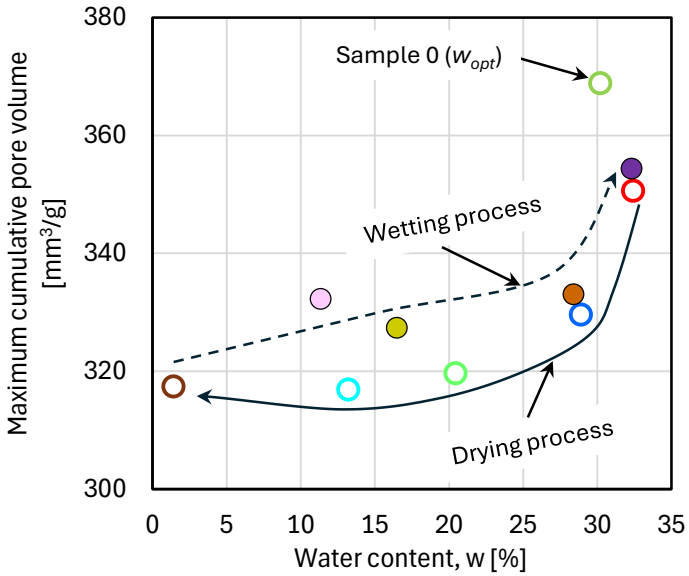

Figure 5.7.: Evolution of max. CPV over water content

suction. However, as shown in the zoomed-in view (Fig. 5.8), the macropores are strongly influenced by changes in water content or suction, which are often accompanied by the formation of flocculated structures. Samples 3, 4, and 5 show a distinct second peak over a certain pore diameter range, in contrast to samples 0, 1, and 2. This observation aligns with the findings of Cuisinier & Laloui (2004). Interestingly, the slight increase in void

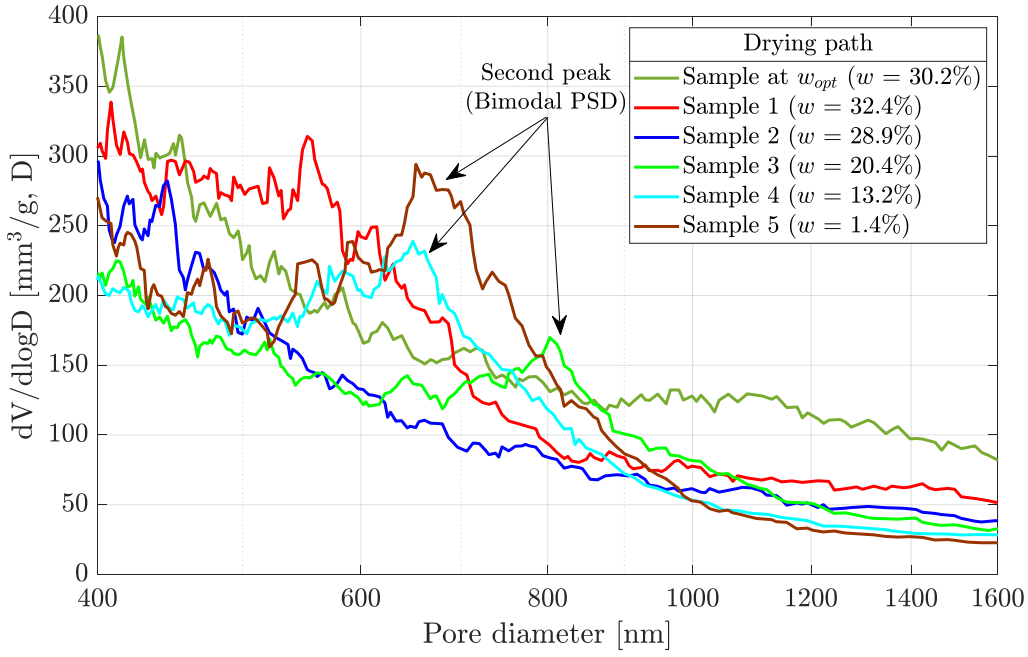

Figure 5.8.: A zoomed-in view of the differential pore volume of samples following the drying path within the pore diameter range of 400 nm to 1600 nm

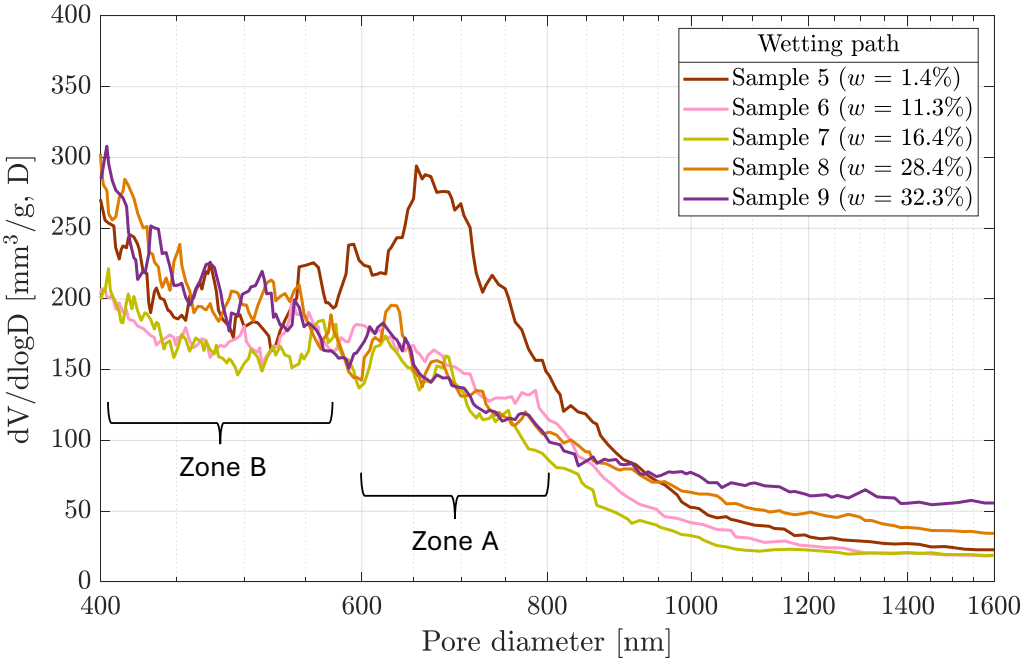

Figure 5.9.: A zoomed-in view of the differential pore volume of samples following the wetting path within the pore diameter range of 400 nm to 1600 nm

ratio in the soil shrinkage curve as the water content drops below 10% (Fig. 5.6b) may correspond to the slight increase in max. CPV as water content decreases from 13.2% (sample 4) to 1.4% (sample 5).

Along the wetting path, a reverse trend in the PSD is observed: a transition from a bimodal to an unimodal distribution. Sivakumar et al. (2006) hypothesized that aggregates expand into the larger inter-aggregate voids under low confinement during wetting. As shown in Figures 4.13 to 4.16, the increase in water content has minimal influence on micropores (approximately 300 to 400 nm). However, the bimodal PSD with a pronounced second peak observed in sample 5 disappears as the water content increases from 1.4% to 11.3% (sample 6), as shown in the zoomed-in view (Fig. 5.9). As water content increases further, zone A in Fig. 5.9 remains mostly unchanged, while an upward shift in the PSD curve is observed in zone B. This shift is attributed to the swelling of aggregates (Sivakumar et al. 2006).

5.4. Biaxial compression tests

In this section, the results of the biaxial compression test (BCT) series, as described in Section 4.5, are further analyzed with focus on the determination of suction stress derived from the BCT series. Firstly, the background to determine the suction stress from the BCT is described. Secondly, the suction stress derived from the BCT on the compacted samples with vertical cutting direction (B-VC) and horizontal cutting direction (B-HC) is presented and discussed. Details of sample cutting direction are shown in Figure 3.10.

Suction stress is derived from the biaxial test results following the procedure described in Section 2.8.2 of the State-of-the-art chapter. Figure 5.10 shows a projection of the failure surface onto the shear stress against net normal stress plane. In this figure, the Mohr circle representation of the failure envelope in the space of net normal stress and shear stress of BCT at saturated and unsaturated conditions is presented.

In Figure 5.10, c'_i is the apparent cohesion at unsaturated conditions (with results expressed in terms of total stress), meanwhile c'_0 is the cohesion derived from the BCT at saturated conditions (with results expressed in terms of effective stress). φ'_0 is the friction angle derived from the BCT at saturated conditions.

Following the assumption within the framework of the effective stress concept, the friction angle derived from BCT under unsaturated conditions, φ'_i, is assumed to be equal to φ'_0 (i.e., the friction angle is considered constant regardless of variations in suction or water

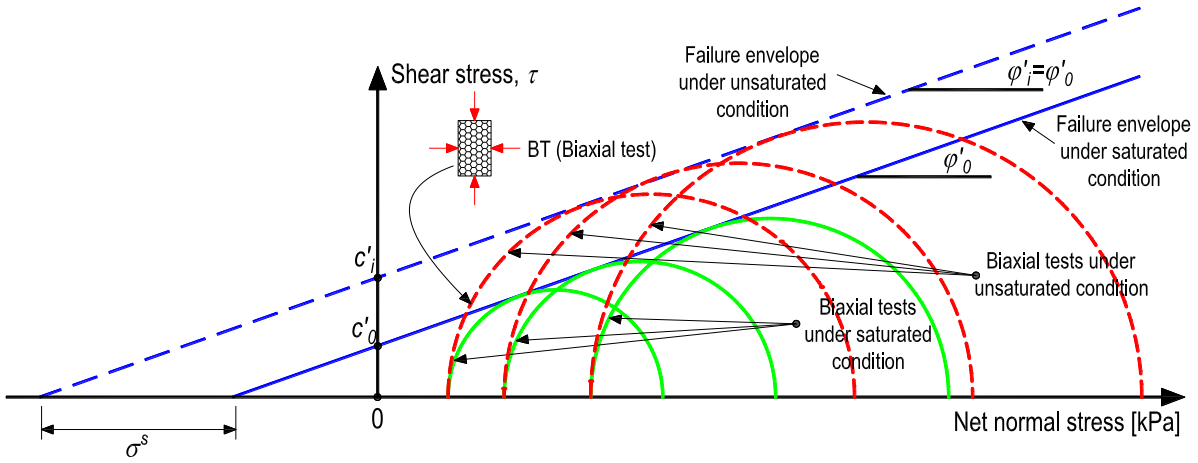

Figure 5.10.: Conceptual illustration for the determination of suction stress from biaxial test results, where dashed lines and circles represent the test results in total stress, and solid lines and circles represent the test results in effective stress (adapted from the concept of Lu & Likos 2004)

content). Consequently, only c'_i is presumed to vary with suction or water content. Suction stress σ^s is derived using Eq. 2.28 shown in Section 2.8.2 of the State-of-the-art chapter.

Figure 5.11a presents the experimental results, obtained from the test series along the drying path (B-VC-D), in the t-s space. Each test series, conducted at a constant suction but different net confining pressures, yields a set of three stress points at failure conditions. Each set of three stress points is linearly fitted under the assumption of a constant friction angle despite variations in suction or water content ($\varphi'_i = \varphi'_0$). This implies that only the intercept of the fitted line with the vertical axis (t axis) is presumed to change with water content or suction. By extending the linear fit lines to their intersection with the vertical axis, cohesion is determined using Eq. 5.3:

$$c'_i = \frac{a_i}{\cos \varphi'_0} \tag{5.3}$$

In Eq. 5.3, a_i represents the intersection of the linear fit lines with the vertical axis t. Figure 5.11b illustrates the cohesion derived from the series B-VC-D as a function of water content. It is evident that cohesion increases as water content decreases or suction increases.

Similarly, Figure 5.11c presents the experimental results in the t-s space from the test series conducted along the wetting path (B-VC-W). Figure 5.11d depicts cohesion as a

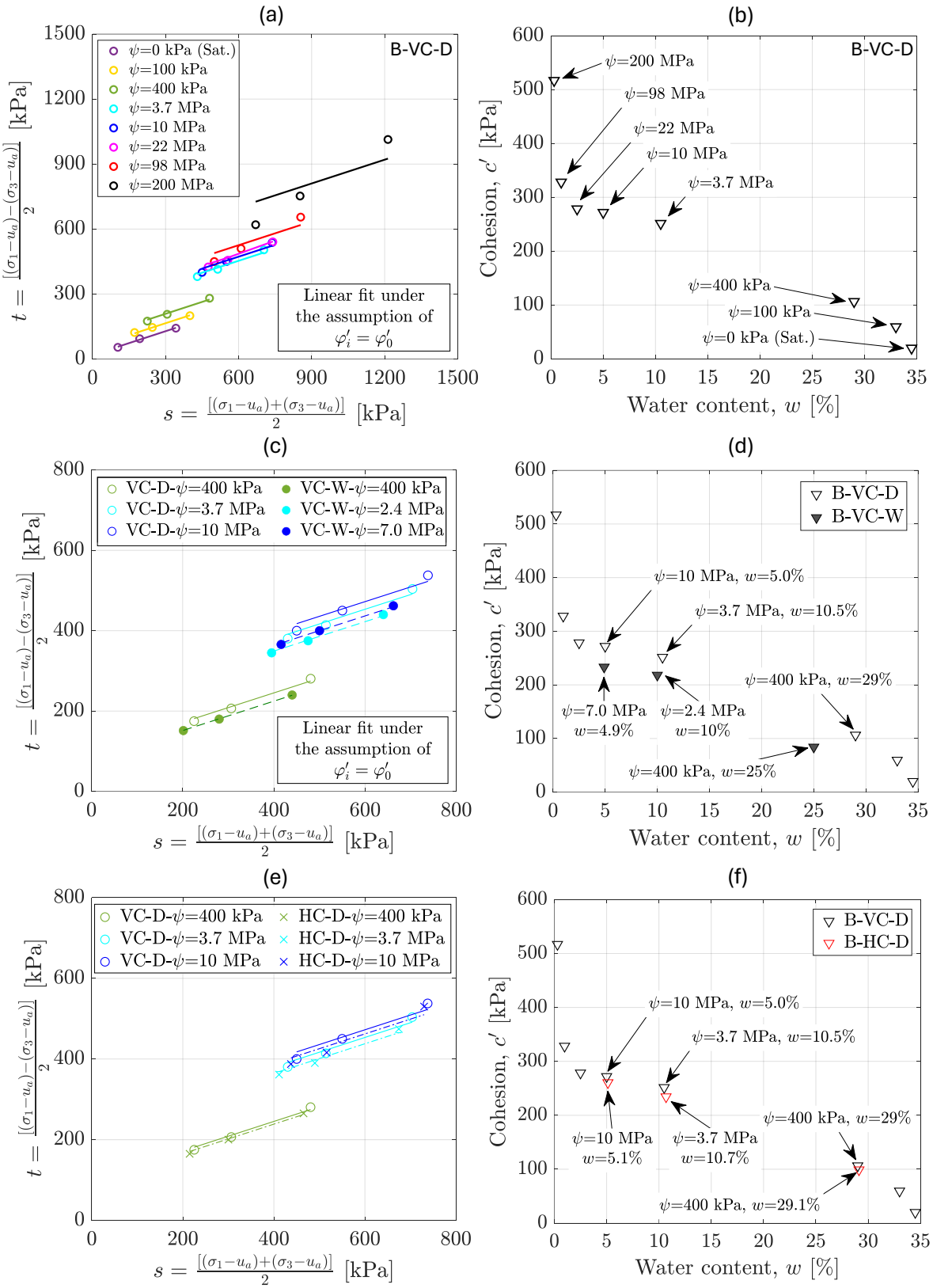

Figure 5.11.: Biaxial compression test results in $s-t$ space with linear fit lines of measured data and calculated cohesion (assuming a constant friction angle with varying suction) from (a, b) drying path test series (B-VC-D), (c, d) wetting path test series (B-VC-W), and (e, f) horizontal cutting-drying test series (B-HC-D)

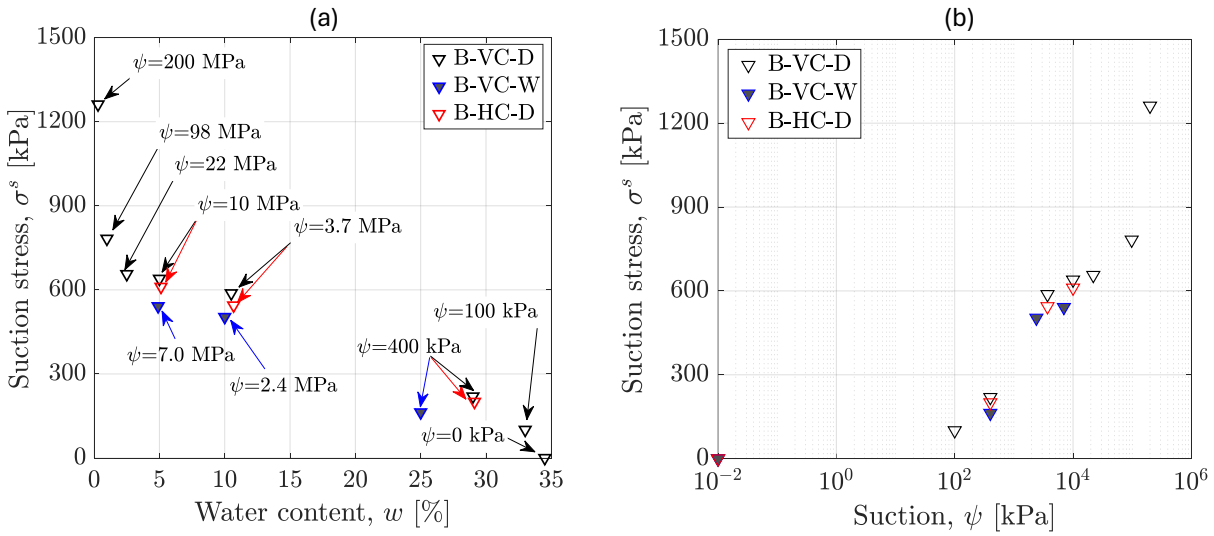

Figure 5.12.: Suction stress determined from all biaxial compression test series: (a) as a function of water content, and (b) as a function of suction

function of water content for these tests. In general, the cohesion of samples in the B-VC-W test series decreases as water content increases.

A comparison between the test series B-VC-D and B-VC-W presented in Figure 5.11c shows that samples on the drying path exhibit a higher peak deviator stress (t) than those on the wetting path, regardless of whether they have the same water content but different suction or the same suction but different water content. Consequently, the linear fit lines for the B-VC-D test series are positioned higher than those for the B-VC-W test series. Figure 5.11d shows a comparison between the cohesion derived from the test series B-VC-D and B-VC-W. In Fig. 5.11d, at suction $\psi = 400$ kPa, the cohesion derived from the drying path test series (B-VC-D) is higher than that from the wetting path test series (B-VC-W). This discrepancy is attributed to hysteresis effects. Hysteresis effects are also observed in the SWCC test results and the pore size distribution (PSD) analysis. At a given suction, samples following the drying path retain higher water content than those on the wetting path, as illustrated in the SWCC (Figure 5.1). Guan et al. (2010) conducted a series of triaxial tests on samples subjected to both drying and wetting paths and concluded that, at the same suction level, due to the higher water content, samples on the drying path exhibit a larger water-soil particle contact area. This increased contact enhances interparticle forces, thereby improving the shear strength of the soil samples. For the remaining samples on the wetting path, although having the same water content as the sample on the drying path ($w = 10\%$ and $w = 5\%$), the samples on the wetting

path have lower suction values which result in lower values of peak deviator stress (Fig. 5.11c) and cohesion (Fig. 5.11d) than those on the drying path.

A comparison between the biaxial test series B-VC-D and B-HC-D is provided in Fig. 5.11e and Fig. 5.11f. Samples from the vertical cutting direction exhibit slightly higher peak deviator stress than those from the horizontal cutting direction. Consequently, the linear fit lines for the B-VC-D test series are positioned slightly higher than those for the B-HC-D test series. Therefore, in Figure 5.11f, at a given water content or suction, the cohesion of samples in the vertical cutting direction series (B-VC-D) is slightly higher than that in the horizontal cutting direction series (B-HC-D). Rahardjo et al. (2016) conducted SWCC measurements on samples extracted from both vertical and horizontal cutting directions of a compacted soil block and found that the SWCC is not significantly affected by hydraulic anisotropy. Therefore, in the present study, it is assumed that the SWCC is independent of hydraulic anisotropy and that suction remains the same for samples extracted in both vertical and horizontal cutting directions. Attom & Al-Akhras (2008) conducted a series of unconfined compression tests on undisturbed clayey soil and found that samples extracted in the vertical cutting direction exhibited higher unconfined compressive strength than those extracted in the horizontal cutting direction. This finding highlights the influence of anisotropy on the shear strength of undisturbed clayey soils. Similarly, Rowshanzamir & Askari (2010) investigated the strength anisotropy of compacted clayey soil and reported differences in shear strength between samples extracted parallel to and perpendicular to the compaction direction.

Figure 5.12a presents the suction stress derived from all test series, based on Eq. 2.28, as a function of water content, while Figure 5.12b shows the corresponding suction stress as a function of suction. In general, suction stress increases as water content decreases or as suction increases. This trend aligns with the suction stress characteristic curve (SSCC) proposed for clayey soils by Lu & Likos (2006) and Lu et al. (2010). However, due to the lack of experimental data within the water content range of 10% to 29%, it is challenging to accurately assess the trend of suction stress in this interval. Therefore, conducting additional experiments within this range is recommended for future research. The suction stress derived from the biaxial test series B-VC-W is significantly lower than that obtained from B-VC-D, which is attributed to hysteresis effects, as discussed previously. In contrast, the difference in suction stress between the biaxial test series B-VC-D and B-HC-D with vertical or horizontal cutting direction is generally small.

5.5. Direct shear tests

In this section, the results of the direct shear test (DST) series, as described in Section 4.6, are further analyzed with focus on the determination of suction stress derived from this test series. Firstly, the background to determine the suction stress from this test series is described. Secondly, the calculated suction stress is presented.

Similar to the BCT series, Figure 5.13 shows a projection of the failure surface under saturated and unsaturated conditions onto the shear stress against net normal stress plane. Suction stress σ^s is derived using Eq. 2.28 shown in Section 2.8.2 of the State-of-the-art chapter.

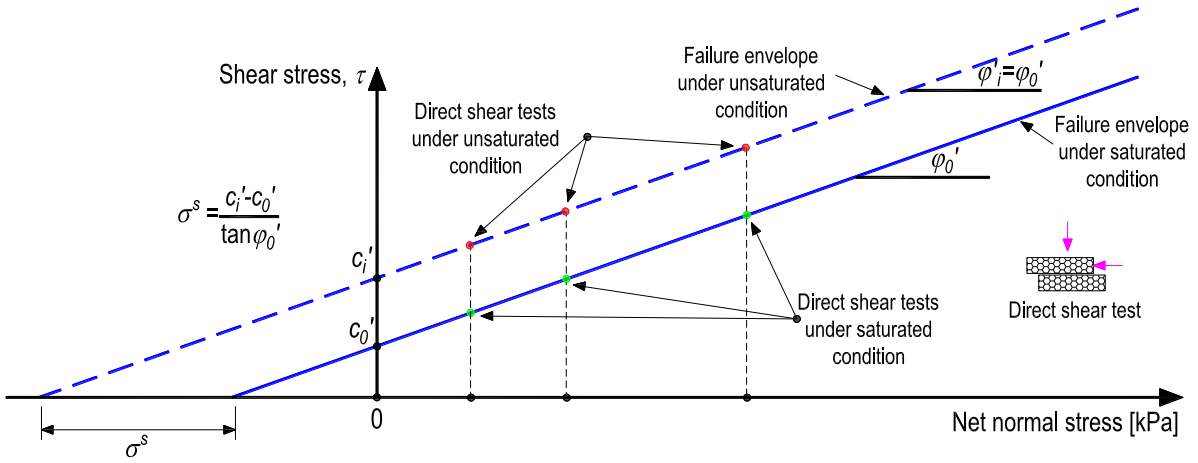

Figure 5.13.: Conceptual illustration for the determination of suction stress from direct shear test results, where dashed lines represent the test results in total stress, and solid lines represent the test results in effective stress (adapted from the concept of Lu & Likos 2004)

In Figure 5.13, c_i' is the cohesion at unsaturated condition (with results expressed in terms of total stress), meanwhile c_0' and φ_0' are the cohesion and the friction angle, respectively, derived from the DST at saturated conditions (with results expressed in terms of effective stress).

Table 5.4.: Shear strength parameters from different tests under saturated conditions

Parameter	Direct shear tests (10 x 10 x 2 cm)	Biaxial tests	Triaxial tests	Direct shear tests (6 x 6 x 2 cm)
c_0' (kPa)	59.5	19.87	7.36	3.1
φ_0' (°)	8.7	21.50	21.55	19.1

Under saturated conditions, the shear strength parameters are determined as $\varphi'_0 = 8.7°$ and $c'_0 = 59.5$ kPa. Table 5.4 shows a summary of shear strength parameters obtained from different types of tests under saturated conditions. The friction angle obtained from DST (10 x 10 x 2 cm) is much lower than that obtained from the biaxial compression tests (BCT) and triaxial compression tests (TCT). Meanwhile, the cohesion shows an opposite trend. On the other hand, a series of DST were conducted on saturated samples which have the same initial condition like DST (10 x 10 x 2 cm) but with dimensions of 6 x 6 x 2 cm using a conventional direct shear device (Wykeham Farrance Eng. Ltd., England). These tests were performed under the same net normal stress (50, 100, and 200 kPa) as those conducted on the larger samples (10 x 10 x 2 cm). The results of these tests are presented in the Appendix. In general, at a given net normal stress, the shear strength of the 10 x 10 x 2 cm samples is higher than that of the 6 x 6 x 2 cm samples. The cohesion of the larger samples ($c'_0 = 59.5$ kPa) is significantly higher than that of the smaller samples ($c'_0 = 3.1$ kPa), whereas the friction angle for the larger samples ($\varphi'_0 = 8.7°$) is considerably lower than that of the smaller samples ($\varphi'_0 = 19.1°$). This discrepancy may be attributed to boundary effects. The size of the direct shear sample influences the proximity of boundaries to the failure plane, where stress gradients and edge effects may impact the measured properties, as noted by Morgenstern & Tchalenko 1967. Another possible explanation is that the failure plane in smaller samples contains fewer aggregates compared to larger samples, leading to variations in the measured shear strength parameters. Cerato & Lutenegger (2006) investigated the influence of specimen size on the friction angle of sand and observed that for well-graded, angular sands, the friction angle decreases as sample size increases. Similarly, Dadkhah et al. (2010) examined the effect of shear box size on the shear strength parameters of clayey sand, reporting that larger and medium-scale direct shear boxes yielded higher cohesion and lower friction angles compared to small-scale direct shear boxes. On the other hand, unlike the device used for the larger samples (10 x 10 x 2 cm), where the load plate and upper frame of the shear box are fixed and not rotatable, the device used for the smaller samples (6 x 6 x 2 cm) is free for rotation of the load plate and upper frame of the shear box during testing. This potential rotation may have contributed to the differences observed in the shear strength parameters between these two test series. Although there is a discrepancy between the shear strength parameters as shown in Table 5.4, the stress-strain curves obtained from the DST (10 x 10 x 2 cm), as shown in section 4.6, indicate that the test series form a self-contained dataset. Moreover, the primary objective of these tests is to determine suction stress, which is calculated based on the difference between the

shear strength obtained under unsaturated conditions and that obtained under saturated conditions.

Figure 5.14a shows the relationship between shear strength (τ) and net normal stress ($\sigma - u_a$) from the tests series along the drying path (DS-D). Following the assumption within the framework of the effective stress concept in unsaturated soils, the friction angle derived from DST under unsaturated conditions, φ'_i, has been assumed to be equal to the friction angle at saturated conditions φ'_0 (i.e., the friction angle is considered constant regardless of variations in suction or water content). Consequently, only c'_i is considered to vary with suction or water content.

The linear fit lines are generated under this assumption. Figure 5.14b shows the cohesion, which was determined by extending the linear fit lines to their intersection with the vertical axis of shear strength, as a function of water content. Evidently, the shear strength and thus also cohesion increases with decreasing water content. Figure 5.14c shows a comparison between the tests series along the wetting (DS-W) and drying path in terms of shear strength versus net normal stress. The cohesion derived from the DS-W was obtained similarly to the DS-D and is shown in Figure 5.14d. In general, the shear strength and cohesion of samples in the drying path series (DS-D) is higher than that in the wetting path series (DS-W) which is attributed to hysteresis effects.

Figure 5.14e shows the suction stress as a function of water content, while Figure 5.14f presents the suction stress as a function of suction for both the DS-D and DS-W. Overall, the suction stress increases as water content decreases or suction increases. For the test series DS-D, suction stress increase gradually from the saturated condition to a water content of about 0.98% or suction of 98 MPa, followed by a sharp increase in suction stress as water content drops below 0.98% (ψ = 98 MPa). However, due to the lack of experimental data within the water content range of 10% to 32%, accurately assessing the trend of suction stress in this interval remains challenging. Therefore, conducting additional experiments within this range is recommended for future research.

5.6. Unconfined compression tests

In this section, the results of the unconfined compression test (UCT) series, as described in Section 4.7, are further analyzed with focus on the determination of suction stress. Firstly, the background to determine the suction stress from this kind of test is described. Secondly, the determined suction stress is presented.

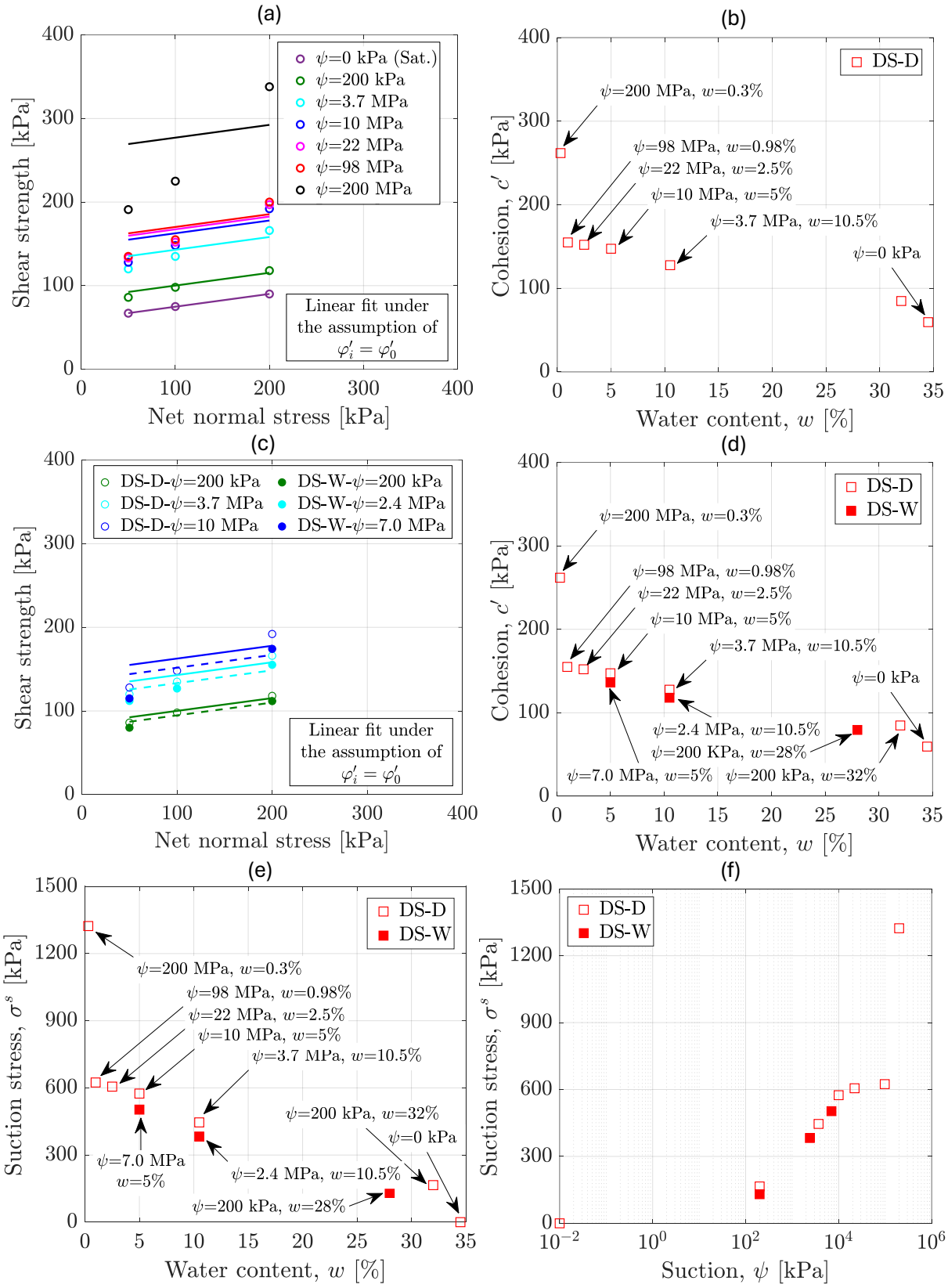

Figure 5.14.: (a),(c) Direct shear test results in τ vs. $(\sigma - u_a)$ space with linear fit lines of measured data (assuming a constant friction angle with varying suction), and (b), (d) cohesion, determined from the linear fit lines, as a function of water content, and (e), (f) suction stress as a function of water content and suction, respectively

Similar to the BCT, Figure 5.15 shows a projection of the failure surface under saturated and unsaturated conditions onto the shear stress against net normal stress plane. Suction stress σ^s is derived using Eq. 2.28 introduced in Section 2.8.2 of the State-of-the-art chapter. Again, the suction stress was calculated under the assumption that the friction angle is independent of variations in suction.

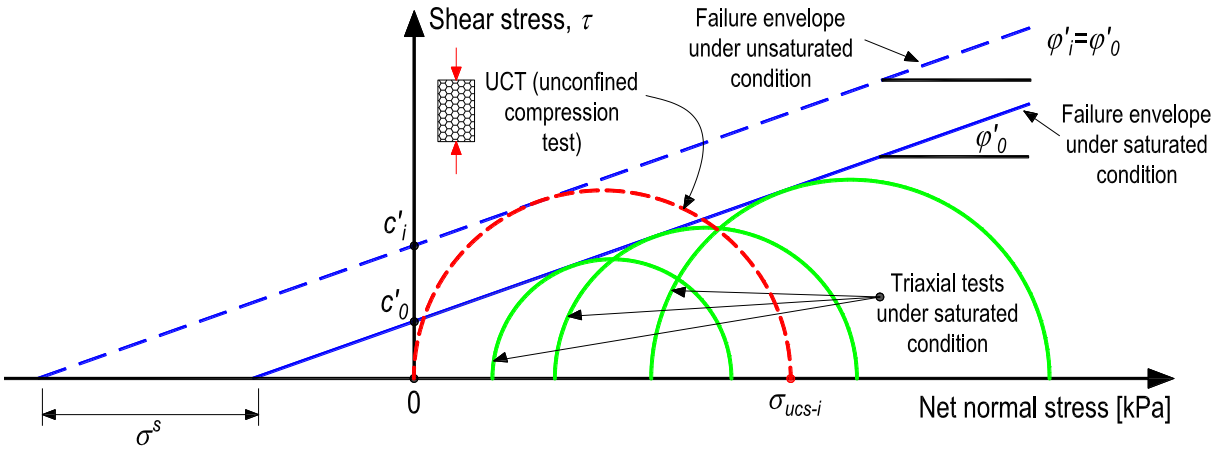

Figure 5.15.: Conceptual illustration for the determination of suction stress from unconfined compression test results, where dashed lines and circles represent the test results in total stress, and solid lines and circles represent the test results in effective stress (adapted from the concept of Lu & Likos 2004)

In Figure 5.15, c'_i is the apparent cohesion at unsaturated condition, meanwhile c'_0 and φ'_0 are shear strength parameters at saturated condition. Vanapalli & Fredlund (1997) determined the contribution of suction to the undrained shear strength at unsaturated conditions using the shear strength parameters derived from triaxial tests at saturated conditions. Similarly, in the current study, the same procedure was applied.

Figure 5.16a presents the suction stress derived from the test series conducted along the drying path (UC-D) and the wetting path (UC-W) as a function of water content, while Figure 5.16b shows the corresponding suction stress as a function of suction. In general, suction stress increases as water content decreases or suction increases. This trend aligns with the suction stress characteristic curve (SSCC) proposed for clayey soils by Lu & Likos (2006) and Lu et al. (2010). For both the drying and wetting paths, the SSCC exhibits a sigmoidal shape when plotted against water content or suction.

For the drying path, suction stress increases gradually as water content decreases from the initial condition to approximately 26% ($\psi \approx 1000$ kPa). In the range of 26% to about

2.5% water content, the slope of the SSCC decreases, indicating a slower rate of suction stress increase. When water content drops below 2.5% or suction exceeds approximately 22 MPa, suction stress rises sharply. It is important to note that the boundaries defining these regions are determined based on observable changes in the slope of the suction stress curve.

Similarly, for the wetting path, suction stress also increases gradually as water content decreases from the initial condition to approximately 26% ($\psi \approx 300$ kPa). Within the range of 26% to about 2.5% water content, a reduced slope is again observed, indicating a more gradual increase in suction stress. When water content falls below 2.5% or suction exceeds approximately 17 MPa, suction stress shows a sharp rise. As with the drying path, the regional boundaries are defined by changes in the slope and the general trend of the SSCC within each region.

The hysteresis effect on suction stress is evident along the drying and wetting paths within the water content range of approximately 28% to 5%. Outside of this range, the influence of hysteresis on suction stress becomes less pronounced.

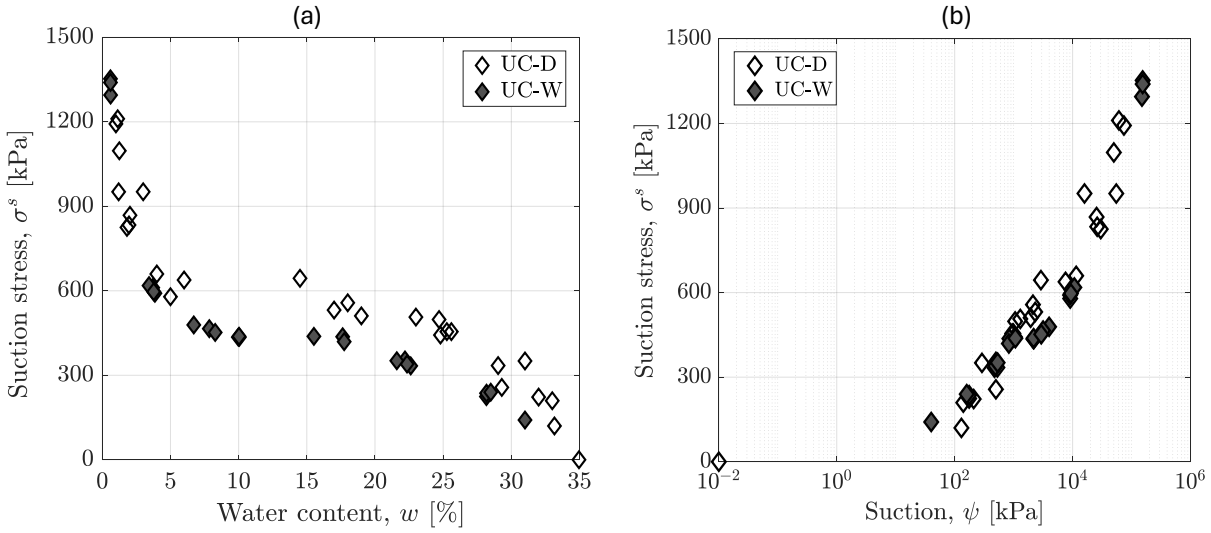

Figure 5.16.: Suction stress determined from unconfined compression tests along drying path and wetting path: (a) as a function of water content, and (b) as a function of suction

5.7. Uniaxial tensile tests

In this section, the results of uniaxial tensile test (UTT) series, as described in Section 4.8, are further analyzed with focus on the determination of suction stress derived from the UTT series.

Similar to BCT, DST, and UCT, the state of stress at failure for UTT may be represented by employing an extended Mohr-Coulomb diagram. A similar application was adopted by some previous studies (Lu & Likos 2006; Lu et al. 2009; Yin & Vanapalli 2018; and Salimi et al. 2021). Figure 5.17 shows a projection of the failure surface under saturated and unsaturated conditions onto the shear stress against net normal stress plane. σ_{uts-i} is the uniaxial tensile strength under unsaturated conditions, σ^s is calculated using Eq. 2.31 (see Section 2.8.2 of the State-of-the-art chapter). The suction stress was determined based on the assumption that the friction angle remains unchanged regardless of variations in suction. To calculate suction stress from uniaxial tensile tests, c'_0 and φ'_0 were obtained from the triaxial compression test series under saturated conditions.

Figure 5.18a presents the suction stress obtained from the test series conducted along the drying path (UT-D) and the wetting path (UT-W) as a function of water content, while Figure 5.18b depicts the corresponding suction stress as a function of suction. In general, suction stress increases as water content decreases or suction increases. This trend is consistent with the SSCC proposed for clayey soils by Lu & Likos (2006) and Lu et al. (2010).

For the drying path, suction stress increases gradually as the water content decreases from the initial condition to approximately 26% ($\psi \approx 1000$ kPa). Within the water content range of approximately 26% to 2.5%, the slope of the SSCC decreases, and suction stress fluctuates around 230 kPa. Finally, when the water content drops below 2.5% or suction exceeds approximately 22 MPa, suction stress exhibits a sharp increase, reaching up to 315 kPa.

For the wetting path, suction stress is generally similar to that obtained from the drying path up to a water content of approximately 27%. However, within the water content range of approximately 27% to 15%, suction stress remains mostly unchanged but is lower than that derived from the drying path. As the water content decreases below 15%, suction stress increases significantly, and when the water content drops below 10%, the suction stress derived from the wetting path becomes relatively similar to that from the drying path.

The hysteresis effect on suction stress is evident along the drying and wetting paths within the water content range of approximately 27% to 10%. Outside of this range, the influence of hysteresis on suction stress becomes less pronounced.

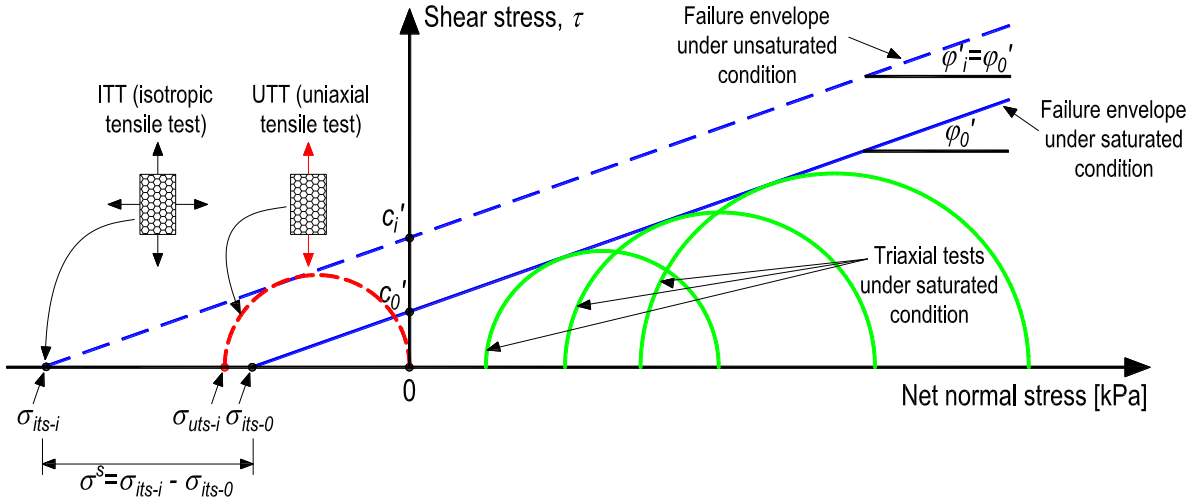

Figure 5.17.: Conceptual illustration for the determination of suction stress from uniaxial tensile test results, where dashed lines and circles represent the test results in total stress, and solid lines and circles represent the test results in effective stress (adapted from the concept of Lu & Likos 2004)

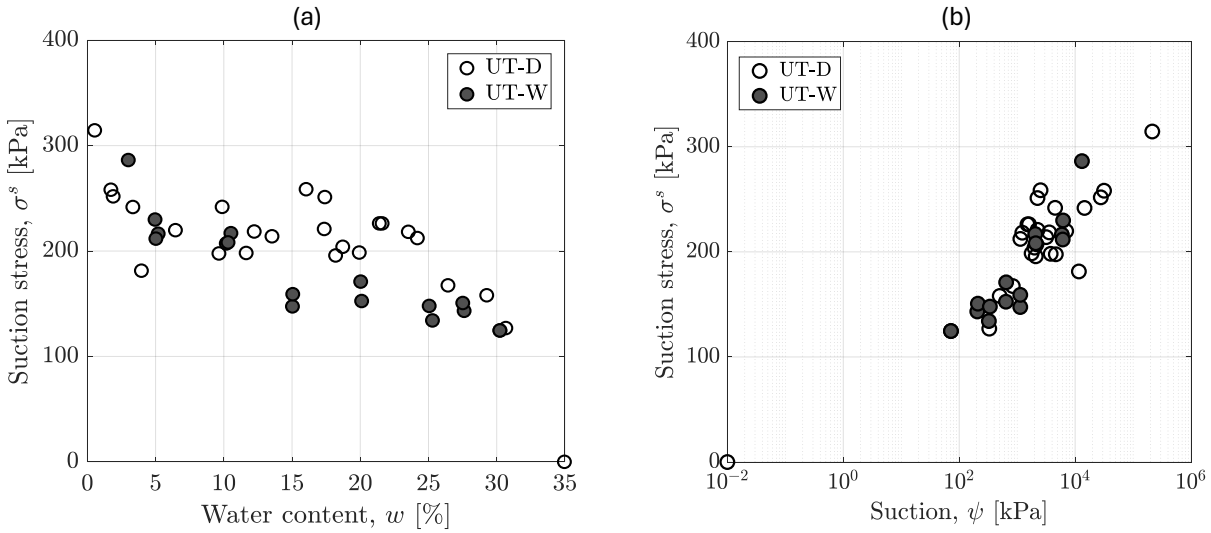

Figure 5.18.: Suction stress determined from uniaxial tensile tests along drying path and wetting path: (a) as a function of water content, and (b) as a function of suction

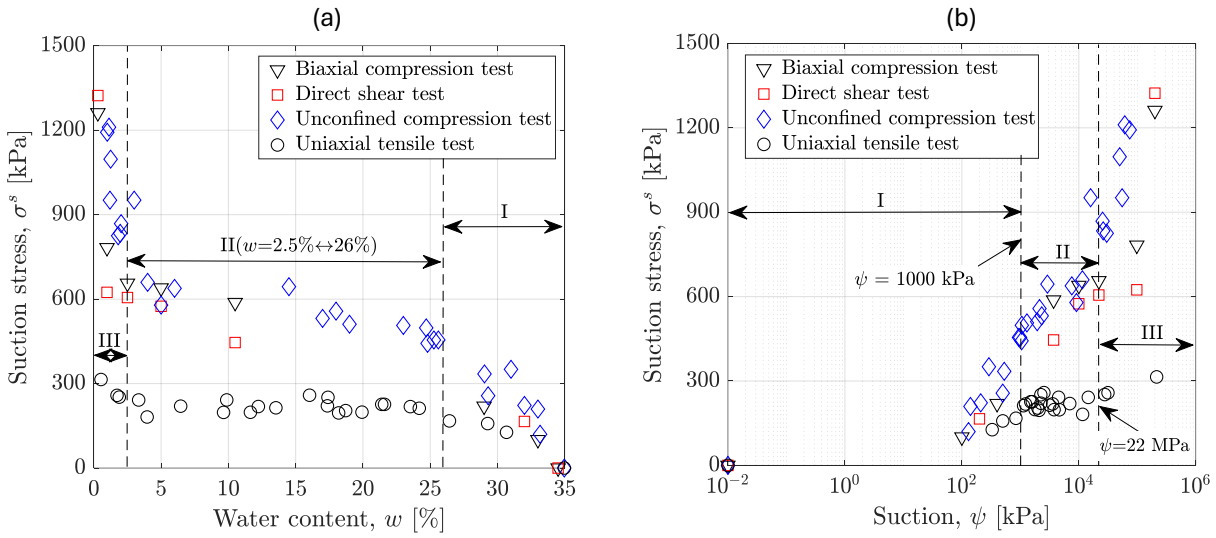

Figure 5.19.: Comparison of suction stress derived from different element tests along drying path: (a) as a function of water content, and (b) as a function of suction

5.8. Comparisons of measured suction stress derived from different element tests

Figure 5.19 compares suction stress derived from different test types as a function of water content (Fig. 5.19a) and suction (Fig. 5.19b) along the drying path. Similarly, Figure 5.20 presents a comparison of suction stress derived from different test types, also as a function of water content (Fig. 5.20a) and suction (Fig. 5.20b), along the wetting path. For the drying path, the suction stress characteristic curves (SSCC) can be divided into three distinct regions due to the change in slope of the SSCC. In region I, suction stress increases almost linearly as the water content decreases from the initial condition to approximately 26%. In region II, the slope of the suction stress curve decreases, indicating a more gradual increase in suction stress. Finally, in region III, when the water content drops below 2.5% or suction exceeds approximately 22 MPa, suction stress exhibits a sharp increase. For the wetting path, although only a limited number of experiments were conducted, the hysteresis effect within region III is not significant (as discussed above). By including the final measurement from the drying path, the trends of suction stress versus water content and suction on the wetting path closely resemble those observed on the drying path within these regions. Therefore, the same regional boundaries used for the SSCC on the drying path were also applied to the wetting path.

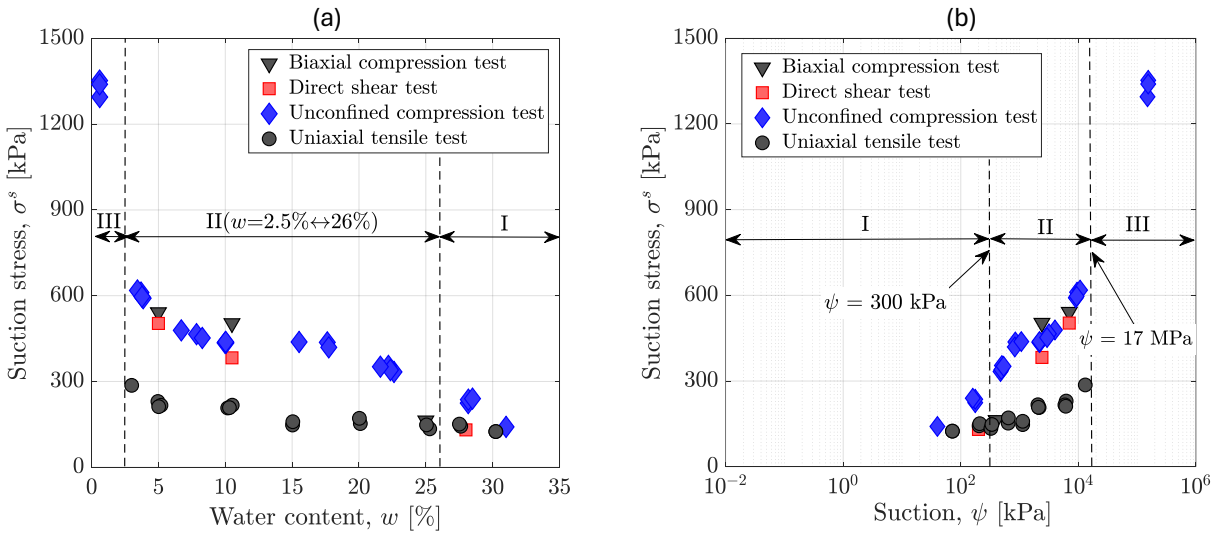

Figure 5.20.: Comparison of suction stress derived from different element tests along wetting path: (a) as a function of water content, and (b) as a function of suction

In general, suction stress derived from uniaxial tensile tests (UTT) is significantly lower than that obtained from shear tests conducted in the compression regime (BCT, DST, and UCT), as observed in both the drying and wetting paths.

For the drying path:

- In region I, the ratio of suction stress from the shear tests in the compression regime to that from the UTT gradually increases from 1 to approximately 2.2.
- In region II, this ratio increases slightly from about 2.2 to 2.6.
- In region III, as the water content decreases further or suction increases, the ratio rises sharply from approximately 2.6 to 4.3.

For the wetting path:

- In region III, although tensile test data are unavailable at very dry states, considering the final measurement from the drying path as the starting point for the wetting path, the ratio of suction stress derived from shear tests to that from the UTT ranges approximately from 4.3 to 2.
- In region II and I, the ratio of suction stress from the shear tests (BCT, DST, and UCT) to that from the UTT gradually decreases from 2 to around 1.

This discrepancy is primarily attributed to the different interparticle forces that dominate at failure. As noted by Khalili et al. (2022), physicochemical effects are predomi-

nantly intra-aggregate phenomena. In tensile tests, the failure plane may form between aggregates, meaning that only large-pore (inter-aggregate) capillary forces contribute significantly to suction stress. In contrast, during shear tests conducted under compression, physicochemical forces cause aggregates to behave like pseudo-grains. This results in interlocking between aggregates, which enhances the shear resistance of the soil during deformation. The development of the failure plane is associated with the rolling or breakage of these aggregates. As water content decreases and suction increases within the aggregates, physicochemical forces become more dominant, leading to stiffer pseudo-grain behaviour. Consequently, suction stress derived from shear tests in the compression regime is generally higher than that obtained from tensile tests. Pourzargar (2017) measured suction stress using both tensile and triaxial tests on compacted kaolin and also observed discrepancies between the results obtained from these two types of tests. The author attributed these differences to the structure of compacted kaolin. Specifically, tensile strength is primarily influenced by soil-water interactions within relatively large inter-aggregate pores, where large-pore capillary forces are dominant. In contrast, shear strength is significantly affected by interactions within small intra-aggregate pores, where both small-pore capillary forces and physicochemical forces are dominant, leading to higher suction stress values.

On the other hand, on the drying path, suction stress derived from the biaxial compression tests (BCT), the direct shear tests (DST), and the unconfined compression tests (UCT) are relatively similar in regions I and II. An exception is the suction stress derived from DST at 10.5% ($\psi = 3.7$ MPa), which is significantly lower than that from the other shear tests. However, in region III, where physicochemical forces dominate (Lu & Likos 2006, Vesga 2008, Lu et al. 2010, Akin & Likos 2020), the suction stress derived from DST remains lower than that obtained from BCT, which in turn is lower than that from UCT. On the wetting path, in general, the difference between the suction stress from BCT, DST, and UCT is less pronounced in region I and II. However, due to the lack of the experiments in region III, it is difficult to assess the differences in suction stress between these tests.

The difference between the suction stresses in region III along the drying path among the shear tests in the compression regime is attributed to the following possible reasons: Different stress conditions and failure strains (with failure strain in BCT being approximately twice as high as in UCT, see Fig. 4.19 and Fig. 4.38) lead to different structural developments within the shear zones. Larger deformations under more constrained conditions may result in more localized behaviour and greater changes in the shear zone

structure. These changes may include an increase in particle spacing, thereby reducing van der Waals forces. Moreover, some water bridges between particles in slit pores may break, decreasing the number of active force-transmitting contacts. This effect is likely even more pronounced in the DST, where shear deformation is concentrated along a predefined failure plane, often accompanied by significant dilation within the shear band. Such highly localized movement disrupts capillary bridge continuity and weakens interparticle attractions, leading to the lowest suction stress observed among the three test types. Based on a thermodynamic treatment, Jiang et al. (2017) concluded that the contribution of interparticle forces to the effective stress - through the effective stress parameter χ or suction stress - depends on the soil porosity, which can vary during loading. This implies that local variations in void ratio or pore structure during deformation can lead to different suction stress values.

Additionally, a significant increase in the friction angle was observed in the low water content region (i.e., from the end of region II to region III) in both the BCT (see Fig. 4.21) and DST (see Fig. 4.33). As explained above, at higher suction levels, physicochemical forces within aggregates become more dominant (Khalili et al. 2022), causing aggregates to behave increasingly like stiff pseudo-grains, which alters the shear behaviour significantly. The material becomes more brittle, and the friction angle increases accordingly. These differences lead to variations in the dominant interparticle forces and thus in the magnitude of the suction stress derived. Additionally, the number of aggregate-to-aggregate contacts and the relative influence of different interparticle forces on shear zone behaviour may vary depending on the specific test method employed.

Thus, the deviations in suction stress in region III reflect how different loading conditions influence the development of soil structure and the effectiveness of interparticle forces under unsaturated conditions especially within the suction range where the physicochemical forces are dominant. An effective approach to capturing the rearrangement of particles or aggregates within shear zones under different test conditions is to perform morphological analysis using techniques such as Environmental Scanning Electron Microscopy (ESEM) or morphological method. These methods enable direct visualization of particle orientations, contact points, and potential fabric changes induced by shear deformation. By comparing ESEM images or morphological methods taken after testing, in particular from regions surrounding the shear zone across different test types, valuable insights can be gained into how various loading conditions influence microstructural evolution and interparticle forces.

At very high suctions (about 200 MPa), nearly all water is retained in micropores, stabilizing both void ratio and suction stress across all tests, explaining the eventual convergence of values.

To conclude, as outlined in Chapter 1, it is expected that suction stress derived from different test types on the same soil under identical conditions should be consistent over a wide suction range. However, the results of this study reveal that suction stress obtained from uniaxial tensile tests differs significantly from that derived from shear tests conducted in the compression regime. This discrepancy raises questions about the uniqueness and general applicability of the effective stress concept in unsaturated soils. Nevertheless, when considering only the shear tests in the compression regime (i.e., BCT, DST, and UCT), the suction stress values are in relatively good agreement up to a suction level of approximately 10 MPa. Beyond this threshold, however, noticeable deviations in suction stress among these tests emerge, further challenging the validity of the effective stress concept at higher suctions. In addition, the results from BCT and DST indicate a significant increase in the friction angle at high suction levels. This observation challenges the validity of the constant friction angle assumption when applying the effective stress concept to unsaturated soils.

6. Prediction of suction stress

6.1. Introduction

As outlined in the introduction of this thesis, a comprehensive experimental and analytical framework has been established to validate the effective stress concept through the suction stress approach. The previous chapter (Chapter 5) presented the suction stress values (σ^s) derived from various element tests, highlighting both the validity and limitations of the effective stress concept. This chapter focuses on the application of two well-established theoretical equations - those proposed by Khalili & Khabbaz (1998) and Lu et al. (2010) - to predict suction stress. A subsequent comparison between the measured and predicted suction stress values is presented. Additionally, the measured suction stress is fitted to a new equation proposed by Zhang & Lu (2020), which allows for a quantitative separation of capillary and adsorption contributions within the overall suction stress formulation.

6.2. Prediction of suction stress

6.2.1. Khalili & Khabbaz (1998)'s equation

As discussed in the State-of-the-art chapter, Khalili & Khabbaz (1998) proposed an equation (Eq. 2.19) to determine the effective stress parameter X. This equation was originally formulated for the drying path using ψ_{AEV}. In this study, the same equation is also applied to the wetting path, incorporating ψ_{AExV}. Consequently, suction stress was computed using Eq. 2.20, as outlined in the State-of-the-art chapter.

Figure 6.1a illustrates the variation of the effective stress parameter X along both the drying and wetting paths as a function of suction, while Figure 6.1b presents the corresponding suction stress response. As depicted in Figure 6.1a, X remains equal to 1 within the suction range from zero to $\psi_{AEV} = 650$ kPa for the drying path and $\psi_{AExV} = 400$ kPa for the wetting path. Beyond these threshold values, X decreases significantly. Con-

sequently, the suction stress σ^s is equal to the suction when the suction is below ψ_{AEV} in the drying path and ψ_{AExV} in the wetting path. As suction increases beyond these values, the suction stress characteristic curves (SSCC) deviate from the 1:1 line, as shown in Figure 6.1b. Furthermore, Figure 6.1c illustrates the SSCC in terms of suction stress versus water content. In general, the SSCC exhibits a sigmoidal shape, similar to the soil-water characteristic curve (SWCC). The maximum suction stress reaches approximately 17 MPa along the drying path and around 13 MPa along the wetting path.

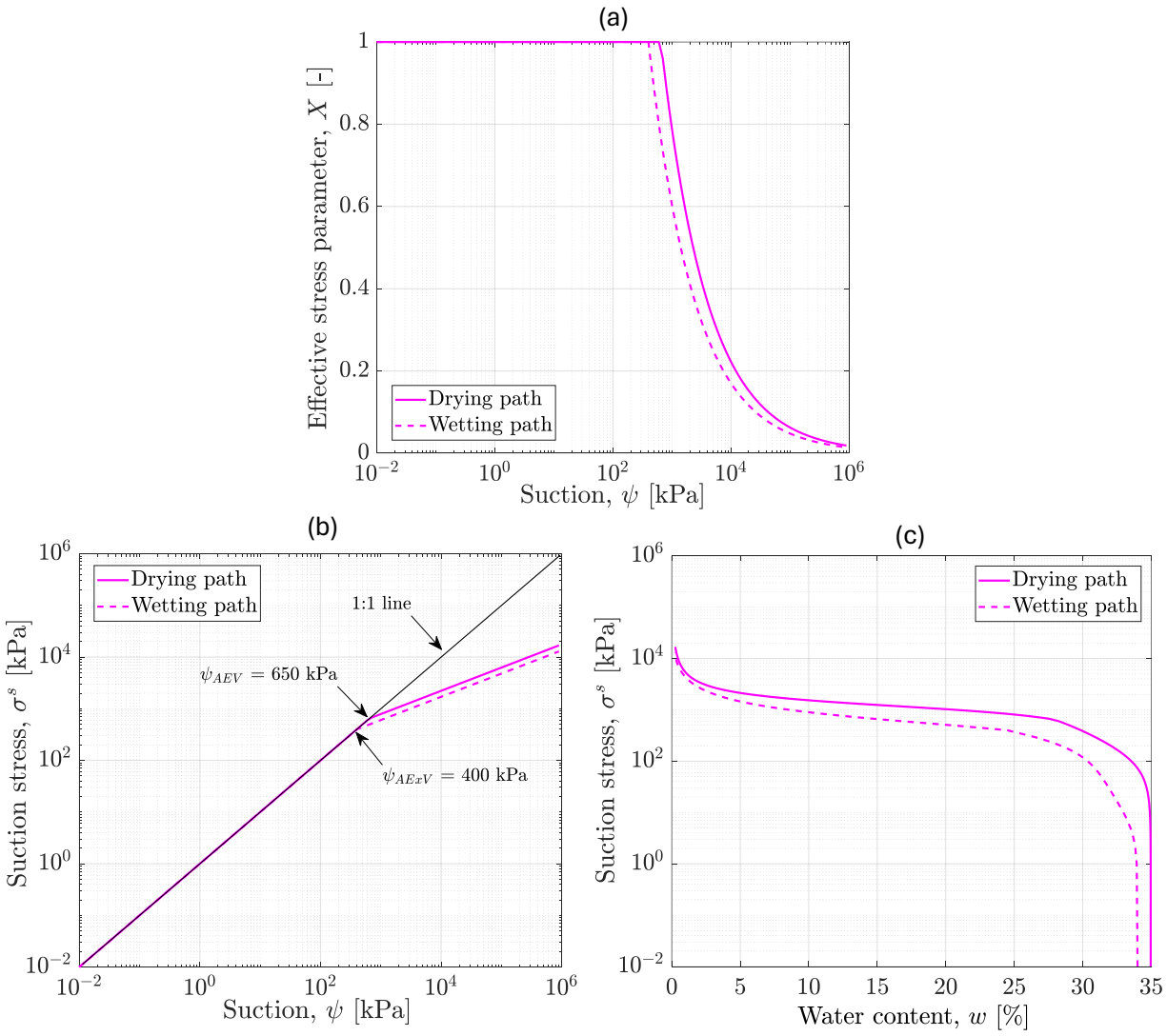

Figure 6.1.: Determination of suction stress along the drying and wetting path using the equation of Khalili & Khabbaz (1998): (a) effective stress parameter as a function of suction, (b) suction stress as a function of suction, and (c) suction stress as a function of water content

6.2.2. Lu et al. (2010)'s equation

As discussed in the State-of-the-art chapter, Lu et al. (2010) proposed an equation (Eq. 2.21) to determine suction stress by adopting the effective degree of saturation, S_e, from the soil-water characteristic curve (SWCC) model introduced by Van Genuchten (1980) (see Eq. 2.6) as the effective stress parameter, X. This equation was originally formulated for the drying path, but a similar approach has been applied to the wetting path in several studies (Oh & Lu 2014; Almahbobi 2018).

In this study, in addition to adopting S_e from the SWCC model by Van Genuchten (1980), suction stress was also calculated using S_e derived from the SWCC model proposed by Durner (1994) (see Eq. 2.9), which considers a bimodal SWCC, as described in the State-of-the-art chapter. This is because the model by Durner (1994) provides the best fit to both the drying and wetting paths of the measured SWCC. The fitting parameters used to derive S_e are presented in Table 4.1.

Figure 6.2a presents the effective stress parameter, derived from the fitted curves of the Van Genuchten (1980) and Durner (1994) models, as a function of suction. Figure 6.2b displays the suction stress characteristic curve (SSCC) in terms of suction stress versus suction, while Figure 6.2c illustrates the SSCC in terms of suction stress versus water content. As shown in Fig. 6.2a, along the drying path, the X (or S_e) derived from the model of Durner (1994) is higher than that from the model of Van Genuchten (1980) within the suction range of approximately 500 kPa to 5 MPa. Conversely, along the wetting path, the X derived from Van Genuchten (1980) remains higher than that from Durner (1994) across the entire suction range.

As illustrated in Fig. 6.2b, suction stress increases with increasing suction. In general, suction stress is approximately equal to suction up to about 300 kPa along the drying path and up to about 100 kPa along the wetting path. Beyond these suction thresholds, the SSCC deviates from the 1:1 line. Figure 6.2c further confirms that the SSCC exhibits a sigmoidal shape, consistent with the trend of the SSCC predicted using the equation proposed by Khalili & Khabbaz (1998). Notably, the SSCC displays hysteresis between the drying and wetting paths, similar to the behavior observed in the SWCC. The maximum suction stress is approximately 6.5 MPa for the drying path and 6.0 MPa for the wetting path, which are significantly lower than the maximum suction stress values obtained using the equation by Khalili & Khabbaz (1998).

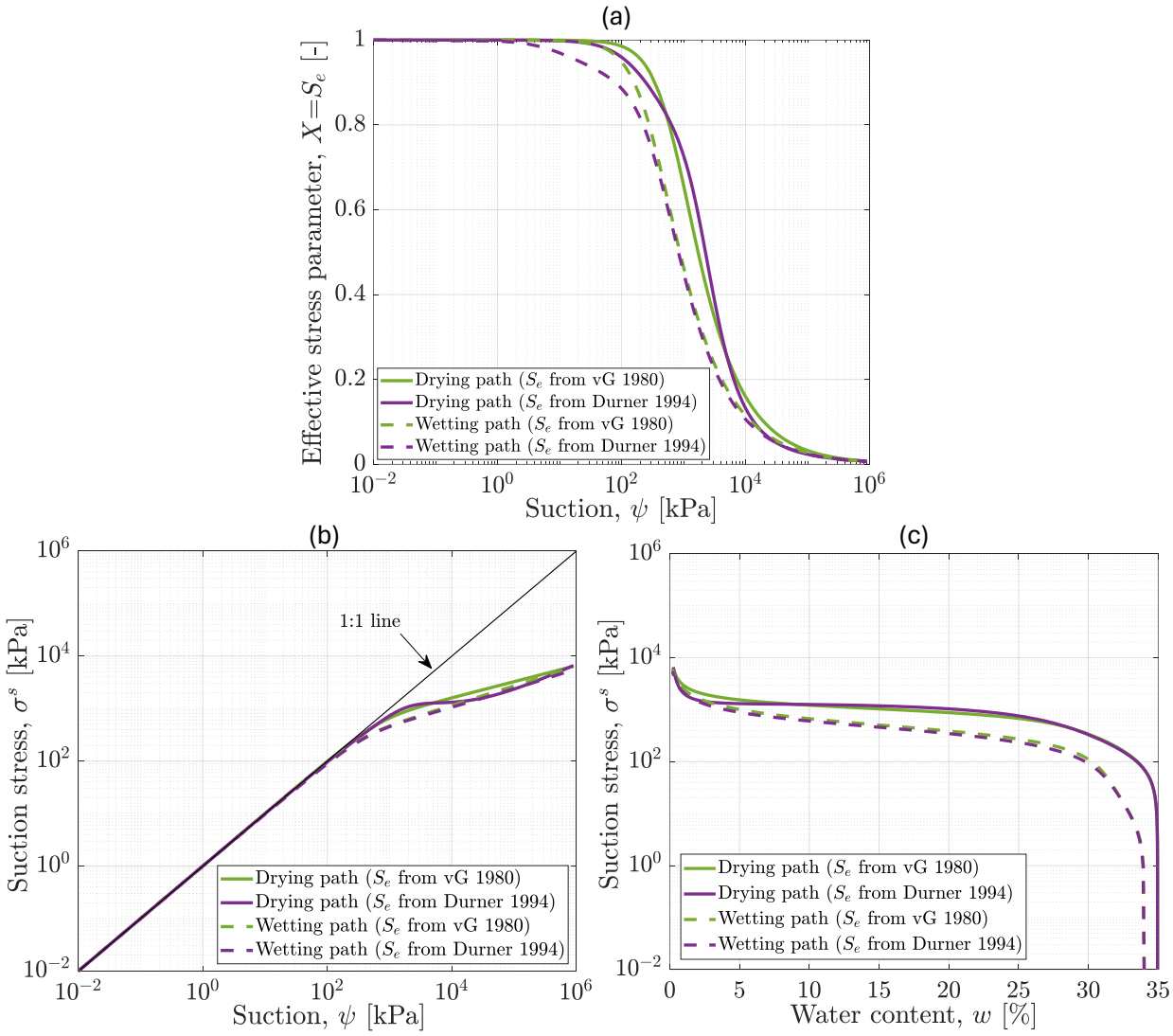

Figure 6.2.: Determination of suction stress along the drying and wetting path using the equation of Lu et al. (2010): (a) effective stress parameter as a function of suction, (b) suction stress as a function of suction, and (c) suction stress as a function of water content

6.3. Comparison between predicted and measured suction stress

This section presents a comparison between predicted and measured suction stress. For the drying path, Figure 6.3 shows the comparison between measured and predicted suction stress in terms of suction (Fig. 6.3a) and water content (Fig. 6.3b). In general, all predicted SSCCs exhibit higher values than the measured suction stress obtained from uniaxial tensile tests (UTT). However, the SSCC predicted using the equation by Khalili

& Khabbaz (1998) aligns relatively well with the suction stress derived from the shear tests in the compression regime (i.e., BCT, DST, and UCT) up to a suction of approximately 400 kPa, corresponding to a water content of about 29.8%. Similarly, the SSCC predicted using the equation by Lu et al. (2010) matches relatively well the suction stress derived from this test group up to a suction of approximately 500 kPa, corresponding to a water content of about 28.5%. However, beyond these threshold values, all prediction equations tend to overestimate the measured suction stress. The fact that many validation studies were limited to suctions lower than or close to these values may explain why this overestimation behaviour has not been widely recognized in previous research.

Despite the significant overestimation of suction stress at higher suction values, the bimodal approach, in which S_e is derived from the SWCC model proposed by Durner (1994), successfully captures the plateau-like behavior of suction stress within the water content range of 26% to 2.5%. Additionally, this approach accurately reproduces the sharp increase in suction stress observed at water contents lower than 2.5%.

For the wetting path, Figure 6.4 presents the comparison between measured and predicted suction stress in terms of suction (Fig. 6.4a) and water content (Fig. 6.4b). The equation proposed by Khalili & Khabbaz (1998) accurately predicts the suction stress derived from the UTT up to a suction of 100 kPa and the suction stress derived from the UCT up to a suction of approximately 200 kPa. Meanwhile, the equation proposed by Lu et al. (2010) provides reasonable predictions for the suction stress obtained from the UTT and DST up to a suction of 200 kPa, as well as for the suction stress derived from the UCT up to a suction of approximately 1000 kPa. Beyond these threshold values, all predictive equations tend to overestimate the measured suction stress. Due to the absence of experimental data between 400 kPa and 1000 kPa for the DST and BCT, a definitive assessment of the validity of these predictive methods for these tests remains inconclusive.

By conducting a series of triaxial compression tests on silt material, Alsherif & McCartney (2014) observed that the equation proposed by Lu et al. (2010) tends to overestimate the measured suction stress at very low water contents or high suction levels. Similarly, Pourzargar (2017) compared suction stress derived from tensile and triaxial compression tests with predicted values using the equation by Lu et al. (2010). The author reported that the measured and predicted suction stress aligned reasonably well over a wide range of degrees of saturation (or suction) for pure sand and a sand-kaolin mixture (70% sand + 30% kaolin). However, as the kaolin content increased (50% sand + 50% kaolin), the equation accurately predicted suction stress from triaxial tests but overestimated values derived from tensile tests across a degree of saturation range from 1 to 0.05. Akin & Likos

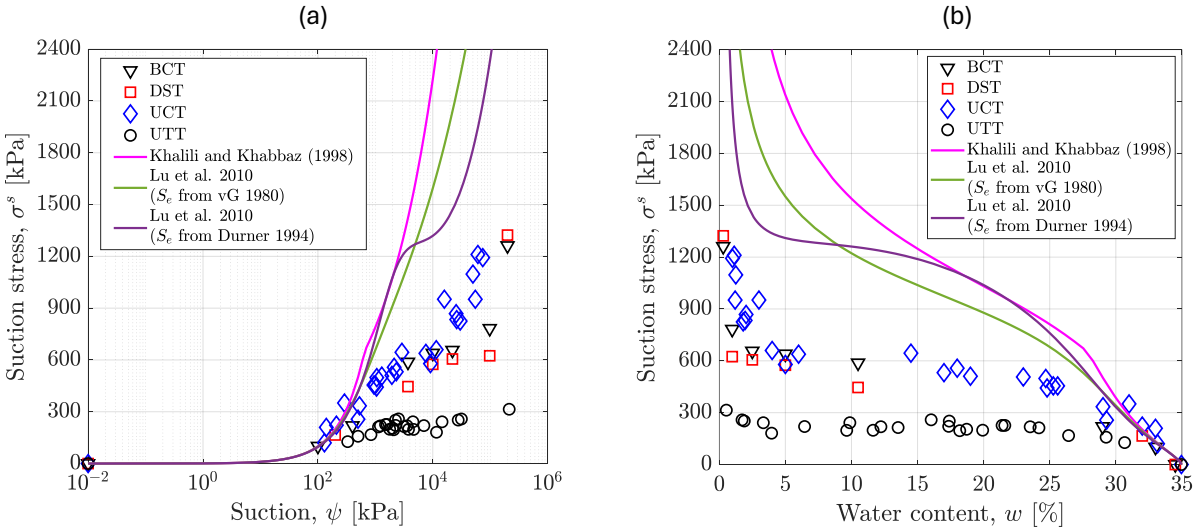

Figure 6.3.: A comparison of suction stress derived from different element tests along drying path: (a) as a function of water content, and (b) as a function of suction

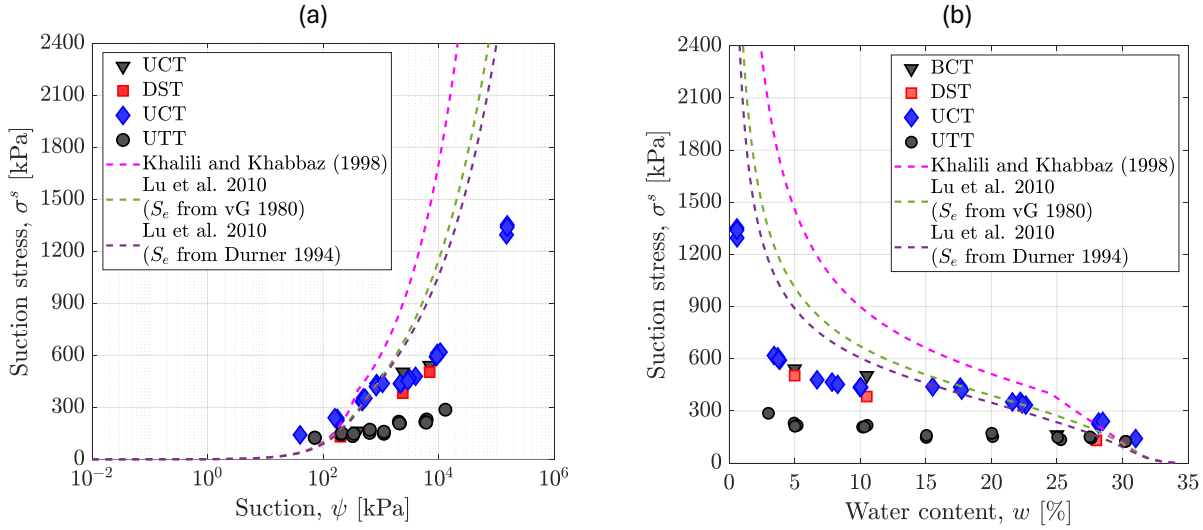

Figure 6.4.: A comparison of suction stress derived from different element tests along wetting path: (a) as a function of water content, and (b) as a function of suction

(2020) also intended to validate the equation by Lu et al. (2010) and found that, for coarse-grained soils such as sands and gravels without fines, the equation predicts suction stress accurately. However, for clayey soils, it overestimates suction stress at intermediate and high suction levels. They concluded that capillary internal forces dominate water retention in fine-grained soils at high saturation, while short-ranged adsorption forces, which become significant at intermediate to low saturation, are not effectively captured

by the equation. Niu et al. (2024) conducted a series of triaxial compression tests on Nanyang weakly expansive soil samples to validate predictive suction stress equations by comparing measured and predicted shear strengths. Their findings indicated that the predictive equation based on the method by Khalili & Khabbaz (1998) provided reasonable results up to a suction of 38 MPa. As shown in Figures 6.3 and 6.4, the findings of the present study further confirm these conclusions, highlighting the limitations of existing suction stress equations. Jiang et al. (2017) emphasized that current formulations for the effective stress parameter or suction stress neglect the effect of changes in soil porosity during loading, and therefore fail to adequately capture both shear failure and volumetric responses.

These observations underscore the need for future research to refine existing suction stress equations or to develop new formulations that can more accurately represent measured suction stress at intermediate and high suction levels. Furthermore, future models should consider the influence of varying loading conditions on suction stress magnitude to improve predictive capability across different testing scenarios.

6.4. Application of Zhang & Lu (2020) SSCC equation

As discussed in the State-of-the-art chapter, Zhang & Lu (2020) proposed an equation to determine suction stress as a function of water content (see Eq. 2.22 to 2.26). A key advantage of this equation, compared to the suction stress equation introduced by Lu et al. (2010), is its ability to quantitatively separate the contributions of capillary and adsorption effects within the overall suction stress formulation. However, this equation requires measured suction stress values and cannot directly predict suction stress. Table 6.1 provides the fitting parameters obtained by applying the suction stress equation from Zhang & Lu (2020) to measured suction stress from the BCT, DST, UCT, and UTT.

For the drying path, Fig. 6.5 presents the best-fit results of the equation with suction stress derived from the BCT, DST, and UCT test group (Fig. 6.5a) and from the tensile test (Fig. 6.5b). Similarly, for the wetting path, Fig. 6.6 shows the best-fit results with suction stress derived from the BCT, DST, and UCT test group (Fig. 6.6a) and from the UTT (Fig. 6.6b). The equation of Zhang & Lu (2020) can reproduce quite well the experimental data of the present study. In addition, the suction stress derived from the BCT, DST and UCT can be described reasonably well by the same set of parameters, while a separate set of parameters is needed for the UTT.

As illustrated in these figures, capillary suction stress dominates within the water content range from the saturated state to approximately 5%. As the water content decreases below 5%, capillary suction stress diminishes significantly. Zhang & Lu (2020) suggested that, in clayey soils, the presence of very fine particles leads to the formation of extremely small capillary pores capable of generating high tensile stresses. However, the water subjected to these high tensile stresses exists in a metastable state and may undergo cavitation below the cavitation pressure, a phenomenon not accounted for in the suction stress equation of Lu et al. (2010).

As the water content decreases below 5%, adsorptive suction stress increases sharply. Adsorptive suction stress primarily originates from van der Waals attraction, electrical double-layer (EDL) repulsion, and pore water pressure between adjacent particles (Lu & Likos 2006; Zhang & Lu 2020). These forces strongly depend on the interparticle distance. At low water content, the reduced distance between clay particles alters the balance between interparticle forces. As water content decreases, the diffuse double-layer thickness contracts, reducing electrostatic repulsion and allowing particles to move closer together (Lu & Zhang 2019). This increased proximity enhances van der Waals attractive forces, leading to particle aggregation (Mitchell & Soga 2005) and the formation of a denser, more interlocked soil structure (Chowdhury & Azam 2016; Cheng et al. 2024). This phenomenon is supported by the particle size distribution (PSD) determination result at low water content, which exhibits a distinct bimodal pattern indicative of aggregate formation. During wetting, this bimodal distribution transitions back to a unimodal state. The dominance of attractive forces at low water content results in stronger interparticle contacts, contributing to higher shear strength and increased apparent cohesion in compacted kaolin, thereby leading to higher suction stress.

Table 6.1.: Fitting parameters obtained by applying the suction stress equation of Zhang & Lu (2020) to measured suction stress data from BCT, DST, UCT, and UTT

Parameter	Drying path		Wetting path	
	BCT, DST, UCT	UTT	BCT, DST, UCT	UTT
w_s [-]	0.35	0.35	0.34	0.34
w^{ss}_{tran} [-]	0.025	0.025	0.025	0.025
α^{ss} [-]	0.0016	0.0036	0.0025	0.005
n^{ss}	2.021	2.101	1.869	1.944
β [-]	2.5	3.8	2.2	4
σ^s_{dry} [kPa]	1312.3	314	1312.3	314

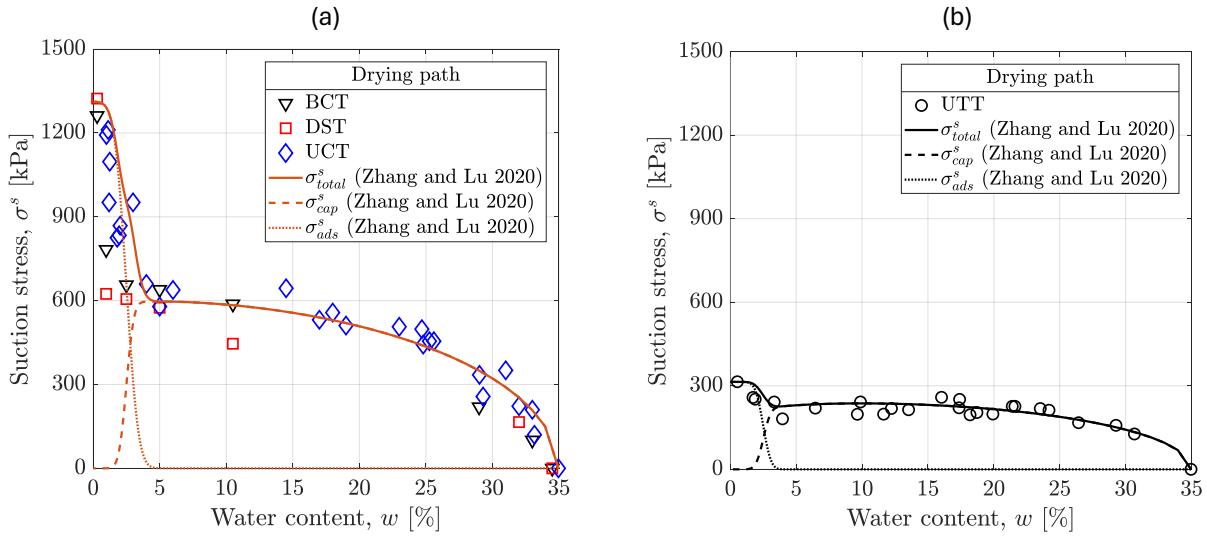

Figure 6.5.: Fitting of the equation of Zhang & Lu (2020) to the data of suction stress derived from different element tests along drying path: (a) data from BCT, DST and UCT, and (b) data from UTT

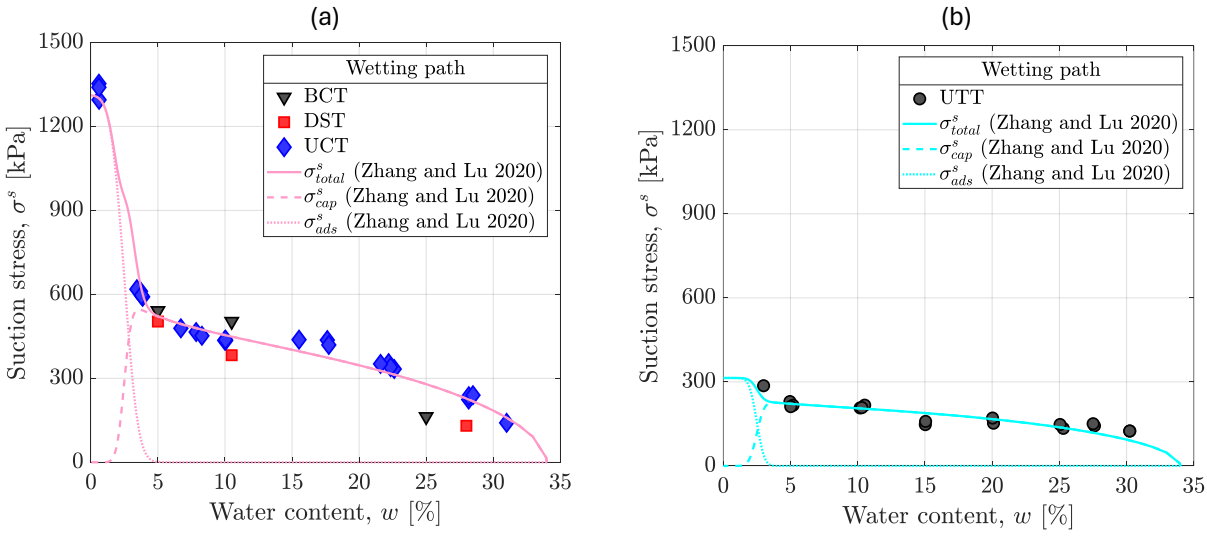

Figure 6.6.: Fitting of the equation of Zhang & Lu (2020) to the data of suction stress derived from different element tests along wetting path: (a) data from BCT, DST and UCT, and (b) data from UTT

7. Conclusions and recommendations

7.1. Summary and conclusion

Terzaghi (1936)'s effective stress principle was extended to unsaturated soils by Bishop (1959), who introduced an effective stress parameter, χ, to account for the influence of suction on soil strength and deformation. Building on this, Lu & Likos (2006) and Lu et al. (2010) proposed a micromechanical framework introducing the concept of suction stress, a macroscopic stress variable that incorporates both capillary and physicochemical interactions. This framework offers a direct means of quantifying the portion of suction that contributes to effective stress. Various formulations have since been proposed to evaluate either the effective stress parameter χ or suction stress itself.

Experimentally, suction stress is typically determined by comparing the mechanical response of unsaturated soils to that under saturated conditions. Ideally, when initial conditions such as structure, void ratio, degree of saturation, and suction are identical, suction stress derived from different test methods on the same soil should yield consistent results across a wide suction range. However, most previous investigations have been based on a single type of test and have been limited to relatively low suction levels (generally below 1500 kPa), which limits their generalizability. To date, a thorough experimental study incorporating multiple testing methods over an extended suction range is still lacking, yet remains essential for validating the uniqueness and applicability of the effective stress concept in unsaturated soils.

To address these gaps, this study established a comprehensive experimental dataset by conducting multiple laboratory tests, including biaxial compression tests (BCT), direct shear tests (DST), unconfined compression tests (UCT), and uniaxial tensile tests (UTT). These tests were performed on compacted Amberger kaolin along both drying and wetting paths, covering a wide range of suction levels. Suction stress values derived from different test types were systematically compared. Additionally, selected predictive equations for suction stress were applied and evaluated against the experimental data.

To support the main objective, detailed investigations of the soil-water characteristic curve (SWCC), soil shrinkage curve (SSC), and pore-size distribution (PSD) were also conducted. These complementary characterizations are essential for applying various models to predict suction stress and for gaining deeper insight into the macroscopic behaviour of the tested material.

The key findings from this study are categorized and summarized in the following.

7.1.1. Validity of the effective stress concept over a wide suction range

1. The results from biaxial compression tests (BCT) and direct shear tests (DST) in this study indicate a significant increase in the friction angle at high suction levels. However, the stress state at failure (e.g., obtained from shear or tensile tests) is commonly represented using an extended Mohr-Coulomb framework, in which the friction angle is typically assumed to remain constant regardless of suction level. The observation of increasing friction angle at higher suction levels (above 10 MPa in BCT and 3.7 MPa in DST) challenges the validity of the constant friction angle assumption when applying the effective stress concept to unsaturated soils. Nevertheless, in line with the conventional assumption of a constant friction angle, suction stress values were derived from various element tests.

2. Suction stress derived from uniaxial tensile tests differs markedly from that obtained from shear tests conducted in the compression regime (i.e., BCT, DST, and UCT). This discrepancy is primarily attributed to the different interparticle forces that dominate at failure. In tensile tests, the failure plane often develops between aggregates, where only capillary forces within large inter-aggregate pores contribute to suction stress. Conversely, in shear tests under compression, physicochemical interactions cause aggregates to behave as pseudo-grains, promoting interlocking between them and enhancing shear resistance. As a result, suction stress derived from shear tests in the compression regime is consistently higher than that from tensile tests. This notable difference sets into question the uniqueness and broad applicability of the effective stress concept in unsaturated soils.

3. For the shear tests conducted in the compression regime (i.e., BCT, DST, and UCT), the suction stress values derived from the different types of tests show relatively good agreement up to a suction level of 10 MPa. However, beyond this threshold, noticeable deviations emerge among the test results. These discrepancies are attributed

to differences in stress conditions and strain levels at failure, which lead to varying structural developments within the shear zones. This observation further challenges the validity and applicability of the effective stress concept at higher suction levels.

7.1.2. Validation of several suction stress equations

1. The suction stress characteristic curve (SSCC) of the studied soil was predicted using two well-established equations: the model proposed by Khalili & Khabbaz (1998) and the closed-form equation by Lu et al. (2010). The results indicate that both predictive equations align reasonably well with the measured suction stress in the high water content region (i.e., at low suction levels). However, at intermediate and low water contents (corresponding to intermediate and high suction levels), both models significantly overestimate suction stress. This discrepancy may be attributed to the omission of short-ranged adsorption forces, which become increasingly dominant at intermediate to high suction levels (Akin & Likos, 2020). Another possible explanation is the neglect of changes in soil porosity during loading, a factor highlighted by Jiang et al. (2017) as critical in accurately capturing suction stress behaviour.
2. While the model proposed by Zhang & Lu (2020) provided a good fit to the experimentally derived suction stress values, it is important to note that this model requires measured suction stress data and, therefore, cannot directly predict suction stress without prior experimental input. However, it allows for a quantitative separation of capillary and adsorption contributions within the overall suction stress formulation.

7.2. Recommendations

Although an exhaustive experimental study was carried out during the course of this research, certain recommendations may be made for future work building up on the results, some of which are as follows:

1. Future research should include additional experiments using BCT and DST at intermediate and high suction levels to better assess the extent of the discrepancy between the suction stress derived from these tests and that obtained from UCT and UTT.

2. One approach to capturing the rearrangement of particles or aggregates in shear zones under different test types is to conduct morphological analysis using techniques like Environmental Scanning Electron Microscopy (ESEM) or morphological analysis on the surface of the shear plane. These method allow for direct visualization of particle orientations, contact points, and potential fabric changes resulting from shear deformation. By comparing ESEM images taken from the shear zone and surrounding areas, obtained from different test types, valuable insights can be gained into how varying loading conditions influence microstructural evolution.
3. Developing new formulations that can more accurately predict suction stress at intermediate and high suction levels. Furthermore, future models should consider the influence of varying loading conditions on suction stress magnitude to improve predictive capability across different testing scenarios.
4. This study focused on compacted kaolin, a relatively homogeneous fine-grained soil. Future research should investigate the suction stress behaviour of different soil types, including silts and natural clayey soils with varying mineralogy and fabric, to assess the general applicability of the suction stress approach.
5. The experimental results demonstrated a pronounced hysteresis effect between drying and wetting paths. Future research should also investigate the long-term evolution of suction stress under cyclic wetting-drying conditions which would provide insights into the durability and stability of unsaturated soils in geotechnical applications.

Bibliography

Abedi-Koupai, J. & Mehdizadeh, H. (2008), 'Estimation of Osmotic Suction from Electrical Conductivity and Water Content Measurements in Unsaturated Soils', *Geotechnical Testing Journal* **31**(2), 142–148.

Agus, S. S. (2005), An Experimental Study on Hydro-Mechanical Characteristics of Compacted Bentonite-Sand Mixtures, PhD thesis, Bauhaus-Universität Weimar.

Agus, S. S. & Schanz, T. (2003), Vapour equilibrium technique for tests on a highly compacted bentonite-sand mixture, *in* 'Proceedings of the International Conference on Problematic Soils, Nottingham, United Kingdom', Vol. 2003, pp. 467–474.

Agus, S. S. & Schanz, T. (2005), 'Comparison of four methods for measuring total suction', *Vadose Zone Journal* **4**(4), 1087–1095.

Ahmadinezhad, A., Jafarzadeh, F. & Sadeghi, H. (2019), 'Combination of water head control and axis translation techniques in new unsaturated cyclic simple shear tests', *Soil Dynamics and Earthquake Engineering* **126**, 105818.

Aitchison, G. D. (1965), Moisture equilibria and moisture changes in soils beneath covered areas, *in* 'A Symposium in Print / Edited by Gordon D. Aitchison', Butterworths, Sydney.

Akin, I. D. & Likos, W. J. (2020), 'Suction stress of clay over a wide range of saturation', *Geotechnical and Geological Engineering* **38**, 283–296.

Al-Mahbashi, A. M., Elkady, T. Y. & Al-Shamrani, M. A. (2018), 'Hysteresis soil-water characteristic curves of highly expansive clay', *European Journal of Environmental and Civil Engineering* **22**(9), 1041–1059.

Alabdullah, J. (2010), Testing Unsaturated Soil for Plane Strain Conditions: A New Double-Wall Biaxial Device, PhD thesis, Bauhaus-Universität Weimar.

Almahbobi, S. (2018), Experimental Study of Volume Change and Shear Strength Behaviour of Statically Compacted Collapsible Soil, PhD thesis, Cardiff University.

Alonso, E., Pereira, J.-M., Vaunat, J. & Olivella, S. (2010), 'A microstructurally based effective stress for unsaturated soils', *Géotechnique* **60**(12), 913–925.

Alonso, E., Pinyol, N. & Gens, A. (2013), 'Compacted soil behaviour: Initial state, structure and constitutive modelling', *Géotechnique* **63**(6), 463–478.

Alsherif, N. A. & McCartney, J. S. (2014), 'Effective Stress in Unsaturated Silt at Low Degrees of Saturation', *Vadose Zone Journal* **13**(5).

ASTM (D4542-95) (2000), 'Standard test method for pore water extraction and determination of the soluble salt content of soils by refractometer'.

Attom, M. F. & Al-Akhras, N. M. (2008), 'Investigating anisotropy in shear strength of clayey soils', *Proceedings of the Institution of Civil Engineers - Geotechnical Engineering* **161**(5), 269–273.

Bai, F. Q. & Liu, S. H. (2012), 'Measurement of the shear strength of an expansive soil by combining a filter paper method and direct shear tests', *Geotechnical Testing Journal* **35**(3), 451–459.

Baille, W. (2014), Hydro-Mechanical Behaviour of Clays: Significance of Mineralogy, PhD thesis, Ruhr-Universität Bochum, Lehrstuhl für Grundbau, Boden-und Felsmechanik.

Banerjee, A. (2017), Response of Unsaturated Soils under Monotonic and Dynamic Loading over Moderate Suction States, PhD thesis, The University of Texas at Arlington.

Bani Hashem, E. & Houston, S. L. (2016), 'Volume Change Consideration in Determining Unsaturated Soil Properties for Geotechnical Applications', *International Journal of Geomechanics* **16**(6), D4015003.

Bao, C. G., Gong, B.-w. & Zhan, L.-t. (1998), Properties of unsaturated soils and slope stability of expansive soils, *in* 'Keynote Lecture, Proceedings of the 2nd International Conference on Unsaturated Soils (UNSAT 98). Beijing, China', Vol. 1, pp. 71–98.

Bear, J. (1972), *Dynamics of Fluids in Porous Media*, American Elsevier Publishing Company, Inc., New York.

Birle, E., Heyer, D. & Vogt, N. (2008), 'Influence of the initial water content and dry density on the soil–water retention curve and the shrinkage behavior of a compacted clay', *Acta Geotechnica* **3**, 191–200.

Bishop, A. W. (1959), 'The principal of effective stress', *Teknisk ukeblad* **39**, 859–863.

Bishop, A. W. (1961), The experimental study of partly saturated soil in the triaxial apparatus, *in* 'Proc. 5th International Conference on Soil Mechanics and Foundation Engineering, Paris, 1961', Vol. 1, pp. 13–21.

Bishop, A. W., Alpan, I., Blight, GE. & Donald, IB. (1960), 'Factors controlling the strength of partly saturated cohesive soils'.

Bishop, A. W. & Blight, G. E. (1963), 'Some Aspects of Effective Stress in Saturated and Partly Saturated Soils', *Géotechnique* **13**(3), 177–197.

Blatz, J. A., Cui, Y.-J. & Oldecop, L. (2008), 'Vapour equilibrium and osmotic technique for suction control', *Geotechnical and Geological Engineering* **26**, 661–673.

Blatz, J. & Graham, J. (2000), 'A system for controlled suction in triaxial tests', *Géotechnique* **50**(4), 465–469.

Boivin, P., Garnier, P. & Tessier, D. (2004), 'Relationship between Clay Content, Clay Type, and Shrinkage Properties of Soil Samples', *Soil Science Society of America Journal* **68**(4), 1145–1153.

Bolt, G. H. (1956), 'Physico-Chemical Analysis of the Compressibility of Pure Clays', *Géotechnique* **6**(2), 86–93.

Bolt, G. H. & Frissel, M. J. (1960), 'Thermodynamics of soil moisture.', *Netherlands Journal of Agricultural Science* **8**(1), 57–78.

Braudeau, E., Costantini, J. M., Bellier, G. & Colleuille, H. (1999), 'New Device and Method for Soil Shrinkage Curve Measurement and Characterization', *Soil Science Society of America Journal* **63**(3), 525–535.

Buckingham, E. (1907), 'Studies on the movement of soil moisture', *US Dept. Agic. Bur. Soils Bull.* **38**.

Bulolo, S. & Leong, E.-C. (2023), Interpretation of constant suction direct shear test, *in* 'E3S Web of Conferences', Vol. 382, EDP Sciences, p. 05003.

Bulolo, S., Leong, E. C. & Kizza, R. (2021), 'Tensile strength of unsaturated coarse and fine-grained soils', *Bulletin of Engineering Geology and the Environment* **80**, 2727–2750.

Cai, G., Zhou, A., Liu, Y., Xu, R. & Zhao, C. (2020), 'Soil water retention behavior and microstructure evolution of lateritic soil in the suction range of 0–286.7 MPa', *Acta Geotechnica* **15**(12), 3327–3341.

Cavalcante, A. L. B. & Mascarenhas, P. V. S. (2021), 'Efficient approach in modeling the shear strength of unsaturated soil using soil water retention curve', *Acta Geotechnica* **16**(10), 3177–3186.

Cerato, A. B. & Lutenegger, A. J. (2006), 'Specimen size and scale effects of direct shear box tests of sands', *Geotechnical Testing Journal* **29**(6), 507–516.

Chae, J., Kim, B., Park, S.-w. & Kato, S. (2010), 'Effect of suction on unconfined compressive strength in partly saturated soils', *KSCE Journal of Civil Engineering* **14**, 281–290.

Chali, E. & Maleki, M. (2021), 'Experimental study on mechanical behavior of unsaturated silty sand in constant equivalent granular void ratio', *Geotechnical and Geological Engineering* **39**, 735–750.

Chapman, D. L. (1913), 'LI. *A contribution to the theory of electrocapillarity*', *The London, Edinburgh, and Dublin Philosophical Magazine and Journal of Science* **25**(148), 475–481.

Cheng, Q., Zhang, S.-X., Tang, C.-S., Tian, B.-G. & Shi, B. (2024), 'Thermal effects on tensile strength of a compacted soil', *Canadian Geotechnical Journal* pp. cgj–2023–0487.

Cho, G. C. & Santamarina, J. C. (2001), 'Unsaturated Particulate Materials—Particle-Level Studies', *Journal of Geotechnical and Geoenvironmental Engineering* **127**(1), 84–96.

Chowdhury, R. H. & Azam, S. (2016), 'Unsaturated shear strength properties of a compacted expansive soil from Regina, Canada', *Innovative Infrastructure Solutions* **1**(1), 47.

Christ, F., Lieske, W., Herz, C. & Wichtmann, T. (2022), 'Evaluation of the Penetration Behavior of Viscous Fluids into Porous Media in the Context of Volume Determination', *Geotechnical Testing Journal* **45**(4), 819–836.

Coleman, J. D. (1962), 'Stress strain relations for partly saturated soil', *Corespondence to Geotechnique* **12**(4), 348–350.

Collins, B. D. & Sitar, N. (2009), 'Geotechnical Properties of Cemented Sands in Steep Slopes', *Journal of Geotechnical and Geoenvironmental Engineering* **135**(10), 1359–1366.

Coop, M. R. & Atkinson, J. H. (1993), 'The mechanics of cemented carbonate sands', *Géotechnique* **43**(1), 53–67.

Cornelis, W. M., Corluy, J., Medina, H., Diaz, J., Hartmann, R., Van Meirvenne, M. & Ruiz, M. E. (2006), 'Measuring and modelling the soil shrinkage characteristic curve', *Geoderma* **137**(1-2), 179–191.

Cresswell, H. P., Green, T. W. & McKenzie, N. J. (2008), 'The Adequacy of Pressure Plate Apparatus for Determining Soil Water Retention', *Soil Science Society of America Journal* **72**(1), 41–49.

Cui, Y. J. & Delage, P. (1993), On the elasto-plastic behavior of an unsaturated silt, *in* 'Unsaturated Soils', pp. 115–126.

Cui, Y. J. & Delage, P. (1996), 'Yielding and plastic behaviour of an unsaturated compacted silt', *Géotechnique* **46**(2), 291–311.

Cui, Y. J., Loiseau, C. & Delage, P. (2002), Microstructure changes of a confined swelling soil due to suction controlled hydration, *in* 'Proceedings of the 3rd International Conference on Unsaturated Soils (UNSAT 2002), Recife, Brésil. Sous La Direction de J. FT Jucá, TMP de Campos et FAM Marinho', Vol. 2, pp. 593–598.

Cuisinier, O. & Laloui, L. (2004), 'Fabric evolution during hydromechanical loading of a compacted silt', *International Journal for Numerical and Analytical Methods in Geomechanics* **28**(6), 483–499.

Dadkhah, R., Ghafoori, M., Ajalloeian, R. & Lashkaripour, G. R. (2010), 'The effect of Scale Direct Shear Tests on The Strength parameters of Clayey Sand in Isfahan city, Iran', *Journal of Applied Sciences* **18**.

Delage, P. (1987), Unnouvel appareil triaxial pour les sols non satures, *in* '9th Eur. Conf. of Soil Mechanics', pp. 26–28.

Delage, P., Audiguier, M., Cui, Y.-J. & Howat, M. D. (1996), 'Microstructure of a compacted silt', *Canadian Geotechnical Journal* **33**(1), 150–158.

Delage, P. & Cui, Y. J. (2008), 'An evaluation of the osmotic method of controlling suction', *Geomechanics and Geoengineering* **3**(1), 1–11.

Delage, P., Romero, E. & Tarantino, A. (2008), 'Recent developments in the techniques of controlling and measuring suction in unsaturated soils', *Unsaturated soils. Advances in geo-engineering* pp. 49–68.

Delage, P. & Suraj de Silva, G. P. R. (1992), 'Negative pore pressure and compacted soils', *Raul J. Marsal* **225**, 232.

Dong, Y. & Wang, L. (2021), 'Determination of Soil-Shrinkage Curve Using Transient Water Evaporation Method', *International Journal of Geomechanics* **21**(5), 04021040.

Durner, W. (1994), 'Hydraulic conductivity estimation for soils with heterogeneous pore structure', *Water Resources Research* **30**(2), 211–223.

Edlefsen, N. & Anderson, A. (1943), 'Thermodynamics of soil moisture', *Hilgardia* **15**(2), 31–298.

Elgabu, H. M. (2013), Critical Evaluation of Some Suction Measurement Techniques, PhD thesis, Cardiff University.

Encalada López, D. A., Najdi, A., Mendes, J., Prat Catalán, P. & Ledesma Villalba, A. (2023), Influence of compaction on the soil shrinkage and swelling curves, *in* 'E3S Web of Conferences', Vol. 382, EDP Sciences.

Escario, V. & Saez, J. (1986), 'The shear strength of partly saturated soils', *Geotechnique* **36**(3), 453–456.

Espinoza, D. N. & Santamarina, J. C. (2010), 'Ant tunneling—a granular media perspective', *Granular Matter* **12**, 607–616.

Estabragh, A. R., Parsaei, B. & Javadi, A. A. (2015), 'Laboratory investigation of the effect of cyclic wetting and drying on the behaviour of an expansive soil', *Soils and foundations* **55**(2), 304–314.

Fleureau, J.-M., Kheirbek-Saoud, S., Soemitro, R. & Taibi, S. (1993), 'Behavior of clayey soils on drying–wetting paths', *Canadian Geotechnical Journal* **30**(2), 287–296.

Fredlund, D. G. (2006), 'Unsaturated Soil Mechanics in Engineering Practice', *Journal of Geotechnical and Geoenvironmental Engineering* **132**(3), 286–321.

Fredlund, D. G. & Morgenstern, N. R. (1976), 'Constitutive relations for volume change in unsaturated soils', *Canadian Geotechnical Journal* **13**(3), 261–276.

Fredlund, D. G. & Morgenstern, N. R. (1977), 'Stress State Variables for Unsaturated Soils', *Journal of the Geotechnical Engineering Division* **103**(5), 447–466.

Fredlund, D. G. & Rahardjo, H. (1993*a*), 'An overview of unsaturated soil behaviour', *Geotechnical special publication* pp. 1–1.

Fredlund, D. G. & Rahardjo, H. (1993*b*), *Soil Mechanics for Unsaturated Soils*, John Wiley & Sons.

Fredlund, D. G. & Zhang, F. (2013), Combination of shrinkage curve and soil-water characteristic curves for soils that undergo volume change as soil suction is increased, *in* 'Proceedings of the 18th International Conference on Soil Mechanics and Geotechnical Engineering', ISSMGE, London, pp. 2–6.

Fredlund, D. & Xing, A. (1994), 'Equations for the soil-water characteristic curve', *Canadian Geotechnical Journal* **31**(4), 521–532.

Fredlund, M. D., Wilson, G. W. & Fredlund, D. G. (2002), Representation and estimation of the shrinkage curve, *in* 'Unsaturated Soils: Proceedings of the Third International Conference, UNSAT2002, Recife, Brazil, 10-13 March 2002', Vol. 1, Taylor & Francis US, Recife, Brazil, pp. 145–149.

Futai, M. M. & Almeida, MSS. (2005), 'An experimental investigation of the mechanical behaviour of an unsaturated gneiss residual soil', *Géotechnique* **55**(3), 201–213.

Gao, Y., Sun, D., Zhou, A. & Li, J. (2020), 'Predicting Shear Strength of Unsaturated Soils over Wide Suction Range', *International Journal of Geomechanics* **20**(2), 04019175.

Gao, Y., Sun, D., Zhu, Z. & Xu, Y. (2019), 'Hydromechanical behavior of unsaturated soil with different initial densities over a wide suction range', *Acta Geotechnica* **14**(2), 417–428.

Gapak, Y., Das, G., Yerramshetty, U. & Bharat, T. V. (2017), 'Laboratory determination of volumetric shrinkage behavior of bentonites: A critical appraisal', *Applied Clay Science* **135**, 554–566.

Gardner, W. & Widtsoe, J. A. (1921), 'The movement of soil moisture', *Soil Science* **11**(3), 215–232.

Garven, E. A. & Vanapalli, S. K. (2006), Evaluation of Empirical Procedures for Predicting the Shear Strength of Unsaturated Soils, *in* 'Unsaturated Soils 2006', American Society of Civil Engineers, Carefree, Arizona, United States, pp. 2570–2592.

Giese, R. F. (2008), The Surface Thermodynamic Properties of Clay Minerals, *in* W. M. Carty, ed., 'Ceramic Engineering and Science Proceedings', John Wiley & Sons, Inc., Hoboken, NJ, USA, pp. 33–33.

Giráldez, J. V. & Sposito, G. (1983), 'A General Soil Volume Change Equation: II. Effect of Load Pressure', *Soil Science Society of America Journal* **47**(3), 422–425.

Gouy, MJJPTA. (1910), 'Sur la constitution de la charge électrique à la surface d'un électrolyte', *J. Phys. Theor. Appl.* **9**(1), 457–468.

Groenevelt, P. H. & Grant, C. D. (2001), 'Re-evaluation of the structural properties of some British swelling soils', *European Journal of Soil Science* **52**(3), 469–477.

Guan, G. S. (2012), Hysteresis Effects on Mechanical Behaviour of Unsaturated Soils, PhD thesis, Nanyang Technological University.

Guan, G. S., Rahardjo, H. & Choon, L. E. (2010), 'Shear Strength Equations for Unsaturated Soil under Drying and Wetting', *Journal of Geotechnical and Geoenvironmental Engineering* **136**(4), 594–606.

Haines, W. B. (1923), 'The volume-changes associated with variations of water content in soil', *The Journal of agricultural science* **13**(3), 296–310.

Hamaker, H. C. (1937), 'The London—van der Waals attraction between spherical particles', *physica* **4**(10), 1058–1072.

Hamid, T. B. & Miller, G. A. (2009), 'Shear strength of unsaturated soil interfaces', *Canadian Geotechnical Journal* **46**(5), 595–606.

He, M., Szuchmacher Blum, A., Aston, D. E., Buenviaje, C., Overney, R. M. & Luginbühl, R. (2001), 'Critical phenomena of water bridges in nanoasperity contacts', *The Journal of Chemical Physics* **114**(3), 1355–1360.

Head, K. H. (2006), *Manual of Soil Laboratory Testing*, Vol. 2, third edn.

Heibrock, G. (1996), Zur Rissbildung Durch Austrocknung in Mineralischen Abdichtungsschichten an Der Basis von Deponien, PhD thesis, Instituts f¨ur Grundbau der Ruhr-Universität Bochum.

Heibrock, G., König, D., Datcheva, M., Pourzargar, A., Alabdullah, J. & Schanz, T. (2018), 'Prediction of effective stress in partially saturated sand–kaolin mixtures', *Geomechanics for Energy and the Environment* **15**, 85–94.

Heibrock, G., König, D., Wang, Y., Eberweiser, T., Jung, T., Le, C. M. & Wichtmann, T. (2023), Zur Boden-Wasserinteraktion beim Schrumpfen von Kaolin, *in* 'Vorträge Der Fachsektionstage Geotechnik - Interdisziplinäres Forum 2023', Deutsche Gesellschaft für Geotechnik eV (DGGT) German Geotechnical Society, Congress Centrum Würzburg.

Heibrock, G., Zeh, RM. & Witt, KJ. (2005), Tensile strength of compacted clays, *in* 'Unsaturated Soils: Experimental Studies: Proceedings of the International Conference "From Experimental Evidence towards Numerical Modeling of Unsaturated Soils," Weimar, Germany, September 18–19, 2003 Volume I', Springer, pp. 395–412.

Hilf, J. W. (1956), *An Investigation of Pore-Water Pressure in Compacted Cohesive Soils*, University of Colorado at Boulder.

Hillel, D. (1981), *Fundamentals of Soil Physics.*, Academic Press, Inc. (London) Ltd., London.

Hirmas, D. R., Giménez, D., Mome Filho, E. A., Patterson, M., Drager, K., Platt, B. F. & Eck, D. V. (2016), Quantifying Soil Structure and Porosity Using Three-Dimensional Laser Scanning, *in* A. E. Hartemink & B. Minasny, eds, 'Digital Soil Morphometrics', Springer International Publishing, Cham, pp. 19–35.

Ho, D. Y. F., Fredlund, D. G. & Rahardjo, H. (1992), 'Volume change indices during loading and unloading of an unsaturated soil', *Canadian Geotechnical Journal* **29**(2), 195–207.

Hoffmann, C., Romero, E. & Alonso, E. E. (2005), Combining different controlled-suction techniques to study expansive clays, *in* 'Advanced Experimental Unsaturated Soil Mechanics EXPERUS 2005', pp. 61–67.

Hossain, M. A. & Yin, J.-H. (2015), 'Dilatancy and Strength of an Unsaturated Soil-Cement Interface in Direct Shear Tests', *International Journal of Geomechanics* **15**(5), 04014081.

Ismail, M. A., Joer, H. A., Sim, W. H. & Randolph, M. F. (2002), 'Effect of Cement Type on Shear Behavior of Cemented Calcareous Soil', *Journal of Geotechnical and Geoenvironmental Engineering* **128**(6), 520–529.

Israelachvili, J. N. (2011), *Intermolecular and Surface Forces*, Academic press.

Jain, S., Wang, Y. H. & Fredlund, D. G. (2015), 'Non-contact sensing system to measure specimen volume during shrinkage test', *Geotechnical Testing Journal* **38**(6), 936–949.

Jennings, JE. (1961), 'A revised effective stress law for use in the prediction of the behaviour of unsaturated soils', *Pore pressure and suction in soils* pp. 26–30.

Jiang, Y., Chen, W., Wang, G., Sun, G. & Zhang, F. (2017), 'Influence of initial dry density and water content on the soil–water characteristic curve and suction stress of a reconstituted loess soil', *Bulletin of Engineering Geology and the Environment* **76**, 1085–1095.

Kardani, N., Zhou, A., Shen, S.-L. & Nazem, M. (2021), 'Estimating unconfined compressive strength of unsaturated cemented soils using alternative evolutionary approaches', *Transportation Geotechnics* **29**, 100591.

Kasama, K., Zen, K. & Iwataki, K. (2006), 'Undrained shear strength of cement-treated soils', *Soils and Foundations* **46**(2), 221–232.

Kassiff, G. & Shalom, A. B. (1971), 'Experimental Relationship Between Swell Pressure and Suction', *Géotechnique* **21**(3), 245–255.

Kayadelen, C., Tekinsoy, M. A. & Taşkıran, T. (2007), 'Influence of matric suction on shear strength behavior of a residual clayey soil', *Environmental geology* **53**, 891–901.

Kayser, T., Baille, W., Tafili, M. & Wichtmann, T. (2023), Coupled hydro-mechanical behaviour of a Kaolin Clay in the context of the geothermal use of geotechnical structures, *in* 'E3S Web of Conferences', Vol. 382, EDP Sciences, p. 23002.

Khalili, N. (2018), 'Guidelines for the application of effective stress principle to shear strength and volume change determination in unsaturated soils', *Australian Geomechanics Journal* **53**(1), 37–47.

Khalili, N., Habte, M. A. & Zargarbashi, S. (2008), 'A fully coupled flow deformation model for cyclic analysis of unsaturated soils including hydraulic and mechanical hystereses', *Computers and Geotechnics* **35**(6), 872–889.

Khalili, N. & Khabbaz, M. H. (1998), 'A unique relationship for χ for the determination of the shear strength of unsaturated soils', *Géotechnique* **48**(5), 681–687.

Khalili, N., Romero, E. & Marinho, F. A. (2022), 'State of the Art Report. Advances in Unsaturated Soil Mechanics: Constitutive modelling, experimental investigation, and field instrumentation', *Proceedings of the 20th ICSMGE-State of the Art and Invited Lectures—Rahman and Jaksa, Sydney, Australia* pp. 1–5.

Khalili, NGFA., Geiser, F. & Blight, GE. (2004), 'Effective stress in unsaturated soils: Review with new evidence', *International journal of Geomechanics* **4**(2), 115–126.

Kim, D. J., Vereecken, H., Feyen, J., Boels, D. & Bronswijk, J. J. B. (1992), 'On the characterization of properties of an unripe marine clay soil: I. Shrinkage processes of an unripe marine clay soil in relation to physical ripening', *Soil Science* **153**(6), 471–481.

Klausner, Y. (1991), *Fundamentals of Continuum Mechanics of Soils*, Springer-Verlag, London.

Klute, A. (1986), 'Water retention: Laboratory methods. Methods of soil analysis: Part 1-Physical and mineralogical methods, 635-662'.

Kodikara, J., Barbour, S. L. & Fredlund, D. G. (1999), Changes in clay structure and behaviour due to wetting and drying, *in* 'Proceedings 8th Australia New Zealand Conference on Geomechanics: Consolidating Knowledge', Vol. 179, Australian Geomechanics Society.

Konrad, J.-M. & Lebeau, M. (2015), 'Capillary-based effective stress formulation for predicting shear strength of unsaturated soils', *Canadian Geotechnical Journal* **52**(12), 2067–2076.

Lade, P. V. (2016), *Triaxial Testing of Soils*, John Wiley & Sons.

Lambe, T. W. (1964), 'Methods of Estimating Settlement', *Journal of the Soil Mechanics and Foundations Division* **90**(5), 43–67.

Lauritzen, C. W. & Stewart, A. J. (1942), 'Soil-volume changes and accompanying moisture and pore-space relationships.', *Soil Science Society of America Journal* **6**, 113–116.

Le, C. M., Sarkar, D., König, D., Goudarzy, M. & Wichtmann, T. (2023), 'Small and Intermediate Strain Characteristics of a Partially Saturated Sand–Clay Mixture', *International Journal of Geomechanics* **23**(8), 04023115.

Lee, I.-M., Sung, S.-G. & Cho, G.-C. (2005), 'Effect of stress state on the unsaturated shear strength of a weathered granite', *Canadian Geotechnical Journal* **42**(2), 624–631.

Lee, J., Fratta, D. & Akin, I. (2022), 'Shear strength and stiffness behavior of fine-grained soils at different surface hydration conditions', *Canadian Geotechnical Journal* **59**(7), 1071–1082.

Leong, E. C. & Rahardjo, H. (1997), 'Review of Soil-Water Characteristic Curve Equations', *Journal of Geotechnical and Geoenvironmental Engineering* **123**(12), 1106–1117.

Leong, E.-C., Tripathy, S. & Rahardjo, H. (2003), 'Total suction measurement of unsaturated soils with a device using the chilled-mirror dew-point technique', *Géotechnique* **53**(2), 173–182.

Leong, E. C., Tripathy, S. & Rahardjo, H. (2004), 'A modified pressure plate apparatus', *Geotechnical Testing Journal* **27**(3), 322–331.

Li, L. & Zhang, X. (2019), 'A new approach to measure soil shrinkage curve', *Geotechnical Testing Journal* **42**(1), 1–18.

Li, L., Zhang, X. & Li, P. (2019), 'Evaluating a new method for simultaneous measurement of soil water retention and shrinkage curves', *Acta Geotechnica* **14**, 1021–1035.

Li, X. & Zhang, L. M. (2009), 'Characterization of dual-structure pore-size distribution of soil', *Canadian Geotechnical Journal* **46**(2), 129–141.

Li, X., Zhang, L. M. & Li, J. H. (2009), 'Development of a modified axis translation technique for measuring SWCCs for gravel soils at very low suctions', *Geotechnical testing journal* **32**(6), 478–488.

Lieske, W., Tripathy, S., Baille, W. & Schanz, T. (2020), 'An alternative approach for determining suction of polyethylene glycols for soil testing', *Géotechnique Letters* **10**(1), 45–49.

Likos, W. J., Wayllace, A., Godt, J. & Lu, N. (2010), 'Modified direct shear apparatus for unsaturated sands at low suction and stress', *Geotechnical Testing Journal* **33**(4), 286–298.

Lin, B. & Cerato, A. B. (2013), 'Hysteretic soil water characteristics and cyclic swell–shrink paths of compacted expansive soils', *Bulletin of Engineering Geology and the Environment* **72**(1), 61–70.

Lins, Y. (2010), Hydro-Mechanical Properties of Partially Saturated Sand, PhD thesis, Ruhr-Universität Bochum, Lehrstuhl für Grundbau, Boden-und Felsmechanik.

Lins, Y., Schanz, T. & Fredlund, D. G. (2009), 'Modified pressure plate apparatus and column testing device for measuring SWCC of sand', *Geotechnical Testing Journal* **32**(5), 450–464.

Liu, G., Toll, D. G., Kong, L. & Asquith, J. D. (2020), 'Matric suction and volume characteristics of compacted clay soil under drying and wetting cycles', *Geotechnical Testing Journal* **43**(2), 464–479.

Liu, H., Rahardjo, H., Satyanaga, A. & Du, H. (2023), 'Use of osmotic tensiometers in the determination of soil-water characteristic curves', *Engineering Geology* **312**, 106938.

Liu, L., Wan, K.-T. & Liu, K.-K. (2021), 'Influence of Relative Humidity on Interparticle Capillary Adhesion', *Langmuir* **37**(43), 12714–12722.

Lloret, A., Villar, M. V., Sánchez, M., Gens, A., Pintado, X. & Alonso, E. E. (2003), 'Mechanical behaviour of heavily compacted bentonite under high suction changes', *Géotechnique* **53**(1), 27–40.

London, F. (1930), 'Zur Theorie und Systematik der Molekularkräfte', *Zeitschrift für Physik* **63**(3), 245–279.

Lourenço, S. D., Gallipoli, D., Toll, D. G., Augarde, C. E. & Evans, F. D. (2011), 'A new procedure for the determination of soil-water retention curves by continuous drying using high-suction tensiometers', *Canadian Geotechnical Journal* **48**(2), 327–335.

Lu, N. & Dong, Y. (2017), 'Correlation between Soil-Shrinkage Curve and Water-Retention Characteristics', *Journal of Geotechnical and Geoenvironmental Engineering* **143**(9), 04017054.

Lu, N., Godt, J. W. & Wu, D. T. (2010), 'A closed-form equation for effective stress in unsaturated soil', *Water Resources Research* **46**(5).

Lu, N., Kim, T.-H., Sture, S. & Likos, W. J. (2009), 'Tensile Strength of Unsaturated Sand', *Journal of Engineering Mechanics* **135**(12), 1410–1419.

Lu, N. & Likos, W. J. (2004), *Unsaturated Soil Mechanics*, Wiley.

Lu, N. & Likos, W. J. (2006), 'Suction stress characteristic curve for unsaturated soil', *Journal of Geotechnical and Geoenvironmental Engineering* **132**(2), 131–142.

Lu, N. & Zhang, C. (2019), 'Soil Sorptive Potential: Concept, Theory, and Verification', *Journal of Geotechnical and Geoenvironmental Engineering* **145**(4), 04019006.

Macari, E. J., Parker, J. K. & Costes, N. C. (1997), 'Measurement of volume changes in triaxial tests using digital imaging techniques', *Geotechnical Testing Journal* **20**(1), 103–109.

Malaya, C. & Sreedeep, S. (2012), 'Critical Review on the Parameters Influencing Soil-Water Characteristic Curve', *Journal of Irrigation and Drainage Engineering* **138**(1), 55–62.

Mangelsdorf, C. S. & White, L. R. (1990), 'Effects of stern-layer conductance on electrokinetic transport properties of colloidal particles', *Journal of the Chemical Society, Faraday Transactions* **86**(16), 2859–2870.

Marcial, D., Delage, P. & Cui, Y. J. (2002), 'On the high stress compression of bentonites', *Canadian Geotechnical Journal* **39**(4), 812–820.

Marinho, F. A., Take, W. A. & Tarantino, A. (2008), 'Measurement of matric suction using tensiometric and axis translation techniques', *Geotechnical and Geological Engineering* **26**, 615–631.

McGarry, D. & Malafant, K. W. J. (1987), 'The Analysis of Volume Change in Unconfined Units of Soil1', *Soil Science Society of America Journal* **51**(2), 290.

Mendes, J., Gallipoli, D., Boeck, F. & Tarantino, A. (2020), 'A comparative study of high capacity tensiometer designs', *Physics and Chemistry of the Earth, Parts A/B/C* **120**, 102901.

Mendes, J., Toll, D. G. & Evans, F. (2012), A Double Cell Triaxial System for Unsaturated Soils Testing, *in* C. Mancuso, C. Jommi & F. D'Onza, eds, 'Unsaturated Soils: Research and Applications', Springer Berlin Heidelberg, Berlin, Heidelberg, pp. 5–10.

Miller, C. J., Yesiller, N., Yaldo, K. & Merayyan, S. (2002), 'Impact of Soil Type and Compaction Conditions on Soil Water Characteristic', *Journal of Geotechnical and Geoenvironmental Engineering* **128**(9), 733–742.

Miller, E. E. & Miller, R. D. (1956), 'Physical theory for capillary flow phenomena', *Journal of Applied Physics* **27**(4), 324–332.

Mishra, P. N., Scheuermann, A. & Bhuyan, M. H. (2021), 'A unified approach for establishing soil water retention and volume change behavior of soft soils', *Geotechnical Testing Journal* **44**(5), 1197–1216.

Mishra, P. N., Scheuermann, A., Bore, T. & Li, L. (2019), 'Salinity effects on soil shrinkage characteristic curves of fine-grained geomaterials', *Journal of Rock Mechanics and Geotechnical Engineering* **11**(1), 181–191.

Mishra, P. N., Zhang, Y., Bhuyan, M. H. & Scheuermann, A. (2020), 'Anisotropy in volume change behaviour of soils during shrinkage', *Acta Geotechnica* **15**, 3399–3414.

Mitchell, J. K. & Soga, K. (2005), *Fundamentals of Soil Behavior*, Vol. 3, John Wiley & Sons New York.

Monroy, R., Zdravkovic, L. & Ridley, A. (2010), 'Evolution of microstructure in compacted London Clay during wetting and loading', *Géotechnique* **60**(2), 105–119.

Morgenstern, N. R. & Tchalenko, J. S. (1967), 'Microscopic Structures in Kaolin Subjected to Direct Shear', *Géotechnique* **17**(4), 309–328.

Mualem, Y. (1974), 'A conceptual model of hysteresis', *Water Resources Research* **10**(3), 514–520.

Mualem, Y. (1976), 'A new model for predicting the hydraulic conductivity of unsaturated porous media', *Water Resources Research* **12**(3), 513–522.

Ng, C. W., Cui, Y., Chen, R. U. I. & Delage, P. (2007), 'The axis-translation and osmotic techniques in shear testing of unsaturated soils: A comparison', *Soils and Foundations* **47**(4), 675–684.

Ng, C. W., Zhan, L. T. & Cui, Y. J. (2002), 'A new simple system for measuring volume changes in unsaturated soils', *Canadian Geotechnical Journal* **39**(3), 757–764.

Ng, C. & Zhou, C. (2014), 'Cyclic behaviour of an unsaturated silt at various suctions and temperatures', *Géotechnique* **64**(9), 709–720.

Niu, G., Sun, D., Kong, L., Shao, L., Wang, H. & Wang, Z. (2024), 'Investigation into the shear strength of a weakly expansive soil over a wide suction range', *Acta Geotechnica* **19**(5), 3059–3073.

Nuth, M. & Laloui, L. (2008), 'Effective stress concept in unsaturated soils: Clarification and validation of a unified framework', *International Journal for Numerical and Analytical Methods in Geomechanics* **32**(7), 771–801.

Öberg, AL. & Sällfors, G. (1997), 'Determination of shear strength parameters of unsaturated silts and sands based on the water retention curve', *Geotechnical Testing Journal* **20**(1), 40–48.

Oh, S. & Lu, N. (2014), 'Uniqueness of the suction stress characteristic curve under different confining stress conditions', *Vadose Zone Journal* **13**(5), vzj2013–04.

Oh, W. T. & Vanapalli, S. (2018), 'Undrained shear strength of unsaturated soils under zero or low confining pressures in the vadose zone', *Vadose Zone Journal* **17**(1), 1–13.

Oldecop, L. A. & Alonso, E. E. (2004), 'Testing rockfill under relative humidity control', *Geotechnical Testing Journal* **27**(3), 269–278.

Olphen, H. V. (1977), *An Introduction to Clay Colloid Chemistry, for Clay Technologists, Geologists, and Soil Scientists.*, second edn.

Olsen, P. A. & Haugen, L. E. (1998), 'A new model of the shrinkage characteristic applied to some Norwegian soils', *Geoderma* **83**(1-2), 67–81.

Oualmakran, M., Mercatoris, B. & François, B. (2016), 'Pore-size distribution of a compacted silty soil after compaction, saturation, and loading', *Canadian Geotechnical Journal* **53**(12), 1902–1909.

Pan, H., Qing, Y. & Pei-yong, L. (2010), 'Direct and indirect measurement of soil suction in the laboratory', *Electronic Journal of Geotechnical Engineering* **15**(3), 1–14.

Pasha, A. Y., Khoshghalb, A. & Khalili, N. (2016), 'Pitfalls in Interpretation of Gravimetric Water Content–Based Soil-Water Characteristic Curve for Deformable Porous Media', *International Journal of Geomechanics* **16**(6), D4015004.

Patil, U. D. (2014), Response of Unsaturated Silty Sand over a Wider Range of Suction States Using a Novel Double-Walled Triaxial Testing System, PhD thesis, The University of Texas at Arlington.

Patil, U. D., Hoyos, L. R., Puppala, A. J. & Congress, S. S. C. (2020), 'Suction Stress Characteristic Curves of Cohesive-Frictional Soils from Multiple Suction-Controlled Testing Methods', *International Journal of Geomechanics* **20**(7), 04020077.

Pellissier, J. P. (1991), 'The toluene and wax-freezing method of determining volumetric free swell', *Geotechnical Testing Journal* **14**(3), 309–314.

Peng, X. & Horn, R. (2005), 'Modeling Soil Shrinkage Curve across a Wide Range of Soil Types', *Soil Science Society of America Journal* **69**(3), 584–592.

Péron, H., Hueckel, T. & Laloui, L. (2007), 'An improved volume measurement for determining soil water retention curves', *Geotechnical Testing Journal* **30**(1), 1–8.

Peters, A. & Durner, W. (2008*a*), 'A simple model for describing hydraulic conductivity in unsaturated porous media accounting for film and capillary flow', *Water Resources Research* **44**(11), 2008WR007136.

Peters, A. & Durner, W. (2008*b*), 'Simplified evaporation method for determining soil hydraulic properties', *Journal of Hydrology* **356**(1-2), 147–162.

Pham, H. Q. (2001), An Engineering Model of Hysteresis for Soil-Water Characteristic Curves, PhD thesis, University of Saskatchewan.

Pham, H. Q., Fredlund, D. G. & Barbour, S. L. (2005), 'A study of hysteresis models for soil-water characteristic curves', *Canadian Geotechnical Journal* **42**(6), 1548–1568.

Philip, J. R. (1957), 'The theory of infiltration: 4. Sorptivity and algebraic infiltration equations', *Soil science* **84**(3), 257–264.

Pourzargar, A. (2017), Application of Suction Stress Concept to Partially Saturated Compacted Soils, PhD thesis, Ruhr-Universität Bochum, Lehrstuhl für Grundbau, Boden- und Felsmechanik.

Pourzargar, A., König, D., Heibrock, G., Datcheva, M. & Schanz, T. (2014), 'Comparison of measured and predicted suction stress in partially saturated compacted mixtures of sand and clay', *Vadose Zone Journal* **13**(5).

Puppala, A. J., Katha, B. & Hoyos, L. R. (2004), 'Volumetric shrinkage strain measurements in expansive soils using digital imaging technology', *Geotechnical Testing Journal* **27**(6), 547–556.

Raghuram, A. S. S., Negi, P. S., Basha, B. M. & Moghal, A. A. B. (2024), 'Effect of Sample Size, Dry Unit Weight, and Hysteresis of Expansive Soil on SWCC and Finite Slope Stability', *International Journal of Geosynthetics and Ground Engineering* **10**(2), 18.

Rahardjo, H., Chatterjea, K., Leong, E.-C. & Wang, J.-Y. (2016), 'Effect of hydraulic anisotropy on soil–water characteristic curve', *Soils and Foundations* **56**(2), 228–239.

Rahardjo, H. & Leong, E. C. (2006), Suction Measurements, *in* 'Unsaturated Soils 2006', American Society of Civil Engineers, Carefree, Arizona, United States, pp. 81–104.

Rahardjo, H., Satyanaga, A., Mohamed, H., Yee Ip, S. C. & Shah, R. S. (2019), 'Comparison of soil–water characteristic curves from conventional testing and combination of small-scale centrifuge and dew point methods', *Geotechnical and Geological Engineering* **37**, 659–672.

Rahardjo, H., Shen, Y., Tsen-Tieng, D. L., Ramos-Rivera, J., Nong, X.-F. & Hamdany, A. H. (2021), 'New osmotic tensiometer development', *Geotechnical Testing Journal* **44**(3), 722–740.

Richards, L. A. (1931), 'Capillary conduction of liquids through porous mediums', *Physics* **1**(5), 318–333.

Ridley, A. M. & Wray, W. K. (1996), Suction measurement: A review of current theory and practices., *in* '1st International Conference on Unsaturated Soils', pp. 1293–1322.

Romero, E., Gens, A. & Lloret, A. (1999), 'Water permeability, water retention and microstructure of unsaturated compacted Boom clay', *Engineering Geology* **54**(1-2), 117–127.

Romero, E. & Simms, P. H. (2008), 'Microstructure investigation in unsaturated soils: A review with special attention to contribution of mercury intrusion porosimetry and environmental scanning electron microscopy', *Geotechnical and Geological engineering* **26**, 705–727.

Rossi, A. M., Hirmas, D. R., Graham, R. C. & Sternberg, P. D. (2008), 'Bulk Density Determination by Automated Three-Dimensional Laser Scanning', *Soil Science Society of America Journal* **72**(6), 1591–1593.

Rowshanzamir, M. A. & Askari, A. M. (2010), 'An investigation on the strength anisotropy of compacted clays', *Applied Clay Science* **50**(4), 520–524.

Roy, S. & Rajesh, S. (2018), 'Influence of confining pressure on water retention characteristics of compacted soil', *Indian Geotechnical Journal* **48**, 327–341.

Salimi, K., Cerato, A. B., Vahedifard, F. & Miller, G. A. (2021), 'General Model for the Uniaxial Tensile Strength Characteristic Curve of Unsaturated Soils', *Journal of Geotechnical and Geoenvironmental Engineering* **147**(7), 04021051.

Santamarina, J. C. & Cho, G.-C. (2004), Soil behaviour: The role of particle shape, *in* 'Advances in Geotechnical Engineering: The Skempton Conference: Proceedings of a Three Day Conference on Advances in Geotechnical Engineering, Organised by the Institution of Civil Engineers and Held at the Royal Geographical Society, London, UK, on 29–31 March 2004', Thomas Telford Publishing, pp. 604–617.

Schindler, U. (1980), 'Ein Schnellverfahren zur Messung der Wasserleitfähigkeit im teilgesättigten Boden an Stechzylinderproben', *Archiv für Acker- und Pflanzenbau und Bodenkunde - Archives of Agronomy and Soil Science* **24**, 1–7.

Schindler, U., Durner, W., Von Unold, G. & Müller, L. (2010), 'Evaporation Method for Measuring Unsaturated Hydraulic Properties of Soils: Extending the Measurement Range', *Soil Science Society of America Journal* **74**(4), 1071–1083.

Sharanya, A. G., Mudavath, H. & Thyagaraj, T. (2021), 'Review of methods for predicting soil volume change induced by shrinkage', *Innovative Infrastructure Solutions* **6**, 1–16.

Sibley, J. W. & Williams, D. J. (1989), 'A procedure for determining volumetric shrinkage of an unsaturated soil', *Geotechnical Testing Journal* **12**(3), 181–187.

Sillers, W. S. & Fredlund, D. G. (2001), 'Statistical assessment of soil-water characteristic curve models for geotechnical engineering', *Canadian Geotechnical Journal* **38**(6), 1297–1313.

Sivakumar, V. (1993), A Critical State Framework for Unsaturated Soil., PhD thesis, University of Sheffield.

Sivakumar, V., Tan, W. C., Murray, E. J. & McKinley, J. D. (2006), 'Wetting, drying and compression characteristics of compacted clay', *Géotechnique* **56**(1), 57–62.

Soleimani Fard, H. (2015), Study on the Hydro-Mechanical Behavior of Fiber Reinforced Fine Grained Soils, with Application to the Preservation of Historical Monuments, PhD thesis, Ruhr-Universität Bochum, Lehrstuhl für Grundbau, Boden-und Felsmechanik.

Soltani, A., Azimi, M., O'Kelly, B. C., Baghbani, A. & Taheri, A. (2024), 'Statistical Reappraisal of the Wax and Mercury Methods for Shrinkage Limit Determinations of Fine-Grained Soils', *Geotechnical and Geological Engineering* **42**(6), 5317–5333.

Spagnoli, G., Stanjek, H. & Sridharan, A. (2012), 'Influence of ethanol/water mixture on the undrained shear strength of pure clays', *Bulletin of Engineering Geology and the Environment* **71**, 389–398.

Sreedeep, S. & Singh, D. N. (2006), 'Methodology for determination of osmotic suction of soils', *Geotechnical & Geological Engineering* **24**, 1469–1479.

Sreedeep, S. & Singh, D. N. (2011), 'Critical Review of the Methodologies Employed for Soil Suction Measurement', *International Journal of Geomechanics* **11**(2), 99–104.

Sridharan, A. (1968), Some Studies on the Strength of Partly Saturated Clays, PhD thesis, Purdue University.

Sridharan, A. (2014), 'Soil clay mineralogy and physico-chemical mechanisms governing the fine-grained soil behaviour', *Indian Geotechnical Journal* **44**(4), 371–399.

Sridharan, A. & Jayadeva, M. S. (1982), 'Double layer theory and compressibility of clays', *Géotechnique* **32**(2), 133–144.

Sun, D. A., Sheng, D. C., Cui, H. B. & Li, J. (2006), Effect of Density on the Soil-Water-Retention Behaviour of Compacted Soil, *in* 'Unsaturated Soils 2006', American Society of Civil Engineers, Carefree, Arizona, United States, pp. 1338–1347.

Sutton, M. A., Orteu, J.-J. & Schreier, H. W. (2009), *Image Correlation for Deformation and Shape Measurements: Basic Concepts, Theory and Applications*, Springer.

Tariq, A.-u.-R. & Durnford, D. S. (1993), 'Soil volumetric shrinkage measurements: A simple method', *Soil Science* **155**(5), 325–330.

Tatsuoka, F., Sakamoto, M., Kawamura, T. & Fukushima, S. (1986), 'Strength and deformation characteristics of sand in plane strain compression at extremely low pressures', *Soils and Foundations* **26**(1), 65–84.

Tekinsoy, M. A., Kayadelen, C., Keskin, M. S. & Söylemez, M. (2004), 'An equation for predicting shear strength envelope with respect to matric suction', *Computers and Geotechnics* **31**(7), 589–593.

Terzaghi, K. (1936), The shearing resistance of saturated soils and the angle between the planes of shear, *in* 'First International Conference on Soil Mechanics, 1936', Vol. 1, pp. 54–59.

Terzaghi, K. (1943), *Theoretical Soil Mechanics*, John Wiley and Sons, Inc, New York.

Tessier, D. (1984), Étude Expérimentale de l'organisation Des Matériaux Argileux-Hydratation, Gonflement et Structuration Au Cours de La Dessication et de La Réhumectation, PhD thesis, Paris Diderot University (Paris VII).

Thom, R., Sivakumar, R., Sivakumar, V., Murray, E. J. & Mackinnon, P. (2007), 'Pore size distribution of unsaturated compacted kaolin: The initial states and final states following saturation', *Géotechnique* **57**(5), 469–474.

Tinjum, J. M., Benson, C. H. & Blotz, L. R. (1997), 'Soil-Water Characteristic Curves for Compacted Clays', *Journal of Geotechnical and Geoenvironmental Engineering* **123**(11), 1060–1069.

Toll, D. G. & Ali Rahman, Z. (2017), 'Critical state shear strength of an unsaturated artificially cemented sand', *Géotechnique* **67**(3), 208–215.

Tripathy, S., Elgabu, H. & Thomas, H. R. (2012), 'Matric suction measurement of unsaturated soils with null-type axis-translation technique', *Geotechnical Testing Journal* **35**(1), 91–102.

Tripathy, S., Sridharan, A. & Schanz, T. (2004), 'Swelling pressures of compacted bentonites from diffuse double layer theory', *Canadian Geotechnical Journal* **41**(3), 437–450.

Tripathy, S., Tadza, M. Y. M. & Thomas, H. R. (2014), 'Soil-water characteristic curves of clays', *Canadian Geotechnical Journal* **51**(8), 869–883.

Upreti, K. & Leong, E.-C. (2018), Measurement of Soil Shrinkage Curve Using Photogrammetry, *in* 'PanAm Unsaturated Soils 2017', American Society of Civil Engineers, Dallas, Texas, pp. 71–80.

Van Genuchten, M. T. (1980), 'A closed-form equation for predicting the hydraulic conductivity of unsaturated soils', *Soil Science Society of America Journal* **44**(5), 892–898.

Vanapalli, S. K. & Fredlund, D. G. (1997), Interpretation of undrained shear strength of unsaturated soils in terms of stress state variables, *in* 'Proceedings of the 3rd Brazilian Symposium on Unsaturated Soils, Rio de Janeiro', pp. 22–25.

Vanapalli, S. K. & Fredlund, D. G. (2000), Comparison of Different Procedures to Predict Unsaturated Soil Shear Strength, *in* 'Advances in Unsaturated Geotechnics', American Society of Civil Engineers, Denver, Colorado, United States, pp. 195–209.

Vanapalli, S. K., Fredlund, D. G. & Pufahl, D. E. (1999), 'The influence of soil structure and stress history on the soil–water characteristics of a compacted till', *Géotechnique* **49**(2), 143–159.

Vanapalli, S. K., Fredlund, D. G., Pufahl, D. E. & Clifton, A. W. (1996), 'Model for the prediction of shear strength with respect to soil suction', *Canadian geotechnical journal* **33**(3), 379–392.

Vanapalli, S. K., Nicotera, M. V. & Sharma, R. S. (2009), Axis Translation and Negative Water Column Techniques for Suction Control, *in* A. Tarantino, E. Romero & Y.-J. Cui, eds, 'Laboratory and Field Testing of Unsaturated Soils', Springer Netherlands, Dordrecht, pp. 33–48.

Vanapalli, S. K., Sillers, W. S. & Fredlund, M. D. (1998), The meaning and relevance of residual state to unsaturated soils, *in* '51st Canadian Geotechnical Conference', Vol. 8, Edmonton Alberta, Canada.

Vesga, L. F. (2005), Mechanics of Crack Propagation in Clays under Dynamic Loading, PhD thesis, University of Pittsburgh.

Vesga, L. F. (2008), 'Equivalent Effective Stress and Compressibility of Unsaturated Kaolinite Clay Subjected to Drying', *Journal of Geotechnical and Geoenvironmental Engineering* **134**(3), 366–378.

Wanatowski, D. (2005), Strain Softening and Instability of Sand under Plane-Strain Conditions, PhD thesis, Nanyang Technological University.

Wendroth, O., Ehlers, W., Hopmans, J. W., Kage, H., Halbertsma, J. & Wösten, J. H. M. (1993), 'Reevaluation of the Evaporation Method for Determining Hydraulic Functions in Unsaturated Soils', *Soil Science Society of America Journal* **57**(6), 1436–1443.

Wijaya, M. & Leong, E. C. (2014), Modelling shrinkage behaviour of soft soils, *in* 'Proceedings of Soft Soils 2014', Soft Soil Engineering International Conference, Bandung, Indonesia.

Wijaya, M. & Leong, E. C. (2016), 'Performance of high-capacity tensiometer in constant water content oedometer test', *International Journal of Geo-Engineering* **7**(1), 13.

Wijaya, M., Leong, E. C. & Rahardjo, H. (2015), 'Effect of shrinkage on air-entry value of soils', *Soils and Foundations* **55**(1), 166–180.

Wind, G. P. (1966), Capillary conductivity data estimated by a simple method, Technical report.

Yang, H., Rahardjo, H., Leong, E.-C. & Fredlund, D. G. (2004), 'Factors affecting drying and wetting soil-water characteristic curves of sandy soils', *Canadian Geotechnical Journal* **41**(5), 908–920.

Yin, P. & Vanapalli, S. K. (2018), 'Model for predicting tensile strength of unsaturated cohesionless soils', *Canadian Geotechnical Journal* **55**(9), 1313–1333.

Zhai, Q. & Rahardjo, H. (2012), 'Determination of soil–water characteristic curve variables', *Computers and Geotechnics* **42**, 37–43.

Zhang, C. & Lu, N. (2020), 'Unified effective stress equation for soil', *Journal of Engineering Mechanics* **146**(2), 04019135.

Zhang, J., Niu, G., Li, X. & Sun, D. (2020), 'Hydro-mechanical behavior of expansive soils with different dry densities over a wide suction range', *Acta Geotechnica* **15**, 265–278.

Zhou, A., Huang, R. & Sheng, D. (2016), 'Capillary water retention curve and shear strength of unsaturated soils', *Canadian Geotechnical Journal* **53**(6), 974–987.

Zhou, W.-H., Xu, X. & Garg, A. (2016), 'Measurement of unsaturated shear strength parameters of silty sand and its correlation with unconfined compressive strength', *Measurement* **93**, 351–358.

A. Appendix A

A.1. MIP

The determination of the pore size distribution (PSD) by MIP was conducted in the construction chemistry laboratory at RUB. Cuboid-shaped specimens, measuring 5 mm on each side, were cut from the prepared samples at specific water content values. A prerequisite for MIP analysis is that the samples must be thoroughly dried without disturbing the pore structure. To achieve this, freeze-drying was employed. The sample preparation for MIP involved two key steps:

- Step 1: Begin by preparing a liquid nitrogen chamber (see Fig. A.1a) and a plastic cup (see Fig. A.1b) with a perforated lid. The samples, each measuring approximately 5 mm in all dimensions, were rapidly submerged into the liquid nitrogen. The presence of water within the samples initially caused bubble formation. The aim of this step was to transition the water within the sample from the liquid phase to the solid phase. Once the bubbles ceased - indicating that the water within the sample had completely solidified - the sample was carefully removed, placed into the plastic cup, and sealed with the perforated lid.
- Step 2: The plastic cups containing the samples were then placed into a freeze dryer (see Fig. A.1b), which was set to a pressure of 1 mbar. In the freeze dryer the water within the sample was sublimated directly from the solid phase to the gas phase. The samples were vacuumed in the freeze dryer for 24 hours to ensure a thorough reduction of ambient gas pressure. Afterward, the samples were carefully retrieved from the freeze dryer and stored in sealed glass jars to prevent moisture absorption. The samples were subsequently transferred to the chemical laboratory for pore size distribution analysis using two pressure porosimeters.

Figure A.1 shows the freeze dryer device and tools used in this study to prepare the sample for MIP determination.

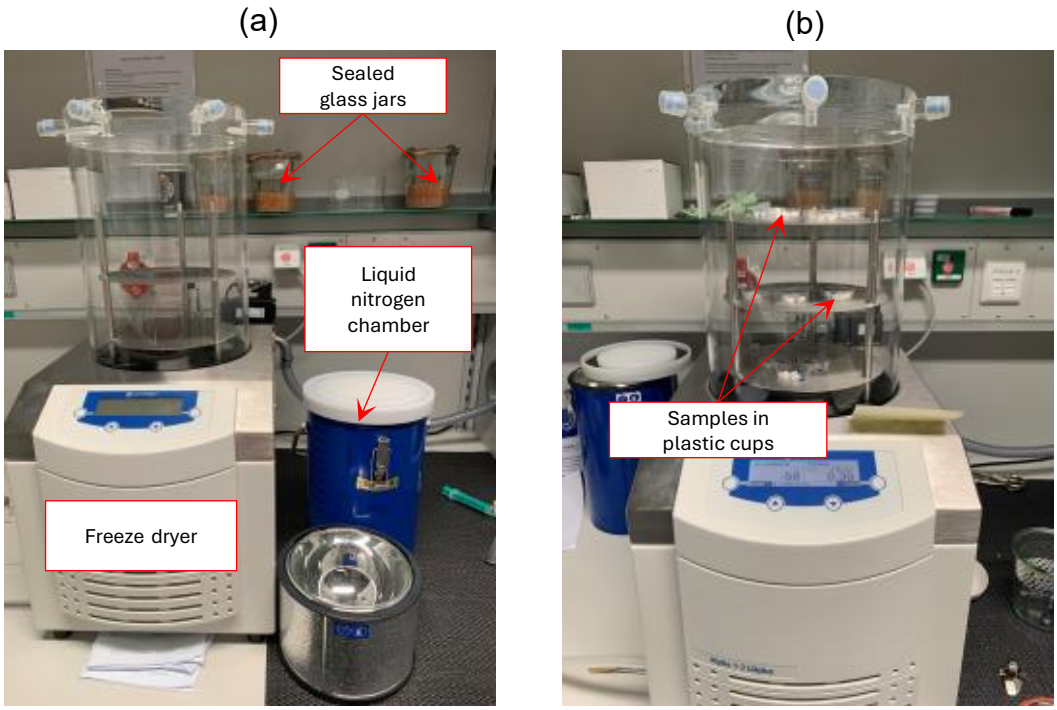

Figure A.1.: The freeze dryer device used in this study

A.2. Installation and saturation of the ceramic discs for biaxial compression tests

The installation and saturation procedure for the ceramic discs used in the biaxial compression tests is as follows:

- Step 1: The metal plates with ceramic discs were first placed in a plastic container filled with deaired water. The container was then placed inside a chamber connected to a vacuum pump, which was operated for 24 hours to minimize air entrapment within the ceramic discs. Subsequently, the metal plates were removed from the container and mounted onto the top cap and bottom platen of the biaxial device, as described in Step 2.
- Step 2: The water line beneath the ceramic discs of the top cap and bottom platen was connected to a twin burette (volume change indicator) filled with deaired, distilled water, with the connecting pipes also filled with water. One end of the twin burette was attached to the water line, while the other end was connected to an air pressure regulator on the pressure control panel. The metal plates were mounted

onto the top cap and bottom platen using six screws, with all assembly performed underwater to avoid air entrapment between components. During assembly, a pressure of 10 kPa was applied to the twin burette to ensure continuity of the water phase in the pressure line. Figure A.2 illustrates the top cap and bottom platen during the assembly. After the screws were securely fastened, the top cap and bottom platen were placed inside the outer cell, which was then sealed.

- Step 3: The outer cell was filled with deaired water to a level approximately 2 cm below the top cap, ensuring that both the top cap and bottom platen were fully submerged. The valves connecting the water pressure line beneath the ceramic discs to the twin burette were kept open, while the air pressure line from the control panel was connected to a valve on the outer cell's top cap. Air pressure was then gradually increased beyond the air-entry value of the ceramic disc, applying pressure above the water surface and thereby indirectly pressurizing the water. As a result, water flowed from the outer cell through the ceramic disc into the twin burette. The flow rate was monitored against the applied air pressure, allowing the permeability of the ceramic disc to be assessed and ensuring that no leaks or cracks were present in the assembly. This pressure was maintained for 8 hours, during which water continuously flowed through the discs into the burette, ensuring full saturation and the removal of any entrapped air bubbles from the water pressure line.
- Step 4: After 8 hours, the air pressure was gradually reduced to atmospheric levels, and water was drained from the outer cell. The water line remained connected, and a water pressure of 10 kPa was continuously maintained.

A.3. Installation and saturation of the ceramic discs used in direct shear tests

The installation and saturation procedure for the ceramic discs used in direct shear tests is as follows:

- Step 1: The metal plate with the ceramic disc were first placed in a plastic container filled with deaired water. The container was then placed inside a chamber connected to a vacuum pump, which was operated for 24 hours to minimize air entrapment within the ceramic discs.

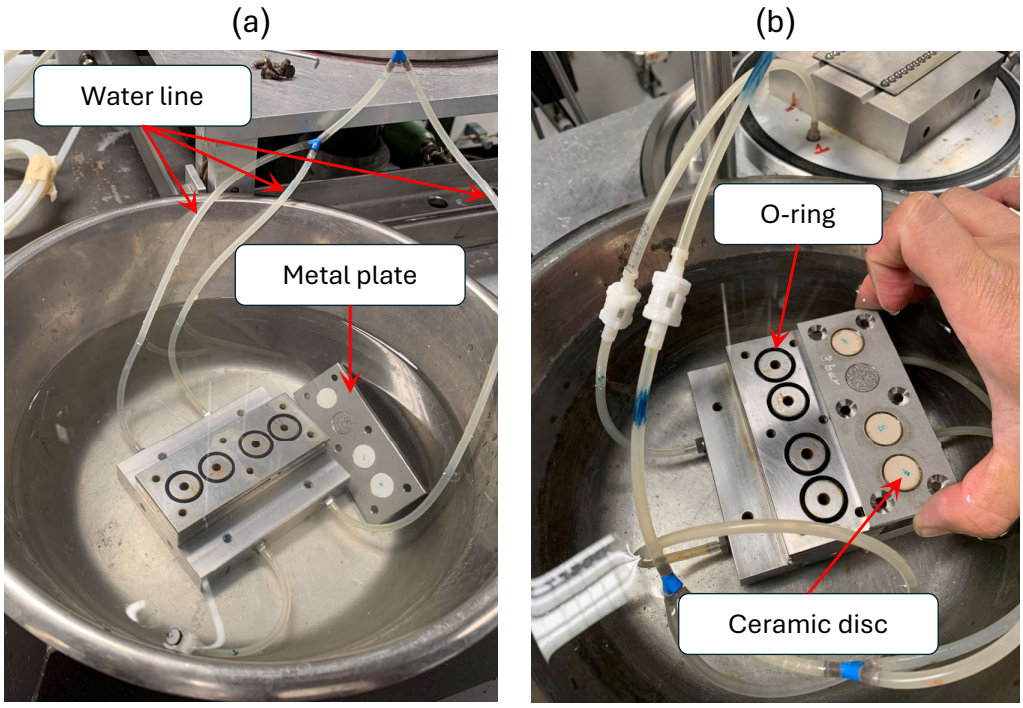

Figure A.2.: Assembly of the metal plate to the bottom platen): (a) preparation of the assembly, and (b) during the assembly

- Step 2: Following the vacuum process, the metal plate with the ceramic disc was installed in the lower half of the shear box. A water line beneath the ceramic disc was connected to an open burette. After that deaired water was poured into the cell to a level approximately 3 cm above the ceramic disc. The cell was then assembled and carefully sealed.
- Step 3: Air pressure was applied through a valve on the top cap of the cell and gradually increased to 400 kPa, exceeding the ceramic disc's air-entry value (AEV = 3 bar). This pressure, applied above the water surface, forced water to flow from the cell through the ceramic disc into the open burette. The pressure was maintained for 3 hours, during which continuous water flow through the disc ensured complete saturation of the ceramic disc.
- Step 4: Once the ceramic disc was fully saturated, the air pressure was gradually reduced to atmospheric levels. The water line remained connected, with a water level maintained at one meter, corresponding to a water pressure of 10 kPa.

B. Appendix B

B.1. Effect of direct shear sample size on shear strength parameters at saturated conditions

Figure B.1a presents the shear stress-horizontal displacement curves for both sample sizes (6 x 6 x 2 cm and 10 x 10 x 2 cm) under saturated conditions, while Figure B.1b illustrates the variation in shear strength as a function of net normal stress for both series. In general, at a given net normal stress, the shear strength of the 10 x 10 x 2 cm samples is higher than that of the 6 x 6 x 2 cm samples. Additionally, the cohesion of the larger samples (c'_0 = 59.5 kPa) is significantly higher than that of the smaller samples (c'_0 = 3.1 kPa), whereas the friction angle for the larger samples (φ'_0 = 8.7°) is lower than that of the smaller samples (φ'_0 = 19.1°).

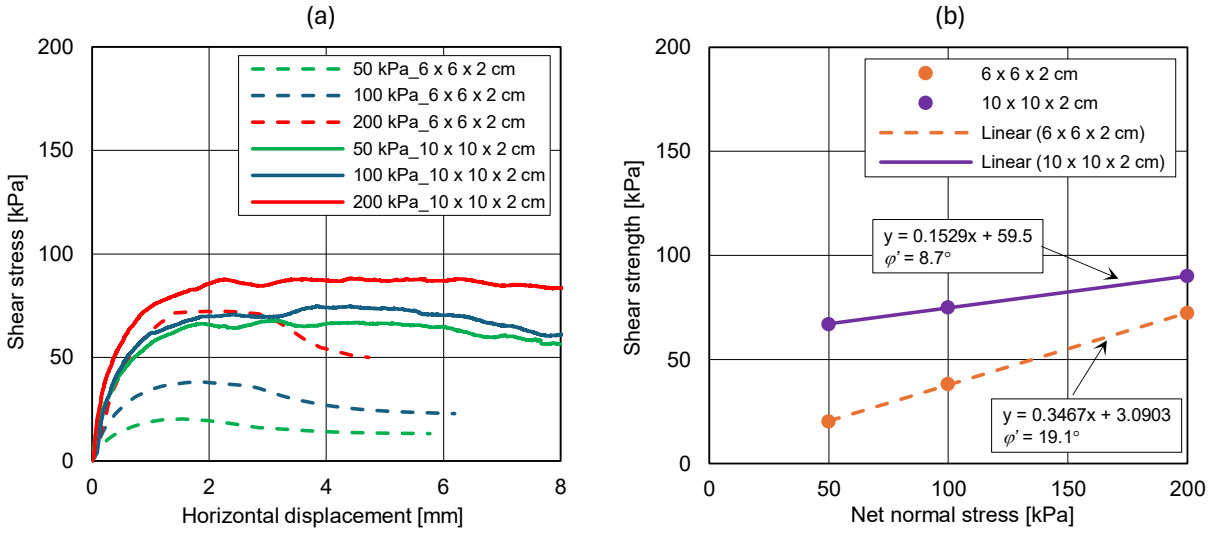

Figure B.1.: Comparison of the direct shear test results at saturated conditions from two sizes of shear boxes (6 x 6 x 2 cm and 10 x 10 x 2 cm): (a) shear stress vs. horizontal displacement, and (b) shear strength vs. net normal stress

Schriftenreihe des Lehrstuhls für Bodenmachanik, Grundbau und Umweltgeotechnik der Ruhr-Universität Bochum

Herausgeber: H.L. Jessberger

1 (1979) **Hans Ludwig Jessberger**
Grundbau und Bodenmechanik an der Ruhr-Universität Bochum

2 (1978) **Joachim Klein**
Nichtlineares Kriechen von künstlich gefrorenem Emschermergel

3 (1979) **Heinz-Joachim Gödecke**
Die Dynamische Intensivverdichtung wenig wasserdurchlässiger Böden

4 (1979) **Poul V. Lade**
Three Dimensional Stress-Strain Behaviour and Modeling of Soils

5 (1979) **Roland Pusch**
Creep of soils

6 (1979) **Norbert Diekmann**
Zeitabhängiges, nichtlineares Spannungs-Verformungsverhalten von gefrorenem Schluff unter triaxialer Belastung

7 (1979) **Rudolf Dörr**
Zeitabhängiges Setzungsverhalten von Gründungen in Schnee, Firn und Eis der Antarktis am Beispiel der deutschen Georg-von-Neumayer- und Filchner-Station

8 (1984) **Ulrich Güttler**
Beurteilung des Steifigkeits- und Nachverdichtungsverhaltens von ungebundenen Mineralstoffen

9 (1986) **Peter Jordan**
Einfluss der Belastungsfrequenz und der partiellen Entwässerungsmöglichkeiten auf die Verflüssigung von Feinsand

10 (1986) **Eugen Makowski**
Modellierung der künstlichen Bodenvereisung im grundwasserdurchströmten Untergrund mit der Methode der finiten Elemente

11 (1986) **Reinhard A. Beine**
Verdichtungswirkung der Fallmasse auf Lastausbreitung in nichtbindigem Boden bei der Dynamischen Intensivverdichtung

12 (1986) **Wolfgang Ebel**
Einfluss des Spannungspfades auf das Spannungs-Verformungsverhalten von gefrorenem Schluff im Hinblick auf die Berechnung von Gefrierschächten

13 (1987) **Uwe Stoffers**
Berechnungen und Zentrifugen-Modellversuche zur Verformungsabhängigkeit der Ausbaubeanspruchung von Tunnelausbauten in Lockergestein

14 (1988) **Gerhard Thiel**
Steifigkeit und Dämpfung von wassergesättigtem Feinsand unter Erdbebenbelastung

15 (1991) **Mahmud Thaher**
Tragverhalten von Pfahl-Platten-Gründungen im bindigen Baugrund,
Berechnungsmodelle und Zentrifugen-Modellversuche

16 (1992) **Rainer Scherbeck**
Geotechnisches Verhalten mineralischer Deponieabdichtungsschichten
bei ungleichförmiger Verformungswirkung

17 (1992) **Martin M. Bizialiele**
Torsional Cyclic Loading Response of a Single Pile in Sand

18 (1993) **Michael Kotthaus**
Zum Tragverhalten von horizontal belasteten Pfahlreihen aus langen Pfählen in Sand

19 (1993) **Ulrich Mann**
Stofftransport durch mineralische Deponieabdichtungen:
Versuchsmethodik und Berechnungsverfahren

20 (1992) **Festschrift anlässlich des 60. Geburtstages von**
Prof. Dr.-Ing. H. L. Jessberger
20 Jahre Grundbau und Bodenmechanik an der Ruhr-Universität Bochum

21 (1993) **Stephan Demmert**
Analyse des Emissionsverhaltens einer Kombinationsabdichtung im Rahmen der
Risikobetrachtung von Abfalldeponien

22 (1994) **Diethard König**
Beanspruchung von Tunnel- und Schachtausbauten in kohäsionslosem Lockergestein
unter Berücksichtigung der Verformung im Boden

23 (1995) **Thomas Neteler**
Bewertungsmodell für die nutzungsbezogene Auswahl von Verfahren zur Altlastensanierung

24 (1995) **Ralph Kockel**
Scherfestigkeit von Mischabfall im Hinblick auf die Standsicherheit von Deponien

25 (1996) **Jan Laue**
Zur Setzung von Flachfundamenten auf Sand unter wiederholten Lastereignissen

26 (1996) **Gunnar Heibrock**
Zur Rissbildung durch Austrocknung in mineralischen Abdichtungsschichten
an der Basis von Deponien

27 (1996) **Thomas Siemer**
Zentrifugen-Modellversuche zur dynamischen Wechselwirkung zwischen Bauwerken
und Baugrund infolge stoßartiger Belastung

28 (1996) **Viswanadham V. S. Bhamidipati**
Geosynthetic Reinforced Mineral Sealing Layers of Landfills

29 (1997) **Frank Trappmann**
Abschätzung von technischem Risiko und Energiebedarf bei Sanierungsmaßnahmen
für Altlasten

30 (1997) **André Schürmann**
Zum Erddruck auf unverankerte flexible Verbauwände

31 (1997) **Jessberger, H. L. (Herausgeber)**
Environment Geotechnics, Report of ISSMGE Technical Committee TC 5
on Environmental Geotechnics

Herausgeber: Th. Triantafyllidis

32 (2000) **Triantafyllidis, Th. (Herausgeber)**
Boden unter fast zyklischer Belastung: Erfahrung und Forschungsergebnisse (Workshop)

33 (2002) **Christof Gehle**
Bruch- und Scherverhalten von Gesteinstrennflächen mit dazwischenliegenden Materialbrücken

34 (2003) **Andrzej Niemunis**
Extended hypoplastic models for soils

35 (2004) **Christiane Hof**
Über das Verpressankertragverhalten unter kalklösendem Kohlensäureangriff

36 (2004) **René Schäfer**
Einfluss der Herstellungsmethode auf das Verformungsverhalten von Schlitzwänden in weichen bindigen Böden

37 (2005) **Henning Wolf**
Zur Scherfugenbänderung granularer Materialien unter Extensionsbeanspruchung

38 (2005) **Torsten Wichtmann**
Explicit accumulation model for non-cohesive soils under cyclic loading

39 (2008) **Christoph M. Loreck**
Die Entwicklung des Frischbetondruckes bei der Herstellung von Schlitzwänden

40 (2008) **Igor Arsic**
Über die Bettung von Rohrleitungen in Flüssigböden

41 (2009) **Anna Arwanitaki**
Über das Kontaktverhalten zwischen einer Zweiphasenschlitzwand und nichtbindigen Böden

Herausgeber: T. Schanz

42 (2009) **Yvonne Lins**
Hydro-Mechanical Properties of Partially Saturated Sand

43 (2010) **Tom Schanz (Herausgeber)**
Geotechnische Herausforderungen beim Umbau des Emscher-Systems
Beiträge zum RuhrGeo Tag 2010

44 (2010) **Jamal Alabdullah**
Testing Unsaturated Soil for Plane Strain Conditions: A New Double-Wall Biaxial Device

45 (2011) **Lars Röchter**
Systeme paralleler Scherbänder unter Extension im ebenen Verformungszustand

46 (2011) **Yasir Al-Badran**
Volumetric Yielding Behavior of Unsaturated Fine-Grained Soils

47 (2011) **Usque ad finem**
Selected research papers

48 (2012) **Muhammad Ibrar Khan**
Hydraulic Conductivity of Moderate and Highly Dense Expansive Clays

49 (2014) **Long Nguyen-Tuan**
Coupled Thermo-Hydro-Mechanical Analysis: Experimental and Back Analysis

50 (2014) **Tom Schanz (Herausgeber)**
Ende des Steinkohlenbergbaus im Ruhrrevier: Realitäa und Perspektiven für die Geotechnik Beiträge zum RuhrGeo Tag 2014

51 (2014) **Usque ad finem**
Selected research papers

52 (2014) **Houman Soleimani Fard**
Study on the Hydro-Mechanical Behaviour of Fiber Reinforced Fine Grained Soils with Application to the Preservation of Historical Monuments

53 (2014) **Wiebke Baille**
Hydro-Mechanical Behavior of Clays - Significance of Mineralogy

54 (2014) **Qasim Abdulkarem Jassim Al-Obaidi**
Hydro-Mechanical Behavior of Collapsible Soils

55 (2015) **Veselin Zarev**
Model Identification for the Adaption of Numerical Simulation Models - Application to Mechanized Shield Tunneling

56 (2015) **Meisam Goudarzy**
Micro and Macro Mechanical Assessment of Small and Intermediate Strain Properties of Granular Material

57 (2016) **Oliver Detert**
Analyse einer selbstregulierenden interaktiven Membrangründung für Schüttkörper auf geringtragfähigen Böden

58 (2016) **Yang Yang**
Analyses of Heat Transfer and Temperature-induced Behaviour in Geotechnics

59 (2016) **Alborz Pourzargar**
Application of suction stress concept to partially saturated compacted soils

60 (2017) **Hanna Haase**
Multiscale analysis of clay-polymer composites for Geoenvironmental applications

61 (2017) **Kavan Khaledi**
Constitutive modeling of rock salt with application to energy storage caverns

62 (2017) **Nina Silvia Müthing**
On the consolidation behavior of fine-grained soils under cyclic loading

63 (2017) **Elham Mahmoudi**
Probabilistic analysis of a rock salt cavern with application to energy storage systems

64 (2017) **Negar Rahemi**
Evaluation of liquefaction behavior of sandy soils using critical state soil mechanics and instability concept

65 (2018) **Chenyang Zhao**
A contribution to modeling of mechanized tunnel excavation

66 (2019) **Tom Schanz (Herausgeber)**
Innovationen im Spezialtiefbau und in der Umweltgeotechnik
Geotechnik Beiträge zum RuhrGeo Tag 2014

67 (2019) **Linzhi Lang**
Hydro-Mechanical Behaviour of Bentonite-Based Materials Used for Disposal of Radioactive Wastes

68 (2019) **Usama Al-Anbaki**
Hydraulic Interaction of Soil and Nonwoven Geotextiles under Unsaturated Conditions

69 (2019) **Abhishek Rawat**
Coupled Hydro-mechanical Behavior of a Compacted Bentonite-Sand Mixture: Experimental and Numerical Investigations

Herausgeber: T. Wichtmann

70 (2019) **Mahmoud Qarmout**
Tunnel face stability using Kinematical Element Method (KEM)

71 (2021) **Raoul Hölter**
Optimal Experimental Design in Geotechnical Engineering

72 (2022) **Wolfgang Lieske**
Impact of polymer constitution on the hydro-mechanical behaviour of modified bentonite for the application in geotechnical and geoenvironmental engineering

73 (2022) **Patrick Staubach**
Contributions to the numerical modelling of pile installation processes and high-cyclic loading of soils

74 (2022) **Lingyun Li**
On the hydromechanical behaviour of loess and its effect on slope stability under rainfall infiltration

75 (2022) **Debdeep Sarkar**
Influence of particle characteristics on the behaviour of granular materials under static, cyclic and dynamic loading

76 (2023) **Torsten Wichtmann (Herausgeber)**
Umbau des Emscher-Systems - Geotechnische Erfahrungen
Beiträge zum RuhrGeo Tag 2023

77 (2023) **Abbas Farhat**
Fluidization and erosion of cemented granular materials. Experimental characterization and micromechanical simulation

78 (2023) **Andrea Geppetti**
Experimental and numerical investigations on the behaviour of tailing storage facilities under seismic loading

79 (2023) **Mohammad Hassan Sanayei**
Micromechanical modelling for the analysis of piping erosion in cemented soils for suction-assisted offshore foundations

80 (2024) **Christoph Schmüdderich**
Contributions to the stability assessment of slopes subjected to seismic loading

81 (2024) **Thomas Barciaga**
Constitutive modeling of natural clay with application to mechanized tunneling

82 (2024) **Cristian Rodriguez**
Contributions to the modelling of large deformations of soils: A particle-based approach

83 (2025) **Florian Christ**
Experimental investigations on the hydro-mechanical behaviour of clay shales for tunnelling relevant boundary conditions

84 (2025) **Alireza Jebeli**
On the influence of a heterogeneous pore structure on collapse behavior of sandy soils

85 (2025) **Maximilian Schoen**
Numerical analysis of tunnel excavation in swellable clay shales

86 (2025) **Qian Gu**
On the effects of grain shape, gradation, fabric and stress state on the small-strain stiffness of granular soils

87 (2025) **Cuong Manh Le**
Experimental validation of the effective stress concept in unsaturated soils using the suction stress approach across multiple test types and a wide suction range